



CATALYTIC ENHANCEMENT OF HYDRATION OF CO₂
USING NICKEL NANOPARTICLES FOR CARBON CAPTURE
AND STORAGE

A thesis submitted in partial fulfilment of the requirement for the degree of

Doctor of Philosophy (PhD) at Newcastle University

Gaurav Ashok Bhaduri

B.E. (Chemical)

NANOSCALE SCIENCE AND NANOTECHNOLOGY GROUP
SCHOOL OF CHEMICAL ENGINEERING AND ADVANCED MATERIALS
NEWCASTLE UNIVERSITY

UK

JULY 2015

Abstract:

The capture and storage of atmospheric CO₂ as mineral carbonates, is one of the safest ways to combat global warming. The slow CO₂ hydration rate is one limitation of the mineralization process. The current study presents the discovery of nickel nanoparticles (NiNPs) as a catalyst for enhancing the rate of CO₂ hydration for mineralization carbon capture and storage. The NiNPs at an optimum concentration of 30 ppm, increased the saturation concentration by three folds as compared with deionized water alone. The mechanism of the reaction on NiNPs surface is also proposed. The kinetics of catalysis of CO₂ hydration was additionally studied using stopped flow spectrophotometry and pH changes in buffer solution upon addition of saturated CO₂ solution. To distinguish between physical gas-liquid transfer and catalysis, other inorganic nanoparticles (NiO and Fe₂O₃) have been studied. The effect of CO₂ partial pressure on NiNPs catalysis was studied. Nickel nanowires (NiNWs) were synthesised and tested for catalysis of CO₂ hydration. The photocatalytic activity of NiNPs was evaluated under artificial solar irradiation compared with that in the dark. The results suggest that the surface plasmonic resonance (SPR) of NiNPs enhances the rate of water dissociation on the NiNPs surface leading to higher rate of CO₂ hydration under solar irradiation. The effect of temperature on the catalytic activity of NiNPs is evaluated. Optimum activity was observed at room temperature (20-30 °C). Application of NiNPs catalysis was investigated for CaCO₃ precipitation and the rate of CO₂ absorption in 50 wt% carbonate solutions. Vapour-liquid equilibrium studies of CO₂-H₂O in presence of nanoparticles (Ni, Fe₂O₃ and NiO) found that

the presence of nanoparticles decreases the surface tension of DI water, responsible for the increase in CO₂ saturation concentration. Additionally a novel method for mineralization of CO₂ using gypsum and sodium chloride was developed including design of a customized reactor.

Dedicated
to my
Maternal and (late) paternal grandmothers
Mrs J.T. Chakraborty and (Late) Mrs M.J. Bhaduri
for their strength and support and belief in me
AND
My parents Mr A.K. Bhaduri and Mrs I.A. Bhaduri
for helping chase my dream.

Acknowledgements:

I would like to take this opportunity to show my appreciation and gratitude to all the people who have made this work possible. Firstly I would like to thank God for giving me good health and patience to keep striving and chase my dreams. I would like to thank my supervisor Dr Lidija Siller for her endless support, guidance and care during the last three years of my PhD studies at Newcastle.

I would also like to extend my thanks to Dr Jonathan Lee, Dr Alasdair Charles, Dr Mohammed A.H Alamiry, Dr Mohammed A. Salem, Prof Galip Akay, Dr Kamila Bhodoo and Dr Jarka Glassey for their help and support during the studies. I would like to thank Prof Richard Henderson, Prof David Fulton, Dr Benjamin Horrocks, Dr Emier Tuit and Dr Scott Watson from the School of Chemistry for their help and permission to use lab-space and equipments. I would like to thank Dr Michel R.C. Hunt and Dr Budhika G. Mendis from Durham University for their help. I would like to thank Prof Wenfeng Shugguan, Dr Jian Yuan, Mr Zou Guchu all of Prof Shugguan's research group from Shanghai Jiao Tong University, P.R. China, for their help, support and hospitality. I would like to thank Dr B.D. Kulkarni from National Chemical Laboratory, India for his help and support for the silver nanoparticle work.

I would also like to thank all our non-teaching and technical staff at the School of Chemical Engineering and Advanced Materials including, Mrs Kay Garrick, Ms Justine McGruther, Mr Craig Clark, Ms Emma Bell, Mrs Angelina Coutts, Ms Julie Coomber, Mr Rob Dixon, Mr Paul Stirling, Mr Chris Dunn and the

most important person Mr Neville Dickman who helped me make all the small and tiny rigs and pieces for the experimentation.

I would like to thank Dr Sam Niel and Dr Daniel Colgate from the Business Development, Newcastle University and Dr Daniel Woollaston from Harrison Goddard Foote LLP for their help with the patent applications.

I would like to thank all my group members Dr Ross Little, Dr Sunthon Piticharoenphun, Dr Yayuk Astuti, Mrs Naglaa H.S. Nasralla, Mrs Khamael Abulnaja, Mr Xiao Han, Ms Jiabin Wang and Mr Khalil Hassan for the help support and fun times we have had together in the last few years. I would also like to thank the MEng and MS students Mr Bilal Mujaffar, Mr Shun Toei, Mr James Warrell, Ms Samantha McGarth, Ms Fay Williamson, Mr Richard Sandiwx and Mr Patrick Corsby for the fun time and giving me an opportunity to teach them and learn a lot myself.

I would like to thank School of Chemical Engineering and Advanced Materials for the Teaching Scholarship. I would also like to thank Engineering and Physical Science Research Council for funding the photocatalytic research conducted in collaboration with Shanghai Jiao Tong University.

Last but not the least I would like to thank my parents for their endless support during the studies. All my friends that I met here at Newcastle and back home in India for their help and support.

Patents and Publications

Patents:

1. L. Šiller, G.A. Bhaduri, "Carbon capture", WO2013/171480 (A3)

Publications: (related to the thesis)

1. G.A. Bhaduri, L. Šiller, "Nickel nanoparticles catalyse reversible hydration of carbon dioxide for mineralization carbon capture and storage" Catal. Sci. Technol., 3, 2013, 1234.
2. G.A. Bhaduri, R. Henderson, L. Šiller, "Reply to the 'Comment on "Nickel nanoparticles catalyse reversible hydration of carbon dioxide for mineralization carbon capture and storage"' by D. Britt, Catal. Sci. Technol., 2013, 3, DOI: 10.1039/C3CY00142C", Catal. Sci. Technol., 3, 2013, 2197
3. G.A. Bhaduri, M.A.H. Alamiry, L. Šiller, "Nickel nanoparticles for enhancing carbon capture", J Nanomater, Article reference number 581785

Publications: (not included in the thesis)

1. G.A. Bhaduri, R. Little, R.B. Khomane, S.U. Lokhande, B.D. Kulkarni, B.G. Mendis, L. Šiller, "Green synthesis of silver nanoparticles using sunlight", J. Photochem. Photobio. A, Chem., 358, 2013, 1.
2. X. Han, F. Williamson, G.A. Bhaduri, A. Harvey, L. Šiller, "Synthesis and characterization of ambient pressure dried composites of silica and Aerogel matrix and embedded nickel nanoparticles", J Supercritical Fluids, in press. doi:10.1016/j.supflu.2015.06.017

Table of Contents

Abstract	i
Acknowledgement	iv
Table of contents	vii
List of figures	xvi
List of tables	xxix
List of abbreviations.....	xxx
1. Chapter 1: Introduction	1
1.1. Greenhouse gases: types and sources	2
1.2. Governmental framework and policies	4
1.3. Technological developments in CCS	7
1.4. Aim of this work	9
1.5. Summary of the chapters	10
References	13
2. Chapter 2: Carbon capture and CO ₂ mineralization: review	16
2.1. Carbon cycle, CO ₂ emissions and global warming	17
2.2. Carbon Capture and Storage: An Overview	18
2.2.1. CO ₂ capture technology	18
2.2.2. Capture process	21

2.2.3. Storage of CO ₂	22
2.2.3.1. Selection of Mineral source	27
2.2.3.2. Dissolution/Activation of metal ions in mineral sources	29
2.2.3.3. Hydration of CO ₂ : non-catalytic and catalytic	33
2.2.3.4. Precipitation of mineral carbonate	47
References.....	49
3. Chapter 3: Experimental methodology	80
3.1. Chemical and equipment used for experimentation	81
3.2. Experimental procedure	82
3.2.1. Preparation of nickel nanoparticle (NiNPs) suspension	82
3.2.2. CO ₂ saturation in DI water and nanoparticle suspension	82
3.2.3. CO ₂ absorption in DI water and nanoparticle suspension (gas-liquid reactions)	83
3.2.4. Leaching of Ni ²⁺ ions in carbonic acid solution and influence on CO ₂ hydration	87
3.2.5. CO ₂ hydration kinetic study using saturated CO ₂ solution in DI water (liquid-liquid reaction)	90
3.2.5.1. CO ₂ hydration kinetics using stopped flow spectrophotometer	91

3.2.5.2.	CO ₂ hydration kinetics using pH change method by saturated CO ₂ solution	94
3.2.6.	Carbonate absorption of CO ₂	95
3.2.7.	Synthesis of Nickel nanowires (NiNWs)	96
3.2.8.	Photo-catalysed hydration of CO ₂ by NiNPs	96
3.2.9.	Role of temperature on CO ₂ hydration reaction	99
3.2.10.	Calcium carbonate precipitation experiment	99
3.2.11.	Absorption of CO ₂ in potassium carbonate solution	100
3.2.12.	Heat treatment of nickel nanoparticles and its effect on catalytic CO ₂ hydration reaction	101
3.2.13.	Mineralization of CO ₂ using gypsum and sodium chloride ..	101
3.2.14.	Validation of mass transport of ions in bridge reactor	105
3.3.	Characterization techniques	106
3.3.1.	High-resolution and transmission electron microscopy	107
3.3.2.	Scanning electron microscopy	109
3.3.3.	Energy dispersive X-ray spectroscopy	111
3.3.4.	Selected area electron diffraction	112
3.3.5.	X-ray diffraction	115
3.3.6.	X-ray photoelectron spectroscopy	118

3.3.7.	Fourier transform infrared spectroscopy	124
3.3.8.	Dynamic light scattering	128
3.3.9.	Zeta potential measurement	132
3.3.10.	UV-Visible spectroscopy	134
3.3.11.	Surface area determination of nanoparticles	136
	References	140
4.	Chapter 4: Catalytic activity of NiNPs for hydration of CO ₂ (Part I)	145
4.1.	HRTEM and XRD of NiNPs	146
4.2.	CO ₂ saturation experiments	148
4.3.	CO ₂ hydration kinetics (gas-liquid reaction)	150
4.4.	Chemical characterization of the NiNPs surface before and after CO ₂ bubbling	156
4.5.	Mechanism. of hydration reaction by NiNPs	159
4.6.	Conclusion	160
	References	161
5.	Chapter 5: Catalytic activity of NiNPs for hydration of CO ₂ (Part II)	164
5.1.	Comment by David Britt	165
5.2.	Stopped flow spectrophotometric analysis of reaction kinetics	165

5.3. CO ₂ hydration kinetics using pH change method using saturated CO ₂ solution	167
5.4. NiNPs enhancement of CO ₂ absorption kinetics in carbonate solutions	168
5.5. Comparison of catalytic activity of different inorganic nanoparticles for CO ₂ hydration	171
5.5.1. HRTEM and XRD of the Fe ₂ O ₃ and NiO nanoparticles	171
5.5.2. CO ₂ saturation and CO ₂ hydration kinetics	174
5.5.3. Chemical characterization of the oxide nanoparticle surface before and after CO ₂ bubbling	182
5.6. Effect of partial pressure of CO ₂ on NiNPs catalysis	187
5.7. Catalytic activity if synthesised nickel nanowires for hydration of CO ₂	189
5.7.1. HRTEM, SEM and XRD of nickel nanowires	189
5.7.2. CO ₂ saturation and catalytic activity of NiNWs for hydration of CO ₂	191
5.7.3. Chemical characterization of NiNWs surfaces before and after CO ₂ bubbling	192
5.8. Conclusion	195
References	196

6. Chapter 6: Catalytic activity of NiNPs for hydration of CO ₂ (Part III): Photo-catalysis and temperature dependence	200
6.1. Photo-catalysed hydration of CO ₂ by NiNPs	201
6.1.1. CO ₂ hydration kinetics in absence and presence of light (with and without IR filter)	201
6.1.2. Chemical characterization of the NiNPs before and after CO ₂ bubbling	204
6.1.3. Discussion on photochemical effect on hydration of CO ₂ (catalytic and non-catalytic)	205
6.2. Temperature dependent study of kinetics of CO ₂ hydration	207
6.2.1. Effect of temperature on the saturation of CO ₂ in presence of NiNPs	207
6.2.2. Kinetic study of CO ₂ hydration at different temperatures	208
6.3. Conclusions	210
References	212
7. Chapter 7: Catalytic activity of NiNPs for hydration of CO ₂ (Part IV): Possible applications	216
7.1. CaCO ₃ precipitation yields and analysis	216
7.2. Enhancement of CO ₂ absorption rate in 50 wt% potassium carbonate solution	219

7.3. Temperature treatment of NiNPs	222
7.3.1. Chemical characterization of NiNPs after temperature treatment	222
7.3.2. Catalytic activity of NiNPs for CO ₂ hydration	225
7.4. Conclusion	226
References	227
8. Chapter 8: Vapour-liquid equilibrium of CO ₂ -H ₂ O system in presence of nanoparticles	229
8.1. Vapour-liquid equilibrium of CO ₂ -H ₂ O	229
8.2. CO ₂ -H ₂ O equilibrium in nanoparticle suspensions	231
8.3. Distinguishing between adsorbed and free CO _{2(aq)} in NiNPs suspension	233
8.4. Effect of temperature on CO ₂ equilibrium concentration in NiNPs suspension	234
8.5. Discussion on VLE of CO ₂ -H ₂ O system in presence of nanoparticles	235
8.6. Conclusion	238
References	239
9. Chapter 9: Mineralization of CO ₂ using gypsum and sodium chloride in novel bridge reactor	241
9.1. Mineralization of CO ₂ using “Bridge Reactor”	241

9.2. Chemical characterization of precipitate obtained in bridge reactor	242
9.3. Precipitation yields of CaCO ₂ in bridge reactor and control	244
9.4. Mass transfer studied in the “Bridge Reactor”	248
9.5. Conclusions	252
References	253
10. Chapter 10: Conclusion and Roadmap to the future.....	255
10.1. Overall conclusion of the thesis	255
10.2. Suggestions for future work	258
10.2.1. Application to mineralization of CO ₂	258
10.2.2. Immobilization of NiNPs	258
10.2.3. Optimization of transport properties of the bridge reactor ...	258
10.2.4. Study of the influence of nanoparticles on vapour-liquid equilibrium	259
References	260
11. Appendix	
11.1. Appendix-I : Calculations for concentration of CO ₂ using titration	261
11.2. Appendix II: Calculations and comparison of theoretical and experimental rate of hydration of CO ₂ (catalysed and uncatalysed)	263

11.3.	Appendix-III: The emission spectra of the solar simulator with and without filter has been presented as obtained from the manufacturer	265
11.4.	Appendix-IV: Curve fitting of CO ₂ absorption in 50% potassium carbonate solution in presence and absence of NiNPs	266

List of Figures

Figure No.	Title	Page No.
Figure 1.1	Schematic of the Earth's carbon-based bio-geo-chemical cycle pre industrial era and post-industrial era.	2
Figure 1.2	Percentage distribution of the various GHGs emitted by burning of fossil fuels.	3
Figure 1.3	CO ₂ emission in 2008 from various sectors.	4
Figure 1.4	Top five CO ₂ emitting countries of 2008 (published in 2010).	5
Figure 1.5	Changes in CO ₂ emissions in the year 2011-2012.	7
Figure 2.1	CO ₂ increase in the atmosphere since industrial revolution.	17
Figure 2.2	Various fuel combustion and capture mechanisms for CCS.	19
Figure 2.3	Estimation of storage capacity for CO ₂ in terms of time and quantity for various sequestration methods.	23
Figure 2.4	Classification of the mineralization process.	25
Figure 2.5	Schematic illustration of the mineral carbonation process (solid-gas) developed by Åbo Akademi University for 12 vol% CO ₂ gas content, AS- ammonium sulphate.	30

Figure 2.6	Reaction mechanism of Carbonic anhydrase for hydration of CO ₂ .	39
Figure 2.7	Carbonate equilibrium diagram.	47
Figure 3.1	Concentration profiles for gas-liquid-solid (very fine particles): diffusion of solute A and the surface reaction are parallel.	85
Figure 3.2	pH change when CO ₂ is bubbled in 0.1 M Tris-HCl buffer in absence (o) and presence of human carbonic anhydrase (HCA)(▼), bovine carbonic anhydrase (BCA) (◆), hemocytes from diseased shell (HDS) (□) and extra pallial fluid (EPF) (Δ) extracted from oysters (Crassostrea Gigas).	86
Figure 3.3	Pourbaix diagram for nickel at 25 °C (a) concentration of [Ni _(aq)] _{tot} = 10 ⁻⁶ M and (b) concentration of [Ni _(aq)] _{tot} = 10 ⁻⁸ M	88
Figure 3.3	Schematic of the operation of stopped flow spectrophotometer.	92
Figure 3.4	Example showing the fitting of the change in the absorbance of phenolphthalein (o) with an exponential function (solid line).	93
Figure 3.5	Experimental setup for the photochemical enhancement of NiNPs hydration of CO ₂ .	97

Figure 3.6	The experimental setup and chemical reactions involved for mineralization of CO ₂ using gypsum and sodium chloride.	102
Figure 3.7	Light projecting microscope (left) and electron microscope (right) compared schematically.	108
Figure 3.8	Signal type generated by electron-specimen interactions.	110
Figure 3.9	Schematic diagram showing the working of the SEM.	111
Figure 3.10	Schematic of the diffraction pattern obtained in SAED.	113
Figure 3.11	Schematic representation of $\theta/2\theta$ diffraction in Bragg-Brentano geometry.	115
Figure 3.12	Schematic explaining relevant energy terms in XPS of solid surfaces. An X-ray (of energy $h\nu$) generates a vacancy in the core electron in solid sample having a binding energy of E_B . The emitted electron has to overcome the work function ϕ_s of the sample and the energy is measured by the analyser with reference to the Fermi energy E_F of the emitted electron diminished by the work function ϕ_s and ϕ_W .	119
Figure 3.13	Universal curve of electron inelastic mean free path (λ) dependence on electron energy for different elements.	121
Figure 3.14	Schematic of a conventional XPS machine.	123

Figure 3.15	Schematic of the working of the FTIR.	125
Figure 3.16	Example of Fourier transform used for conversion of interferogram data to FTIR spectrum.	127
Figure 3.17	Various vibrations observed in a molecule on absorbance of IR light. The carbon atom is bonded to other atoms in the molecule (to have four bonds) not shown in figure. The figure also does not show the recoil of the C atom, which is necessary but is very small as compared to movement of the light H atoms.	128
Figure 3.18	Autocorrelation function obtained from the varying intensity of light obtained in the dynamic light scattering experiment from Zetasizer Nano ZS (Malverin, UK). (autocorrelation function on top, time dependent intensity on bottom left and particle size distribution on bottom right.)	131
Figure 3.19	Surface plasmonic resonance observed in silver nanoparticles and nanorods influenced by the incident electromagnetic field.	135
Figure 3.20	Different isotherms obtained from BET isotherm where there abscissa represents the relative partial pressure of the adsorbent (P/P_0) and the ordinate represents the amount of adsorbent adsorbed on the surface.	138

Figure 4.1	High Resolution Transmission Electron Microscopy images of NiNPs as purchased and particle size distribution.	146
Figure 4.2	Energy dispersive x-ray spectroscopy of NiNPs.	147
Figure 4.3	Selected area electron diffraction of the NiNPs.	147
Figure 4.4	X-ray diffraction pattern of Nickel nanoparticles.	147
Figure 4.5	Average values of increase in the amount of CO ₂ absorbed in aqueous suspension of NiNPs as a function of particle concentration at room temperature and atmospheric pressure.	148
Figure 4.6	Dynamic light scattering results of NiNPs at different concentrations suspended in DI water.	149
Figure 4.7	Average values of pH and ionic conductivity changes during bubbling of CO ₂ through DI water and aqueous NiNPs suspension. (a) pH change starting from pH above 6, (b) ionic conductivity change corresponding to pH change from above 6, (c) pH changes starting at pH value below 6 and (d) ionic conductivity change corresponding to pH change from below 6.	152
Figure 4.8	Average values of conductivity change of the Ni	154

	nanoparticle suspension compared to that of the blank and Ni suspension when bubbled with CO ₂ for (a) pH above 6 and (b) pH below 6.	
Figure 4.9	Average values of pH changes during bubbling of CO ₂ through DI water and 0.005 ppm Ni ²⁺ solution and 30 ppm NiNPs suspension.	156
Figure 4.10	XPS spectra of NiNPs before bubbling of CO ₂ ; (A) O 1s and (B) Ni 2p.	158
Figure 4.11	XPS spectra of NiNPs after bubbling with carbon dioxide; (A) O 1s, (B) Ni 2p _{3/2} and (C) C 1s.	160
Figure 4.12	Schematic of the reaction mechanism of hydration of CO ₂ by NiNPs.	160
Figure 5.1	Kinetic constants as a function of Na ₂ CO ₃ concentration and an example of the exponential fit for the data.	166
Figure 5.2	Average values of pH dependent hydration of CO ₂ in presence of NiNPs at different pH A) at pH 7 using Bis-Tris-HCl buffer and B) at pH 11.5 using sodium carbonate solution.	167
Figure 5.3	pH profiles during bubbling of CO ₂ in sodium and potassium carbonate solutions with and without NiNPs.	169

Figure 5.4	TEM images of the Fe ₂ O ₃ nanoparticles (a, b, and c) and particle size distribution (d).	172
Figure 5.5	TEM images of the NiO nanoparticles (a, b, and c) and particle size distribution (d).	173
Figure 5.6	X-ray diffraction pattern of a) Fe ₂ O ₃ NPs (Fe ₂ O ₃ planes in black and α-FeOOH planes in red) and b) NiONPs respectively.	174
Figure 5.7	Average values of increase in the saturation concentration of CO ₂ absorbed in aqueous suspension of Fe ₂ O ₃ NPs, NiONPs and NiNPs as a function of particle concentration at room temperature and atmospheric pressure.	175
Figure 5.8	Dynamic light scattering data obtained for different nanoparticles suspended in DI water at concentration of 10 ppm, 20 ppm, 30 ppm and 40 ppm respectively.	176
Figure 5.9	Zeta potential values for different nanoparticles (Fe ₂ O ₃ NPs- circles, NiNPs- squares, NiONPs-triangles) suspended in DI water at different concentration, measured at room temperature and atmospheric pressure.	178
Figure 5.10	Average values of pH change when CO ₂ is bubbled	180

	through DI water and 30 ppm concentration of a) Fe_2O_3 suspension, b) NiONPs suspension and c) NiNPs suspension.	
Figure 5.11	XPS spectrum of Fe_2O_3 NPs before (a. Fe2p, b. O1s) and after CO_2 bubbling (c. Fe2p and d. O1s).	183
Figure 5.12	XPS spectrum of Fe_2O_3 NPs after CO_2 bubbling a) Fe2p, b) O1s and c) C1s.	184
Figure 5.13	XPS spectrum of NiONPs before CO_2 bubbling (a. Ni2p, b. O1s) (c. Ni2p and d. O1s).	185
Figure 5.14	XPS spectrum of NiONPs after CO_2 bubbling a) Ni2p, b) O1s and c) C 1s.	186
Figure 5.15	a) Average values pH changes when 12% CO_2 -Air mixture is bubbled in DI water and 30ppm NiNPs suspension, b) average values of pH change when 12% and 100% CO_2 is bubbled in 30 ppm NiNPs suspension and c) average values of pH change when 12% and 100% CO_2 is bubbled in DI water.	188
Figure 5.16	a) SEM image and b) EDX of the synthesised NiNWs and C) TEM image of the synthesised NiNWs.	190
Figure 5.17	XRD pattern of the synthesised NiNWs.	190

Figure 5.18	Average values of increase in the saturation concentration of CO ₂ absorbed with NiNPs and NiNWs suspension as a function of particle concentration at room temperature and atmospheric pressure.	191
Figure 5.19	Average values of change in pH when CO ₂ is bubbled through the liquid at atmospheric pressure and maintained at room temperature, a) in DI water and 30 ppm NiNWs suspension and b) in DI water and 30 ppm NiNPs suspension.	192
Figure 5.20	X-ray photoemission spectroscopy of NiNWs surface before (a Ni 2p _{3/2} & b O 1s) CO ₂ bubbling.	192
Figure 5.21	XPS spectra of NiNWs after bubbling with carbon dioxide, (a) Ni 2p _{3/2} , (b) O 1s and (C) C 1s.	194
Figure 6.1	The average values of change in pH of DI water (squares) and NiNPs suspension (circle) when CO ₂ is bubbled (a) in the presence of solar simulator with wavelength range of 200-2400 nm and (b) in the dark.	201
Figure 6.2	Average values of pH change profile when CO ₂ is bubbled in DI water (square) or NiNPs suspension (circle) with light but in the (a) absence and (b) presence of IR filter with solar simulator emission wavelength	203

	range of 200-1200 nm.	
Figure 6.3	XPS spectrum of NiNPs a) before bubbling and b) after bubbling of CO ₂ under solar irradiation without filter.	204
Figure 6.4	UV-Vis absorption spectrum of 30 ppm NiNPs suspension.	206
Figure 6.5	Average values of saturated CO ₂ concentration in DI water and NiNPs suspension as a function of increase in temperature.	208
Figure 6.6	Average values of change in pH of DI water (square) or NiNPs suspension (circle) when CO ₂ is bubbled through liquid maintained at temperatures (a) 10 °C, (b) 20 °C, (c) 30 °C, (d) 40 °C, (e) 50 °C and (f) 60 °C.	209
Figure 7.1	Average values of CaCO ₃ precipitate obtained by addition of CaCl ₂ and NaOH in DI water and NiNPs suspension after CO ₂ bubbling at different time intervals.	217
Figure 7.2	Average values of precipitate of CaCO ₃ by NaOH and CaCl ₂ solution; a) Control and b) with NiNPs.	218
Figure 7.3	SEM images of the precipitate of CaCO ₃ obtained in presence of NiNPs catalysed hydration of CO ₂ using NaOH and CaCl ₂ .	218

Figure 7.4	XRD of the precipitate of CaCO_3 obtained in presence of NiNPs catalysed hydration of CO_2 using NaOH and CaCl_2 . Insert is the magnification of the later end of the XRD pattern to show the Ni [111] peak.	219
Figure 7.5	Average values of gravimetric uptake of CO_2 in potassium carbonate solution (with and without NiNPs circles and squares, respectively) with a fine bubbler (Pyrex 1).	220
Figure 7.6	XPS results of the NiNPs before (a. Ni $2p_{3/2}$, c. O 1s, e. C1s and g. survey) heat treatment and after (b. Ni $2p_{3/2}$, d. O 1s, f. C1s and h. survey) heat treatment at 150 °C for 8 hours in air.	224
Figure 7.7	X-ray diffraction pattern of the NiNPs (a) before and (b) after heat treatment at 150 °C for 8 hours.	225
Figure 7.8.	Average values of pH changes during bubbling of CO_2 through DI water (a) heat treated NiNPs (at 150 °C for 8 hours in air) suspension and (b) without heat treatment.	225
Figure 8.1	Average values of CO_2 equilibrium concentration in different nanoparticle suspension at different nanoparticle concentration.	232
Figure 8.2	Average amount of CaCO_3 precipitated when CO_2 is	233

	bubbled in DI water or 30 ppm NiNPs suspension under the same different bubbling time.	
Figure 8.3	Average values of CO ₂ equilibrium concentration at different temperatures in DI water and 30 ppm NiNPs suspension.	234
Figure 8.4	Average values of surface tension of different nanoparticle suspensions at different nanoparticle concentration at room temperature. (Square- NiNPs, Circle- Fe ₂ O ₃ NPs and Triangle- NiONPs)	236
Figure 9.1	FTIR spectra of the CaCO ₃ samples obtained from control and bridge reactors and CaSO ₄ ·2H ₂ O (gypsum).	242
Figure 9.2	XRD spectra of the precipitated CaCO ₃ in control and bridge reactor showing two crystal polymorphs of calcium carbonate (calcite and vaterite).	243
Figure 9.3	a) Percentage yield of CaCO ₃ in bridge reactor and control, b) percentage conversion of CaSO ₄ in bridge reactor and control.	244
Figure 9.4	a) the pink colourless interface (between carbonate solution and NaCl solution-acid side of the reactor) before the start of the reaction and b) the pink colourless interface (between carbonate solution and NaCl	246

	solution) at the end of 300 min observed in the bridge in the acid side of the reactor.	
Figure 9.5	Pictures showing the changes in colour of phenolphthalein during reaction of sodium carbonate and gypsum for a) control sample after 230 min of reaction, b) base side of bridge reactor after 230 min of reaction, c) control sample after 250 min of reaction and d) base side of bridge after 250 min of reaction.	247
Figure 9.6	Dye diffusion test for bridge reactor with concentration of 0.1 M Na ₂ CO ₃ (right hand side cell) and DI water dilution. (a) 0 min, (b) 60 min, (c) 120 min, (d) 180 min, (e) 240 min, and (f) 300 min.	250
Figure 9.8	Dye diffusion test for bridge reactor with concentration of 0.3 M Na ₂ CO ₃ (right hand side cell) without dilution. (a) 0 min, (b) 60 min, (c) 120 min, (d) 180 min, (e) 240 min, and (f) 300 min.	251

List of Tables

Table No.	Title	Page No.
Table 1.1	List of proposed CCS equipped power plants in Europe and their progress.	6
Table 2.1	Various sources of alkaline earth metals used for carbon mineralization.	28
Table 2.2	List of additives added for accelerated dissolution of alkaline earth metals from mineral rocks and industrial wastes.	31
Table 2.3	Reported kinetic constants of non-catalysed and catalysed hydration of CO ₂ .	37
Table 2.4	Activity of Carbonic anhydrase (free and immobilized) enzyme.	43
Table 4.1	Dialysis results of Ni ²⁺ ion leaching from NiNPs in carbonic acid solution	155
Table 5.1	The nanoparticle aggregate size obtained (in nm) from DLS of different nanoparticle suspensions with increase in nanoparticle concentration.	177
Table 7.1	Rate of CO ₂ absorption in K ₂ CO ₃ solutions in with and without of NiNPs.	222

List of Abbreviations

BET	Brunner-Emmet-Teller
CA	Carbonic anhydrase
CCS	Carbon capture and storage
DLS	Dynamic light scattering
EDX	Energy dispersive X-ray spectroscopy
EOR	Enhanced oil recovery
EU	European Union
FBR	Fluidised bed reactor
Fe ₂ O ₃ NPs	Iron (II) oxide nanoparticles
FTIR	Fourier transform infrared spectroscopy
GHGs	Greenhouse gases
HRTEM	High resolution transmission electron microscope
IEA	International Energy Agency
IPCC	Intergovernmental panel on climate change
MOF	Metallorganic framework
NiNPs	Nickel nanoparticles
NiONPs	Nickel oxide nanoparticles

O&G	Oil and gas
SAED	Selected area electron diffraction
SEM	Scanning electron microscope
TEM	Transmission electron microscope
UHV	Ultra high vacuum
UNFCCC	United Nations Framework Convention on Climate Change
UK	United Kingdom
XPS	X-ray photoemission spectroscopy
XRD	X-ray diffraction

Introduction

The current scenario of global climate change has been widely recognised as an event of high concern, with the threat of melting of the polar ice caps followed by the rise of oceanic levels [1, 2]. This concern has resulted due to the increase of the greenhouse gases (GHGs) emitted by the anthropogenic human activity, accelerated by the industrial revolution in the 1800's, followed by rapid industrialization and commercial growth [2]. The release of carbon trapped in the lithosphere (as fossil fuels) into the atmosphere due to industrial activities (including power generation, transportation, deforestation, etc) outside the bio-geo-chemical cycle, has led to the increase of the GHG concentration in the atmosphere [3]. This has been illustrated schematically in figure 1.1. Figure 1.1 shows that the CO₂ flux from the lithosphere to the atmosphere has increased after the industrial revolution. The accumulation of the GHG, increases the amount of heat trapped in the

atmosphere thereby increasing the global atmospheric temperatures, this is known as Greenhouse effect. There has been an international consensus on the reduction of the GHG emissions in the current decade in order to mitigate the global climate change [4]. The development and implementation of technology for reduction of GHG emission and its safe long-term storage away from the atmosphere is termed as Carbon Capture and Storage (CCS) (or Carbon Capture and Sequestration).

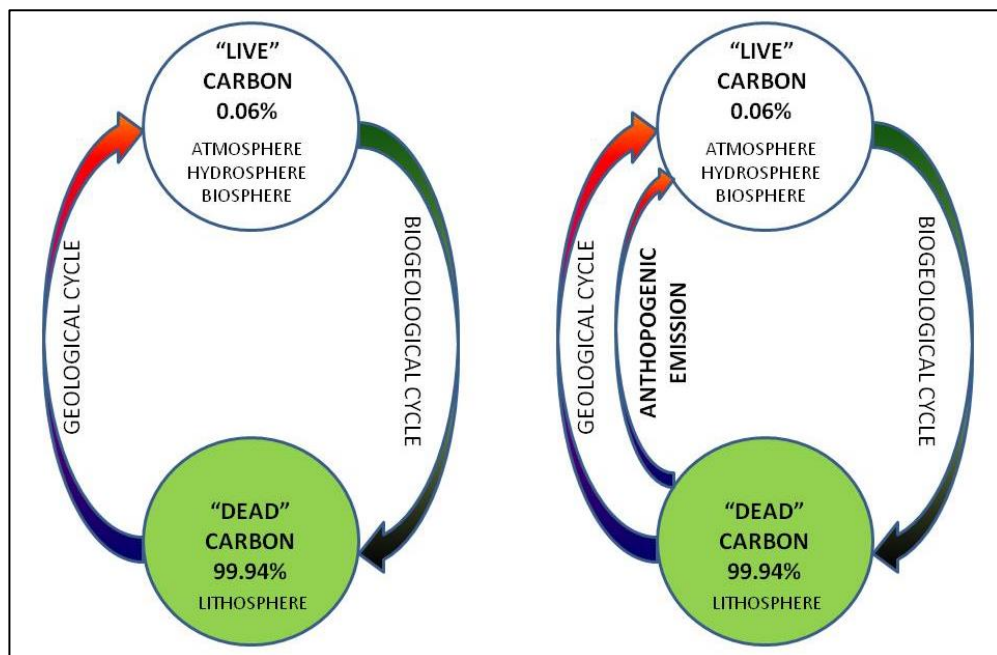


Figure 1.1: Schematic of the Earth's carbon-based bio-geo-chemical cycle pre industrial era and post-industrial era [3].

1.1 Greenhouse gases: types and sources

There are a number of GHGs identified by the United Nations Framework Convention on Climate Change (UNFCCC), [4-6] these include carbon dioxide (CO₂), methane (CH₄), nitrous oxide (N₂O), hydrofluorocarbons (HFCs), perfluorocarbons (PFCs), sulphur hexafluoride (SF₆) and nitrogen trifluoride (NF₃). The percentage distribution of these emitted GHGs can be seen in figure 1.2 as presented by the recent report by the Intergovernmental Panel on

Climate Change (IPCC) [7]. CO₂ is the primary product emitted in large quantity as compared to other GHGs due to anthropogenic emission. Therefore majority of the research and governmental policies are concentrated in the reduction of CO₂ emissions.

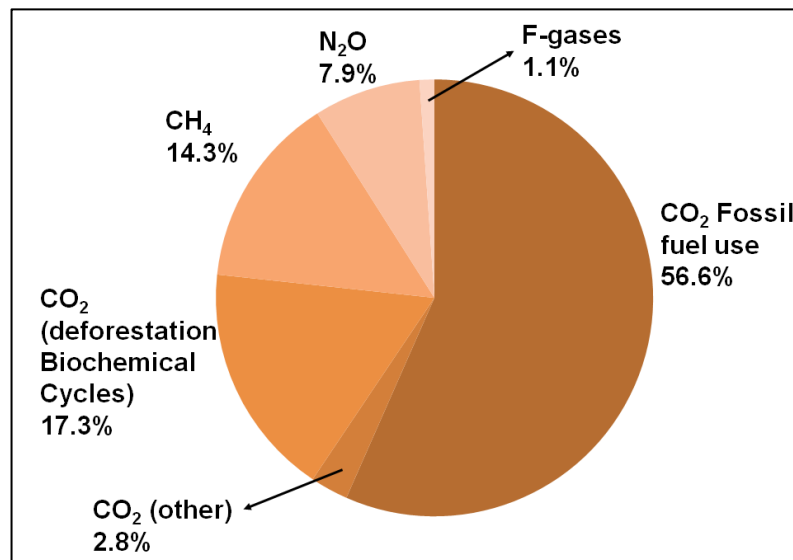


Figure 1.2: Percentage distribution of the various GHGs emitted by burning of fossil fuels [7]

The emission of the CO₂ from various sectors (in 2008) can be seen in figure 1.3 [8]. Electricity and heat generation are one of the major sectors which depend heavily on the fossil fuel reserves. In 2008 it was the largest emitter of CO₂ and thus is the first priority to be addressed in the CCS strategy for emission reduction. 41% of the global emission of CO₂ was solely from the electricity and heat generation and many countries like Australia, China, India, Poland and South Africa largely depend on coal as fuel for electricity generation [8]. It has been reported by International Energy Agency (IEA) that in 2010 the GHG emission from the energy sector accounted for two-third of the global GHG emissions [1]. The large dependence on coal for energy production has made it a priority sector for implementation of CCS. Great deal of strategy

planning and policies have been associated with the implementation of CCS to current and proposed coal based power plants [9].

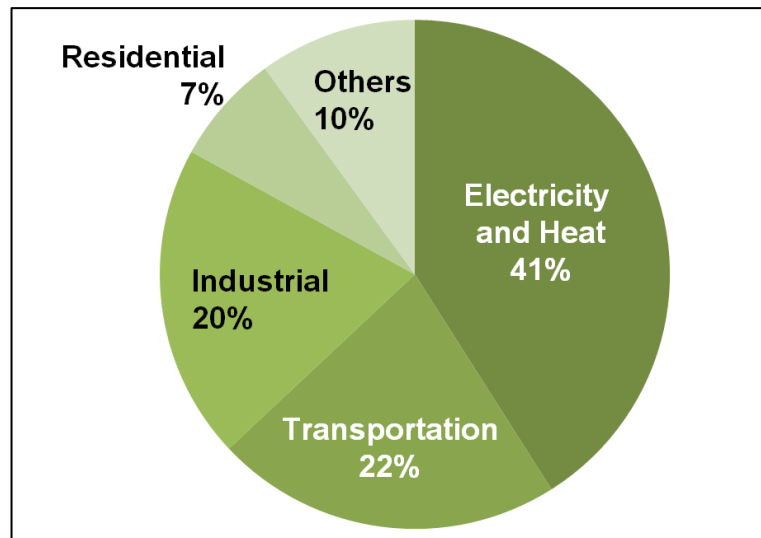


Figure 1.3: CO₂ emission in 2008 from various sectors [8]

1.2 Governmental framework and policies:

The United Nations Intergovernmental Panel on Climate Change (IPCC) has given recommendations that there needs to be a reduction in the GHG emissions globally resulting into the Kyoto protocol being passed in 2006 [4, 5]. The first stage of the protocol stated in 2008 and ended in 2012, which requested the participating countries to reduce their emission by 5% to the end of 2012, as compared to the benchmark emissions of 1990 and the second phase began in 2013 that implies that the emissions be further reduced by 18% by 2020 [6]. The implementation of the protocol specially focuses on the developed countries but dismisses the countries in the southern hemisphere and the United States of America [10]. The figure 1.4 shows the 5 major contributors of global CO₂ emission, followed by Germany, Canada, United Kingdom, Iran and South Korea [8].

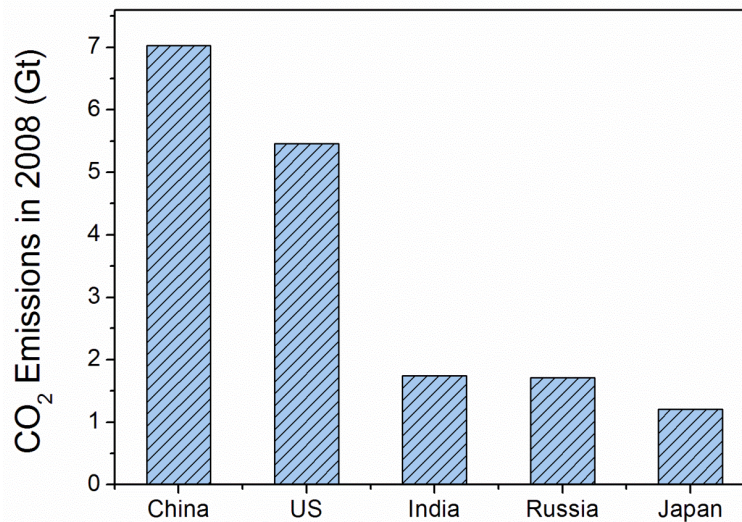


Figure 1.4: Top five CO₂ emitting countries of 2008 (published in 2010) [8].

The deployment and demonstration of CCS is an important aspect of the Kyoto Protocol. Governmental policies need to address this by proper demonstration of CCS projects [11]. The UK government passed the Climate Change Act in 2008 to become the first to set a long range target for CO₂ reduction by 80% in 2050, compared to the CO₂ emissions of 1990 in its domestic market [12, 13]. This law followed the post combustion capture competition of 2007, which would support to develop capture facility for coal-fired power plant [12, 14]. The 2010 Energy Act narrowed the competition down to only two competitors, owing to the new economic reforms in the electrical market in 2011. The two competitors were E.ON power and Scottish power, the former of which withdrew their bid due to the reduction in the CCS leverage by the UK government, leaving the later as the only contender in the post combustion capture competition [12].

In the European Union, twelve projects (table 1.1) have been identified aspiring for CCS demonstration [15] but the only three to four of which seem to be feasible to have a start up by 2020 [16]. There still exist a major uncertainty

in the development, demonstration and deployment of CCS technology provided by government support in the developed world [12].

Table 1.1: List of proposed CCS equipped power plants in Europe and their progress [15]

Country	Project	Capture	Storage	Status comments
UK	Peterhead (gas)	Post	Offshore	Storage site front end engineering and design completed
	Drax (coal)	Oxy	Offshore	
	Don valley (coal)	Pre	Offshore	Cancelled following withdrawal of UK govt. support (Oct, 2012)
	Teeside (coal)	Pre	Offshore	
	Captain (coal)	Pre	Offshore	Not an applicant for new entrants reserve 300 round 1 funding
Netherlands	ROAD (coal)	Post	Offshore	All front end engineering and design completed and permitting near completion (2012)
	Green Hydrogen (hydrogen)	cryogenic	Offshore	
France	Floranges (steel)	Top gas recycle	Onshore	Host facility currently idled and facing an uncertain future (Oct, 2012)
Italy	Porto Tolle (coal)	Post	Offshore	Subject to permitting challenge (overuled 2011)
Spain	Compostilla (coal)	Oxy	Onshore	Not an applicant for new entrants reserve 300 round 1 funding
Poland	Bechatow (coal)	Post	Onshore	
Romania	Getica (coal)	Post	Onshore	
Germany	Jaeschwalde (coal)	Oxy	Onshore	Project cancelled Dec, 2011

China and India are taken to be emerging economies that could become large potential emitters over the years, but the Kyoto Protocol does not explicitly

require the developing countries to obey reduction in CO₂ emissions [10]. Figure 1.5 shows the emissions of CO₂ in the year 2011-2012 of six of the top ten global emitters from the IEA World Energy Outlook, 2013 [1]. There is a need for international cooperation on CCS demonstration to bridge the knowledge gap between the CCS rhetoric and technical progress that is essential for climate change mitigation efforts [17, 18]. Also developing economies like China and India need emphasis on the CCS regulation policies [17, 19, 20]. The urgency of the problem of CCS implementation can be estimated by the fact that, at a global level, each year delay in taking appropriate policy decision would lead to an additional cost of 300 billion GB pounds in terms of mitigation costs between now and 2030 [21].

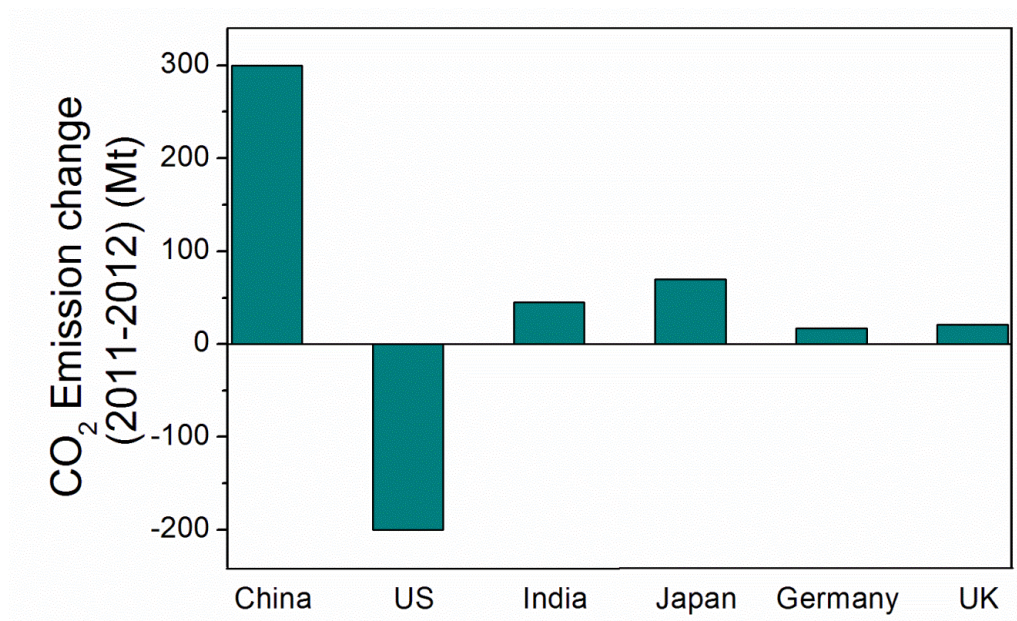


Figure 1.5: Changes in CO₂ emissions in the year 2011-2012 [1].

1.3 Technological developments in CCS

CCS is not a developed technology but an emerging market and thus full scale demonstration of CCS is an important factor for policy regulations [7, 11].

The stages that are part of CCS include capture, transportation and storage [7, 16]. A detailed overview of the CCS phases is provided in chapter 2.

There have been various technologies that have been suggested for the optimal use of fossil fuel resources (including coal) for power-plant usage in electricity generation. These include technologies for combustion of the fuel, the various techniques used for separation/purification of the CO₂ generated during combustion, followed by transportation and safe storage of CO₂ [18, 22-25]. The technologies need to be developed keeping the current power plant structure in mind and policies need to be developed to avoid carbon lock-in [26, 27]. Carbon lock in is defined as "*creating persistent market and policy failures that can inhibit the diffusion of carbon-saving technologies despite their apparent environmental and economic advantages*" [26]. The emphasis on the research and development on the CCS is recommended on an urgency basis [21].

The storage of CO₂ becomes an important aspect to be covered in CCS [28]. The conversion of CO₂ to biomass provides short term storage of CO₂ leading to a later emission of the carbon into the atmosphere [29, 30]. Another prospect of storage is geological storage, (underground in depleted oil wells/coal seams) or as mineral salts [28]. The motivation for geological storage of CO₂ is based on the Enhanced Oil Recovery (EOR) that is used in the oil and gas industry, which is a mature technology. In EOR, the CO₂ generated in the oil and gas processing is used to extract crude out of the depleting oil wells [15]. This is an effective method for a long-term storage but it is still covered by limitations of leakages [31]. The conversion of CO₂ to mineral carbonates, even though considered safest method of CO₂ storage [7, 16, 28], however is limited

by slow kinetics rates in the conversion process from CO₂ to carbonates [29] (discussed in detail in chapter 2).

1.4 Aims of this work

The kinetic limitations observed during mineralization of CO₂ include the slow hydration of CO₂ (see section 2.3.3, chapter 2) and low dissolution rates of natural mineral rocks (see section 2.3.2, chapter 2). Therefore, the motivation of this work was to develop a novel method for wet-chemical carbonation of CO₂. In particular, the use of nickel nanoparticles to catalyse the hydration of CO₂ and the use of gypsum as a calcium source for mineralization was investigated and found to be successful, as reported in chapter 4 and 9, respectively.

The inspiration for the use of nickel nanoparticles (NiNPs) to catalyse CO₂ mineralisation originated from the observation of nickel metal in sea urchin exoskeletons [32,33], and the role that it was suspected to have in bio-mineralisation. Given the success of other bio-inspired/bio-mimetic approaches to problems as diverse as ultra-strong materials [34-36] to camouflage and colouring [37] nickel nanoparticles were considered to be a worthwhile starting point to explore methods for improvement in CO₂ mineralisation.

The fact that sea water contains SO₄²⁺ ions as the second most abundant ions after Cl⁻ and the observation that some natural springs which have high sulphate content in the aquatic environment [38, 39] also precipitate CaCO₃ naturally led to intuitively select a sulphate based calcium source for the mineralization process. Gypsum (CaSO₄·H₂O) is a natural source of calcium sulphate, available in plentiful and relatively cheap, is explored as a calcium source for the mineralization process.

Based on the above approach, the specific aims addressed in the work presented in this thesis are:

- The investigation and proof of concept of NiNP catalysed hydration of CO₂.
- To understand the steps involved in the catalytic process of CO₂ hydration using NiNPs.
- To validate catalytic activity of NiNPs using different methods for reaction kinetic evaluation common in the literature.
- To compare the activity of NiNPs with other nanoparticles (i.e. Al₂O₃, Fe₂O₃ and NiO) that are suggested to have similar catalytic activity for hydration of CO₂.
- To understand influence of sunlight and temperature on NiNP catalysed hydration of CO₂.
- Application of NiNPs to enhance CO₂ mineralization and the rate of CO₂ absorption (in carbonate solutions).
- Development of a novel process for mineralization of CO₂ using gypsum, sodium carbonate and sodium chloride.
- Construction of a novel reactor for the above mentioned mineralization process.
- To study the transfer of ions through a salt bridge under the influence of a concentration gradient.

1.5 Summary of the chapters

The thesis has the following structure. Chapter 2 reviews the technical literature of carbon capture and storage with emphasis on mineralization

storage of CO₂. The experimental procedures for all the experiments and analytical techniques used are presented in chapter 3.

Chapter 4 presents the results of a study on the catalytic activity of NiNPs for hydration of CO₂. The process based upon the study reported in this chapter has been patented [40] and published [41, 42]. The study of the catalytic hydration of CO₂ using NiNPs was qualitatively evaluated and verified against methods used in the literature, the results of which are presented and discussed in chapter 5. Different nanoparticles (Fe₂O₃ and NiO) were also examined to determine any similar activity or mass transfer enhancement on the hydration of CO₂. These results are also presented in chapter 5.

In chapter 6 it is demonstrated that the NiNPs are photoactive and their photo-activity was investigated in detail. The results show that NiNPs absorb light in the visible range leading to enhancement in its catalytic activity. The dependence of the catalytic activity of the NiNPs on temperature is also presented in chapter 6. It was observed that NiNPs had optimum activity between 20-30°C. NiNPs were also used to enhance precipitation of CaCO₃ and absorption in carbonate solutions. The results of enhancement processes are described and discussed in chapter 7.

The presence of the nanoparticles (Ni, Fe₂O₃ and NiO) in de-ionised water was observed to have affected the CO₂-H₂O vapour liquid equilibrium by increasing the equilibrium concentration of CO₂ in de-ionised water. Comments on the effect of nanoparticles on CO₂-H₂O equilibrium are presented in chapter 8. Change in surface tension of nanoparticle suspension is suggest as one of the reasons for the change in CO₂-H₂O equilibrium.

The last part of the thesis introduces a novel method for mineralization of CO₂ using gypsum and sodium chloride and results have been presented in chapter 9 in the thesis. A novel reactor was designed for the mineralization process consisting of a salt bridge. The results demonstrate that CO₂ can be mineralized using this novel process and reactor. The concept of transfer of ions through a salt bridge under a concentration gradient is examined and discussed in chapter 9. It was observed that ions can be transferred through the salt bridge under a concentration gradient. Chapter 10 comprises concluding remarks and future work.

References

- [1] IEA, Redrawing the Energy-Climate Map, World Energy Outlook Special Report, International Energy Agency, France, 2013.
- [2] J.D. Shakun, P.U. Clark, F. He, S.A. Marcott, A.C. Mix, Z. Liu, B. Otto-Bliesner, A. Schmittner, E. Bard, Global warming preceded by increasing carbon dioxide concentrations during the last deglaciation, *Nature*, 484 (2012) 49-54.
- [3] H.E. Dunsmore, A geological perspective on global warming and the possibility of carbon dioxide removal as calcium carbonate mineral, *Energy Conversion and Management*, 33 (1992) 565-572.
- [4] U.N., United Nations Framework Convention on Climate Change, United Nations, New York, 1992.
- [5] U.N., Kyoto Protocol to the United Nations Framework Convention on Climate Change, United Nations, New York, 1998.
- [6] U.N., Doha Amendment to the Kyoto Protocol, United Nations, New York, 2012.
- [7] B. Mertz, O.R. Davidson, P.R. Bosch, R. Dave, L.A. Meyer, IPCC, 2007: Climate Change 2007: Mitigation. Contribution of the Working Group III to the Fourth Assessment Report of the Intergovernmental Panel on Climate Change, in, Cambridge University Press, Cambridge, United Kingdom and New York, NY, USA, 2007.
- [8] IEA, CO₂ Emission from Fuel Combustion Highlights (2010 Edition), in, International Energy Agency, France, 2010.
- [9] N. Markusson, S. Haszeldine, 'Capture ready' regulation of fossil fuel power plants – Betting the UK's carbon emissions on promises of future technology, *Energy Policy*, 38 (2010) 6695-6702.
- [10] A. Ghezloun, A. Saidane, N. Oucher, S. Chergui, The Post-Kyoto, *Energy Procedia*, 36 (2013) 1-8.
- [11] M. Krahe, W. Heidug, J. Ward, R. Smale, From demonstration to deployment: An economic analysis of support policies for carbon capture and storage, *Energy Policy*, 60 (2013) 753-763.
- [12] B. Evar, Conditional inevitability: Expert perceptions of carbon capture and storage uncertainties in the UK context, *Energy Policy*, 39 (2011) 3414-3424.
- [13] S. Bouzalakos, M.M. Maroto-Valer, Overview of carbon dioxide (CO₂) capture and storage technology, in: M.M. Maroto-Valer (Ed.) *Developments and Innovation in Carbon Dioxide (CO₂) Capture and Storage Technology*, Volume 1 - Carbon Dioxide (CO₂) Capture, Transport and Industrial Applications, Woodhead Publishing, Cambridge, 2010, pp. 1-24.

- [14] CCSA, A strategy for CCS in UK and beyond, Carbon Capture and Storage Association, London, 2011.
- [15] V. Scott, What can we expect from Europe's carbon capture and storage demonstrations?, *Energy Policy*, 54 (2013) 66-71.
- [16] EASAC, Carbon capture and storage in Europe, in: EASAC policy report 20, European Academics Science Advisory Council, Germany, 2013, pp. 5-9.
- [17] H. de Coninck, J.C. Stephens, B. Metz, Global learning on carbon capture and storage: A call for strong international cooperation on CCS demonstration, *Energy Policy*, 37 (2009) 2161-2165.
- [18] R. Steeneveldt, B. Berger, T.A. Torp, CO₂ Capture and Storage closing the knowledge-doing gap, *Transactions of IChemE, Part A*, 84 (2006) 739-763.
- [19] X. Zhang, J.-L. Fan, Y.-M. Wei, Technology roadmap study on carbon capture, utilization and storage in China, *Energy Policy*, 59 (2013) 536-550.
- [20] R. Eto, A. Murata, Y. Uchiyama, K. Okajima, Co-benefits of including CCS projects in the CDM in India's power sector, *Energy Policy*, 58 (2013) 260-268.
- [21] R. Nataly Echevarria Huaman, T. Xiu Jun, Energy related CO₂ emissions and the progress on CCS projects: A review, *Renewable and Sustainable Energy Reviews*, 31 (2014) 368-385.
- [22] R. Lal, Carbon sequestration, *Philosophical Transactions of the Royal Society B: Biological Sciences*, 363 (2008) 815-830.
- [23] S. Anderson, R. Newell, Prospectives of Carbon Capture and Storage Technologies, *Annual Review of Environmental Resources*, 29 (2004) 109-142.
- [24] F. Johnson, Perspective on CO₂ capture and storage, *Greenhouse Gases Science and Technology*, 1 (2011) 119-133.
- [25] C.W. Jones, CO₂ capture from dilute gases as a component of modern global carbon management, *Annual Reviews of Chemical and Biomolecular Engineering*, 2 (2011) 31-52.
- [26] G.C. Unruh, Understanding carbon lock-in, *Energy Policy*, 28 (2000) 817-830.
- [27] G.C. Unruh, J. Carrillo-Hermosilla, Globalizing carbon lock-in, *Energy Policy*, 34 (2006) 1185-1197.
- [28] K.S. Lackner, A Guide to CO₂ Sequestration, *Science*, 300 (2003) 1677-1678.
- [29] B. Freedman, G. Stinson, P. Lacoul, Carbon credits and the conservation of natural areas, *Environmental Reviews*, 17 (2009) 1-19.

- [30] A. Levasseur, M. Brandao, P. Lesage, M. Margni, D. Pennington, R. Clift, R. Samson, Valuing temporary carbon storage, *Nature Climate Change*, 2 (2012) 6-8.
- [31] O.R. Harvey, N.P. Qafoku, K.J. Cantrell, G. Lee, J.E. Amonette, C.F. Brown, Geochemical Implications of Gas Leakage associated with Geologic CO₂ Storage—A Qualitative Review, *Environmental Science & Technology*, 47 (2012) 23-36.
- [32] L. Šiller, Toxicology in Sea Urchin due to silver nanoparticles, Personal Communication, 2010.
- [33] S. Piticharoenphun, Investigation into the availability of man-made nanoparticles and their interaction with exposed sea urchin (*Paracentrotus lividus*), PhD Thesis, Chemical Engineering and Advanced Materials, Newcastle University, Newcastle upon tyne, 2013, pp. 224.
- [34] U.G.K. Wegst, H. Bai, E. Saiz, A.P. Tomsia, R.O. Ritchie, Bioinspired structural materials, *Nature Materials*, 14 (2015) 23-36.
- [35] J. Aizenberg, P. Fratzl, Biological and Biomimetic Materials, *Advanced Materials*, 21 (2009) 387-388.
- [36] A.R. Studart, Towards High-Performance Bioinspired Composites, *Advanced Materials*, 24 (2012) 5024-5044.
- [37] M. Kolle, A. Lethbridge, M. Kreysing, J.J. Baumberg, J. Aizenberg, P. Vukusic, Bio-Inspired Band-Gap Tunable Elastic Optical Multilayer Fibers, *Advanced Materials*, 25 (2013) 2239-2245.
- [38] D. Lucas, J.E. Andrews, A re-examination of reported lacustrine vaterite formation in Holkham Lake, Norfolk, U.K, *Journal of Sedimentary Research*, 66 (1996) 474-476.
- [39] S.E. Grasby, Naturally precipitating vaterite (μ -CaCO₃) spheres: unusual carbonates formed in an extreme environment, *Geochimica et Cosmochimica Acta*, 67 (2003) 1659-1666.
- [40] L. Šiller, G.A. Bhaduri, Carbon capture, World Patent WO2013/171480 (A2), 2013.
- [41] G.A. Bhaduri, L. Šiller, Nickel nanoparticles catalyse reversible hydration of carbon dioxide for mineralization carbon capture and storage, *Catalysis Science & Technology*, 3 (2013) 1234-1239.
- [42] G.A. Bhaduri, R.A. Henderson, L. Šiller, Reply to the 'Comment on "Nickel nanoparticles catalyse reversible hydration of carbon dioxide for mineralization carbon capture and storage"' by D. Britt, *Catal. Sci. Technol.*, 2013, 3, DOI: 10.1039/C3CY00142C, *Catalysis Science & Technology*, 3 (2013) 2197-2198.

Carbon capture and CO₂

Mineralization: Review

Carbon capture and storage (CCS) is a term used to collectively describe the process of separation, transportation and safe storage of CO₂ away from the atmosphere. Chapter 2 will introduce and discuss the various technological and research aspects of CCS with focus on the mineralization carbon capture and storage. The chapter begins with the various methods used and proposed for the combustion of fossil fuels (that include, post combustion capture, pre combustion capture, oxy-fuel process and combustion looping), followed by the methods used for the separation of CO₂ used in post combustion capture. The chapter then reviews the various storage possibilities of CO₂, out of which mineralization storage has been discussed in detail.

2.1 Carbon cycle, CO₂ emissions and global warming.

The carbon cycle is the movement of carbon (in all its forms i.e. organic and inorganic) within the bio-geo-chemical cycle. Figure 1.1 shows the movement of carbon in the bio-geo-chemical cycle and the intervention of the human anthropogenic activities to unbalance and increase the CO₂ flux into the atmosphere [1]. The increase of CO₂ in the atmosphere, leads to greenhouse effect which increases the global temperatures resulting in melting of the polar ice caps and increase in the oceanic levels around the globe [2]. This increase in CO₂ concentration in the atmosphere also leads to an increase in oceanic acidification, as the oceans try to maintain the equilibrium of CO₂ with the atmosphere [3].

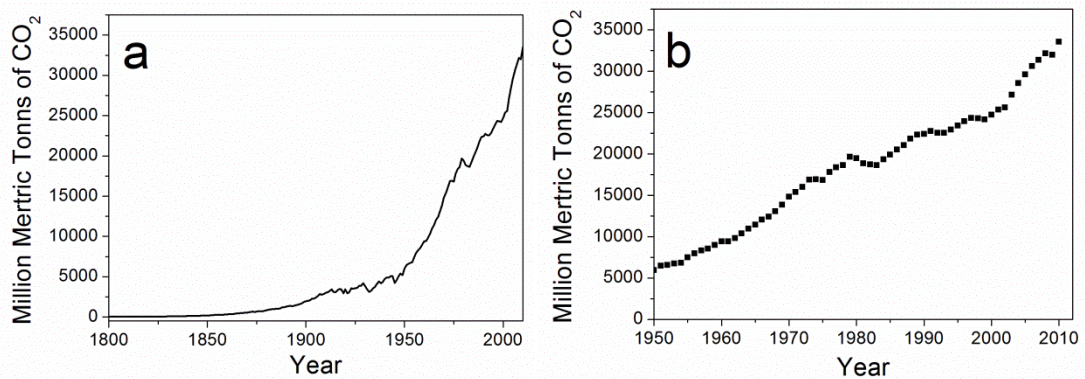


Figure 2.1 CO₂ increase in the atmosphere since industrial revolution (Reconstructed from Boden *et al.* [4]).

Figure 2.1a shows the global CO₂ emissions during the last 210 years and figure 2.1b shows an expanded view of emissions in the last 60 years [4]. Since industrialization, in the 1900, there has been an exponential increase in the CO₂ emissions (figure 2.1a) that has increased by 5.5 times in the last 60 years (figure 2.1b). In order to mitigate the increase in the amount of CO₂ in the atmosphere efforts are taken to reduce CO₂ emissions (section 1.2, Chapter 1).

These efforts include efficient power utilization by the means of process intensification, the use of renewable power sources and CCS. Even though there is an increasing impetus to use renewable resources for power generation, the transition to renewables is slow as these are developing technologies [5, 6] and our dependence of fossil fuels and coal for power generation is still intact [7]. Hence CCS plays an important role to reduce the CO₂ from entering the atmosphere [8].

2.2 Carbon Capture and Storage: An Overview

CCS has developed a lot of interest over the last decade. It expands into various topics related to CO₂ emissions that are under scientific investigation [8]. It encompasses the development and application of the various methods of separation (or capture) of CO₂ [9-11] along with the various fuel combustion technologies [12, 13]. It includes the method of transportation of the purified CO₂ and its safe long term storage [14]. There are various propositions that have been offered for the storage and utilization of CO₂, these include storage in natural sinks (terrestrial and oceanic) [3], conversion into useful chemicals [15-19], storage in geological formations such as depleted oil well or saline aquifers (terrestrial or oceanic) [2, 20] and conversion into mineral salts [21, 22]. Recently there has been an emphasis on life cycle analysis studies of the new CCS projects to ensure sustainability of the process [23].

2.2.1 CO₂ capture technology

Carbon capture from the power generation process is an important field in CCS [14, 24, 25]. The capture of CO₂ done after the combustion process is known as post-combustion capture, before the combustion process is called as pre-combustion capture and the capture of CO₂ done when fuel is combusted in

presence of pure oxygen is the so-called oxy-fuel process [24]. Another novel method of combustion is to carry the oxygen from the air in an oxygen carrier and then react it with the fuel separately, known as chemical looping combustion (CLC) [26, 27]. These are the four different modifications that are made to the combustion process, in order to accommodate CCS in power generation process and are summarised in figure 2.2.

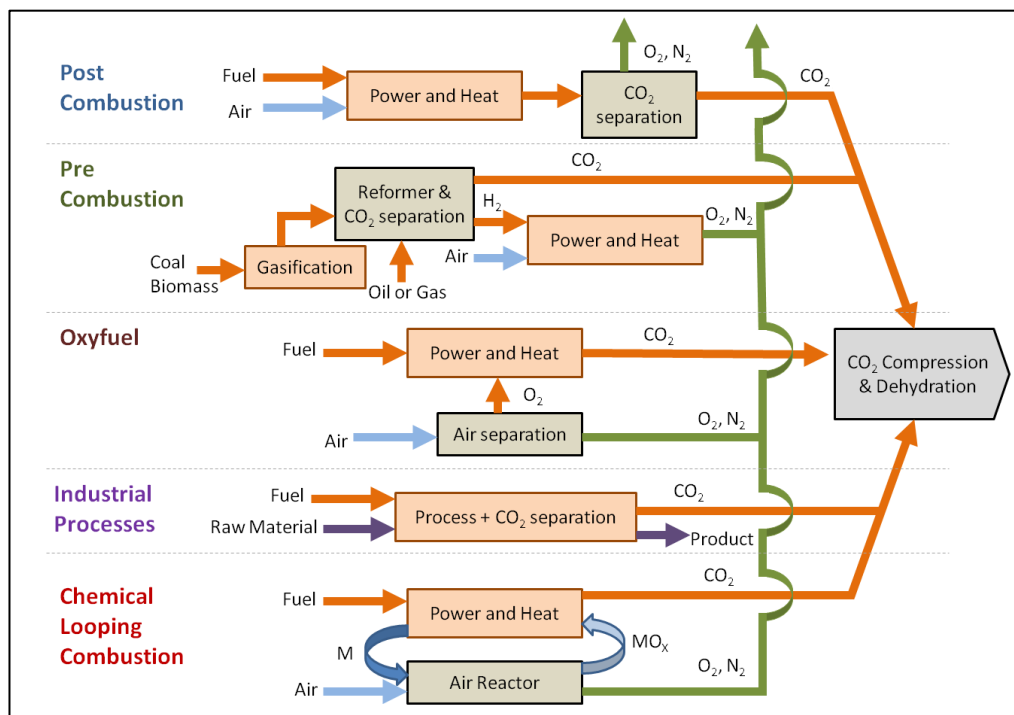


Figure 2.2: Various fuel combustion and capture mechanisms for CCS.

Post-combustion process is the most traditional process that is widely used for power generation or industrial processes. In this method the fuel, such as coal or fossil fuel is burnt in the boiler and the flue gas is then treated [28]. Currently the purification process consist of removal of SO_x, NO_x and CO as an integral part of power generation (due to governmental regulations [2]) and removal of CO₂ is desired to be added into the process (see figure 2.2). Post-combustion capture is a mature technology that has been utilized by the Oil and Gas (O&G) industry [8]. The purified CO₂ in the O&G sector is then compressed and pumped in the oil well for enhanced oil recovery (EOR) [29].

In this method there fossil fuel (natural gas, coal or biomass) is converted to synthesis gas (syngas) and then fed to the boiler. Syngas is a mixture of CO₂ and H₂ that is produced by steam reforming of natural gas or liquid hydrocarbon [30, 31], gasification of coal [32-34] and biomass [34-36]. In this process the CO₂ is generated and removed before the fuel (i.e. hydrogen) enters the boiler. Therefore the process is called as pre-combustion capture technology [37, 38]. A block diagram of the process is presented in figure 2.2. The gasification process generates a mixture of CO₂ and H₂ with some traces of CO [39]. The capture of CO₂ is less intensive and is more cost effective than the post-combustion process.

The oxy fuel process comprises of the combustion of fuel in the complete oxygen atmosphere as compared to air in conventional combustion process. Air consists mainly of N₂ and O₂ and in conventional air combustion process some of the heat generated is lost as sensible heat to N₂. This limitation is overcome by oxy-fuel combustion. Combustion of carbon based fuels under complete oxygen environment enhances combustion efficiency and provides a cost effective downstream sequestration of CO₂ [12, 40-42].

In CLC the oxygen required for the combustion of fuel is provided by an oxygen carrier such as metal oxides (Fe₃O₄, Cu₂O, CaO etc [43, 44]. In CLC firstly the metal (or metal oxide) ($3Fe + 4H_2O \rightarrow Fe_3O_4 + 4H_2$, [44]) is oxidized in presence of air in one fluidized bed reactor (FBR), then transferred and reduced in another FBR in presence of a fuel ($2C + Fe_3O_4 \rightarrow 3Fe + CO_2$, [44]). The fuel and air do not mix and streams of CO₂ and water can be generated. After condensation of steam, pure stream of CO₂ suitable for sequestration is available, reducing downstream processing [45-48].

2.2.2 Capture process

The separation of CO₂ from exhaust stream is another field of active study in CCS [14, 49, 50]. The traditional methods of CO₂ separation includes amine and carbonate absorption for CCS projects has been recently reviewed [51, 52]. Even though these technologies are used for decades in the oil and gas sector, the cost of its utilization for separation of CO₂ from power plants is high [53]. Therefore optimization of these processes to lower operating costs, for example by using different catalysts for enhancing CO₂ absorption rates are still an active area of research (further discussed in section 2.3.3). New absorption materials such as ionic liquids are also been studied [50, 54-56]. Ionic liquids have higher CO₂ loading capacities and enhanced CO₂ absorption rates as compared to amine and carbonate solutions [50, 54-56]. Addition of solid particles in absorbers can also increase their absorption capacity [57, 58].

Adsorption separation of CO₂ is another industrially used technique [59]. The most commonly used adsorbents are zeolites, activated carbon and amine treated adsorbents (like silica or alumina) [25]. The adsorption process can be physical or chemical [60]. One of the physical adsorbents that show high CO₂ separation potential are metallorganic frameworks (MOF) [61-64]. The MOF's are highly porous and crystalline in the structure and can hold high concentrations of CO₂ within their structures (i.e. 2400 mg of CO₂/g of MOF at room temperature and ~50 atm pressure) [63]. Chemically modifying the surface with amine groups leads to chemical adsorption systems [60], alkaline earth metal oxides (like CaO or MgO) are also affective chemical adsorbents that can capture hydrated CO₂ and can be regenerated by simple heat treatment

[65]. Grassin and co-workers [66-69] that aqueous layers on adsorbent materials can increase their adsorption capacity.

Another method of CO₂ separation is the use of membranes [70]. Membranes can be solid membranes [71-73], polymeric membranes [74-76] or liquid membranes [77-79]. Solid membranes find applications in high temperature separation i.e. above 200 °C (especially ceramic membranes [72]) while polymeric and liquid membranes are used for lower temperature separations i.e. below 150 °C [55, 76]. Cryogenic distillation is another method that is suggested for separation of CO₂ [9, 11, 49]. In this method the CO₂ is distilled at cryogenic temperatures (i.e. -150 °C) which is a physical process. The process of cryogenic distillation is used for separation of air constituents, but application to CCS is novel [25]. This process is limited with the cost of the refrigerant required to reach such low temperatures [25].

2.2.3 Storage of CO₂.

The storage of CO₂ for long term away from the atmosphere is the main priority of CCS. Various storage or sequestration methods have been proposed and each one of them have a limited capacity (both in terms of time and quantity) to store CO₂. These traditional storage options include conversion to biomass, reused as fine chemicals or fuels, underground storage in saline aquifers, depleted oil wells or un-mineable coal mines and conversion to mineral carbonates [2]. The figure 2.3 shows the distribution of the CO₂ storage capacity of the various proposed options. Recently there have been a few new suggestions for the oceanic storage of CO₂ these as bicarbonate solutions [80] or as solid H₂CO₃ [81] both of which have been recently proposed. Hamelers *et al.* [82] proposed a novel method of generating energy from CO₂ emissions by

using the difference in concentrations of CO₂ from emissions and air to generate electricity. Xie *et al.* [83] demonstrated that electricity can be generated along with CO₂ capture and mineralization using a novel CO₂-mineralization fuel cell.

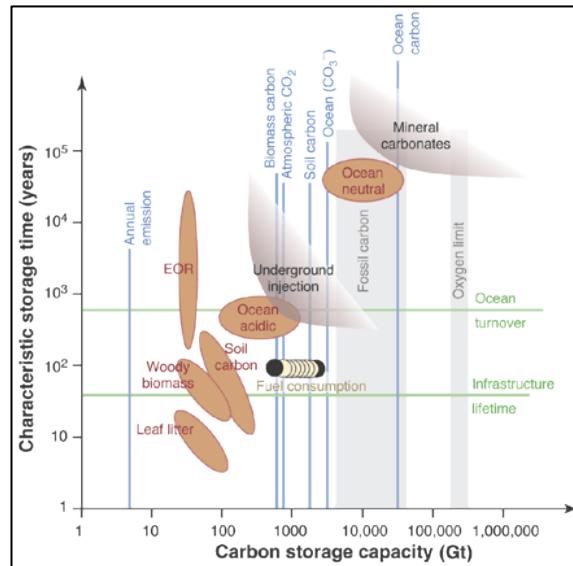


Figure 2.3: Estimation of storage capacity for CO₂ in terms of time and quantity for various sequestration methods [21].

One of the easiest method for the storage of CO₂ is conversion to carbohydrates or proteins by plants and stored as biomass [84]. The capacity of CO₂ storage as biomass is about 1.4 ± 0.7 Gt/yr in terrestrial biomass and about 5-10 Gt/yr in oceanic environment biomass [9]. Even though biomass traps CO₂ the longevity of such storage is very short because CO₂ is released back into the atmosphere during biomass degradation (seen from figure 2.3). Baral and Guha [85] promoted afforestation as low economic remedy for CO₂ sequestration and Freedmen *et al.* [3] suggest providing carbon credits for conservation of natural areas increases urban encroachment into forest lands. Further option is the use of biofuels (such as biodiesel) [86, 87], so CO₂ emissions from the transport sector is recycled [88, 89].

There has been a great effort of research that has been dedicated to the conversion of CO₂ to utility chemicals. Most of the process are commercially viable, the major limitation is that the demand of these chemicals is far less than the CO₂ production. These include various alkanes, alcohols, aldehydes, formic acid and other organic compounds [17-19]. New catalysts are developed for the reduction of CO₂ [16] and formation of C-C carbon chains for generation of these utility chemicals [15]. There also exist various electrochemical and electrocatalytic methods that have been used for the conversion of CO₂ to utility chemicals [90]. Using this methodology of recycling CO₂ into the value chain would lead to utilization of the waste CO₂ and help develop carbon neutral technologies [18].

Geological storage is the most efficient and easiest technique for the safe storage of CO₂ [2]. Used extensively in the oil and gas industry, it leads to storage of liquefied CO₂ in depleted oil wells (i.e. EOR) or saline aquifers or unmineable coal seams. Underground geological storage is an option that has attracted governmental interest in many countries [2]. Even though this is the most cost effective option of CO₂ storage (figure 2.3) there are also some limitations. A constant monitoring of the CO₂ injection wells and the entire injected area is needed all the time in order to detect any possible leaks [91, 92]. In the case of saline aquifers, the pH of the aquifer alters in the presence of the CO₂ (pH becomes more acidic) leading to the concern of the integrity of the cap rock [93-95].

Mineral storage is one of the safest ways to remove the CO₂ from the atmosphere and lock it into the lithosphere [2, 21, 96, 97]. The process of CO₂ capture is envisioned by the natural weathering of rocks [22], because the

products of mineralization are thermodynamically more stable than other forms of carbon. The earth's crust comprises of about 1.5×10^{17} tonnes of CO_2 equivalent trapped in the form of calcium carbonate [98, 99]. The carbonate minerals have high capacity and high longevity for storage of CO_2 as compared to other methods (see figure 2.3). The major limitation that is slow reaction kinetics of the mineralization process [97, 100].

There are various steps in the mineralization process. Figure 2.4 shows the classification of the mineralization process of CO_2 to carbonate minerals [101].

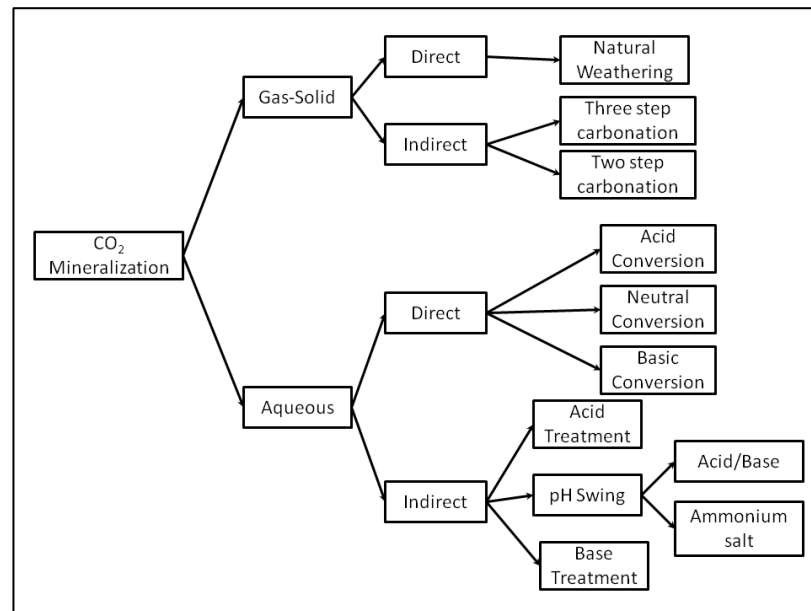


Figure 2.4: Classification of the mineralization process (modified from Wang [101])

The reaction type for the mineralization process depends on the reacting materials such as gas-solid or aqueous reaction. In the gas-solid process the mineral source (mainly solid) is reacted directly with CO_2 either from atmosphere (like in natural weathering of rocks [100, 102]) or indirectly by treating the mineral with chemical treatment (for example conversion of olivine to serpentine using high temperature and pressure hydrolysis) to enhance its activity and then reacting it with CO_2 [103-105]. Direct mineralization process

using CO₂ and minerals is a slow process and it can be accelerated by reducing the grain size of the mineral rock [100].

Direct carbonation reaction involves chemical treatment of the parent mineral to make it chemically active for reaction with CO₂. This can be achieved by either a two-step process consisting of activation of the initial mineral (mainly serpentine) by heat treatment into an oxide (i.e. MgO) followed by carbonation with CO₂ [106, 107]. Otherwise following a three step procedure comprising of the initial heat treatment to mineral oxide, as above, followed by hydration into a hydroxide (i.e. Mg(OH)₂). The hydroxide is then reacted with CO₂ to form mineral carbonate. The three step process is more energy efficient than the two step method [106]. The three step process is optimised using ammonium salts to enhance the reaction rates and conversion to carbonates [103, 104, 108-111]. After optimization the mineralization process still requires high temperatures >300 °C and high pressures >20 bar.

The aqueous mineralization is less energy consuming when compared to gas-solid mineralization, but is limited by the dissolution rate of the alkaline earth metals from the source mineral [112]. The aqueous mineralization is classified as direct or indirect (figure 2.4) [101, 112]. The direct aqueous mineralization involves high pressure and temperature carbonation of the mineral rock (like olivine or waste slags) in acidic, basic or neutral medium where dissolution and carbonation takes place simultaneously [105, 113, 114]. The indirect aqueous mineralization consists of the treatment with acid or base followed by carbonation. A special method developed for this is pH swing method [115] where the alkali earth metals (Ca or Mg) are leached by an acid and then exposed to a base to be mineralised, for example use of mineral acid-

base (like HCl and NaOH) [115, 116] or using ammonium salts (like NH_4HSO_4 and NH_4OH) [101, 117-120]). Bodor *et al.* [121] used nickel nanoparticles (NiNPs) to enhance the mineralization of CO_2 in steel slags and found that solid to liquid ratio is an important factor in aqueous mineralization.

In summary, the mineralization process depends on selection of mineral sources (source of the alkaline earth metal), removal/activation of the alkaline earth metal from the mineral source, reaction of the alkaline earth metal with CO_2 to form a carbonate and precipitation of the carbonate mineral. Each of these factors influences the speed and energy efficiency of mineralization of CO_2 and these factors will be discussed below.

2.2.3.1 Selection of Mineral Source:

Alkaline earth metals like Mg and Ca are the most promising candidates for mineralization of CO_2 . Carbonate salts (of Ca and Mg) are thermodynamically stable and occur due to natural weathering of rocks. Depending on the source, of Ca and Mg; it can be classified into two categories natural mineral rocks and industrial wastes. Naturally occurring rocks include silicates, sulphates and phosphates. Many industries, like iron and steel, cement, etc., produce wastes that are rich in alkaline metals and can be used as a source for CO_2 mineralization [122]. Table 1 lists the various sources of alkaline earth metals used for the carbonation reaction with reference found in literature. The use of industrial wastes are identified as excellent sources of Ca and Mg for point source emitters like iron and steel or cement industries [112, 122]. The industrial process could also economically and technically benefit from the reuse of the obtained CaCO_3 in the process becoming CO_2 and

calcium neutral. The reutilization of industrial wastes within the existing process would lead to better and sustainable production.

Table 2.1: Various sources of alkaline earth metals used for carbon mineralization.

Type of sources	Name	Formula	References
Natural	Olivine	$(\text{Mg,Fe})_2\text{SiO}_4$	[21, 22, 96, 97, 102, 105, 113, 114, 117, 123-142]
	Serpentine	$\text{Mg}_3\text{Si}_2\text{O}_5(\text{OH})_4$	[101, 103, 104, 106, 108-111, 115-117, 119, 120, 127, 132, 143-164]
	Chrysotile	$\text{Mg}_3(\text{Si}_2\text{O}_5)(\text{OH})_4$	[165]
	Phlogopite	$\text{KMg}_3\text{AlSi}_3\text{O}_{10}(\text{OH})_2$	[128]
	Albite	$\text{NaAlSi}_3\text{O}_8$	[166, 167]
	Wollastonite	CaSiO_3	[128, 132, 168-176]
	Anorthite	$\text{CaAl}_2\text{Si}_2\text{O}_8$	[167]
	Phlogopite	$\text{KMg}_3\text{AlSi}_3\text{O}_{10}(\text{OH})_2$	[128]
	Harzburgite	$\text{CaMgSiO}_2\text{O}_6+(\text{Fe, Al})$	[177]
	Portlandite	$\text{Ca}(\text{OH})_2$	[65, 178-180]
	Brucite	$\text{Mg}(\text{OH})_2$	[107, 133, 181-184]
	Gypsum	$\text{CaSO}_4 \cdot 2\text{H}_2\text{O}$	This study
	Natural brines		[1, 185]
Industrial	Steel slag		[121, 173, 174, 186-207]
	Flue gas desulfurization gypsum		[208-212]
	Cement wastes		[196, 213-218]
	Paper Mill Waste		[217, 219]
	Coal fly ash		[185, 220-224]
	Red mud		[212, 217, 225-227]
	Mining wastes		[133, 190, 196, 214, 228-235]
	Municipal waste fly ash		[217, 236-240]
	Air pollution control system residue		[241]
	Industrial brines		[192, 193, 242-249]
	Magnesium chloride	MgCl_2	[250-254]

2.2.3.2 Dissolution/activation of metal ions in mineral sources

Table 2.1 gives a summary of the minerals and commercial alkali metal sources used for carbonation. The research involving natural sources have been focused on serpentine [101, 103, 104, 106, 108-111, 115-117, 119, 120, 127, 132, 143-164] due to the ease of extraction of Mg ions from it and its abundance in nature. The researches on the industrial sources have been focussed on steel slag waste [121, 173, 174, 186-207] due to its abundance (see table 1). The carbonation of mineral wastes has been demonstrated prior to the climate change paradigm [234]. Since the suggestion of silicates to be one of the major contenders for carbon capture [22] there has been extensive research on it (table 1). Natural minerals are thermodynamically more stable than the industrial waste material, therefore a lot of effort has been on the leaching/extraction of alkaline earth metals from them [112, 173, 197].

For gas-solid capture there are methods suggested for activation of the surface on the natural mineral by chemical modification [103, 104, 169, 255]. These include, conversion of the Mg rich serpentine to brucite for mineralization with CO₂ [103, 106, 108, 109, 146-150, 228] or treating (serpentine or olivine) via physical treatment (i.e. high temperature) or chemical treatment (use of acids and bases) to increase surface activity [255]. The research carried out at Åbo Akademi University (Finland) on the activation of Mg rich mineral (serpentine) have made direct carbonation in the gas-solid reaction regime more cost effective than before and have been simulated for pilot scale systems using Aspen Plus [106, 149, 186, 256]. Figure 2.5 shows the schematic of their process intensification [149, 186]. Fe²⁺ oxidation to hematite (Fe₂O₃) before the dehydroxylation process increases resistance to mass transfer and thermal

treatment during the dehydroxylation process of silicate rocks [156]. Steel slag wastes have shown better carbonation with minimal treatment compared to mineral rocks because of their low thermodynamic stability [187].

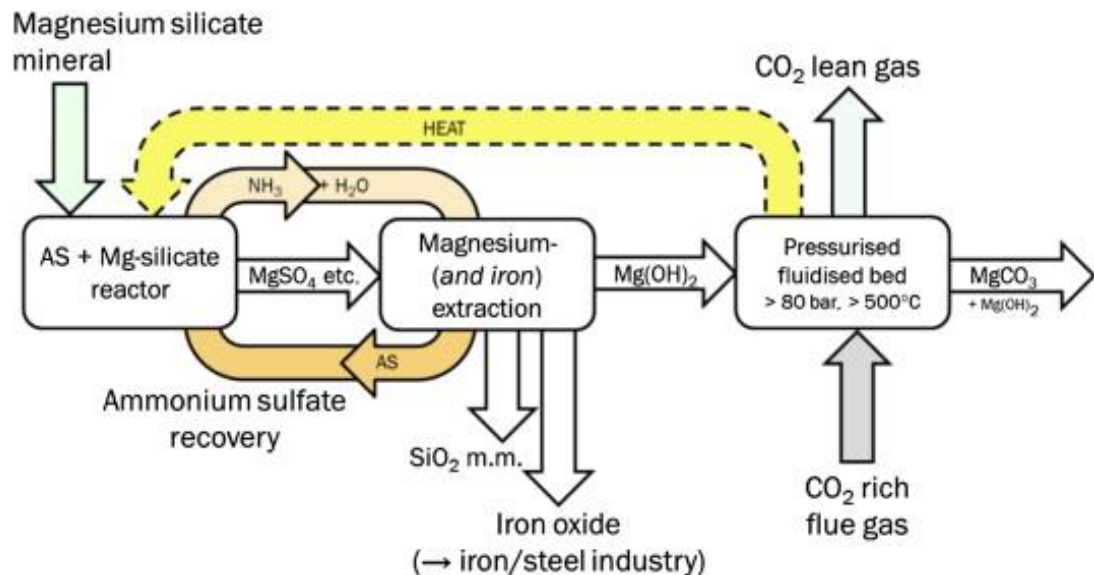


Figure 2.5 Schematic illustration of the mineral carbonation process (solid-gas) developed by Åbo Akademi University for 12 vol% CO₂ gas content [149, 186], AS- ammonium sulphate.

In aqueous method for mineralization leaching of the mineral salt is one of the major rate limiting step in the mineralization of CO₂. Various mineral acids (i.e. H₂SO₄, HCl, HNO₃, HF) [144, 152, 153, 155, 257], organic acids (i.e. fomic acid, glutamic acid, etc.) [116, 129, 143, 144, 188, 189] and their combinations [116, 143] have been tested to leach alkaline earth metals from the mineral rocks (table 2.2). Of all the acids listed in table 2, NH₄HSO₄ is found to be the most efficient of H₂SO₄ > HCl > HNO₃ in leaching of Mg²⁺ from serpentine [144, 151]. Basic salts (mainly ammonium salts) have also been suggested for leaching of M²⁺ ions from natural minerals [115, 166, 211, 248]. Matoro-Valer's group used ammonium sulphate NH₄HSO₄ to dissolve minerals [101, 118-120, 151]. Serpentine showed better Mg leaching than Olivine under similar process conditions [117, 127]. It was suggested that the silica formed during the reaction

of serpentine or olivine with leaching agents caused diffusion mass transfer limitation (i.e. diffusion of Mg^{2+} within the solid matrix in to the solution) for Mg dissolution in silicate rocks [115].

Industrial wastes (blast furnace slag) along with industrial brines (cold-rolling waste water) prove more energy effective method for metal ion leaching and CO_2 mineralization [192, 193, 258, 259]. Pan *et al.* [192, 193, 258, 259] demonstrated using a rotating packed bed (RPB) reactor intensified mineralization process. The RPB increased the mass transfer coefficient of the gas, increasing the efficiency of the process [192, 193, 258, 259].

Table 2.2: List of additives added for accelerated dissolution of alkaline earth metals from mineral rocks and industrial wastes.

Nature	Additive	Formula	Reference
Acidic	Acetic acid	CH_3COOH	[110, 116, 144, 169, 170, 176, 189, 191, 201]
	Aluminium nitrate	$Al(NO_3)_3$	[207]
	Aluminium sulphate	$Al_2(SO_4)_3$	[207]
	Ammonium chloride	NH_4Cl	[151, 194, 195, 201, 222, 230]
	Ammonium di-hydrogen phosphate	$NH_4H_2PO_4$	[207]
	Ammonium nitrate	NH_4NO_3	[194, 195, 207, 222]
	Ammonium hydrogen sulphate	NH_4HSO_4	[117, 119, 127, 151, 260]
	Ammonium sulphate	$(NH_4)_2SO_4$	[110, 148, 151, 207]
	Ascorbic acid	$C_6H_8O_6$	[176]
	Carbonic acid	H_2CO_3	[128]
	Citric acid	$C_6H_8O_7$	[176, 216]
	Ethylene-diamine-tetraacetic-acid (EDTA)	$C_{10}H_{16}N_2O_8$	[115, 116, 176]
	Formic acid	$HCOOH$	[110, 144]
	Gluconic acid	$HOCH_2(CHOH)_4COOH$	[176]
	Glutamic acid	$C_5H_9NO_4$	[176]

Nature	Additive	Formula	Reference
	Hydroflouric acid	HF	[257]
	Hydrochloric acid	HCl	[110, 115, 125, 136, 144, 145, 155, 160, 171, 255]
	Iminodiacetic acid	HN(CH ₂ CO ₂ H) ₂	[176]
	Nitric acid	HNO ₃	[144, 145, 172, 188, 192, 198, 207, 235]
	Nitrilotriacetic acid	(C ₆ H ₉ NO ₆)	[176]
	Orthophosphoric acid	H ₃ PO ₄	[115, 116]
	Oxalic acid	C ₂ H ₂ O ₄	[115, 116, 176]
	Phosphoric acid	H ₃ PO ₄	[255]
	Picolinic acid	C ₆ H ₅ NO ₂	[176]
	Potassium hydrogen phthalate	C ₈ H ₅ O ₄ K	[116]
	Propionic acid	CH ₃ CH ₂ COOH	[207]
	Phthalic acid	C ₈ H ₆ O ₄	[176]
	Sodium citrate	NaH ₂ C ₆ H ₅ O ₇	[216]
	Sodium nitrate	NaNO ₃	[132]
	Succinic acid	C ₄ H ₆ O ₄	[170]
	Sulphuric acid	H ₂ SO ₄	[110, 144, 151, 152, 162-164, 207, 255]
Basic	Ammonia	NH ₃	[254, 261]
	Ammonium hydroxide	NH ₄ OH	[109, 115]
	Diammonium hydrogen phosphate	(NH ₄) ₂ HPO ₄	[207]
	Diethanol Amine	C ₂ H ₇ NO ₂	[262]
	Dipotassium Phosphate	K ₂ HPO ₄	[116]
	Lithium hydroxide	LiOH	[130, 132, 136]
	Mono ethanol amine	C ₂ H ₇ NO	[262, 263]
	Methyl diethanol amine	CH ₃ N (C ₂ H ₄ OH) ₂	[262]
	Potassium hydroxide	KOH	[242]
	Potassium bicarbonate	KHCO ₃	[137]
	Rubidium bicarbonate	RbHCO ₃	[137]

Nature	Additive	Formula	Reference
	Sodium bicarbonate	NaHCO ₃	[105, 113, 114, 123, 134, 135, 137, 138, 140, 264]
	Sodium hydroxide	NaOH	[165, 172, 175, 198, 207, 255]
	Tributyl phosphate	C ₁₂ H ₂₇ O ₄ P	[206, 207]
	Urea	(NH ₂) ₂ CO	[207]
Neutral	Ammonium acetate	CH ₃ COONH ₄	[194, 207, 222]
	Calcium chloride	CaCl ₂ ·2H ₂ O	[116]
	Magnesium chloride	MgCl ₂	[167, 264]
	Sodium acetate	CH ₃ COONa	[154]
	Sodium chloride	NaCl	[105, 113, 114, 123, 124, 132, 134, 138, 140, 142, 167, 187, 213, 264]
	Sodium nitrate	NaNO ₃	[130]
	Sodium oxalate	Na ₂ (COO) ₂	[129, 154]
Biological	<i>Acidithiobacillus sp</i>		[159]
	<i>Dunaliella sp</i>		[265]
	<i>Sporosarcina pasteurii</i>		[266]
	<i>Carbonic Anhydrase</i>		Discussed in next section 2.3.3

2.2.3.3 Hydration of CO₂: non-catalytic and catalytic

CO₂ is one of the major components of the atmosphere and it has an important role in the bio-geo-chemical cycle of the globe. The oceans use carbonate equilibrium as an important mechanism to maintain the sustainability of life within the oceanic environment. Carbon dioxide in the solution environment exists in four forms: CO_{2(aq)}, carbonic acid (H₂CO₃), bicarbonate ion (HCO₃⁻) or as carbonate ion (CO₃²⁻). Their interaction with water, in aqueous solutions results in displacement of the H₃O⁺ and OH⁻ equilibrium, which is represented by the pH of the solution [267, 268].

In the aqueous route for mineralization of CO_2 the reaction of water molecules with CO_2 is another rate limiting parameter. In order for aqueous carbonation to proceed the CO_2 must react with water to form carbonic acid. The reaction of CO_2 with water has been studied since 1900 because it is one of the most important steps in photosynthesis [269, 270]. In 1960 the review by Kern [271] explains different experimental procedures that have been used to determine the hydration rate of CO_2 . Of these procedures there have been various methods that have been modified [272] or no longer in use (i.e. differential manometric method, thermometric) and recently only stopped-flow method is used for measuring the hydration reaction kinetics [271, 273, 274]. A detailed explanation on theories underlying the different methodologies are presented in chapter 3, section 3.1.

The first report on the slow hydration rate of CO_2 was reported by McBain in 1912 [275]. McBain [275] studied the change of the colour of phenolphthalein indicator while titrating CO_2 saturated solution against NaOH solution and observed that the near neutral pH the solution turns to pink (reaches endpoint) and then returns back to being colourless. This is a slow phenomenon and can also be observed using thymol blue which is yellow at pH below 6, green at pH 7 and blue at pH 8, showing similar phenomena [267, 271]. This slow change in colour is attributed to the slow hydration rate of CO_2 following reaction mechanism R1 (see below). The reason for this slow rate of to form carbonic acid is because in order to form one molecule of carbonic acid the CO_2 molecule has to be associated with 4 molecules of water [276, 277]. This $\text{CO}_2 (\text{H}_2\text{O})_4$ is the mechanistic rate limiting step of the CO_2 hydration reaction suggested by quantum chemical calculations [276-278].

The hydration of CO₂ is strongly influenced by pH of the solution. There are two reaction regimes for the hydration of CO₂ depending on the pH of the solution [267, 268, 271, 279]. These include the H₂O mechanism at pH < 8 and the OH⁻ mechanism at pH >10 (Reactions R1 and R3, respectively) [271]



and



Both the reaction mechanisms mentioned above have different reaction rates; the reaction in the presence of OH⁻ ions ($k = 8500 \text{ sec}^{-1}\text{M}^{-1}$) is faster than at lower pH values (pH < 8) ($k = 0.03 \text{ sec}^{-1}$) [271]. Therefore to control the initial pH of solutions there have been various kinetic rate studies done in buffer solutions. Dennard and Williams [280] found that presence of few buffer solutions (i.e. phosphate, arsenate, etc.) weakly catalyse the hydration reaction while others (the carbonate buffers in particular) are non-catalytic. Table 2.3 lists the various rate constants for hydration reaction (reported so far in literature) for non-catalysed and catalysed system. It can be seen that there is a wide variation in the reported kinetic values observed during a century of research in this area, this may be due to the adaptation made in the experimental methodology due to novel chemical analysis technological development and/or further understanding [271].

It has been observed that the rate of reaction of carbonic acid with alkaline absorption solutions is faster than with $\text{CO}_{2(\text{aq})}$ [288, 289]. Therefore when CO_2 is separated using reacting absorption process, the rate of mass transfer (rate of CO_2 absorption) is dependent on the rate of reaction of CO_2 with the solvent. There have also been various reports on the use of catalysts to enhance the mass transfer of CO_2 in carbonate and amine solutions [279, 281-296]. These are organic or inorganic molecules [286, 290] or nanostructures [297, 298] that enhance the hydration of CO_2 increasing the rate of reaction therefore the rate of mass transfer rates of CO_2 absorption. The CO_2 hydration is an important part of CO_2 absorption in amine or carbonate solutions, but the operating pH range is also important in the experimental procedure. Often studies of the absorption of CO_2 into basic solutions do not calculate or measure the rate constant of reaction but use them from the literature (for example the values of rate constants given by Danckwerts and Sharma [299] or Dennard and Williams [280] or see Table 2.3). Also often it is assumed that the reaction takes place at a pH above 10 [279], where the OH based reaction mechanism (R3) dominates [271]. Since reaction rate constant values have not been calculated or measured in these studies [279, 281-296], they have not been discussed in detail.

All the catalysts in table 2.3 along with carbonic anhydrase (table 2.4) are molecular catalysts that are used for hydration of CO_2 which are therefore described as a biphasic (gas-liquid) reaction. Bhaduri and Šiller [57] were the first to report the use of solid catalyst for the hydration of CO_2 . There are very limited studies that have been reported for gas-liquid-solid catalysis [300, 301] and to the best of the authors knowledge none for CO_2 hydration reaction (see further discussed chapter 3, section 3.1).

Table 2.3: Reported kinetic constants of non-catalysed and catalysed hydration of CO₂

Additive/catalyst	Solvent	Formula	Rate constant	Reference
Pure water (non-catalysed)				
	Water		0.035 s ⁻¹	[302]
	Water		2.6 x 10 ⁻² s ⁻¹ M ⁻¹	[274]
	Water		0.0375 s ⁻¹	[303]
	Water		0.0257 s ⁻¹	[304]
	Water		0.0132 s ⁻¹ M ⁻¹	[305]
	Water		6.64x10 ⁻⁴ s ⁻¹ M ⁻¹	[273]
	Water		0.029 s ⁻¹	[274]
	Water		0.037 s ⁻¹	[306]
	Water		0.038 s ⁻¹	[307]
	Water		0.044 s ⁻¹	[308]
	Sea water		0.037 s ⁻¹	[309]
Buffer solutions (non-catalysed)				
Phosphate	Water	HPO ₄ ²⁻	0.3 s ⁻¹ M ⁻¹	[274]
	Water	HPO ₄ ²⁻	0.049 s ⁻¹	[308]
	Water	HPO ₄ ²⁻	0.0337 s ⁻¹ M ⁻¹	[305]
Imidazone	Water	(CH ₂) ₂ N(NH)CH	6830 s ⁻¹ M ⁻¹	[310]
Catalysed reactions				
Acetaldehyde hydrate	Carbonate	CH ₃ CH(OH) ₂	0.1253 s ⁻¹ M ⁻¹	[299]
Arginine	Carbonate	NH ₂ C(NH)NHC ₃ H ₆ C(NH ₂)COOH	13045 s ⁻¹	[311]
Arsenite	Carbonate	AsO ₃ ³⁻	310 s ⁻¹ M ⁻¹	[312]
	Carbonate	AsO ₃ ³⁻	126 s ⁻¹ M ⁻¹	[313]
	Water	AsO ₂ ⁻	2000 s ⁻¹ M ⁻¹	[280]
	Water	HAsO ₄ ²⁻	5 s ⁻¹ M ⁻¹	[280]
Arsenious acid	Phosphate	As(OH) ₃	0.345 s ⁻¹ M ⁻¹	[299]
	Veronal	As(OH) ₃	5.2 s ⁻¹ M ⁻¹	[299]
	Carbonate	As(OH) ₃	19 s ⁻¹ M ⁻¹	[299]
Boric acid	Water	B(OH) ₄ ⁻	1 s ⁻¹ M ⁻¹	[280]
	Imidazone	B(OH) ₄ ⁻	35.3 s ⁻¹ M ⁻¹	[310]

Additive/catalyst	Solvent	Formula	Rate constant	Reference
Butyl chloral hydrate	Carbonate	$\text{CH}_3\text{CHClCCl}_2\text{CH}(\text{OH})_2$	$12.2 \text{ s}^{-1}\text{M}^{-1}$	[299]
Chloral hydrate	Carbonate	$\text{CCl}_3\text{CH}(\text{OH})_2$	$30 \text{ s}^{-1}\text{M}^{-1}$	[299]
Chloral alcoholate	Carbonate	$\text{CCl}_3\text{CH}(\text{OH})\text{OC}_2\text{H}_5$	$32 \text{ s}^{-1}\text{M}^{-1}$	[299]
Diacetyl hydrate	Carbonate	$\text{CH}_3\text{COC}(\text{OH})_2\text{CH}_3$	$0.515 \text{ s}^{-1}\text{M}^{-1}$	[299]
Hypobromous acid	Water	BrO^-	$10000 \text{ s}^{-1}\text{M}^{-1}$	[280]
Hypochlorous acid	Water	ClO^-	$50000 \text{ s}^{-1}\text{M}^{-1}$	[280]
	Carbonate	ClO^-	$3040 \text{ s}^{-1}\text{M}^{-1}$	[313]
Copper sulphate	Imidazone	CuSO_4	$2.5 \text{ s}^{-1}\text{M}^{-1}$	[274]
Ethanol	Carbonate	$\text{C}_2\text{H}_5\text{OH}$	$2.16 \text{ s}^{-1}\text{M}^{-1}$	[314]
Formaldehyde	Carbonate	HCHO	$28.20 \text{ s}^{-1}\text{M}^{-1}$	[312, 314]
	Carbonate	HCHO	$28.4 \text{ s}^{-1}\text{M}^{-1}$	[313]
Fructose	Carbonate	$\text{C}_6\text{H}_{12}\text{O}_6$	$20.21 \text{ s}^{-1}\text{M}^{-1}$	[314]
Germanic acid	Water	$\text{Ge}(\text{OH})_4$	$2000 \text{ s}^{-1}\text{M}^{-1}$	[280]
	Phosphate	$\text{Ge}(\text{OH})_4$	$0.572 \text{ s}^{-1}\text{M}^{-1}$	[299]
	Veronal	$\text{Ge}(\text{OH})_4$	$8.8 \text{ s}^{-1}\text{M}^{-1}$	[299]
	Carbonate	$\text{Ge}(\text{OH})_4$	$25.5 \text{ s}^{-1}\text{M}^{-1}$	[299]
Glucose	Carbonate	$\text{C}_6\text{H}_{12}\text{O}_6$	$19.59 \text{ s}^{-1}\text{M}^{-1}$	[314]
Glycerin	Carbonate	$(\text{HO})\text{CHCH}(\text{OH})\text{CH}(\text{OH})$	$4.07 \text{ s}^{-1}\text{M}^{-1}$	[314]
Glyoxal hydrate	Carbonate	$\text{CH}(\text{OH})_2\text{CH}(\text{OH})_2$	$1.28 \text{ s}^{-1}\text{M}^{-1}$	[299]
Methanol	Carbonate	CH_3OH	$0.97 \text{ s}^{-1}\text{M}^{-1}$	[314]
	Water	HPO_4^{2-}	$10 \text{ s}^{-1}\text{M}^{-1}$	[280]
	Water	H_2PO_4^-	$2 \text{ s}^{-1}\text{M}^{-1}$	[280]
Methylene glycol	Carbonate	$\text{CH}_2(\text{OH})_2$	$0.52 \text{ s}^{-1}\text{M}^{-1}$	[299]
Saccharose	Carbonate	$\text{C}_{12}\text{H}_{22}\text{O}_{11}$	$40.84 \text{ s}^{-1}\text{M}^{-1}$	[312]
Selenic acid	Water	SeO_4^{2-}	$6000 \text{ s}^{-1}\text{M}^{-1}$	[280, 314]
Silicic acid	Water	H_3SiO_4^-	$1000 \text{ s}^{-1}\text{M}^{-1}$	[280]
	Carbonate	H_4SiO_4	$0.9 \text{ s}^{-1}\text{M}^{-1}$	[299]
	Water	SiO_3^{2-}	$1000 \text{ s}^{-1}\text{M}^{-1}$	[280]
Telluric acid	Water	$\text{Te}(\text{OH})_6$	$700 \text{ s}^{-1}\text{M}^{-1}$	[280]
	Carbonate	$\text{Te}(\text{OH})_6$	$4.6 \text{ s}^{-1}\text{M}^{-1}$	[299]
Telluric acid	Water	$\text{Te}(\text{OH}_4\text{O}_2)^{2-}$	$4000 \text{ s}^{-1}\text{M}^{-1}$	[280]

Additive/catalyst	Solvent	Formula	Rate constant	Reference
Sodium acetate	Sodium chloride	$C_2H_3NaO_2$	$8.9 s^{-1}$	[315]
Zinc sulphate	Imidazone	$ZnSO_4$	$6 s^{-1}M^{-1}$	[274]

The most important and efficient catalyst that has been studied for the hydration of CO_2 is carbonic anhydrase (CA) [316, 317]. CA is a bio catalyst that has a high conversion rate for reversible hydration of CO_2 , highest being for human CA II with a rate constant of $1.1 \times 10^6 s^{-1}$ [318]. CA is a Zn metallo-enzyme that exists in 5 different families ($\alpha, \beta, \gamma, \delta,$ and ζ) [319-324]. The various types of CA depend in the number of Zn ions and monomeric units on the enzyme [320]. There is no particular protein sequence between the various families of CA, but all of them have a Zn ion as an active site [319, 320] (except for ζ family which has a Cd ion as an active site [321, 322]).

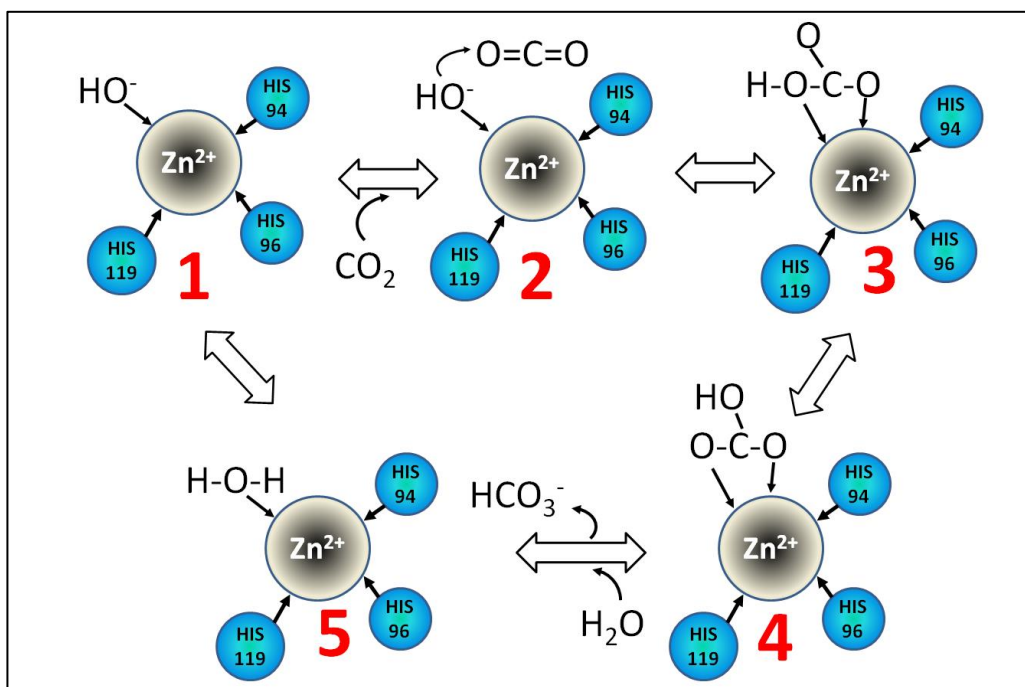


Figure 2.6: Reaction mechanism of Carbonic anhydrase for hydration of CO_2 (adapted from [317]).

Figure 2.5 shows the hydration mechanism of CA as adapted from Lee *et al.* [325]. The process of catalysis begins with the hydroxide ion on the Zn^{2+} ion

bound within the CA (step 1). This is then attacked by the CO₂ molecule to form the bicarbonate ion (step 2-3). This bicarbonate ion then rearranges the H⁺ ion and followed by desorption of the bicarbonate ion (step 4 and step 5). A water molecule then replaces this bicarbonate ion, followed by H⁺ dissociation leading to the initial form of the CA (step 5 and step 1) [325]. The histidine (HIS) macromolecules help in the displacement and rearrangement of the H⁺ ion within the CA molecule [319]. It is important to note that the deprotonation step of the enzyme is the rate limiting step (in figure 2.5 step 5-1) in CA catalysis [319]. In the absence of a deprotonating media (i.e. a base or buffer) the CA catalysis is rendered ineffective [326].

CA extracted from various sources have been studied as candidates for CCS mineralization applications. These sources include various bacterial CA and fungal CA from *Pseudomonas fragi* [327-331], *Micrococcus lylae* [327-329, 331], *Micrococcus luteus* [327-329], *Bacillus pumilus* [328, 331-338], *Citrobacter freundii* [339], *Aeromonas sp* [340], *Entrobacter sp* [340], *Shigella sp* [340], *Klebsiella sp*[340], *Bacillus mucilaginosus* [341], *Bacillus sp.* [342], *Sulphurihydrogenibium sp*[343, 344], *Escherichia coli* [345], *Bacillus cereus* [346], while the others used bovine carbonic anhydrase purchased from Sigma Aldrich (see table 2.4).

The CA is a water soluble homogenous enzyme and it can be easily lost in the capture and sequestration process as it is difficult to recover [316]. To overcome this drawback it is necessary immobilise the enzyme for repeated use. Table 2.4 lists the various enzyme immobilization studies with the reported kinetic constants. From the table 2.4 it is clear that in the majority of the studies the free enzymes showed better activity than the immobilized enzymes.

Michealis-menten kinetics is the most widely used method for evaluation of biochemical reactions [347, 348]. The Michealies constant K_M for the immobilized enzymes is higher than the free enzymes (in majority of the cases in table 2.4) indicating that the kinetics is mass transfer limited (i.e. the reaction rate is dependent on the diffusion of substrate from the solution to the active site and diffusion of products from the active sites to the solution).

Mirjafari *et al.* [349] calculated the activation energy required for carbonic anhydrase to hydrate the CO_2 molecule to be 700.9115 cal/mol. There are technical limitations in interpreting this reported data as suggested by Mirjafari *et al.* [349] because the experiment was carried out in a buffer but the buffer activity has not been accounted for in data evaluation. In all other studies (table 2.4), the pH change in buffer was used as a qualitative technique for evaluation of CO_2 hydration activity of CA. The kinetic constant for the CO_2 hydration reaction is determined by the hydrolysis of p-nitophenol which is also catalysed by CA having same rate as hydration of CO_2 [328, 331-338]. pH and temperature are two parameters that affect the catalytic activity of CA [349, 350]. It can be seen from the table 2.4 that the optimum pH value for best activity of CA is between 7-8 for both free and immobilized enzymes. The pH affects the reaction rate as the H^+ ion concentration limits the regeneration of the enzyme [350]. The typical temperatures that have been used for the kinetic studies with CA (reported in table 2.4) are between 20-30 °C.

Along with the application for mineralization CA has been used as a catalyst for enhancement of absorption of CO_2 and in separation systems. There have been recent reports on the use of CA in liquid membranes for separation of CO_2 (Trachtenberg and colleagues, Carbozyme Inc) [325, 351-

360], in hollow fibre membranes [361, 362] and in separation processes using amine and carbonate systems [98, 292, 293, 363-374].

Table 2.4: Activity of Carbonic anhydrase (free and immobilized) enzyme.

CA Source	Immobilization Medium	Michealis constant K_m (mM)	Turnover number k_{cat} (s^{-1})	Catalytic Efficiency k_{cat}/K_m ($M^{-1}s^{-1}$)	V_{max} ($mMmin^{-1}$)	pH	Comments	References
<i>B. Pumilus</i>	Free enzyme	1.25	0.60093	486.66	0.02029	7	The single enzyme particle showed 3 times higher catalytic efficiency than free enzyme	[332]
	Single Enzyme particle	6.143	8.579	1396.5	0.02857	7		
<i>B. Pumilus</i>	Free enzyme	1.211	0.01875		1.125*		(*units of V_{max} are $\mu Ms^{-1}mg^{-1}$)	[328]
	Surfactant modified silyated chitosan	4.547	0.0169		1.018*			
<i>B. Pumilus</i>	Free enzyme	0.87			0.00093	7		[335]
	Chitosan beads	2.36			0.00054	7		
<i>B. Pumilus</i>	Free enzyme	1.594	0.330		0.001307	7		[334]
	Chitosan stabilized iron nanoparticles	1.727	0.300		0.001189	7		
<i>B. Pumilus</i>	Free enzyme	0.876	2.3		0.000936	7		[333]
	Mezoporus aluminosilicates AIKIT-5	0.158	1.9		0.002307	7		
<i>B. Pumilus</i>	Free enzyme	1.89			0.00099	7	The V_{max} values for free and immobilized enzymes were same	[338]
	Chitosan derived carbon composite	10.35			0.00099	7		
<i>Bovine CA</i>	Free enzyme			874		8		[375]
	Fe_3O_4 - SiO_2 -octa(amino-phenyl)silsesquioxane			783		8		

CA Source	Immobilization Medium	Michealis constant K_m (mM)	Turnover number k_{cat} (s^{-1})	Catalytic Efficiency k_{cat}/K_m ($M^{-1}s^{-1}$)	V_{max} ($mMmin^{-1}$)	pH	Comments	References
<i>Bovine CA</i>	Free enzyme	12.2	2.02	166.4		7.5	Immobilized enzymes showed better activity than the free enzymes	[376]
	Polyurethane foam	9.6	-	-		7.5		
<i>Bovine CA</i>	Free CA	0.000675			0.306*	8	(*units of V_{max} are $\mu Ms^{-1}mg^{-1}$) The $CaCO_3$ crystalline composite CA are magnetic due to presence of Fe_3O_4 .	[377]
	$CaCO_3$ crystalline composite	0.000707			0.138*	8		
<i>Bovine CA</i>	Free enzyme	9.54		453.2		8		[378]
	Chitosan/ $SiO_2/\gamma Fe_2O_3$ particles	13.87		303.2		8		
<i>Sulphurihydrogenibium sp</i>	Free enzyme	2.8			1414		The CA extracted from <i>Sulphurihydrogenibium sp</i> has lower V_{max} than the bacterial CA.	[343, 344]
<i>Bovine CA</i>	Free enzyme	3.4			5155			
<i>Bovine CA</i>	Free enzyme	56.67	49.51	873.76		8	Catalytic efficiency of crossed linked enzyme with silica beads was close to free enzyme followed by absorbed enzyme on silica beads and covalent attachment of enzyme on silica beads	[379]
	Adsorbed on silica beads SBA-15	60.2	39.77	800.11		8		
	Covalent attachment on silica beads SBA-15	59.6	40.53	690.50		8		
	Crossed linked enzyme aggregation on silica beads SBA-15	65.2	48.25	820.06		8		

CA Source	Immobilization Medium	Michealis constant K_m (mM)	Turnover number k_{cat} (s^{-1})	Catalytic Efficiency k_{cat}/K_m ($M^{-1}s^{-1}$)	V_{max} ($mMmin^{-1}$)	pH	Comments	References
<i>E. Coli</i>	Free enzyme	18.26			0.43478	8-9		[345]
	Chitosan-alginate poly-electrolyte complex	19.12			0.41666	8-9		
<i>Bovine CA</i>	Free enzyme	6.1	0.79	129.51		7	As compared to the above results in this study the Crossed linked enzyme aggregation on silica beads SBA-15 had better efficiency than the free enzyme	[326]
	Adsorbed on silica beads SBA-15	5.8	0.36	62.07		7		
	Covalent attachment on silica beads SBA-15	5.9	0.58	98.30		7		
	Crossed linked enzyme aggregation on silica beads SBA-15	6.3	0.78	123.81		7		
<i>Human CA</i>	Free enzyme	27.29		7768		8	The catalytic efficiency was similar to free enzyme all different immobilized enzymes on silica beads functionalized with amines the best being that of SBA-15 with octa(amino-phenyl) silsesquioxane with high stability.	[380]
	SBA-15 with tetraethylene-pentamine	25.23		7182		8		
	SBA-15 with tris(2-amino-ethyl) amine	25.88		7368		8		
	SBA-15 with octa(amino-phenyl) silsesquioxane	26.59		7569		8		
<i>Human CA II</i>	Nylon tubes		900000			8	Human CA II immobilised in microreactor for feasibility study retaining 90% of activity of HCA	[381]

CA Source	Immobilization Medium	Michealis constant K_m (mM)	Turnover number k_{cat} (s^{-1})	Catalytic Efficiency k_{cat}/K_m ($M^{-1}s^{-1}$)	V_{max} ($mMmin^{-1}$)	pH	Comments	References
<i>Human CA II</i>	Free enzyme		1100000				4 different models have been used to predict the kinetic value all yielding same results	[318]
<i>Human CA</i>	Free enzyme	13.07		1663.35		6.4	The catalytic efficiency of SBA-15-AuNPs with 3-mercaptopropyl-trioxy silicane and SBA-15-AuNPs with 3-amino propyltrioxy silicane was better than just SBA-15.	[382]
	SBA-15	26.85		1480.07		6.4		
	SBA-15-AuNP with 3-amino propyltrioxy silicane	22.35		1514.09		6.4		
	SBA-15-AuNP with 3-mercaptopropyltrioxy silicane	27.75		1612.25		6.4		
<i>Human CA</i>	Free enzyme			1660		6.4	Similar to the previous results [380] the results in this study also show that SBA--AgNPs with octa(amino-phenyl) silsesquioxane has better catalytic activity than other amine functionalized SBA-15.	[383]
	SBA-15-AgNP with tetraethylene-pentamine			1590		6.4		
	SBA-15-AgNP with tris(2-amino-ethyl) amine			1580		6.4		
	SBA-15-AgNP with octa(amino-phenyl) silsesquioxane			1640				

2.2.3.4 Precipitation of mineral carbonate

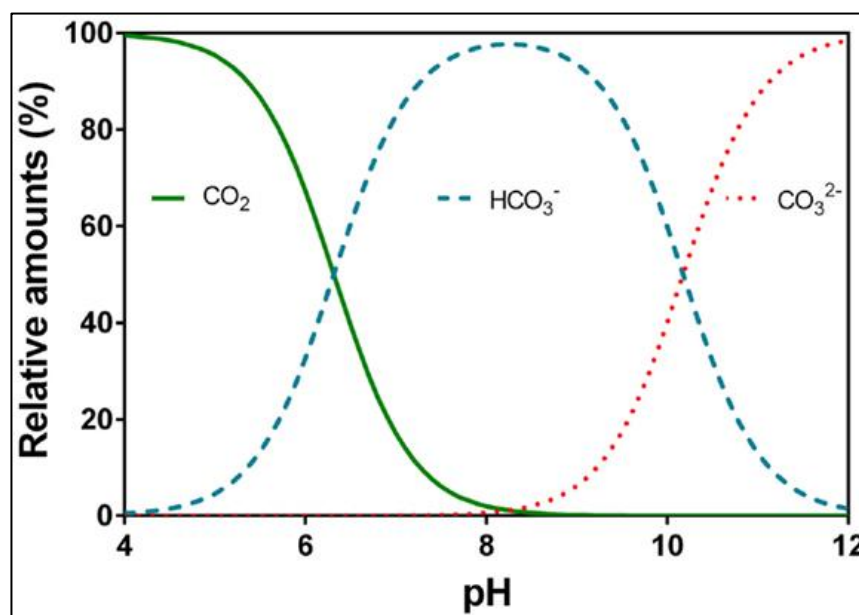


Figure 2.7: Carbonate equilibrium diagram [384].

Figure 2.7 shows the relative distribution of the various ions in aqueous solutions under equilibrium conditions of $\text{CO}_{2(\text{aq})}$, HCO_3^- and CO_3^{2-} at various pH values [384]. During aqueous mineralization of CO_2 the pH of the solution decreases due to the addition of CO_2 . The solubility of carbonates increases as the pH decreases [349, 385] therefore in order to precipitate the carbonate salt out of solution the pH always needs to be in the carbonate zone in figure 2.7. This causes an addition of costs and requirement of a sacrificial alkaline material for the precipitation of the carbonate from solution during mineralization of CO_2 . The most commonly used alkaline material in the mineralization studies is ammonia or NaOH (section 2.3.1-2.3.2). Maroto-Valer's group used recyclable ammonium salts that are converted to basic ammonia which provides suitable pH for the precipitation of carbonate material [101, 118, 119, 151]. The use of buffer solutions in the CA analysis have been successful for mineralization studies [328, 331-338], but the feasibility of using such a system

for industrial process is low. Buffer solutions are the chemical compounds that limit a change in pH when an acid is added to them.

Other than pH, nucleation of the carbonate crystal (CaCO_3 in particular) is also an important step in the precipitation process. This is specific to the use of brine solutions as medium of precipitation because various cations like Mg^{2+} inhibit the precipitation of Ca^{2+} salts [386].

References:

- [1] H.E. Dunsmore, A geological perspective on global warming and the possibility of carbon dioxide removal as calcium carbonate mineral, *Energy Conversion and Management*, 33 (1992) 565-572.
- [2] B. Mertz, O.R. Davidson, P.R. Bosch, R. Dave, L.A. Meyer, IPCC, 2007: *Climate Change 2007: Mitigation. Contribution of the Working Group III to the Fourth Assessment Report of the Intergovernmental Panel on Climate Change*, in, Cambridge University Press, Cambridge, United Kingdom and New York, NY, USA, 2007.
- [3] B. Freedman, G. Stinson, P. Lacoul, Carbon credits and the conservation of natural areas, *Environmental Reviews*, 17 (2009) 1-19.
- [4] T.A. Boden, G. Marland, R.J. Andres, *Global, Regional, and National Fossil-Fuel CO₂ Emissions*, Carbon Dioxide Information Analysis Center, Oak Ridge National Laboratory,, Oak Ridge, Tenn., U.S.A., 2013.
- [5] O. Edenhofer, R. Pichs-Madruga, Y. Sokona, K. Seyboth, P. Matschoss, S. Kadner, T. Zwickel, P. Eickemeier, G. Hansen, S. Schloemer, C. von Stechow, *Renewable Energy Sources and Climate Change Mitigation*, Cambridge University Press, Cambridge, UK, 2011.
- [6] B.J.M. de Vries, D.P. van Vuuren, M.M. Hoogwijk, Renewable energy sources: Their global potential for the first-half of the 21st century at a global level: An integrated approach, *Energy Policy*, 35 (2007) 2590-2610.
- [7] IEA, *Redrawing the Energy-Climate Map in: World Energy Outlook Special Report*, International Energy Agency, France, 2013.
- [8] B. Metz, O. Davidson, H. de Coninck, M. Loos, L. Meyer, *Carbon capture and Storage*, in, Cambridge University Press, Cambridge, UK, 2005.
- [9] H. Yang, Z. Xu, M. Fan, R. Gupta, R.B. Slimane, A.E. Bland, I. Wright, Progress in carbon dioxide separation and capture: A review, *Journal of Environmental Sciences*, 20 (2008) 14-27.
- [10] A. Goeppert, M. Czaun, G.K. Surya Prakash, G.A. Olah, Air as the renewable carbon source of the future: an overview of CO₂ capture from the atmosphere, *Energy & Environmental Science*, 5 (2012) 7833-7853.
- [11] D.M. D'Alessandro, B. Smit, J.R. Long, *Carbon Dioxide Capture: Prospects for New Materials*, *Angewandte Chemie International Edition*, 49 (2010) 6058-6082.
- [12] G. Scheffknecht, L. Al-Makhadmeh, U. Schnell, J. Maier, Oxy-fuel coal combustion—A review of the current state-of-the-art, *International Journal of Greenhouse Gas Control*, 5, Supplement 1 (2011) S16-S35.
- [13] A.A. Olajire, CO₂ capture and separation technologies for end-of-pipe applications – A review, *Energy*, 35 (2010) 2610-2628.

- [14] M.E. Boot-Handford, J.C. Abanades, E.J. Anthony, M.J. Blunt, S. Brandani, N. Mac Dowell, J.R. Fernandez, M.-C. Ferrari, R. Gross, J.P. Hallett, R.S. Haszeldine, P. Heptonstall, A. Lyngfelt, Z. Makuch, E. Mangano, R.T.J. Porter, M. Pourkashanian, G.T. Rochelle, N. Shah, J.G. Yao, P.S. Fennell, Carbon capture and storage update, *Energy & Environmental Science*, 7 (2014) 130-189.
- [15] K. Huang, C.-L. Sun, Z.-J. Shi, Transition-metal-catalyzed C-C bond formation through the fixation of carbon dioxide, *Chemical Society Reviews*, 40 (2011) 2435-2452.
- [16] G. Centi, E.A. Quadrelli, S. Perathoner, Catalysis for CO₂ conversion: a key technology for rapid introduction of renewable energy in the value chain of chemical industries, *Energy & Environmental Science*, 6 (2013) 1711-1731.
- [17] E.A. Quadrelli, G. Centi, J.-L. Duplan, S. Perathoner, Carbon Dioxide Recycling: Emerging Large-Scale Technologies with Industrial Potential, *ChemSusChem*, 4 (2011) 1194-1215.
- [18] M. Peters, B. Köhler, W. Kuckshinrichs, W. Leitner, P. Markewitz, T.E. Müller, Chemical Technologies for Exploiting and Recycling Carbon Dioxide into the Value Chain, *ChemSusChem*, 4 (2011) 1216-1240.
- [19] T. Sakakura, J.-C. Choi, H. Yasuda, Transformation of Carbon Dioxide, *Chemical Reviews*, 107 (2007) 2365-2387.
- [20] K. Michael, A. Golab, V. Shulakova, J. Ennis-King, G. Allinson, S. Sharma, T. Aiken, Geological storage of CO₂ in saline aquifers—A review of the experience from existing storage operations, *International Journal of Greenhouse Gas Control*, 4 (2010) 659-667.
- [21] K.S. Lackner, A Guide to CO₂ Sequestration, *Science*, 300 (2003) 1677-1678.
- [22] W. Seifritz, CO₂ disposal using means of silicates, *Nature*, 345 (1990) 486.
- [23] J.S. Marx, A., P.H. Zapp, M., J.-F.G. Hake, J., Environmental evaluation of CCS using life cycle assessment - A synthesis report, In *Energy Procedia*, 10th International Conference on Greenhouse Gas Control Technologies, 4 (2011) 2448-2456.
- [24] T.F. Wall, Combustion processes for carbon capture, *Proceedings of the Combustion Institute*, 31 (2007) 31-47.
- [25] B.P. Spigarelli, S.K. Kawatra, Opportunities and challenges in carbon dioxide capture, *Journal of CO₂ Utilization*, 1 (2013) 69-87.
- [26] H. Fang, L. Haibin, Z. Zengli, Advancements in development of chemical-looping combustion: A review, *International Journal of Chemical Engineering*, (2009).

- [27] M.M. Hossain, H.I. de Lasa, Chemical-looping combustion (CLC) for inherent CO₂ separations—a review, *Chemical Engineering Science*, 63 (2008) 4433-4451.
- [28] E.S. Rubin, H. Mantripragada, A. Marks, P. Versteeg, J. Kitchin, The outlook for improved carbon capture technology, *Progress in Energy and Combustion Science*, 38 (2012) 630-671.
- [29] D.A. Voormeij, G.J. Simandl, Geological, Ocean, and Mineral CO₂ Sequestration Options: A Technical Review, *Geoscience Canada*, 4 (2004) 11-22.
- [30] R.N. Shreve, G.T. Austin, *Shreve's Chemical process industries*, McGraw-Hill, 1984.
- [31] L. Gradisher, B. Dutcher, M. Fan, Catalytic hydrogen production from fossil fuels via the water gas shift reaction, *Applied Energy*, 139 (2015) 335-349.
- [32] M. Arabloo, A. Bahadori, M.M. Ghiasi, M. Lee, A. Abbas, S. Zendejboudi, A novel modeling approach to optimize oxygen–steam ratios in coal gasification process, *Fuel*, 153 (2015) 1-5.
- [33] A. Gomez, N. Mahinpey, Kinetic study of coal steam and CO₂ gasification: A new method to reduce interparticle diffusion, *Fuel*, 148 (2015) 160-167.
- [34] A. Tchapda, S. Pisupati, A Review of Thermal Co-Conversion of Coal and Biomass/Waste, *Energies*, 7 (2014) 1098-1148.
- [35] L. Emami-Taba, M.F. Irfan, W.M.A. Wan Daud, M.H. Chakrabarti, Fuel blending effects on the co-gasification of coal and biomass – A review, *Biomass and Bioenergy*, 57 (2013) 249-263.
- [36] R.N. André, F. Pinto, C. Franco, M. Dias, I. Gulyurtlu, M.A.A. Matos, I. Cabrita, Fluidised bed co-gasification of coal and olive oil industry wastes, *Fuel*, 84 (2005) 1635-1644.
- [37] C.A. Scholes, K.H. Smith, S.E. Kentish, G.W. Stevens, CO₂ capture from pre-combustion processes—Strategies for membrane gas separation, *International Journal of Greenhouse Gas Control*, 4 (2010) 739-755.
- [38] P. Casero, P. Coca, F. García-Peña, N. Hervás, CO₂ emissions reduction technologies in IGCC: ELCOGAS's experiences in the field, *Greenhouse Gases: Science and Technology*, 3 (2013) 253-265.
- [39] D.J. Roddy, A syngas network for reducing industrial carbon footprint and energy use, *Applied Thermal Engineering*, 53 (2013) 299-304.
- [40] M.A. Habib, H.M. Badr, S.F. Ahmed, R. Ben-Mansour, K. Mezghani, S. Imashuku, G.J. la O, Y. Shao-Horn, N.D. Mancini, A. Mitsos, P. Kirchen, A.F. Ghoneim, A review of recent developments in carbon capture utilizing oxy-fuel combustion in conventional and ion transport membrane systems, *International Journal of Energy Research*, 35 (2011) 741-764.

- [41] M.B. Toftegaard, J. Brix, P.A. Jensen, P. Glarborg, A.D. Jensen, Oxy-fuel combustion of solid fuels, *Progress in Energy and Combustion Science*, 36 (2010) 581-625.
- [42] M.E. Walker, J. Abbasian, D.J. Chmielewski, M.J. Castaldi, Dry Gasification Oxy-combustion Power Cycle, *Energy & Fuels*, 25 (2011) 2258-2266.
- [43] J. Adanez, A. Abad, F. Garcia-Labiano, P. Gayan, L.F. de Diego, Progress in Chemical-Looping Combustion and Reforming technologies, *Progress in Energy and Combustion Science*, 38 (2012) 215-282.
- [44] L.-S. Fan, L. Zeng, W. Wang, S. Luo, Chemical looping processes for CO₂ capture and carbonaceous fuel conversion - prospect and opportunity, *Energy & Environmental Science*, 5 (2012) 7254-7280.
- [45] R. Sharma, A. Delebarre, B. Alappat, Chemical-looping combustion - an overview and application of the recirculating fluidized bed reactor for improvement, *International Journal of Energy Research*, (2014).
- [46] P. Lisbona, A. Martínez, L.M. Romeo, Hydrodynamical model and experimental results of a calcium looping cycle for CO₂ capture, *Applied Energy*, 101 (2013) 317-322.
- [47] M. Rydén, C. Linderholm, P. Markström, A. Lyngfelt, Release of gas-phase O₂ from ilmenite during chemical-looping combustion experiments, *Chemical Engineering and Technology*, 35 (2012) 1968-1972.
- [48] N. Ding, Y. Zheng, W.R. Wang, C. Luo, P.F. Fu, C.G. Zheng, Development and Testing of an Interconnected Fluidized-Bed System for Chemical Looping Combustion, *Chemical Engineering & Technology*, 35 (2012) 532-538.
- [49] S.D. Kenarsari, D. Yang, G. Jiang, S. Zhang, J. Wang, A.G. Russell, Q. Wei, M. Fan, Review of recent advances in carbon dioxide separation and capture, *RSC Advances*, 3 (2013) 22739-22773.
- [50] N. MacDowell, N. Florin, A. Buchard, J. Hallett, A. Galindo, G. Jackson, C.S. Adjiman, C.K. Williams, N. Shah, P. Fennell, An overview of CO₂ capture technologies, *Energy & Environmental Science*, 3 (2010) 1645-1669.
- [51] C.H. Yu, C.H. Huang, C.S. Tan, A review of CO₂ capture by absorption and adsorption, *Aerosol and Air Quality Research*, 12 (2012) 745-769.
- [52] Ö. Yildirim, A.A. Kiss, N. Hüser, K. Leßmann, E.Y. Kenig, Reactive absorption in chemical process industry: A review on current activities, *Chemical Engineering Journal*, 213 (2012) 371-391.
- [53] J.E. Bara, What chemicals will we need to capture CO₂?, *Greenhouse Gases: Science and Technology*, 2 (2012) 162-171.

- [54] T. Makino, M. Sakurai, M. Kanakubo, Solubilities of gases in ionic liquids and its applications to separation processes, *Journal of the Vacuum Society of Japan*, 56 (2013) 88-96.
- [55] X. Zhang, X. Zhang, H. Dong, Z. Zhao, S. Zhang, Y. Huang, Carbon capture with ionic liquids: overview and progress, *Energy & Environmental Science*, 5 (2012) 6668-6681.
- [56] N.V. Rees, R.G. Compton, Electrochemical CO₂ sequestration in ionic liquids; a perspective, *Energy & Environmental Science*, 4 (2011) 403-408.
- [57] G.A. Bhaduri, L. Šiller, Nickel nanoparticles catalyse reversible hydration of carbon dioxide for mineralization carbon capture and storage, *Catalysis Science & Technology*, 3 (2013) 1234-1239.
- [58] H. Liu, B. Liu, L.-C. Lin, G. Chen, Y. Wu, J. Wang, X. Gao, Y. Lv, Y. Pan, X. Zhang, X. Zhang, L. Yang, C. Sun, B. Smit, W. Wang, A hybrid absorption–adsorption method to efficiently capture carbon, *Nature Communications*, 5 (2014).
- [59] R.E. Treybal, *Mass Transfer Operation*, McGraw Hill, New York, 1980.
- [60] A. Samanta, A. Zhao, G.K.H. Shimizu, P. Sarkar, R. Gupta, Post-Combustion CO₂ Capture Using Solid Sorbents: A Review, *Industrial & Engineering Chemistry Research*, 51 (2011) 1438-1463.
- [61] B. Wang, A.P. Côté, H. Furukawa, M. O’Keeffe, O.M. Yaghi, Colossal cages in zeolitic imidazolate frameworks as selective carbon dioxide reservoirs, *Nature*, 453 (2008) 207-211.
- [62] R. Banerjee, A. Phan, B. Wang, C. Knobler, H. Furukawa, M. O’Keeffe, O.M. Yaghi, High-Throughput Synthesis of Zeolitic Imidazolate Frameworks and Application to CO₂ Capture, *Science*, 319 (2008) 939-943.
- [63] H. Furukawa, N. Ko, Y.B. Go, N. Aratani, S.B. Choi, E. Choi, A.Ö. Yazaydin, R.Q. Snurr, M. O’Keeffe, J. Kim, O.M. Yaghi, Ultrahigh Porosity in Metal-Organic Frameworks, *Science*, 329 (2010) 424-428.
- [64] S. Yang, X. Lin, W. Lewis, M. Suyetin, E. Bichoutskaia, J.E. Parker, C.C. Tang, D.R. Allan, P.J. Rizkallah, P. Hubberstey, N.R. Champness, K. Mark Thomas, A.J. Blake, M. Schrader, A partially interpenetrated metal-organic framework for selective hysteretic sorption of carbon dioxide, *Nature Materials*, 11 (2012) 710-716.
- [65] G. Montes-Hernandez, R. Chiriac, F. Toche, F. Renard, Gas–solid carbonation of Ca(OH)₂ and CaO particles under non-isothermal and isothermal conditions by using a thermogravimetric analyzer: Implications for CO₂ capture, *International Journal of Greenhouse Gas Control*, 11 (2012) 172-180.

- [66] J. Baltrusaitis, J. Schuttlefield, E. Zeitler, V.H. Grassian, Carbon dioxide adsorption on oxide nanoparticle surfaces, *Chemical Engineering Journal*, 170 (2011) 471-481.
- [67] J. Baltrusaitis, J.H. Jensen, V.H. Grassian, FTIR Spectroscopy Combined with Isotope Labeling and Quantum Chemical Calculations to Investigate Adsorbed Bicarbonate Formation Following Reaction of Carbon Dioxide with Surface Hydroxyl Groups on Fe_2O_3 and Al_2O_3 , *The Journal of Physical Chemistry B*, 110 (2006) 12005-12016.
- [68] J. Baltrusaitis, V.H. Grassian, Surface reactions of carbon dioxide at the adsorbed water-iron oxide interface, *Journal of Physical Chemistry B*, 109 (2005) 12227-12230.
- [69] J. Baltrusaitis, J.D. Schuttlefield, E. Zeitler, J.H. Jensen, V.H. Grassian, Surface reactions of carbon dioxide at the adsorbed water-oxide interface, *Journal of Physical Chemistry C*, 111 (2007) 14870-14880.
- [70] H. Lin, B.D. Freeman, Materials selection guidelines for membranes that remove CO_2 from gas mixtures, *Journal of Molecular Structure*, 739 (2005) 57-74.
- [71] H. Luo, H. Jiang, K. Efimov, J. Caro, H. Wang, Influence of the preparation methods on the microstructure and oxygen permeability of a CO_2 -stable dual phase membrane, *AIChE Journal*, 57 (2011) 2738-2745.
- [72] M. Zuo, S. Zhuang, X. Tan, B. Meng, N. Yang, S. Liu, Ionic conducting ceramic-carbonate dual phase hollow fibre membranes for high temperature carbon dioxide separation, *Journal of Membrane Science*, 458 (2014) 58-65.
- [73] M. Anderson, Y.S. Lin, Carbonate-ceramic dual-phase membrane for carbon dioxide separation, *Journal of Membrane Science*, 357 (2010) 122-129.
- [74] S. Kim, Y.M. Lee, High performance polymer membranes for CO_2 separation, *Current Opinion in Chemical Engineering*, 2 (2013) 238-244.
- [75] J.K. Adewole, A.L. Ahmad, S. Ismail, C.P. Leo, Current challenges in membrane separation of CO_2 from natural gas: A review, *International Journal of Greenhouse Gas Control*, 17 (2013) 46-65.
- [76] N. Du, H.B. Park, M.M. Dal-Cin, M.D. Guiver, Advances in high permeability polymeric membrane materials for CO_2 separations, *Energy & Environmental Science*, 5 (2012) 7306-7322.
- [77] S. Kasahara, E. Kamio, T. Ishigami, H. Matsuyama, Amino acid ionic liquid-based facilitated transport membranes for CO_2 separation, *Chemical Communications*, 48 (2012) 6903-6905.
- [78] E. Santos, J. Albo, A. Irbien, Acetate based Supported Ionic Liquid Membranes (SILMs) for CO_2 separation: Influence of the temperature, *Journal of Membrane Science*, 452 (2014) 277-283.

- [79] L.J. Lozano, C. Godínez, A.P. de los Ríos, F.J. Hernández-Fernández, S. Sánchez-Segado, F.J. Alguacil, Recent advances in supported ionic liquid membrane technology, *Journal of Membrane Science*, 376 (2011) 1-14.
- [80] G.H. Rau, CO₂ Mitigation via Capture and Chemical Conversion in Seawater, *Environmental Science & Technology*, 45 (2010) 1088-1092.
- [81] J.A. Tossell, H₂CO₃(s): A New Candidate for CO₂ Capture and Sequestration, *Environmental Science & Technology*, 43 (2009) 2575-2580.
- [82] H.V.M. Hamelers, O. Schaetzle, J.M. Paz-García, P.M. Biesheuvel, C.J.N. Buisman, Harvesting Energy from CO₂ Emissions, *Environmental Science & Technology Letters*, (2013).
- [83] H.P. Xie, Y.F. Wang, Y. He, M.L. Gou, T. Liu, J.L. Wang, L. Tang, W. Jiang, R. Zhang, L.Z. Xie, B. Liang, Generation of electricity from CO₂ mineralization: Principle and realization, *Science China Technological Sciences*, 57 (2014) 2335-2343.
- [84] R. Lal, Carbon sequestration, *Philosophical Transactions of the Royal Society B: Biological Sciences*, 363 (2008) 815-830.
- [85] A. Baral, G.S. Guha, Trees for carbon sequestration or fossil fuel substitution: the issue of cost vs. carbon benefit, *Biomass and Bioenergy*, 27 (2004) 41-55.
- [86] J.C. Rooke, A. Léonard, C.F. Meunier, B.-L. Su, Designing Photobioreactors based on Living Cells Immobilized in Silica Gel for Carbon Dioxide Mitigation, *ChemSusChem*, 4 (2011) 1249-1257.
- [87] D.J. Farrelly, C.D. Everard, C.C. Fagan, K.P. McDonnell, Carbon sequestration and the role of biological carbon mitigation: A review, *Renewable and Sustainable Energy Reviews*, 21 (2013) 712-727.
- [88] F. Ma, M.A. Hanna, Biodiesel production: a review, *Bioresource Technology*, 70 (1999) 1-15.
- [89] L.C. Meher, D. Vidya Sagar, S.N. Naik, Technical aspects of biodiesel production by transesterification—a review, *Renewable and Sustainable Energy Reviews*, 10 (2006) 248-268.
- [90] B.P. Sullivan, K. Krist, H.E. Guard, *Electrochemical and electrocatalytic reactions of carbon dioxide*, Elsevier, Amsterdam, 1993.
- [91] O.R. Harvey, N.P. Qafoku, K.J. Cantrell, G. Lee, J.E. Amonette, C.F. Brown, Geochemical Implications of Gas Leakage associated with Geologic CO₂ Storage—A Qualitative Review, *Environmental Science & Technology*, 47 (2012) 23-36.
- [92] Y.-S. Jun, D.E. Giammar, C.J. Werth, Impacts of Geochemical Reactions on Geologic Carbon Sequestration, *Environmental Science & Technology*, 47 (2012) 3-8.

- [93] H. Hellevang, V.T.H. Pham, P. Aagaard, Kinetic modelling of CO₂-water-rock interactions, *International Journal of Greenhouse Gas Control*, 15 (2013) 3-15.
- [94] V. Vilarrasa, S. Olivella, J. Carrera, J. Rutqvist, Long term impacts of cold CO₂ injection on the caprock integrity, *International Journal of Greenhouse Gas Control*, 24 (2014) 1-13.
- [95] J. Song, D. Zhang, Comprehensive Review of Caprock-Sealing Mechanisms for Geologic Carbon Sequestration, *Environmental Science & Technology*, 47 (2012) 9-22.
- [96] K.S. Lackner, D.P. Butt, C.H. Wendt, Progress on binding CO₂ in mineral substrates, *Energy Conversion and Management*, 38, Supplement (1997) S259-S264.
- [97] K.S. Lackner, C.H. Wendt, D.P. Butt, E.L. Joyce Jr, D.H. Sharp, Carbon dioxide disposal in carbonate minerals, *Energy*, 20 (1995) 1153-1170.
- [98] G.M. Bond, J. Stringer, D.K. Brandvold, F.A. Simsek, M.-G. Medina, G. Egeland, Development of Integrated System for Biomimetic CO₂ Sequestration Using the Enzyme Carbonic Anhydrase, *Energy & Fuels*, 15 (2001) 309-316.
- [99] M. Verduyn, H. Geerlings, G.v. Mossel, S. Vijayakumari, Review of the various CO₂ mineralization product forms, *Energy Procedia*, 4 (2011) 2885-2892.
- [100] R.D. Schuiling, Olivine: A supergreen fuel, *Energy, Sustainability and Society*, 3 (2013).
- [101] X. Wang, Carbon dioxide capture and storage by mineralisation using recyclable ammonium salts, PhD Thesis, Innovation Center for Carbon Capture and Storage The University of Nottingham, Nottingham, UK, 2011.
- [102] P. Köhler, J. Hartmann, D.A. Wolf-Gladrow, Geoengineering potential of artificially enhanced silicate weathering of olivine, *Proceedings of the National Academy of Sciences*, 107 (2010) 20228-20233.
- [103] E. Nduagu, Production of Mg(OH)₂ from Mg-silicate rock for CO₂ mineral sequestration, PhD Thesis, Department of Chemical Engineering, Abo Akademi University, Turku, Finland, 2012.
- [104] J. Fagerlund, Carbonation of Mg(OH)₂ in a pressurised fluidised bed for CO₂ sequestration, PhD Thesis, Department of Chemical Engineering, Abo Akademi University, Turku, Finland, 2012.
- [105] W.K. O'Connor, D.C. Dahlin, Nilsen D.N., G.E. Rush, R.P. Walters, P.C. Turner, CO₂ storage in solid form: A study of direct mineral carbonation, in: *Fifth International Conference on Greenhouse Gas Technologies*, Cairns, Australia, 2000.

- [106] R. Zevenhoven, S. Teir, S. Eloneva, Heat optimisation of a staged gas–solid mineral carbonation process for long-term CO₂ storage, *Energy*, 33 (2008) 362-370.
- [107] J. Fagerlund, J. Highfield, R. Zevenhoven, Kinetics studies on wet and dry gas-solid carbonation of MgO and Mg(OH)₂ for CO₂ sequestration, *RSC Advances*, 2 (2012) 10380-10393.
- [108] E. Nduagu, T. Björklöf, J. Fagerlund, E. Mäkilä, J. Salonen, H. Geerlings, R. Zevenhoven, Production of magnesium hydroxide from magnesium silicate for the purpose of CO₂ mineralization – Part 2: Mg extraction modeling and application to different Mg silicate rocks, *Minerals Engineering*, 30 (2012) 87-94.
- [109] E. Nduagu, T. Björklöf, J. Fagerlund, J. Wärnå, H. Geerlings, R. Zevenhoven, Production of magnesium hydroxide from magnesium silicate for the purpose of CO₂ mineralisation – Part 1: Application to Finnish serpentinite, *Minerals Engineering*, 30 (2012) 75-86.
- [110] J. Fagerlund, S. Teir, E. Nduagu, R. Zevenhoven, Carbonation of magnesium silicate mineral using a pressurised gas/solid process, *Energy Procedia*, 1 (2009) 4907-4914.
- [111] J. Highfield, H. Lim, J. Fagerlund, R. Zevenhoven, Activation of serpentine for CO₂ mineralization by flux extraction of soluble magnesium salts using ammonium sulfate, *RSC Advances*, 2 (2012) 6535-6541.
- [112] M.D. Torrontegui, Assessing the mineral carbonation science and technology, MTech Thesis, Institute of Process Engineering, Swiss Federal Institute of Technology Zurich, Zurich, 2010.
- [113] W.K. O'Connor, D.C. Dahlin, G.E. Rush, C.L. Dahlin, W.K. Collins, Carbon dioxide sequestration by direct mineral carbonation: Process mineralogy of feed and products, *Minerals and Metallurgical Processing*, 19 (2002) 95-101.
- [114] W.K. O'Connor, D.C. Dahlin, Nilsen D.N., R.P. Walters, P.C. Turner, Carbon dioxide sequestration by direct mineral carbonation with carbonic acid, in: *Proceedings of the 25th International Technical Conference on Coal Utilization & Fuel Systems*, Clear Water, US, 2000.
- [115] A.-H.A. Park, L.-S. Fan, mineral sequestration: physically activated dissolution of serpentine and pH swing process, *Chemical Engineering Science*, 59 (2004) 5241-5247.
- [116] A.-H.A. Park, R. Jadhav, L.-S. Fan, CO₂ Mineral Sequestration: Chemically Enhanced Aqueous Carbonation of Serpentine, *The Canadian Journal of Chemical Engineering*, 81 (2003) 885-890.
- [117] A. Sanna, A. Lacinska, M. Styles, M.M. Maroto-Valer, Silicate rock dissolution by ammonium bisulphate for pH swing mineral CO₂ sequestration, *Fuel Processing Technology*, 120 (2014) 128-135.

- [118] X. Wang, M.M. Maroto-Valer, Optimization of carbon dioxide capture and storage with mineralisation using recyclable ammonium salts, *Energy*, 51 (2013) 431-438.
- [119] X. Wang, M. Maroto-Valer, Integration of CO₂ capture and storage based on pH-swing mineral carbonation using recyclable ammonium salts, *Energy Procedia*, 4 (2011) 4930-4936.
- [120] X. Wang, M.M. Maroto-Valer, Integration of CO₂ Capture and Mineral Carbonation by Using Recyclable Ammonium Salts, *ChemSusChem*, 4 (2011) 1291-1300.
- [121] M. Bodor, R.M. Santos, Y.W. Chiang, M. Vlad, T.V. Gerven, Impact of Nickel Nanoparticel of Mineral Carbonation, *The Scientific World Journal*, 2014 (2014) 921974.
- [122] M. Bodor, R. Santos, T. Gerven, M. Vlad, Recent developments and perspectives on the treatment of industrial wastes by mineral carbonation — a review, *Central European Journal of Engineering*, 3 (2013) 566-584.
- [123] S.J. Gerdemann, W.K. O'Connor, D.C. Dahlin, L.R. Penner, H. Rush, Ex Situ Aqueous Mineral Carbonation, *Environmental Science & Technology*, 41 (2007) 2587-2593.
- [124] W.K. O'Connor, D.C. Dahlin, G.E. Rush, S.J. Gerdemann, L.R. Penner, Energy and economic evaluation of ex situ aqueous mineral carbonation, in: E.S. Rubin, D.W. Keith, C.F. Gilboy, M. Wilson, T. Morris, J. Gale, K. Thambimuthu (Eds.) *Greenhouse Gas Control Technologies 7*, Elsevier Science Ltd, Oxford, 2005, pp. 2011-2015.
- [125] T.A. Haug, I.A. Munz, R.A. Kleiv, Importance of dissolution and precipitation kinetics for mineral carbonation, *Energy Procedia*, 4 (2011) 5029-5036.
- [126] S. Kwon, M. Fan, H.F.M. Dacosta, A.G. Russell, C. Tsouris, Reaction Kinetics of CO₂ Carbonation with Mg-Rich Minerals, *The Journal of Physical Chemistry A*, 115 (2011) 7638-7644.
- [127] A. Sanna, X. Wang, A. Lacinska, M. Styles, T. Paulson, M.M. Maroto-Valer, Enhancing Mg extraction from lizardite-rich serpentine for CO₂ mineral sequestration, *Minerals Engineering*, 49 (2013) 135-144.
- [128] Y. Abe, A. Iizuka, H. Nagasawa, A. Yamasaki, Y. Yanagisawa, Dissolution rates of alkaline rocks by carbonic acid: Influence of solid/liquid ratio, temperature, and CO₂ pressure, *Chemical Engineering Research and Design*, 91 (2013) 933-941.
- [129] B. Bonfils, C. Julcour-Lebigue, F. Guyot, F. Bodéan, P. Chiquet, F. Bourgeois, Comprehensive analysis of direct aqueous mineral carbonation using dissolution enhancing organic additives, *International Journal of Greenhouse Gas Control*, 9 (2012) 334-346.

- [130] V. Prigiobbe, G. Costa, R. Baciocchi, M. Hänchen, M. Mazzotti, The effect of and salinity on olivine dissolution kinetics at, *Chemical Engineering Science*, 64 (2009) 3510-3515.
- [131] S.J.T. Hangx, C.J. Spiers, Coastal spreading of olivine to control atmospheric CO₂ concentrations: A critical analysis of viability, *International Journal of Greenhouse Gas Control*, 3 (2009) 757-767.
- [132] V. Prigiobbe, M. Hänchen, M. Werner, R. Baciocchi, M. Mazzotti, Mineral carbonation process for CO₂ sequestration, *Energy Procedia*, 1 (2009) 4885-4890.
- [133] G.P. Assima, F. Larachi, J. Molson, G. Beaudoin, Accurate and direct quantification of native brucite in serpentine ores—New methodology and implications for CO₂ sequestration by mining residues, *Thermochimica Acta*, 566 (2013) 281-291.
- [134] G. Gadikota, J. Matter, P. Kelemen, A.-h.A. Park, Chemical and morphological changes during olivine carbonation for CO₂ storage in the presence of NaCl and NaHCO₃, *Physical Chemistry Chemical Physics*, 16 (2014) 4679-4693.
- [135] R. Lafay, G. Montes-Hernandez, E. Janots, R. Chiriac, N. Findling, F. Toche, Simultaneous precipitation of magnesite and lizardite from hydrothermal alteration of olivine under high-carbonate alkalinity, *Chemical Geology*, 368 (2014) 63-75.
- [136] M. Hänchen, V. Prigiobbe, G. Storti, T.M. Seward, M. Mazzotti, Dissolution kinetics of forsteritic olivine at 90–150°C including effects of the presence of CO₂, *Geochimica et Cosmochimica Acta*, 70 (2006) 4403-4416.
- [137] K. Jarvis, R.W. Carpenter, T. Windman, Y. Kim, R. Nunez, F. Alawneh, Reaction Mechanisms for Enhancing Mineral Sequestration of CO₂, *Environmental Science & Technology*, 43 (2009) 6314-6319.
- [138] H. Béarat, M.J. McKelvy, A.V.G. Chizmeshya, D. Gormley, R. Nunez, R.W. Carpenter, K. Squires, G.H. Wolf, Carbon Sequestration via Aqueous Olivine Mineral Carbonation: Role of Passivating Layer Formation, *Environmental Science & Technology*, 40 (2006) 4802-4808.
- [139] H. Todd Schaefer, B.P. McGrail, J.L. Loring, M.E. Bowden, B.W. Arey, K.M. Rosso, Forsterite [Mg₂SiO₄] Carbonation in Wet Supercritical CO₂: An in Situ High-Pressure X-ray Diffraction Study, *Environmental Science & Technology*, 47 (2012) 174-181.
- [140] H.E. King, O. Plümper, A. Putnis, Effect of Secondary Phase Formation on the Carbonation of Olivine, *Environmental Science & Technology*, 44 (2010) 6503-6509.
- [141] J.S. Loring, C.J. Thompson, Z. Wang, A.G. Joly, D.S. Sklarew, H.T. Schaefer, E.S. Ilton, K.M. Rosso, A.R. Felmy, In Situ Infrared Spectroscopic

- Study of Forsterite Carbonation in Wet Supercritical CO₂, *Environmental Science & Technology*, 45 (2011) 6204-6210.
- [142] F. Wang, D.E. Giammar, Forsterite Dissolution in Saline Water at Elevated Temperature and High CO₂ Pressure, *Environmental Science & Technology*, 47 (2012) 168-173.
- [143] S.C. Krevor, K.S. Lackner, Enhancing process kinetics for mineral carbon sequestration, *Energy Procedia*, 1 (2009) 4867-4871.
- [144] S. Teir, H. Revitzer, S. Eloneva, C.-J. Fogelholm, R. Zevenhoven, Dissolution of natural serpentinite in mineral and organic acids, *International Journal of Mineral Processing*, 83 (2007) 36-46.
- [145] S. Teir, R. Kuusik, C.-J. Fogelholm, R. Zevenhoven, Production of magnesium carbonates from serpentinite for long-term storage of CO₂, *International Journal of Mineral Processing*, 85 (2007) 1-15.
- [146] T. Koljonen, H. Siikavirta, R. Zevenhoven, I. Savolainen, CO₂ capture, storage and reuse potential in Finland, *Energy*, 29 (2004) 1521-1527.
- [147] R. Zevenhoven, J. Fagerlund, Mineral sequestration for CCS in Finland and abroad, *World Renewable Energy Congress 2011*, Linköping, Sweden, 2011, pp. 660-667.
- [148] J. Highfield, H. Lim, J. Fagerlund, R. Zevenhoven, Mechanochemical processing of serpentine with ammonium salts under ambient conditions for CO₂ mineralization, *RSC Advances*, 2 (2012) 6542-6548.
- [149] J. Fagerlund, E. Nduagu, I. Romão, R. Zevenhoven, CO₂ fixation using magnesium silicate minerals part 1: Process description and performance, *Energy*, 41 (2012) 184-191.
- [150] I. Romão, E. Nduagu, J. Fagerlund, L.M. Gando-Ferreira, R. Zevenhoven, CO₂ fixation using magnesium silicate minerals. Part 2: Energy efficiency and integration with iron-and steelmaking, *Energy*, 41 (2012) 203-211.
- [151] X. Wang, M.M. Maroto-Valer, Dissolution of serpentine using recyclable ammonium salts for CO₂ mineral carbonation, *Fuel*, 90 (2011) 1229-1237.
- [152] G. Alexander, M.M. Maroto-Valer, P. Gafarova-Aksoy, Evaluation of reaction variables in the dissolution of serpentine for mineral carbonation, *Fuel*, 86 (2007) 273-281.
- [153] J. Zhang, R. Zhang, H. Geerlings, J. Bi, Mg-Silicate Carbonation Based on an HCl- and NH₃-Recyclable Process: Effect of Carbonation Temperature, *Chemical Engineering & Technology*, 35 (2012) 525-531.
- [154] S.C.M. Krevor, K.S. Lackner, Enhancing serpentine dissolution kinetics for mineral carbon dioxide sequestration, *International Journal of Greenhouse Gas Control*, 5 (2011) 1073-1080.

- [155] W. Li, W. Li, B. Li, Z. Bai, Electrolysis and heat pretreatment methods to promote CO₂ sequestration by mineral carbonation, *Chemical Engineering Research and Design*, 87 (2009) 210-215.
- [156] R.D. Balucan, B.Z. Dlugogorski, Thermal Activation of Antigorite for Mineralization of CO₂, *Environmental Science & Technology*, 47 (2012) 182-190.
- [157] R.D. Balucan, B.Z. Dlugogorski, E.M. Kennedy, I.V. Belova, G.E. Murch, Energy cost of heat activating serpentinites for CO₂ storage by mineralisation, *International Journal of Greenhouse Gas Control*, 17 (2013) 225-239.
- [158] M. Werner, M. Verduyn, G. van Mossel, M. Mazzotti, Direct flue gas CO₂ mineralization using activated serpentine: Exploring the reaction kinetics by experiments and population balance modelling, *Energy Procedia*, 4 (2011) 2043-2049.
- [159] I.M. Power, G.M. Dipple, G. Southam, Bioleaching of Ultramafic Tailings by *Acidithiobacillus* spp. for CO₂ Sequestration, *Environmental Science & Technology*, 44 (2009) 456-462.
- [160] P.-C. Lin, C.-W. Huang, C.-T. Hsiao, H. Teng, Magnesium Hydroxide Extracted from a Magnesium-Rich Mineral for CO₂ Sequestration in a Gas-Solid System, *Environmental Science & Technology*, 42 (2008) 2748-2752.
- [161] M.J. McKelvy, A.V.G. Chizmeshya, J. Diefenbacher, H. Béarat, G. Wolf, Exploration of the Role of Heat Activation in Enhancing Serpentine Carbon Sequestration Reactions, *Environmental Science & Technology*, 38 (2004) 6897-6903.
- [162] D.T. Van Essendelft, H.H. Schobert, Kinetics of the Acid Digestion of Serpentine with Concurrent Grinding. 3. Model Validation and Prediction, *Industrial & Engineering Chemistry Research*, 49 (2010) 1588-1590.
- [163] D.T. Van Essendelft, H.H. Schobert, Kinetics of the Acid Digestion of Serpentine with Concurrent Grinding. 2. Detailed Investigation and Model Development, *Industrial & Engineering Chemistry Research*, 48 (2009) 9892-9901.
- [164] D.T. Van Essendelft, H.H. Schobert, Kinetics of the Acid Digestion of Serpentine with Concurrent Grinding. 1. Initial Investigations, *Industrial & Engineering Chemistry Research*, 48 (2009) 2556-2565.
- [165] K.W. Ryu, Y.N. Jang, M.G. Lee, Enhancement of Chrysotile Carbonation in Alkali Solution, *Materials Transactions*, 53 (2012) 1349-1352.
- [166] Z.-H. Mei, S.-Y. Mie, Novel economical chemical engineering reactions for mineralization of CO₂ to combat global warming, *Advanced Materials Research*, 524-527 (2012) 3302-3307.
- [167] S.J.T. Hangx, C.J. Spiers, Reaction of plagioclase feldspars with CO₂ under hydrothermal conditions, *Chemical Geology*, 265 (2009) 88-98.

- [168] S. Teir, S. Eloneva, R. Zevenhoven, Production of precipitated calcium carbonate from calcium silicates and carbon dioxide, *Energy Conversion and Management*, 46 (2005) 2954-2979.
- [169] M. Kakizawa, A. Yamasaki, Y. Yanagisawa, A new CO₂ disposal process via artificial weathering of calcium silicate accelerated by acetic acid, *Energy*, 26 (2001) 341-354.
- [170] J. Bałdyga, M. Henczka, K. Sokolnicka, Utilization of carbon dioxide by chemically accelerated mineral carbonation, *Materials Letters*, 64 (2010) 702-704.
- [171] J. Zhang, R. Zhang, H. Geerlings, J. Bi, A Novel Indirect Wollastonite Carbonation Route for CO₂ Sequestration, *Chemical Engineering & Technology*, 33 (2010) 1177-1183.
- [172] W.J.J. Huijgen, G.-J. Witkamp, R.N.J. Comans, Mechanisms of aqueous wollastonite carbonation as a possible CO₂ sequestration process, *Chemical Engineering Science*, 61 (2006) 4242-4251.
- [173] W.J.J. Huijgen, R.N.J. Comans, G.-J. Witkamp, Cost evaluation of CO₂ sequestration by aqueous mineral carbonation, *Energy Conversion and Management*, 48 (2007) 1923-1935.
- [174] W.J.J. Huijgen, G.J. Ruijg, R.N.J. Comans, G.-J. Witkamp, Energy Consumption and Net CO₂ Sequestration of Aqueous Mineral Carbonation, *Industrial & Engineering Chemistry Research*, 45 (2006) 9184-9194.
- [175] D. Daval, I. Martinez, J. Corvisier, N. Findling, B. Goffé, F. Guyot, Carbonation of Ca-bearing silicates, the case of wollastonite: Experimental investigations and kinetic modeling, *Chemical Geology*, 265 (2009) 63-78.
- [176] H. Zhao, Y. Park, D.H. Lee, A.-H.A. Park, Tuning the dissolution kinetics of wollastonite via chelating agents for CO₂ sequestration with integrated synthesis of precipitated calcium carbonates, *Physical Chemistry Chemical Physics*, 15 (2013) 15185-15192.
- [177] N. Koukouzas, V. Gemeni, H.J. Ziock, Sequestration of CO₂ in magnesium silicates, in Western Macedonia, Greece, *International Journal of Mineral Processing*, 93 (2009) 179-186.
- [178] S.-J. Han, M. Yoo, D.-W. Kim, J.-H. Wee, Carbon Dioxide Capture Using Calcium Hydroxide Aqueous Solution as the Absorbent, *Energy & Fuels*, 25 (2011) 3825-3834.
- [179] B. Fritz, A. Clement, G. Montes-Hernandez, C. Noguera, Calcite formation by hydrothermal carbonation of portlandite: complementary insights from experiment and simulation, *CrystEngComm*, 15 (2013) 3392-3401.

- [180] G. Montes-Hernandez, F. Renard, N. Geoffroy, L. Charlet, J. Pironon, Calcite precipitation from $\text{CO}_2\text{-H}_2\text{O-Ca(OH)}_2$ slurry under high pressure of CO_2 , *Journal of Crystal Growth*, 308 (2007) 228-236.
- [181] L. Zhao, L. Sang, J. Chen, J. Ji, H.H. Teng, Aqueous Carbonation of Natural Brucite: Relevance to CO_2 Sequestration, *Environmental Science & Technology*, 44 (2009) 406-411.
- [182] I.M. Power, A.L. Harrison, G.M. Dipple, G. Southam, Carbon sequestration via carbonic anhydrase facilitated magnesium carbonate precipitation, *International Journal of Greenhouse Gas Control*, 16 (2013) 145-155.
- [183] A.L. Harrison, I.M. Power, G.M. Dipple, Accelerated Carbonation of Brucite in Mine Tailings for Carbon Sequestration, *Environmental Science & Technology*, 47 (2012) 126-134.
- [184] Y. Wang, W. Liu, F. Huang, T. Zou, Z. Lin, The "jump of size" phenomenon in aqueous-nanoparticle reaction system: phase transformation from nano- Mg(OH)_2 to bulk $\text{MgCO}_3\cdot 3\text{H}_2\text{O}$, *CrystEngComm*, 14 (2012) 7165-7169.
- [185] M.G. Nyambura, G.W. Mugeru, P.L. Felicia, N.P. Gathura, Carbonation of brine impacted fractionated coal fly ash: Implications for CO_2 sequestration, *Journal of Environmental Management*, 92 (2011) 655-664.
- [186] M. Slotte, I. Romão, R. Zevenhoven, Integration of a pilot-scale serpentinite carbonation process with an industrial lime kiln, *Energy*, 62 (2013) 142-149.
- [187] R. Baciocchi, G. Costa, A. Poletti, R. Pomi, Influence of particle size on the carbonation of stainless steel slag for CO_2 storage, *Energy Procedia*, 1 (2009) 4859-4866.
- [188] F.J. Doucet, Effective CO_2 -specific sequestration capacity of steel slags and variability in their leaching behaviour in view of industrial mineral carbonation, *Minerals Engineering*, 23 (2010) 262-269.
- [189] S. Teir, S. Eloneva, C.-J. Fogelholm, R. Zevenhoven, Dissolution of steelmaking slags in acetic acid for precipitated calcium carbonate production, *Energy*, 32 (2007) 528-539.
- [190] S. Teir, S. Eloneva, C.-J. Fogelholm, R. Zevenhoven, Carbonation of minerals and industrial by-products for CO_2 sequestration, in: *Proceedings of IGEC-III, 2007. The third International Green Energy Conference, 2007.*
- [191] S. Eloneva, S. Teir, J. Salminen, C.-J. Fogelholm, R. Zevenhoven, Fixation of CO_2 by carbonating calcium derived from blast furnace slag, *Energy*, 33 (2008) 1461-1467.
- [192] S.-Y. Pan, P.-C. Chiang, Y.-H. Chen, C.-D. Chen, H.-Y. Lin, E.E. Chang, Systematic Approach to Determination of Maximum Achievable Capture

Capacity via Leaching and Carbonation Processes for Alkaline Steelmaking Wastes in a Rotating Packed Bed, *Environmental Science & Technology*, 47 (2013) 13677-13685.

[193] S.-Y. Pan, P.-C. Chiang, Y.-H. Chen, C.-S. Tan, E.E. Chang, Ex Situ CO₂ Capture by Carbonation of Steelmaking Slag Coupled with Metalworking Wastewater in a Rotating Packed Bed, *Environmental Science & Technology*, 47 (2013) 3308-3315.

[194] A. Said, H.-P. Mattila, M. Järvinen, R. Zevenhoven, Production of precipitated calcium carbonate (PCC) from steelmaking slag for fixation of CO₂, *Applied Energy*, 112 (2013) 765-771.

[195] H.-P. Mattila, I. Grigaliūnaitė, R. Zevenhoven, Chemical kinetics modeling and process parameter sensitivity for precipitated calcium carbonate production from steelmaking slags, *Chemical Engineering Journal*, 192 (2012) 77-89.

[196] J.K. Stolaroff, G.V. Lowry, D.W. Keith, Using CaO- and MgO-rich industrial waste streams for carbon sequestration, *Energy Conversion and Management*, 46 (2005) 687-699.

[197] W.J.J. Huijgen, R.N.J. Comans, Mineral CO₂ Sequestration by Steel Slag Carbonation, *Environmental Science & Technology*, 39 (2005) 9676-9682.

[198] W.J.J. Huijgen, R.N.J. Comans, Carbonation of Steel Slag for CO₂ Sequestration: Leaching of Products and Reaction Mechanisms, *Environmental Science & Technology*, 40 (2006) 2790-2796.

[199] M.A. Boone, P. Nielsen, T. De Kock, M.N. Boone, M. Quaghebeur, V. Cnudde, Monitoring of Stainless-Steel Slag Carbonation Using X-ray Computed Microtomography, *Environmental Science & Technology*, 48 (2013) 674-680.

[200] D. Zingaretti, G. Costa, R. Baciocchi, Assessment of Accelerated Carbonation Processes for CO₂ Storage Using Alkaline Industrial Residues, *Industrial & Engineering Chemistry Research*, (2013).

[201] J.-l. Li, H.-n. Zhang, A.-j. Xu, J. Cui, D.-f. He, N.-y. Tian, Theoretical and Experimental on Carbon Dioxide Sequestration Degree of Steel Slag, *Journal of Iron and Steel Research, International*, 19 (2012) 29-32.

[202] R.M. Santos, D. Ling, A. Sarvaramini, M. Guo, J. Elsen, F. Larachi, G. Beaudoin, B. Blanpain, T. Van Gerven, Stabilization of basic oxygen furnace slag by hot-stage carbonation treatment, *Chemical Engineering Journal*, 203 (2012) 239-250.

[203] S.-c. Tian, J.-g. Jiang, K.-m. Li, F. Yan, X.-j. Chen, Performance of steel slag in carbonation-calcination looping for CO₂ capture from industrial flue gas, *RSC Advances*, 4 (2014) 6858-6862.

[204] S.-H. Lee, J. Seo, K.-S. You, T. Thriveni, J.-W. Ahn, Synthesis of calcium carbonate powder from air-cooled blast furnace slag under pressurized CO₂ atmosphere, *Geosystem Engineering*, 15 (2012) 292-298.

- [205] S. Tian, J. Jiang, X. Chen, F. Yan, K. Li, Direct Gas–Solid Carbonation Kinetics of Steel Slag and the Contribution to In situ Sequestration of Flue Gas CO₂ in Steel-Making Plants, *ChemSusChem*, 6 (2013) 2348-2355.
- [206] W. Bao, H. Li, Y. Zhang, Selective Leaching of Steelmaking Slag for Indirect CO₂ Mineral Sequestration, *Industrial & Engineering Chemistry Research*, 49 (2010) 2055-2063.
- [207] S. Eloneva, S. Teir, J. Salminen, H. Revitzer, K. Kontu, A.M. Forsman, R. Zevenhoven, C.-J. Fogelholm, Pure calcium carbonate product from the carbonation of a steel making slag, in: 2nd International Conference on Accelerated Carbonation for Environmental and Materials Engineering, Roma, Italy, 2008, pp. 239-248.
- [208] W. Hongqi, S. Ningning, R.J. Donahoe, Carbon Dioxide Sequestration with Flue Gas Desulfurization (FGD) Gypsum, *International Conference on Environmental Science and Information Application Technology*, 2009. ESIAT 2009., 2009, pp. 673-676.
- [209] K. Song, Y.-N. Jang, W. Kim, M.G. Lee, D. Shin, J.-H. Bang, C.W. Jeon, S.C. Chae, Precipitation of calcium carbonate during direct aqueous carbonation of flue gas desulfurization gypsum, *Chemical Engineering Journal*, 213 (2012) 251-258.
- [210] M.g. Lee, Y.N. Jang, K.w. Ryu, W. Kim, J.-H. Bang, Mineral carbonation of flue gas desulfurization gypsum for CO₂ sequestration, *Energy*, 47 (2012) 370-377.
- [211] C. Cárdenas-Escudero, V. Morales-Flórez, R. Pérez-López, A. Santos, L. Esquivias, Procedure to use phosphogypsum industrial waste for mineral CO₂ sequestration, *Journal of Hazardous Materials*, 196 (2011) 431-435.
- [212] P. Renforth, W.M. Mayes, A.P. Jarvis, I.T. Burke, D.A.C. Manning, K. Gruiz, Contaminant mobility and carbon sequestration downstream of the Ajka (Hungary) red mud spill: The effects of gypsum dosing, *Science of The Total Environment*, 421–422 (2012) 253-259.
- [213] H. Jo, Y.-N. Jang, H. Young Jo, Influence of NaCl on mineral carbonation of CO₂ using cement material in aqueous solutions, *Chemical Engineering Science*, 80 (2012) 232-241.
- [214] M. Dri, A. Sanna, M.M. Maroto-Valer, Dissolution of steel slag and recycled concrete aggregate in ammonium bisulphate for CO₂ mineral carbonation, *Fuel Processing Technology*, 113 (2013) 114-122.
- [215] S. Kashef-Haghighi, S. Ghoshal, Physico–Chemical Processes Limiting CO₂ Uptake in Concrete during Accelerated Carbonation Curing, *Industrial & Engineering Chemistry Research*, 52 (2013) 5529-5537.
- [216] P. Renforth, D.A.C. Manning, Laboratory carbonation of artificial silicate gels enhanced by citrate: Implications for engineered pedogenic carbonate

- formation, *International Journal of Greenhouse Gas Control*, 5 (2011) 1578-1586.
- [217] P.J. Gunning, C.D. Hills, P.J. Carey, Accelerated carbonation treatment of industrial wastes, *Waste Management*, 30 (2010) 1081-1090.
- [218] D.N. Huntzinger, J.S. Gierke, S.K. Kawatra, T.C. Eisele, L.L. Sutter, Carbon Dioxide Sequestration in Cement Kiln Dust through Mineral Carbonation, *Environmental Science & Technology*, 43 (2009) 1986-1992.
- [219] R. Pérez-López, G. Montes-Hernandez, J.M. Nieto, F. Renard, L. Charlet, Carbonation of alkaline paper mill waste to reduce CO₂ greenhouse gas emissions into the atmosphere, *Applied Geochemistry*, 23 (2008) 2292-2300.
- [220] M. Back, M. Kuehn, H. Stanjek, S. Peiffer, Reactivity of Alkaline Lignite Fly Ashes Towards CO₂ in Water, *Environmental Science & Technology*, 42 (2008) 4520-4526.
- [221] G. Montes-Hernandez, R. Pérez-López, F. Renard, J.M. Nieto, L. Charlet, Mineral sequestration of CO₂ by aqueous carbonation of coal combustion fly-ash, *Journal of Hazardous Materials*, 161 (2009) 1347-1354.
- [222] L. He, D. Yu, L. Weizhi, J. Wu, M. Xu, A novel method for CO₂ mineralization via direct carbonation of Coal Fly Ash, *Industrial & Engineering Chemistry Research*, 52 (2013) 15138.
- [223] P. Bhattacharyya, K.J. Reddy, Effect of Flue Gas Treatment on the Solubility and Fractionation of Different Metals in Fly Ash of Powder River Basin Coal, *Water Air and Soil Pollution*, 223 (2012) 4169-4181.
- [224] J.-H. Wee, A review on carbon dioxide capture and storage technology using coal fly ash, *Applied Energy*, 106 (2013) 143-151.
- [225] V.S. Yadav, M. Prasad, J. Khan, S.S. Amritphale, M. Singh, C.B. Raju, Sequestration of carbon dioxide (CO₂) using red mud, *Journal of Hazardous Materials*, 176 (2010) 1044-1050.
- [226] D. Bonenfant, L. Kharoune, S.b. Sauvé, R. Hausler, P. Niquette, M. Mimeault, M. Kharoune, CO₂ Sequestration by Aqueous Red Mud Carbonation at Ambient Pressure and Temperature, *Industrial & Engineering Chemistry Research*, 47 (2008) 7617-7622.
- [227] R.C. Sahu, R.K. Patel, B.C. Ray, Neutralization of red mud using CO₂ sequestration cycle, *Journal of Hazardous Materials*, 179 (2010) 28-34.
- [228] I.S. Romão, L.M. Gando-Ferreira, R. Zevenhoven, Combined extraction of metals and production of Mg(OH)₂ for CO₂ sequestration from nickel mine ore and overburden, *Minerals Engineering*, 53 (2013) 167-170.
- [229] M. Dri, A. Sanna, M.M. Maroto-Valer, Mineral carbonation from metal wastes: Effect of solid to liquid ratio on the efficiency and characterization of carbonated products, *Applied Energy*, 113 (2014) 515-523.

- [230] S. Kodama, T. Nishimoto, N. Yamamoto, K. Yogo, K. Yamada, Development of a new pH-swing CO₂ mineralization process with a recyclable reaction solution, *Energy*, 33 (2008) 776-784.
- [231] A. Sanna, M. Dri, M.R. Hall, M. Maroto-Valer, Waste materials for carbon capture and storage by mineralisation (CCSM) – A UK perspective, *Applied Energy*, 99 (2012) 545-554.
- [232] J. Pronost, G. Beaudoin, J. Tremblay, F. Larachi, J. Duchesne, R. Hébert, M. Constantin, Carbon Sequestration Kinetic and Storage Capacity of Ultramafic Mining Waste, *Environmental Science & Technology*, 45 (2011) 9413-9420.
- [233] S.-Y. Pan, E.E. Chang, P.-C. Chiang, CO₂ capture by accelerated carbonation of Alkaline wastes: A review on its principles and applications, *Aerosol and Air Quality Research*, 12 (2012) 770-791.
- [234] K.J. Reddy, W.L. Lindsay, F.W. Boyle, E.F. Redente, Solubility Relationships and Mineral Transformations Associated with Recarbonation of Retorted Shales, *Journal of Environmental Quality*, 15 (1986) 129-133.
- [235] K.J. Reddy, J.I. Drever, V.R. Hasfurther, Effects of a carbon dioxide pressure process on the solubilities of major and trace elements in oil shale solid wastes, *Environmental Science & Technology*, 25 (1991) 1466-1469.
- [236] J. Sun, M.F. Bertos, S.J.R. Simons, Kinetic study of accelerated carbonation of municipal solid waste incinerator air pollution control residues for sequestration of flue gas CO₂, *Energy & Environmental Science*, 1 (2008) 370-377.
- [237] J. Jiang, S. Tian, C. Zhang, Influence of SO₂ in incineration flue gas on the sequestration of CO₂ by municipal solid waste incinerator fly ash, *Journal of Environmental Sciences*, 25 (2013) 735-740.
- [238] S.-Y. Nam, J. Seo, T. Thriveni, J.-W. Ahn, Accelerated carbonation of municipal solid waste incineration bottom ash for CO₂ sequestration, *Geosystem Engineering*, 15 (2012) 305-311.
- [239] X. Li, M.F. Bertos, C.D. Hills, P.J. Carey, S. Simon, Accelerated carbonation of municipal solid waste incineration fly ashes, *Waste Management*, 27 (2007) 1200-1206.
- [240] L. Wang, Y. Jin, Y. Nie, Investigation of accelerated and natural carbonation of MSWI fly ash with a high content of Ca, *Journal of Hazardous Materials*, 174 (2010) 334-343.
- [241] S. Tian, J. Jiang, Sequestration of Flue Gas CO₂ by Direct Gas–Solid Carbonation of Air Pollution Control System Residues, *Environmental Science & Technology*, 46 (2012) 13545-13551.

- [242] M.L. Druckenmiller, M.M. Maroto-Valer, M. Hill, Investigation of Carbon Sequestration via Induced Calcite Formation in Natural Gas Well Brine, *Energy & Fuels*, 20 (2005) 172-179.
- [243] M.L. Druckenmiller, M.M. Maroto-Valer, Carbon sequestration using brine of adjusted pH to form mineral carbonates, *Fuel Processing Technology*, 86 (2005) 1599-1614.
- [244] Q. Liu, M.M. Maroto-Valer, Studies of pH buffer systems to promote carbonate formation for CO₂ sequestration in brines, *Fuel Processing Technology*, 98 (2012) 6-13.
- [245] Q. Liu, M.M. Maroto-Valer, Investigation of the pH effect of a typical host rock and buffer solution on CO₂ sequestration in synthetic brines, *Fuel Processing Technology*, 91 (2010) 1321-1329.
- [246] Q. Liu, M. Mercedes Maroto-Valer, Investigation of the effect of brine composition and pH buffer on CO₂ -brine sequestration, *Energy Procedia*, 4 (2011) 4503-4507.
- [247] W. Wang, X. Liu, P. Wang, Y. Zheng, M. Wang, Enhancement of CO₂ Mineralization in Ca²⁺/Mg²⁺ Rich Aqueous Solutions Using Insoluble Amine, *Industrial & Engineering Chemistry Research*, 52 (2013) 8028-8033.
- [248] Y. Soong, D.L. Fauth, B.H. Howard, J.R. Jones, D.K. Harrison, A.L. Goodman, M.L. Gray, E.A. Frommell, CO₂ sequestration with brine solution and fly ashes, *Energy Conversion and Management*, 47 (2006) 1676-1685.
- [249] W. Wang, M. Hu, Y. Zheng, P. Wang, C. Ma, CO₂ Fixation in Ca²⁺/Mg²⁺ Rich Aqueous Solutions through Enhanced Carbonate Precipitation, *Industrial & Engineering Chemistry Research*, 50 (2011) 8333-8339.
- [250] P. Ballirano, C. De Vito, V. Ferrini, S. Mignardi, The thermal behaviour and structural stability of nesquehonite, MgCO₃·3H₂O, evaluated by in situ laboratory parallel-beam X-ray powder diffraction: New constraints on CO₂ sequestration within minerals, *Journal of Hazardous Materials*, 178 (2010) 522-528.
- [251] V. Ferrini, C. De Vito, S. Mignardi, Synthesis of nesquehonite by reaction of gaseous CO₂ with Mg chloride solution: Its potential role in the sequestration of carbon dioxide, *Journal of Hazardous Materials*, 168 (2009) 832-837.
- [252] C. De Vito, V. Ferrini, S. Mignardi, M. Cagnetti, F. Leccese, Progress in carbon dioxide sequestration via carbonation of aqueous saline wastes, *Periodico di Mineralogia*, 81 (2012) 333-344.
- [253] C. De Vito, V. Ferrini, S. Mignardi, M. Cagnetti, F. Leccese, Ex situ CO₂ mineralization via nesquehonite: A first attempt for an industrial application, 11th International Conference on Environment and Electrical Engineering (EEEIC), 2012, 2012, pp. 323-327.

- [254] S. Mignardi, C. De Vito, V. Ferrini, R.F. Martin, The efficiency of CO₂ sequestration via carbonate mineralization with simulated wastewaters of high salinity, *Journal of Hazardous Materials*, 191 (2011) 49-55.
- [255] M.M. Maroto-Valer, D.J. Fauth, M.E. Kuchta, Y. Zhang, J.M. Andrésen, Activation of magnesium rich minerals as carbonation feedstock materials for CO₂ sequestration, *Fuel Processing Technology*, 86 (2005) 1627-1645.
- [256] H.H. Khoo, P.N. Sharratt, J. Bu, T.Y. Yeo, A. Borgna, J.G. Highfield, T.G. Björklöf, R. Zevenhoven, Carbon Capture and Mineralization in Singapore: Preliminary Environmental Impacts and Costs via LCA, *Industrial & Engineering Chemistry Research*, 50 (2011) 11350-11357.
- [257] W.E. Kline, H.S. Fogler, Dissolution of silicate minerals by hydrofluoric acid, *Industrial & Engineering Chemistry Fundamentals*, 20 (1981) 155-161.
- [258] S.-Y. Pan, P.-C. Chiang, Y.-H. Chen, E.E. Chang, C.-D. Chen, A.-L. Shen, Process Intensification of Steel Slag Carbonation via a Rotating Packed Bed: Reaction Kinetics and Mass Transfer, *Energy Procedia*, 63 (2014) 2255-2260.
- [259] S.-Y. Pan, E.G. Eleazar, E.E. Chang, Y.-P. Lin, H. Kim, P.-C. Chiang, Systematic approach to determination of optimum gas-phase mass transfer rate for high-gravity carbonation process of steelmaking slags in a rotating packed bed, *Applied Energy*, 148 (2015) 23-31.
- [260] A. Sanna, M. Dri, M. Maroto-Valer, Carbon dioxide capture and storage by pH swing aqueous mineralisation using a mixture of ammonium salts and antigorite source, *Fuel*, 114 (2013) 153-161.
- [261] D. Wang, Z. Li, Gas-Liquid Reactive Crystallization Kinetics of Hydromagnesite in the MgCl₂-CO₂-NH₃-H₂O System: Its Potential in CO₂ Sequestration, *Industrial & Engineering Chemistry Research*, 51 (2012) 16299-16310.
- [262] S. Park, J. Min, M.-G. Lee, H. Jo, J. Park, Characteristics of CO₂ fixation by chemical conversion to carbonate salts, *Chemical Engineering Journal*, 231 (2013) 287-293.
- [263] S. Park, M.-G. Lee, J. Park, CO₂ (carbon dioxide) fixation by applying new chemical absorption-precipitation methods, *Energy*, 59 (2013) 737-742.
- [264] H.E. King, H. Satoh, K. Tsukamoto, A. Putnis, Nanoscale Observations of Magnesite Growth in Chloride- And Sulfate-Rich Solutions, *Environmental Science & Technology*, 47 (2013) 8684-8691.
- [265] I.M. Power, S.A. Wilson, D.P. Small, G.M. Dipple, W. Wan, G. Southam, Microbially Mediated Mineral Carbonation: Roles of Phototrophy and Heterotrophy, *Environmental Science & Technology*, 45 (2011) 9061-9068.
- [266] A.C. Mitchell, K. Dideriksen, L.H. Spangler, A.B. Cunningham, R. Gerlach, Microbially Enhanced Carbon Capture and Storage by Mineral-Trapping and

- Solubility-Trapping, *Environmental Science & Technology*, 44 (2010) 5270-5276.
- [267] V.L.J. Snoeyink, David, *Water Chemistry*, John Wiley & Sons, New York, 1980.
- [268] R.E. Loewenthal, G.V.R. Marais, *Carbonate Chemistry of Aquatic Systems: Theory and Applications*, Ann Arbor Science, Ann Arbor, 1976.
- [269] R. Brinkman, R. Margaria, F.J.W. Roughton, The Kinetics of the Carbon Dioxide-Carbonic Acid Reaction, *Philosophical Transactions of the Royal Society of London. Series A, Containing Papers of a Mathematical or Physical Character*, 232 (1934) 65-97.
- [270] F.J.W. Roughton, V.H. Booth, The catalytic effect of buffers on the reaction $\text{CO}_2 + \text{H}_2\text{O} = \text{H}_2\text{CO}_3$, *Biochemical Journal*, 32 (1938) 2049-2069.
- [271] D.M. Kern, The hydration of carbon dioxide, *Journal of Chemical Education*, 37 (1960) 14.
- [272] R.E. Zeebe, D.A. Wolf-Gladrow, H. Jansen, On the time required to establish chemical and isotopic equilibrium in the carbon dioxide system in seawater, *Marine Chemistry*, 65 (1999) 135-153.
- [273] X. Wang, W. Conway, R. Burns, N. McCann, M. Maeder, Comprehensive Study of the Hydration and Dehydration Reactions of Carbon Dioxide in Aqueous Solution, *The Journal of Physical Chemistry A*, 114 (2009) 1734-1740.
- [274] Y. Pocker, D.W. Bjorkquist, Stopped-flow studies of carbon dioxide hydration and bicarbonate dehydration in water and water-D₂. Acid-base and metal ion catalysis, *Journal of the American Chemical Society*, 99 (1977) 6537-6543.
- [275] J.W. Mc Bain, The use of phenolphthalein as an indicator. The slow rate of neutralization of carbonic acid, *Journal of chemical Society Transactions*, 101 (1912) 814-820.
- [276] M.T.R. Nguyen, G. Vanguickenborne, L.G. V. Duijnen, How many water molecules are actively involved in the neutral hydration of carbon dioxide, *Journal of Physical Chemistry A*, 101 (1997) 7379-7388.
- [277] M.T. Nguyen, M.H. Matus, V.E.N. Jackson, V.T. Rustad, J.R. Dixon, A. David, Mechanism of the hydration of carbon dioxide: direct participation of H₂O versus microsolvation, *Journal of Physical Chemistry A*, 112 (2008) 10386-10398.
- [278] K. Adamczyk, P-S. Mirabelle, D. Pines, E. Pines, E.T.J. Nibbering, Real-time observation of carbonic acid formation in aqueous solution, *Science*, 326 (2009) 1690-1694.
- [279] P.V. Danckwerts, *Gas Liquid Reactions*, McGraw Hill Publishers, New York, 1970.

- [280] A.E. Dennard, R.J.P. Williams, The catalysis of the reaction between carbon dioxide and water, *Journal of the Chemical Society A: Inorganic, Physical, Theoretical*, (1966) 812-816.
- [281] A.R. White, T. Ward, CO₂ sequestration in a radial Hele-Shaw cell via an interfacial chemical reaction, *Chaos: An Interdisciplinary Journal of Nonlinear Science*, 22 (2012), 037114.
- [282] U.K. Ghosh, S.E. Kentish, G.W. Stevens, Absorption of carbon dioxide into aqueous potassium carbonate promoted by boric acid, *Energy Procedia*, 1 (2009) 1075-1081.
- [283] N. Kumar, D.P. Rao, Design of a packed column for absorption of carbon dioxide in hot K₂CO₃ solution promoted by arsenious acid, *Gas Separation & Purification*, 3 (1989) 152-155.
- [284] G. Astarita, D.W. Savage, J.M. Longo, Promotion of CO₂ mass transfer in carbonate solutions, *Chemical Engineering Science*, 36 (1981) 581-588.
- [285] R. Pohorecki, The absorption of CO₂ in carbonate—bicarbonate buffer solutions containing hypochlorite catalyst on a sieve plate, *Chemical Engineering Science*, 23 (1968) 1447-1451.
- [286] P.V. Danckwerts, Promotion of CO₂ mass-transfer in carbonate solutions, *Chemical Engineering Science*, 36 (1981) 1741-1742.
- [287] G.M. Richards, G.A. Ratcliff, P.V. Danckwerts, Kinetics of CO₂ absorption—III: First-order reaction in a packed column, *Chemical Engineering Science*, 19 (1964) 325-328.
- [288] P.V. Danckwerts, A.M. Kennedy, D. Roberts, Kinetics of CO₂ absorption in alkaline solutions—II: Absorption in a packed column and tests of surface-renewal models, *Chemical Engineering Science*, 18 (1963) 63-72.
- [289] D. Roberts, P.V. Danckwerts, Kinetics of CO₂ absorption in alkaline solutions—I Transient absorption rates and catalysis by arsenite, *Chemical Engineering Science*, 17 (1962) 961-969.
- [290] P.V. Danckwerts, K.M. McNeil, The effects of catalysis on rates of absorption of CO₂ into aqueous amine—potash solutions, *Chemical Engineering Science*, 22 (1967) 925-930.
- [291] A. Tavares da Silva, P.V. Danckwerts, The effect of halogens on the rate of absorption of carbon dioxide, *Chemical Engineering Science*, 28 (1973) 847-854.
- [292] N.J.M.C. Penders-van Elk, E.S. Hamborg, P.J.G. Huttenhuis, S. Fradette, J.A. Carley, G.F. Versteeg, Kinetics of absorption of carbon dioxide in aqueous amine and carbonate solutions with carbonic anhydrase, *International Journal of Greenhouse Gas Control*, 12 (2013) 259-268.

- [293] S. Zhang, Y. Lu, X. Ye, Catalytic behavior of carbonic anhydrase enzyme immobilized onto nonporous silica nanoparticles for enhancing CO₂ absorption into a carbonate solution, *International Journal of Greenhouse Gas Control*, 13 (2013) 17-25.
- [294] H. Hikita, S. Asai, T. Takatsuka, Absorption of carbon dioxide into aqueous sodium hydroxide and sodium carbonate-bicarbonate solutions, *Chemical Engineering Journal*, 11 (1976) 131-141.
- [295] H. Thee, K.H. Smith, G. da Silva, S.E. Kentish, G.W. Stevens, Carbon dioxide absorption into unpromoted and borate-catalyzed potassium carbonate solutions, *Chemical Engineering Journal*, 181–182 (2012) 694-701.
- [296] S. Park, H.-J. Song, M.-G. Lee, J. Park, Screening test for aqueous solvents used in CO₂ capture: K₂CO₃ used with twelve different rate promoters, *Korean Journal of Chemical Engineering*, 31 (2014) 125-131.
- [297] I. Torres Pineda, J.W. Lee, I. Jung, Y.T. Kang, CO₂ absorption enhancement by methanol-based Al₂O₃ and SiO₂ nanofluids in a tray column absorber, *International Journal of Refrigeration*, 35 (2012) 1402-1409.
- [298] J.W. Lee, Y.T. Kang, CO₂ absorption enhancement by Al₂O₃ nanoparticles in NaCl aqueous solution, *Energy*, 53 (2013) 206-211.
- [299] M.M. Sharma, P.V. Danckwerts, Catalysis by Bronsted bases of the reaction between CO₂ and water, *Transactions of the Faraday Society*, 59 (1963) 386-395.
- [300] L.K. Doraiswami, M.M. Sharma, *Heterogeneous reactions: Analysis, Examples and Reactor Design*, Volume 2, John Wiley & Sons, New York, USA, 1984.
- [301] S. Desikan, L.K. Doraiswami, The diffusion-reaction problems in triphasic catalysis, *Industrial & Engineering Chemistry Research*, 34 (1995) 3524-3537.
- [302] C. Ho, J.M. Sturtevant, The Kinetics of the Hydration of Carbon Dioxide at 25°, *Journal of Biological Chemistry*, 238 (1963) 3499-3501.
- [303] B.H. Gibbons, J.T. Edsall, Rate of Hydration of Carbon Dioxide and Dehydration of Carbonic Acid at 25°, *Journal of Biological Chemistry*, 238 (1963) 3502-3507.
- [304] B.R.W. Pinsent, L. Pearson, F.J.W. Roughton, The kinetics of combination of carbon dioxide with hydroxide ions, *Transactions of the Faraday Society*, 52 (1956) 1512-1520.
- [305] B.R.W. Pinsent, F.J.W. Roughton, The kinetics of combination of carbon dioxide with water and hydroxide ions, *Transactions of the Faraday Society*, 47 (1951) 263-269.
- [306] R.G. Khalifah, The Carbon Dioxide Hydration Activity of Carbonic Anhydrase: I. Stop-Flow kinetic studies on the native human isoenzyme B and C, *Journal of Biological Chemistry*, 246 (1971) 2561-2573.

- [307] M.J. Welch, J.F. Lifton, J.A. Seck, Tracer studies with radioactive oxygen-15. Exchange between carbon dioxide and water, *The Journal of Physical Chemistry*, 73 (1969) 3351-3356.
- [308] E. Magid, B.O. Turbeck, The rates of the spontaneous hydration of CO₂ and the reciprocal reaction in neutral aqueous solutions between 0° and 38°, *Biochimica et Biophysica Acta (BBA) - General Subjects*, 165 (1968) 515-524.
- [309] K.S. Johnson, Carbon dioxide hydration and dehydration kinetics in seawater, *Limnology and Oceanography*, 27 (1982) 849-855.
- [310] D. Guo, H. Thee, G. da Silva, J. Chen, W. Fei, S. Kentish, G.W. Stevens, Borate-Catalyzed Carbon Dioxide Hydration via the Carbonic Anhydrase Mechanism, *Environmental Science & Technology*, 45 (2011) 4802-4807.
- [311] S. Shen, Y. Yang, S. Ren, CO₂ absorption by borate-promoted carbonate solution: Promotion mechanism and vapor liquid equilibrium, *Fluid Phase Equilibria*, 367 (2014) 38-44.
- [312] G. Vázquez, F. Chenlo, G. Pereira, P. Vázquez, Enhancement of the Absorption of CO₂ in Alkaline Buffer Solutions: Joint Action of Two Enhancers, *Industrial & Engineering Chemistry Research*, 38 (1999) 2160-2162.
- [313] M.M. Sharma, P.V. Danckwerts, Fast reactions of CO₂ in alkaline solutions— (a) Carbonate buffers with arsenite, formaldehyde and hypochlorite as catalysts (b) Aqueous monoisopropanolamine (1-amino-2-propanol) solutions, *Chemical Engineering Science*, 18 (1963) 729-735.
- [314] G. Vázquez, F. Chenlo, G. Pereira, Enhancement of the Absorption of CO₂ in Alkaline Buffers by Organic Solutes: Relation with Degree of Dissociation and Molecular OH Density, *Industrial & Engineering Chemistry Research*, 36 (1997) 2353-2358.
- [315] M.J. Medeiros, D. Pletcher, D. Sidorin, The catalysis of carbon dioxide hydration by acetate ion, *Journal of Electroanalytical Chemistry*, 619–620 (2008) 83-86.
- [316] A.C. Pierre, Enzymatic Carbon dioxide Capture, *International Scholarly Research Network ISRN Chemical Engineering*, 2012 (2012) 753687.
- [317] E.V. Kupriyanova, N.A. Pronina, Carbonic anhydrase: Enzyme that has transformed the biosphere, *Russian Journal of Plant Physiology*, 58 (2011) 197-209.
- [318] F. Larachi, Kinetic Model for the Reversible Hydration of Carbon Dioxide Catalyzed by Human Carbonic Anhydrase II, *Industrial & Engineering Chemistry Research*, 49 (2010) 9095-9104.
- [319] S. Lindskog, Structure and mechanism of carbonic anhydrase, *Pharmacology & Therapeutics*, 74 (1997) 1-20.

- [320] K.M. Gilmour, Perspectives on carbonic anhydrase, *Comparative Biochemistry and Physiology Part A: Molecular & Integrative Physiology*, 157 (2010) 193-197.
- [321] Y. Xu, L. Feng, P.D. Jeffrey, Y. Shi, F.M.M. Morel, Structure and metal exchange in the cadmium carbonic anhydrase of marine diatoms, *Nature*, 452 (2008) 56-61.
- [322] O. Amata, T. Marino, N. Russo, M. Toscano, Catalytic activity of a ζ -class zinc and cadmium containing carbonic anhydrase. Compared work mechanisms, *Physical Chemistry Chemical Physics*, 13 (2011) 3468-3477.
- [323] R.S. Rowlett, Structure and catalytic mechanism of the β -carbonic anhydrases, *Biochimica et Biophysica Acta (BBA) - Proteins and Proteomics*, 1804 (2010) 362-373.
- [324] J.G. Ferry, The γ class of carbonic anhydrases, *Biochimica et Biophysica Acta (BBA) - Proteins and Proteomics*, 1804 (2010) 374-381.
- [325] S.-W. Lee, S.-B. Park, S.-K. Jeong, K.-S. Lim, S.-H. Lee, M.C. Trachtenberg, On carbon dioxide storage based on biomineralization strategies, *Micron*, 41 (2010) 273-282.
- [326] M. Vinoba, M. Bhagiyalakshmi, S.K. Jeong, Y. Yoon, II, S.C. Nam, Immobilization of carbonic anhydrase on spherical SBA-15 for hydration and sequestration of CO₂, *Colloids and Surfaces B: Biointerfaces*, 90 (2012) 91-96.
- [327] A. Sharma, A. Bhattacharya, A. Shrivastava, Biomimetic CO₂ sequestration using purified carbonic anhydrase from indigenous bacterial strains immobilized on biopolymeric materials, *Enzyme and Microbial Technology*, 48 (2011) 416-426.
- [328] R. Yadav, S. Wanjari, C. Prabhu, V. Kumar, N. Labhsetwar, T. Satyanarayanan, S. Kotwal, S. Rayalu, Immobilized Carbonic Anhydrase for the Biomimetic Carbonation Reaction, *Energy & Fuels*, 24 (2010) 6198-6207.
- [329] A. Sharma, A. Bhattacharya, Enhanced biomimetic sequestration of CO₂ into CaCO₃ using purified carbonic anhydrase from indigenous bacterial strains, *Journal of Molecular Catalysis B: Enzymatic*, 67 (2010) 122-128.
- [330] A. Sharma, A. Bhattacharya, S. Singh, Purification and characterization of an extracellular carbonic anhydrase from *Pseudomonas fragi*, *Process Biochemistry*, 44 (2009) 1293-1297.
- [331] C. Prabhu, S. Wanjari, A. Puri, A. Bhattacharya, R. Pujari, R. Yadav, S. Das, N. Labhsetwar, A. Sharma, T. Satyanarayanan, S. Rayalu, Region-Specific Bacterial Carbonic Anhydrase for Biomimetic Sequestration of Carbon Dioxide, *Energy & Fuels*, 25 (2011) 1327-1332.
- [332] R. Yadav, N. Labhsetwar, S. Kotwal, S. Rayalu, Single enzyme nanoparticle for biomimetic CO₂ sequestration, *Journal of Nanopart Research*, 13 (2011) 263-271.

- [333] S. Wanjari, C. Prabhu, T. Satyanarayana, A. Vinu, S. Rayalu, Immobilization of carbonic anhydrase on mesoporous aluminosilicate for carbonation reaction, *Microporous and Mesoporous Materials*, 160 (2012) 151-158.
- [334] R. Yadav, M. Joshi, S. Wanjari, C. Prabhu, S. Kotwal, T. Satyanarayanan, S. Rayalu, Immobilization of Carbonic Anhydrase on Chitosan Stabilized Iron Nanoparticles for the Carbonation Reaction, *Water Air and Soil Pollution*, 223 (2012) 5345-5356.
- [335] S. Wanjari, C. Prabhu, R. Yadav, T. Satyanarayana, N. Labhsetwar, S. Rayalu, Immobilization of carbonic anhydrase on chitosan beads for enhanced carbonation reaction, *Process Biochemistry*, 46 (2011) 1010-1018.
- [336] C. Prabhu, S. Wanjari, S. Gawande, S. Das, N. Labhsetwar, S. Kotwal, A.K. Puri, T. Satyanarayana, S. Rayalu, Immobilization of carbonic anhydrase enriched microorganism on biopolymer based materials, *Journal of Molecular Catalysis B: Enzymatic*, 60 (2009) 13-21.
- [337] R. Yadav, T. Satyanarayanan, S. Kotwal, S. Rayalu, Enhanced carbonation reaction using chitosan-based carbonic anhydrase nanoparticles, *Current Science*, 100 (2011) 520-524.
- [338] C. Prabhu, A. Valechha, S. Wanjari, N. Labhsetwar, S. Kotwal, T. Satyanarayanan, S. Rayalu, Carbon composite beads for immobilization of carbonic anhydrase, *Journal of Molecular Catalysis B: Enzymatic*, 71 (2011) 71-78.
- [339] R. Ramanan, K. Kannan, S. Sivanesan, S. Mudliar, S. Kaur, A. Tripathi, T. Chakrabarti, Bio-sequestration of carbon dioxide using carbonic anhydrase enzyme purified from *Citrobacter freundii*, *World Journal of Microbiology and Biotechnology*, 25 (2009) 981-987.
- [340] A. Sharma, A. Bhattacharya, R. Pujari, A. Shrivastava, Characterization of carbonic anhydrase from diversified genus for biomimetic carbon-dioxide sequestration, *Indian Journal of Microbiology*, 48 (2008) 365-371.
- [341] Z. Zhang, B. Lian, W. Hou, M. Chen, X.L. Li, Yuan, *Bacillus mucilafinosus* can capture atmospheric CO₂ by carbonic anhydrase, *African Journal of Microbiology Research*, 5 (2011) 106-112.
- [342] W. Li, L.P. Liu, P.P. Zhou, L. Cao, L.J. Yu, S.Y. Jiang, Calcite precipitation induced by bacteria and bacterially produced carbonic anhydrase, *Current Science*, 100 (2011) 502-508.
- [343] M.E. Russo, G. Olivieri, M. Rossi, C. Capasso, V. De Luca, A. Marzocchella, P. Salatino, Kinetic assesment of thermostable Carbonic Anhydrase for CO₂ capture processes, *Chemical Engineering Transactions*, 27 (2012) 181-186.

- [344] C. Capasso, V. De Luca, V. Carginale, P. Caramuscio, C.F.N. Cavalheiro, R. Cannio, M. Rossi, Characterization and properties of a new thermoactive and thermostable Carbonic Anhydrase, *Chemical Engineering Transactions*, 27 (2012) 271-276.
- [345] M. Oviya, V. Sukumaran, S. Giri, Immobilization and characterization of carbonic anhydrase purified from *E. coli* MO1 and its influence on CO₂ sequestration, *World Journal Microbiology and Biotechnology*, 29 (2013) 1813-1820.
- [346] W. Li, W.-S. Chen, P.-P. Zhou, L.-J. Yu, Influence of enzyme concentration on bio-sequestration of CO₂ in carbonate form using bacterial carbonic anhydrase, *Chemical Engineering Journal*, 232 (2013) 149-156.
- [347] J.E. Bailey, D.F. Ollis, *Biochemical engineering fundamentals*, McGraw-Hill, 1986.
- [348] M.L. Shuler, F. Kargı, *Bioprocess Engineering*, Prentice Hall PTR, 2002.
- [349] P. Mirjafari, K. Asghari, N. Mahinpey, Investigating the Application of Enzyme Carbonic Anhydrase for CO₂ Sequestration Purposes, *Industrial & Engineering Chemistry Research*, 46 (2007) 921-926.
- [350] N. Favre, M.L. Christ, A.C. Pierre, Biocatalytic capture of CO₂ with carbonic anhydrase and its transformation to solid carbonate, *Journal of Molecular Catalysis B: Enzymatic*, 60 (2009) 163-170.
- [351] S.W. Lee, S.B. Park, S.K. Jeong, K.S. Lim, S.H. Lee, M.C. Trachtenberg, On carbon dioxide storage based on biomineralization strategies, *Micron*, 41 (2010) 273-282.
- [352] L. Bao, M.C. Trachtenberg, Modeling CO₂-facilitated transport across a diethanolamine liquid membrane, *Chemical Engineering Science*, 60 (2005) 6868-6875.
- [353] M.C. Trachtenberg, R.M. Cowan, D.A. Smith, D.A. Horazak, M.D. Jensen, J.D. Laumb, A.P. Vucelic, H. Chen, L. Wang, X. Wu, Membrane-based, enzyme-facilitated, efficient carbon dioxide capture, *Energy Procedia*, 2009, pp. 353-360.
- [354] M.C. Trachtenberg, L. Bao, S.L. Goldman, D.A. Smith, X. Wu, Flue gas CO₂ capture by a green liquid membrane, *Proceedings of the 7th International Conference on Greenhouse Gas Control Technologies*, 2004, pp. 1751-1754.
- [355] L. Bao, M.C. Trachtenberg, Facilitated transport of CO₂ across a liquid membrane: Comparing enzyme, amine, and alkaline, *Journal of Membrane Science*, 280 (2006) 330-334.
- [356] J. Ge, R.M. Cowan, C. Tu, M.L. McGregor, M.C. Trachtenberg, Enzyme-based CO₂ capture for advanced life support, *Life support & biosphere science : International Journal of Earth Space*, 8 (2002) 181-189.

- [357] M.C. Trachtenberg, R.M. Cowan, S.L. Goldman, J.J. Ge, Y.J. Qin, M.L. McGregor, C.K. Tu, Enzyme based membrane reactor for CO₂ capture, SAE Technical Papers, (2003), 2003-01-2499.
- [358] L. Bao, S.L. Goldman, M.C. Trachtenberg, CO₂ transfer across a liquid membrane facilitated by carbonic anhydrase, Paper presented to AIChE Annual Meeting, Austin, TX, 2004, pp. 5229-5238.
- [359] R.M. Cowan, J.J. Ge, Y.J. Qin, M.L. McGregor, M.C. Trachtenberg, CO₂ capture by means of an enzyme-based reactor, Annals of New York Academy of Science, 2003, pp. 453-469.
- [360] M.C. Trachtenberg, J.J. Ge, R.M. Cowan, Y.J. Qin, CO₂ capture by enzyme-based facilitated transport, SAE Technical Papers, (2002), 2002-01-2267.
- [361] D.T. Arazawa, H.-I. Oh, S.-H. Ye, C.A. Johnson Jr, J.R. Woolley, W.R. Wagner, W.J. Federspiel, Immobilized carbonic anhydrase on hollow fiber membranes accelerates CO₂ removal from blood, Journal of Membrane Science, 403–404 (2012) 25-31.
- [362] Y.-T. Zhang, X.-G. Dai, G.-H. Xu, L. Zhang, H.-Q. Zhang, J.-D. Liu, H.-L. Chen, Modeling of CO₂ mass transport across a hollow fiber membrane reactor filled with immobilized enzyme, AIChE Journal, 58 (2012) 2069-2077.
- [363] S. Zhang, Z. Zhang, Y. Lu, M. Rostam-Abadi, A. Jones, Activity and stability of immobilized carbonic anhydrase for promoting CO₂ absorption into a carbonate solution for post-combustion CO₂ capture, Bioresource Technology, 102 (2011) 10194-10201.
- [364] R. Dilmore, C. Griffith, Z. Liu, Y. Soong, S.W. Hedges, R. Koepsel, M. Ataai, Carbonic anhydrase-facilitated CO₂ absorption with polyacrylamide buffering bead capture, International Journal of Greenhouse Gas Control, 3 (2009) 401-410.
- [365] Y. Lu, X. Ye, Z. Zhang, A. Khodayari, T. Djukadi, Development of a carbonate absorption-based process for post-combustion CO₂ capture: The role of biocatalyst to promote CO₂ absorption rate, Energy Procedia, 4 (2011) 1286-1293.
- [366] J.R. Collett, R.W. Heck, A.J. Zwoster, Dissolved carbonic anhydrase for enhancing post-combustion carbon dioxide hydration in aqueous ammonia, Energy Procedia, 4 (2011) 240-244.
- [367] G.T. Tsao, The effect of carbonic anhydrase on carbon dioxide absorption, Chemical Engineering Science, 27 (1972) 1593-1600.
- [368] G.T. Tsao, Carbon dioxide absorption in the presence of carbonic anhydrase, Chemical Engineering Science, 33 (1978) 628.
- [369] E. Alper, M. Lohse, W.D. Deckwer, On the mechanism of enzyme-catalysed gas—liquid reactions: Absorption of CO₂, into buffer solutions

- containing carbonic anhydrase, *Chemical Engineering Science*, 35 (1980) 2147-2156.
- [370] E. Alper, W.D. Deckwer, Kinetics of absorption of CO₂ into buffer solutions containing carbonic anhydrase, *Chemical Engineering Science*, 35 (1980) 549-557.
- [371] E. Alper, Comments on the effect of carbonic anhydrase on carbon dioxide absorption, *Chemical Engineering Science*, 33 (1978) 1399-1400.
- [372] I. Iliuta, F. Larachi, New scrubber concept for catalytic CO₂ hydration by immobilized carbonic anhydrase II and in-situ inhibitor removal in three-phase monolith slurry reactor, *Separation and Purification Technology*, 86 (2012) 199-214.
- [373] F. Larachi, O. Lacroix, B.P.A. Grandjean, CO₂ hydration by immobilized carbonic anhydrase in Robinson–Mahoney and packed-bed scrubbers—Role of mass transfer and inhibitor removal, *Chemical Engineering Science*, 73 (2012) 99-115.
- [374] D.-H. Kim, M. Vinoba, W.-S. Shin, K.-S. Lim, S.-K. Jeong, S.-H. Kim, Biomimetic sequestration of carbon dioxide using an enzyme extracted from oyster shell, *Korean Journal Chemical Engineering*, 28 (2011) 2081-2085.
- [375] M. Vinoba, M. Bhagiyalakshmi, S.K. Jeong, S.C. Nam, Y. Yoon, Carbonic Anhydrase Immobilized on Encapsulated Magnetic Nanoparticles for CO₂ Sequestration, *Chemistry – A European Journal*, 18 (2012) 12028-12034.
- [376] E. Ozdemir, Biomimetic CO₂ Sequestration: 1. Immobilization of Carbonic Anhydrase within Polyurethane Foam, *Energy & Fuels*, 23 (2009) 5725-5730.
- [377] E.T. Hwang, H. Gang, J. Chung, M.B. Gu, Carbonic anhydrase assisted calcium carbonate crystalline composites as a biocatalyst, *Green Chemistry*, 14 (2012) 2216-2220.
- [378] P.C. Sahoo, Y.-N. Jang, S.-W. Lee, Immobilization of carbonic anhydrase and an artificial Zn(II) complex on a magnetic support for biomimetic carbon dioxide sequestration, *Journal of Molecular Catalysis B: Enzymatic*, 82 (2012) 37-45.
- [379] M. Vinoba, D.H. Kim, K.S. Lim, S.K. Jeong, S.W. Lee, M. Alagar, Biomimetic Sequestration of CO₂ and Reformation to CaCO₃ Using Bovine Carbonic Anhydrase Immobilized on SBA-15, *Energy & Fuels*, 25 (2010) 438-445.
- [380] M. Vinoba, M. Bhagiyalakshmi, S.K. Jeong, Y. Yoon, II, S.C. Nam, Capture and Sequestration of CO₂ by Human Carbonic Anhydrase Covalently Immobilized onto Amine-Functionalized SBA-15, *The Journal of Physical Chemistry C*, 115 (2011) 20209-20216.

- [381] J. Hanna, I. Iliuta, F. Larachi, M.C. Iliuta, Enzymatic CO₂ capture by immobilized hCA II in an intensified microreactor—Kinetic study of the catalytic hydration, *International Journal of Greenhouse Gas Control*, 15 (2013) 78-85.
- [382] M. Vinoba, K.S. Lim, S.H. Lee, S.K. Jeong, M. Alagar, Immobilization of Human Carbonic Anhydrase on Gold Nanoparticles Assembled onto Amine/Thiol-Functionalized Mesoporous SBA-15 for Biomimetic Sequestration of CO₂, *Langmuir*, 27 (2011) 6227-6234.
- [383] M. Vinoba, M. Bhagiyalakshmi, S.K. Jeong, Y. Yoon, II, S.C. Nam, Carbonic anhydrase conjugated to nanosilver immobilized onto mesoporous SBA-15 for sequestration of CO₂, *Journal of Molecular Catalysis B: Enzymatic*, 75 (2012) 60-67.
- [384] O. Pedersen, T.D. Colmer, K. Sand-Jensen, Underwater photosynthesis of submerged plants – recent advances and methods, *Frontiers in Plant Science*, 4 (2013).
- [385] J.N. Butler, *Carbon dioxide equilibria and their applications*, Lewis Publishers, Chelsea, 1991.
- [386] J.W. Morse, S. He, Influences of T, S and P_{CO2} on the pseudo-homogeneous precipitation of CaCO₃ from sea water: implications of whiting formation, *Marine Chemistry*, 41 (1993) 291-297.

Experimental Methodology

The current chapter explains the experimental methodology used in the identification of NiNPs as a catalyst for hydration of CO₂. The nickel nanoparticles were commercially purchased and characterized before use. The proof of concept, kinetic study and the photo-catalytic activity of NiNPs in catalysing the hydration of CO₂ was carried out in the laboratory. Catalytic activity of other nanoparticles (Fe₂O₃ and NiO) was also studied. The mineralization experiments in the presence of NiNPs are demonstrated. The chemical analysis required for the development of reaction mechanism and determining material properties was carried out using X-ray photoelectron spectroscopy (XPS), X-ray diffraction spectroscopy (XRD) and Fourier Transform Infrared Spectroscopy (FTIR). Material characterization was carried out using transmission electron microscopy (TEM), scanning electron microscopy (SEM), selected area electron diffraction pattern (SAED), energy dispersive X-ray spectroscopy (EDX), X-ray diffraction spectroscopy (XRD), Dynamic light scattering (DLS), UV-Vis spectroscopy and Zeta potential.

3.1 Chemicals and equipment used for experimentation

The nickel nanoparticles (NiNPs) were purchased from NanoTechnology, Korea. 99% CO₂ gas and 12% CO₂-Air cylinders were purchased from BOC. Iron(II) oxide nanoparticles were purchased from NanoAmor, Europe. Hydrochloric acid (0.1M and 27% concentrated), boric acid, calcium chloride, calcium sulphate, Gallium-Indium (Galn) paste, nickel sulphate, nickel chloride, nickel(II) oxide nanoparticles, nitric acid, phenolphthalein indicator (50% alcohol), potassium carbonate, sodium carbonate, sodium chloride, and sodium hydroxide were purchased from Sigma Aldrich, UK and used as received. All the above chemicals were analytical grade. Buffer tablets to prepared standard pH 4, 7 and 10 solutions where purchased from RS components and were mixed with deionized (DI) water. All solutions and samples were prepared in DI water with low conductivity (~1-2 $\mu\text{S}/\text{cm}$).

The equipment used for CO₂ bubbling experiments were 250 ml and 180 ml glass jars were purchased from Wheaton Industries, UK. Custom made glass ware was purchased from Soham Scientific, UK (for CO₂ uptake experiments). BS5, Fisher Scientific water bath was used for circulation or reservoir constant temperature water bath. The NiNPs suspensions were prepared using an ultrasonic water bath (Hilsonic, UK). The pH meters used for the experiments were pH 209 bench top and HI2550 pH meters (Hanna Instruments, UK). The HI2550 is a more advanced pH meter as compared to pH 209 bench top with online pH logging using a computer. The HI2550 would have a better response to a pH change as compared to pH 209 bench top which is determined by the operational amplifier with in the pH meter.

Unfortunately, this information was not available from the manufacturers (Hanna Instruments, UK). The pH meter was calibrated before every experimental run using standard commercial buffers of pH 4, 7 and 10. A pIONneer30 conductivity meter (Radiometer analytical, UK) was used for ionic conductivity measurements.

3.2 Experimental procedure

3.2.1 Preparation of nickel nanoparticle (NiNPs) suspension

The NiNPs suspension was prepared by accurately measuring the NiNPs (depending on the concentration of the suspension) and adding them to the required amount of DI water. Upon addition of NiNPs the mixture was always sonicated for 5 minutes in an ultrasonic water bath at room temperature. Typically the NiNPs stayed in suspension for ~30 minutes.

3.2.2 CO₂ saturation in DI water and nanoparticle suspensions

The CO₂ saturation experiments were carried out in a 20 ml jacked glass reactor (Soham Scientific). 10 ml of low conductivity DI water (or NiNPs suspension in DI water) was added into the reactor and CO₂ gas was bubbled at a flow rate of 1.407 mmol/min (i.e. 122.577 ml/min of CO₂ = 50 ml/min of air), 0.1MPa gauge pressure. The gas was allowed to pass for 30 minutes to attain saturation of the solution. The gas was then switched off and the saturated solution of CO₂ was titrated with 0.1M NaOH solution to estimate the total amount of CO₂ in solution. Care was taken that the titration was carried out when there was a CO₂ environment over the liquid sample and carried out within 10 minutes after the bubbling was stopped [1]. The time for saturation of CO₂ in DI water was determined by initial titration of CO₂ saturated solution after different CO₂ bubbling time intervals of 15, 30 and 60 min. The concentration of

CO₂ in DI water after 15, 30 and 60 min bubbling was 39 ± 2 mM, therefore the titration time was taken as 30 min. Each titration was repeated five times and average of the values are presented in section 4.2, chapter 4.

This procedure was repeated for NiNPs suspensions of different concentration i.e. 10 ppm, 20 ppm, 30 ppm, 40 ppm and 50 ppm respectively. The temperature of the reaction vessel during bubbling of CO₂ and titration was kept constant at 20 °C using a circulating water bath (BS5, Fisher Scientific). Results on saturation experiments are discussed and presented in chapter 4, section 4.2 and chapter 8, section 8.2.

The same procedure was used to study the saturation of CO₂ in suspension of Fe₂O₃NPs and NiONPs in DI water. Results of the CO₂ saturation in Fe₂O₃NPs and NiONPs suspensions and DI water are discussed in chapter 5, section 5.4.2 and in chapter 8, section 8.2. To study the effect of temperature on CO₂ saturation in NiNPs suspension the same procedure was repeated for CO₂ saturation in DI water and NiNPs suspension at temperatures of 10 °C, 20 °C, 30 °C, 40 °C, 50 °C and 60 °C. Detailed results and discussion on this experiment are presented in chapter 6, section 6.2.1 and chapter 8, section 8.4. The same procedure was repeated for nickel nanowires, results are discussed in chapter 5, section 5.6.

3.2.3 CO₂ absorption in DI water and nanoparticle suspension (gas-liquid reactions)

One of the methods for measuring CO₂ hydration kinetics is by bubbling CO₂ in DI water or buffer or basic solutions [2, 3]. When a gas is bubbled in a quiescent liquid, the gas enters the liquid at the interface and in the absence of kinetic constant for the process the concentration is assumed on the basis of

the ideal gas equation (gas side) and Henry's Law (liquid side) [4]. According to Danckwerts [2], in gas absorption with chemical reaction (or gas-liquid reaction in general) the final saturated concentration of gas in the liquid will not obey Henry's Law and will be dependent on the equilibrium of the reaction (for reversible reactions) or extent of the reaction (for non-reversible reactions). In the case of CO₂ and aqueous system the pH of the solvent changes due to generation of carbonic acid following the reaction sequence (considering the quiescent liquid to be DI water [5] or buffer solution of pH < 8 [6])



The assumption made in this analysis is that the physical mass transfer rate (i.e. the rate at which CO_{2(gas)} converts to CO_{2(aq)}) is independent of the presence of the catalyst. The reaction 1 is a phase transfer process depending on the partial pressure of CO₂ in the gas phase [2, 4]. Noyes *et al.* [7] reported the rate of inter phase transfer of CO₂ in water at different pressures of CO₂. The rate constant (or kinetic constant) for reaction 1 for aqueous solutions is 5.5 x 10⁻⁶ m/s under 1 bar pressure of CO₂ [7]. The reaction 3 is an acid dissociation reaction considered to be instantaneous [8]. As reaction 2 is dependent on the amount of CO_{2(aq)} species present, is therefore is proportional the product of the partial pressure of CO₂ and rate constant of reaction 1 which is constant during the reaction.

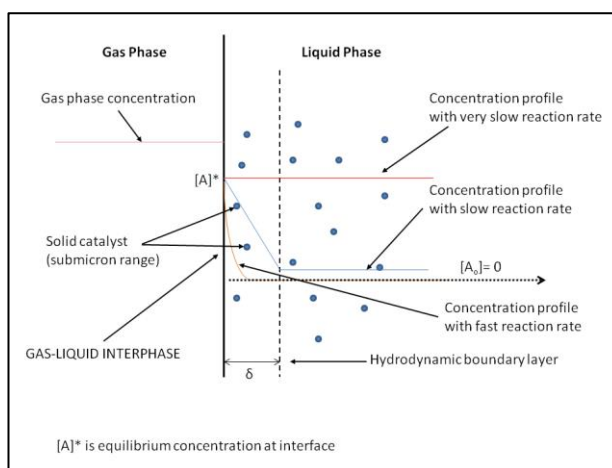


Figure 3.1: Concentration profiles for gas-liquid-solid (very fine particles): diffusion of solute A and the surface reaction are parallel (adapted from Doraiswami and Sharma [9])

The kinetics of hydration of CO_2 is represented by the rate of change in pH indicating the amount of acid formed per unit time. In the catalytic and uncatalysed reaction the gas phase partial pressure of CO_2 and the flow rate of the gas is constant, implying that the phase transfer of $\text{CO}_{2(\text{gas})}$ to $\text{CO}_{2(\text{aq})}$ is constant. The presence of the catalyst does not affect the phase transfer but depending on its catalytic rate, it accelerates the reaction rate within the hydrodynamic boundary layer in a bi-phasic (for CA experiments Kim *et al.* [6]) or tri-phasic (on in the case of NiNPs system [5]) reaction. Figure 3.1 shows the change in concentration of the gas phase reactant A in liquid under different reaction conditions [9].

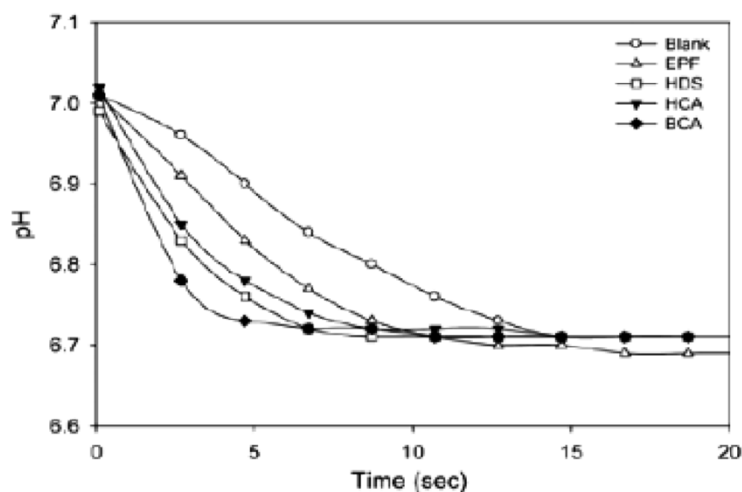


Figure 3.2 pH change when CO_2 is bubbled in 0.1 M Tris(hydroxymethyl)aminomethane-HCl buffer in absence (o) and presence of human carbonic anhydrase (HCA)(\blacktriangledown), bovine carbonic anhydrase (BCA) (\blacklozenge), hemocytes from diseased shell (HDS) (\square) and extra pallial fluid (EPF) (Δ) extracted from oysters (*Crassostrea Gigas*) by Kim *et al.* [6].

Kim *et al.* [6] measured pH change when CO_2 was bubbled in buffer solutions in absence and presence of bovine CA, human CA, hemocytes from diseased shell (HDS) and extra pallial fluid (EPF) extracted from oysters (*Crassostrea Gigas*) to test catalytic activity of these biomolecules for hydration of CO_2 . They observed that the pH change was rapid in the presence of the CA and other biomolecules than in its absence (figure 3.2). This rapid change in pH they concluded was due to the catalytic hydration of CO_2 of CA.

The catalytic activity of NiNPs for hydration of CO_2 was evaluated using similar methodology as Kim *et al.* [6]. The CO_2 absorption rate is carried out in a 250 ml glass jar with a fixed volume (200 ml) of DI water (or 30 ppm NiNPs suspension). The CO_2 gas was sparged into the solution at a flow rate of 1.407 mM/min at 0.1MPa pressure using a glass sinter (Pyrex 1, Sigma Aldrich, UK). The pH changes of the solution were monitored during the bubbling experiments manually using a pH 209 bench top pH meter (Hanna Instruments)

and ionic conductivity are measured simultaneously using pIONneer30 conductivity meter (Radiometer Analytical). The readings are taken in intervals of 20 seconds. The temperature of the sample was maintained at 20 °C by immersing the glass jar in a water bath (BS5, Fisher Scientific). To assess any leaching of the Ni²⁺ ions from the NiNPs, the following methodology was used. 30 ppm of NiNPs were suspended in the DI water and sonicated for 5 min, followed with recording of the change in ionic conductivity of the suspension using pIONneer30 (Radiometer Analytical). Detailed results and discussion on this experiment are presented in chapter 4 section 4.3.

A similar procedure is used for studying the catalytic activity of Fe₂O₃NPs and NiONPs. The pH in these experiments were measured using HI2550 (Hanna Instruments, UK) and recorded on a computer. The results of the pH change studies of Fe₂O₃NPs and NiONPs are discussed in chapter 5 section 5.4. The same experiment was carried out in NiNPs suspensions using 12% CO₂-Air mixture (BOC, UK) to test similar catalytic behaviour. The results of this are discussed in chapter 5 section 5.5.

3.2.4 Leaching of Ni²⁺ ions in carbonic acid solution and influence on CO₂ hydration

Hernandez *et al.* [10] studied the influence of pH on the surface species and dissolution of Ni and NiO microparticles. It is known that Ni²⁺ ions do not leach in DI water but forms a passive Ni(OH)_x layer on the surface of solid Ni [10, 11]. The formation of Ni(OH)_x species leads to the pH of water [10] which is observed in the results in this study (chapter 4, section 4.3). Dissolution of Ni under acidic conditions depends on the nature of the acid and its concentration, for example dilute HNO₃ dissolves Ni whereas concentrated HNO₃ forms a

passive layer on the Ni surface [10]. The low dissolution of solid nickel in solutions because nickel has an electrochemical potential of -0.227V with reference to Standard Hydrogen Electrode (SHE) (see figure 3.3), suggesting that the Ni leaching rate is slow in acidic solutions in absence of an oxidizing agent stronger than H^+ [12]. Hernandez *et al.* [10] reported that in presence of a mineral acid (like HCl) Ni leaching is high (>100 ppm) for $\text{pH} < 4$ but is low (< 50 ppm) between $\text{pH} 4-12$ for studied for 1000 ppm Ni microparticle suspension.

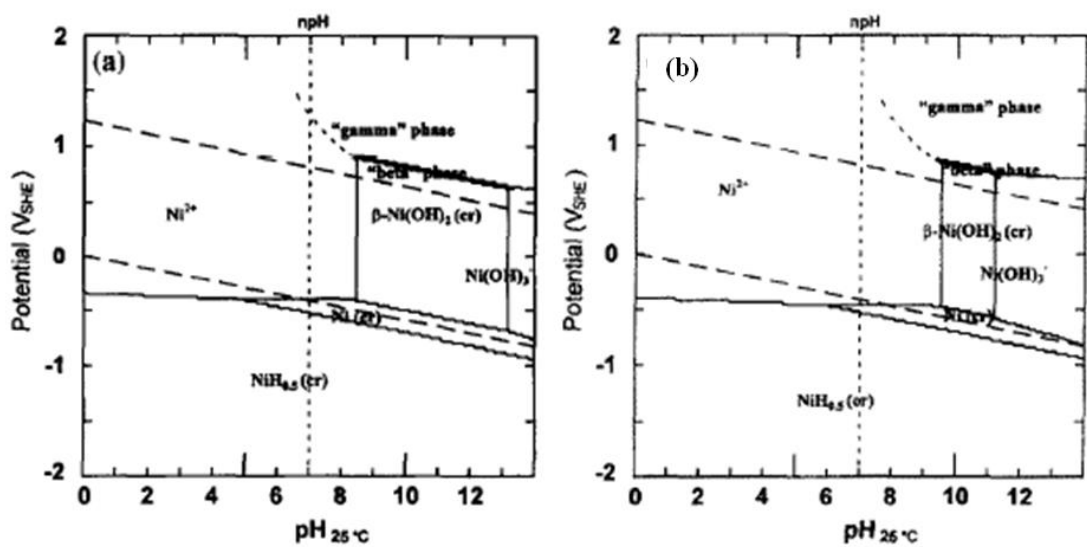


Figure 3.3 Pourbaix diagram for nickel at 25 °C (a) concentration of $[\text{Ni}_{(\text{aq})}]_{\text{tot}} = 10^{-6}$ M and (b) concentration of $[\text{Ni}_{(\text{aq})}]_{\text{tot}} = 10^{-8}$ M [13]

Drodten [14] recently reported a review on corrosion of metallic nickel in carbonic acid. It was reported that corrosion rate of Ni DI water containing CO_2 at pressure of 13.8 bar and temperature of 54-55 °C is 0.002 mm/yr after 7 days and is less lower after 28 and 70 days implying formation of a passive layer. Drodten also reports that corrosion of Ni in presence of CO_2 and O_2 in DI water is 0.08 mm/yr after 20 hours, 0.01 mm/yr after 60 hours and 0 mm/yr after 120 hours. Drodten also states that Ni is corrosion resistant in $\text{CO}_2\text{-H}_2\text{O}$ system up to temperature of 464 °C.

Therefore dialysis is used to determine the leaching of Ni^{2+} ions from NiNPs in carbonic acid (pH 4) by modifying the method described by Piticharoenphun [15]. 100 ml of 30 ppm NiNPs suspension was prepared using the method described in section 3.2.1 in a 180 ml glass jar (Wheaton Industries, UK). To the NiNPs suspension 2-3 pieces of dry ice (solid CO_2 , BOC, UK) is added for rapid saturate the NiNPs suspension. (Dry ice was used instead of bubbling CO_2 (procedure in section 3.3.4 and 3.35) to obtain saturated CO_2 -NiNPs suspension because the CO_2 gas bubbling process is long and the NiNPs would settle in solution and they could not be re-suspended in solution without disturbing the equilibrium concentration of saturated CO_2). The pH of the saturated solution was 4 measured using pH meter HI2550 (Hanna Instruments). A PTFE lid was placed to maintain CO_2 environment in the gas space above the suspension, to completely acidify the NiNPs suspension. The suspension was considered to have achieved equilibrium when the vapours of CO_2 diffused as the pH reading was 4. During the CO_2 saturation process, the glass jar was stirred occasionally to aid mixing of the gas.

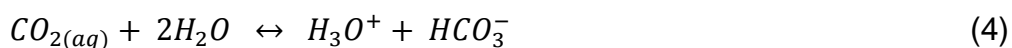
10 ml of the CO_2 saturated NiNPs suspension was added into dialysis membrane (MWCO = 3500 Da; diameter = 11.5 mm, pore size < 2nm) purchased from Spectrum Laboratories, Canada. The membrane was capped on both sides to exclude air. The membrane was placed in into a 2 litre beaker (VWR, UK) containing 1 litre of DI water. The experiment was performed at room temperature. The DI water in the beaker outside the membrane was stirred before collection of DI water for Ni^{2+} ion leaching analysis. 10 ml of DI water was collected from the beaker at 0 min, 30 min and 60 min and kept in 30 ml sample vials (Wheaton Industries, UK) before inductive coupled plasma optical emission spectroscopy (ICP-OES) measurement. The ICP-OES was

carried out at School of Civil Engineering and Geosciences, Newcastle University (with minimum detection limit = 0.01 mg/lit). The results are discussed in chapter 4, section 4.3

To study the influence of Ni²⁺ ions on the hydration of CO₂, CO₂ bubbling experiment was carried out using procedure 2.3.3 using 0.005 ppm NiSO₄ solution. The concentration of NiSO₂ solution was determined from the ICP-OES results of leaching experiment described in the above paragraph. The results are discussed in chapter 4, section 4.3 using HI2550 pH meter to measure pH.

3.2.5 CO₂ hydration kinetic study using saturated CO₂ solution in DI water (liquid-liquid reaction)

Another common method to measure the rate of CO₂ hydration is to prepare a saturated solution of CO₂ in DI water and mix it with a buffer or base while observing the pH change. The following two experimental methods use saturated CO₂ solution to measure CO₂ hydration kinetics. It is known that when CO₂ is bubbled in DI water its pH drops to 4 [8] due to the formation of carbonic acid following the reaction [3].



Depending on the pH of the solution the hydration of CO₂ would follow reaction path 4 at pH 8 or below and the reaction path 5 at pH 10 or above [3] (also discussed in section 2.3.3, chapter 2).



In a pre-saturated CO₂ solution the reaction 4 has reaches an equilibrium, where K₁ is the equilibrium constant given by the equation

$$K_4 = \frac{[HCO_3^-][H_3O^+]}{[CO_{2(aq)}]} = 1.6 \times 10^{-3} \quad (E.3.1)$$

From the equilibrium equation it can be observed that concentration of $CO_{2(aq)}$ is 625 times higher than the concentration of $[H_2CO_3]$. As the concentration of carbonic acid is very small as compared to $CO_{2(aq)}$, as a standard practice, CO_2 saturated solution is termed as $CO_{2(aq)}^*$ or $CO_{2(aq)}$ or $[H_2CO_3^*]$ [8].

$$[H_2CO_3^*] = CO_{2(aq)}^* = [H_2CO_3] + [CO_{2(aq)}] \quad (E.3.2)$$

Any change in the chemical environment of the pre-saturated solution would lead to the change in the equilibrium constant value according to Le Chatelier's principle [3]. When the pre-saturated CO_2 solution is added to a buffer or Na_2CO_3 solution the chemical environment changes and the reaction 1 or 2 (depending on the pH of the solution) move towards the right to attain a new equilibrium state. The rate at which this equilibrium change takes place gives the rate of the forward reaction, which is formation of carbonic acid.

3.2.5.1 CO_2 hydration kinetics using stop flow spectrophotometer

Stopped flow spectrophotometric kinetic analysis was carried out at the Department of Chemistry, Newcastle University. The method is used for the measurement of fast kinetics (i.e. having reaction completion time of 1-5 min) and has been used to measure the kinetics of CO_2 hydration [3, 16]. Figure 3.3 shows the schematic representation of the stopped flow spectrophotometer.

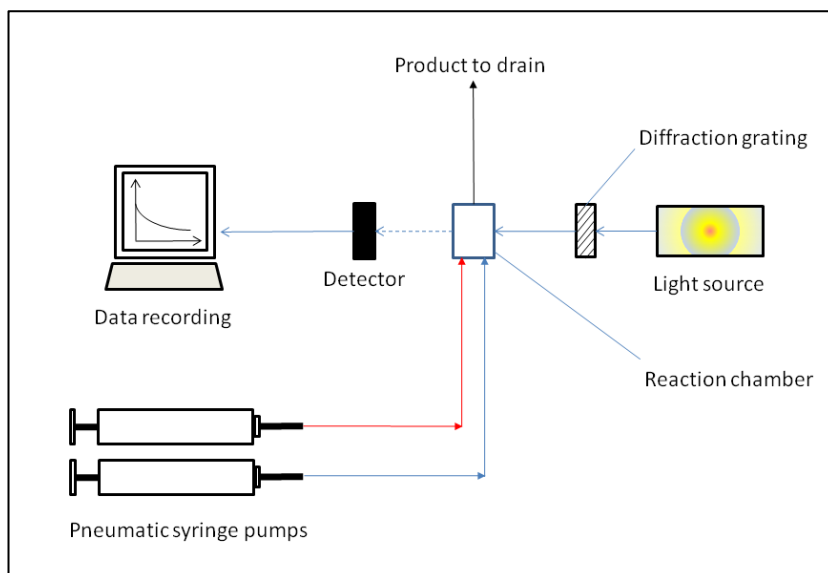


Figure 3.3 Schematic of the operation of stopped flow spectrophotometer [28-32].

The stopped flow spectrometer consists of two syringes operated by a pneumatic syringe pump that is connected to a mixing chamber fitted with UV-Vis optics and detector. During analysis, very small volume of the reactants are mixed in a small reaction chamber and the optical absorbance change with time, at a particular wavelength, is observed [17-21]. The wavelength is selected on the optical absorbance of the chemical, in this study a dye (Phenolphthalein) was used. The rate of optical absorbance change of the chemical compound during the reaction is recorded on the computer. The rate of change in absorbance can be fitted with an appropriate mathematical function to obtain the kinetic constant (or rate constant) of the reaction under observation [17-21]. In this study the change in absorption of phenolphthalein indicates the pH change which is monitored. Figure 3.4 shows an example of the change in the absorption of phenolphthalein data (empty circles) fitted with an exponential curve (solid line).

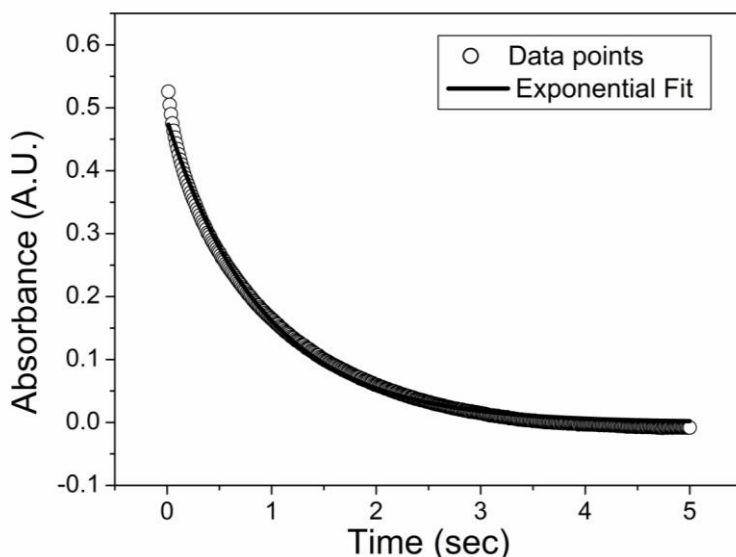


Figure 3.4 Example showing the fitting of the change in the absorbance of phenolphthalein (○) with an exponential function (solid line).

Wang *et al.* [16] recently reported a kinetic study on the hydration of CO_2 using the stopped flow spectrophotometry. The procedure used in this study using the stop flow spectrophotometry followed similar methodology to that of Wang *et al.* with a minor modification. Wang *et al.* used bromothymol blue to monitor the kinetics of the hydration reaction of CO_2 . We observed that bromothymol blue was adsorbed on the NiNPs surface blocking the reaction active sites. Therefore phenolphthalein was used as a dye in this study. As the saturation concentration of CO_2 increases in the presence of NiNPs, the NiNPs were added to the sodium carbonate solution. Various concentrations of sodium carbonate solutions were prepared (i.e. 8 mM, 16 mM, 24 mM, 32 mM and 36 mM) with and without 60 ppm of NiNPs. A saturated solution of CO_2 was prepared by bubbling CO_2 in DI water at 15 °C (38 mM concentration). The kinetic study is performed using the Applied Photophysics SX18MV stopped-flow spectrophotometer. The reaction kinetics is studied by rapid mixing of a given volume of CO_2 saturated solution with that of Na_2CO_3 (with varying

concentration 8-36 mM) in a 1:1 v/v ratio. Phenolphthalein was used as an indicator to follow the reaction kinetics and was monitored by change in colour at the wavelength of 553 nm. The data obtained from the equipment was then processed using Origin 6.1, using an exponential fit. The results obtained in this experiment are discussed chapter 5, section 5.2.

3.2.5.2 CO₂ hydration kinetics using pH change method by saturated CO₂ solution.

The most commonly used method for evaluation of catalytic activity of CA for CO₂ hydration is performed by mixing saturated CO₂ solution with buffer solution and monitoring the pH change (all ref in section 2.2.3.3). This is a qualitative method used for evaluation of the catalytic activity of immobilized or free CA (ref in table 2.4). The role of a buffer is to maintain pH of a solution by absorbing the H⁺ ion from the solution [8]. Therefore by monitoring the pH change a distinct quantitative evaluation of concentration of protonated buffer generated from buffer molecules cannot be determined, as the pH change is not directly proportional to the pH change for buffer solutions [8]. Therefore no quantitative evaluation of kinetics can be done using this method.

The Bis-Tris-HCl buffer was prepared by first mixing the 2,2-Bis(hydroxymethyl)-2,2',2''-nitrilotriethanol (Bis-Tris) buffer in DI water (0.1M), then the pH of the buffer was adjusted to 7 by adding (drop by drop) of concentrated HCl (11.6-12M) under continuous stirring. Bis-Tris-HCl buffer was chosen as the pH is regulated by the hydroxide terminal molecules of the buffer and the surface of NiNPs is also hydroxylated (section 4.4., chapter 4) limiting adsorption of buffer on NiNPs surface. 0.1M Na₂CO₃ solution was also prepared by mixing Na₂CO₃ in DI water. Saturated solution was made by bubbling CO₂ in

DI water for 4 hours until it saturates. The procedure for qualitative kinetic analysis was carried out by the procedure described by Mirjafari *et al.* [23]. 20 ml of Bis-Tris-HCl buffer (or Na₂CO₃ solution 0.1M) was taken in a 50 ml beaker. The pH of the solution was monitored using HI2500 pH meter (Hanna Instruments) in Log mode with data logging after every 5 sec. When the pH log gave 5 stable readings 20 ml of saturated CO₂ solution was added to the Bis-Tris-HCl buffer (or Na₂CO₃ solution 0.1M). The pH was recorded until a stable reading was observed. For the NiNPs catalyst run, 30 ppm suspension of Bis-Tris-HCl buffer (or Na₂CO₃ solution) was prepared and the above process was repeated for this solution.

3.2.6 Carbonate absorption of CO₂

Following the results obtained in the stop flow spectrophotometer experiment, absorption rate experiments were performed in potassium and sodium carbonate solutions. 0.1 M carbonate solutions were prepared by dissolving the required amount of carbonate salt in DI water. 30 ppm NiNPs-carbonate suspension was prepared by adding NiNPs in the prepared carbonate solution (potassium and sodium) followed by sonication for 5 min using ultrasonic bath (Hilsonic) at a constant temperature. The carbonate solution (with and without NiNPs) were then placed in a water bath at 20 °C and the procedure described in section 3.3.3 (CO₂ absorption in DI water and NiNPs) was followed. As the CO₂ reacts with the carbonate solution, the pH of the solution changes. The pH meter used to measure the pH changes was HI2550 (Hanna Instruments) with a computer data logger. The pH changes are recorded in time intervals of 10 sec. Results and discussion on this experiment are presented in chapter 5, section 5.4.

3.2.7 Synthesis of Nickel nanowires (NiNWs)

The NiNWs were prepared by the method demonstrated by Bentley *et al.* [24]. One side of the alumina membrane was painted with Galn paint. This blocked the pores of the membrane from one side and also formed a conductive layer to form the cathode. The membrane was then mounted on a copper plate using electrical insulation tape. This cathode assembly was then placed in a beaker containing solution of nickel coating mixture (solution of $\text{NiSO}_4 \cdot 6\text{H}_2\text{O}$ (300 g/l), $\text{NiCl}_2 \cdot 6\text{H}_2\text{O}$ (45 g/l) and boric acid (45 g/l)) along with a Ni wire as an anode. The cathode and anode were connected to an AA battery. The circuit was connected for 15 min where reduction of Ni^{2+} to Ni^0 takes place inside the pores and Ni from the wire leached into the solution as Ni^{2+} . After this the membrane is removed from the copper plate and the Galn paste is dissolved using concentrated nitric acid. The alumina membrane was then dissolved in 6 M NaOH solution liberating the NiNWs which were then washed several times with water followed with acetone washing.

3.2.8 Photocatalytic activity of nickel nanoparticles for hydration of CO_2

The proof of concept study to test any enhancement in the photocatalytic activity of NiNPs for hydration of CO_2 was performed in collaboration with Prof. W. Shangguan's group at Shanghai Jiao Tong University, P.R. China during my one month visit to the university to China.

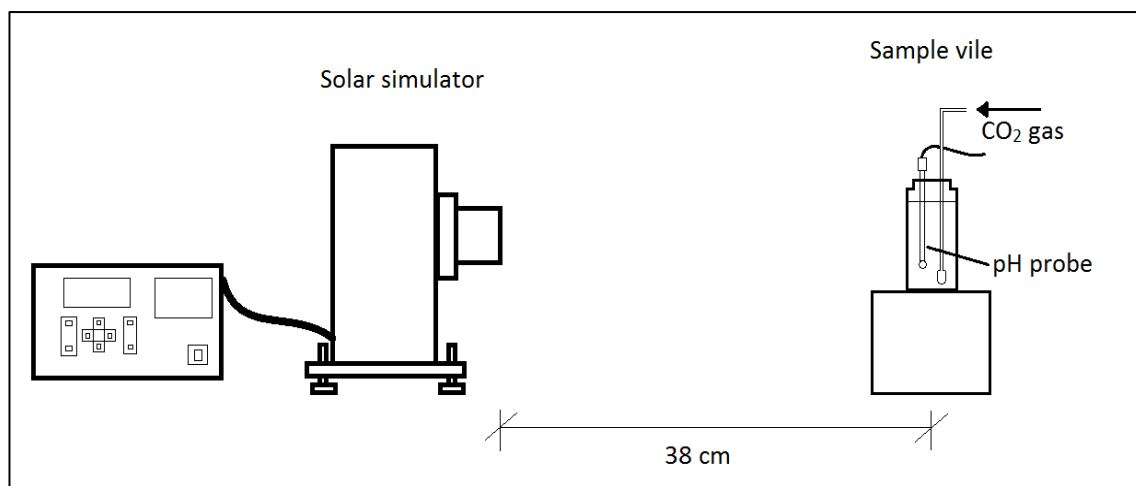


Figure 3.5: Experimental setup for the photochemical enhancement of NiNPs hydration of CO₂.

This experiment was repeated at Newcastle University. The solar simulator used for artificial sunlight was 150W (Xe Ozone Free) Xe arc lamp and an arc lamp power supply (Model 69907) from Oriel Instruments (Newport Corporation, UK). The power of the lamp was measured at the sample vial position (see figure 3.5) using a power meter (Thorlabs, Germany) measuring a band of wavelength between 535-1550 nm and had a power intensity of 47-50 mW/cm². An IR filter was brought from Oriel Instruments (Model 6117) to filter out the IR spectrum. The power of the lamp with the IR filter was measured at the sample vial position (see figure 3.5) and was 41-45 mW/cm² between the wavelength band of 535-1550 nm. Silica clear glass jars of 250 ml were used as a photo-reactor. The pH meter (HI2550) used was with a computer data logger. The pH measurements are recorded for every 10 seconds interval.

The experimental apparatus was setup as shown in figure 3.5. The distance between the light source and the sample was ~38 cm and was kept constant for all the experiments. The data log was started when the pH probe and thermocouple was introduced in DI water (or NiNPs suspension) and the

CO₂ gas was only introduced when the data log had a stable value for over 1 min. (For the ease of analysis the initial values have not been shown in the results.) The sample vile was cooled using a fan to reduce the effect of increase in temperature due to heat generated by the solar simulator. All the experiments were performed at a temperature of 20 ±2 °C. All the experiments were conducted in a dark room. Same procedure was followed for dark and light influenced (with and without IR filter) experiments.

It was found that the pH probe is extremely photosensitive due to the presence of Ag/AgCl reference electrode within the glass electrode. In several occurrences the pH would begin to rise in the experimental environment, the instance the lights inside the dark room were switched off for the dark environment prior to CO₂ introduction. The problem was resolved by calibrating of the pH meter under relative darkness (using only minimal light, i.e. from the LED of the laptop facing away from the pH meter) for the experiments requiring complete darkness or in presence of the solar simulator for those requiring light. Once calibrated under either of the conditions, it was easy to maintain the pH for the duration of the experiment.

After a steady pH value was observed (stable for 1 min) the CO₂ gas was introduced and the pH profiles recorded on the computer. The procedure for the pH profiles was same as that followed in section 3.2.3. The experiment was repeated eight times for individual sample i.e. catalytic and non-catalytic in the presence and absence of light and the mean of the results are discussed in the chapter 6 section 6.1. The computational analysis of the recorded data was done using Origin 6.1 (OriginLab Corporation) software.

3.2.9 Role of temperature on CO₂ hydration reaction

In order to study the influence of temperature on the CO₂ absorption rate in DI water (with and without NiNPs) the following study was performed. The experimental methodology was the same as used previously (as in section 3.2.3) with minor modifications. The CO₂ gas flow rate and the volume of liquid sample was kept same as in section 3.2.3. The temperature of the water bath was varied from 10 (± 1) °C, 20 °C, 40 °C and 60 °C. The maximum temperature was kept at 60 °C as it was below the allowable standards of 65 °C, which is the exit temperature of flue gas from the boiler exhaust [6, 25]. The pH changes were recorded using HI2550 pH meter. Detailed results and discussion on this experiment have been presented in chapter 6 section 6.2.

3.2.10 Calcium Carbonate precipitation experiment

After the experiments on uptake and absorption of CO₂ in DI water (with and without NiNPs) the effectiveness of the catalyst was examined by CaCO₃ precipitation. Similar experiment was tried by Favre *et al.* [1] for Carbonic Anhydrase. 200 ml of DI water (or 30 ppm NiNPs suspension) was taken in a 250 ml glass jar and was bubbled with CO₂ with a flow rate of 1.96 mM/min, at 0.1MPa pressure for 30 min, 1 hour, 2 hours and 4 hours respectively. To the respective CO₂ saturated samples were added 10 ml of 1 M NaOH solution and 10 ml of 0.5 M CaCl₂ solution. Gel formation was observed in the sample containing the NiNPs. The samples were filtered using a vacuum filter and air dried at room temperature for 24 hours. Both the obtained samples were then weighted after drying. Detailed results and discussion on this experiment have been presented in chapter 7 section 7.1 and chapter 8, section 8.3.

3.2.11 Absorption of CO₂ in potassium carbonate solutions

Potassium carbonate are the most commonly used absorbers for CO₂ separation [2]. There have been various enhancers used to enhance the absorption rate of K₂CO₃ solutions as discussed in chapter 2, section 2.3.3. Thus in order to study the influence of NiNPs on the absorption rate of CO₂ in K₂CO₃ solutions the following experiment was carried out. 50% (by weight) K₂CO₃ solution was prepared in 50 ml DI water. For the NiNPs suspension-K₂CO₃ solution, 1.5 mg of NiNPs was added into 50% K₂CO₃ solution and sonicated in the ultrasonic bath at constant temperature. The CO₂ absorption experiment was carried out in a 180 ml glass jar (Wheaton Industries, UK). The solution with the glass bubbler (Pyrex 1) was assembled and weighed before the introduction of CO₂. An initial proof of concept was carried out by bubbling CO₂ through the carbonate solution for 2 hours and then weighed. In another set of experiments the CO₂ was bubbled in the reaction mixture and the total weight of the reaction vessel was measured after the interval of 30 minutes. The CO₂ gas was bubbled at a flow rate of 1.69 mL/min at varying pressure between 0.1-0.2 MPa. The final weight was obtained when there was no further possibility of gas flow through the bubbler. The entire absorption experiment was carried out at 20 °C using a water bath (BS5, Fisher Scientific). This experiment was repeated with new bubbler i.e. an open end 6 mm ID fluoropolymer tubing (RS Components, UK). Detailed results and discussion on this experiment have been presented in chapter 7 section 7.2.

3.2.12 Heat treatment of Nickel Nanoparticles and effect on catalytic CO₂ hydration reaction

For the utilization of the carbonate solution for separation application it is the absorption is carried out at lower temperatures and desorption is carried out at higher temperatures [2]. Thus heat treatment of NiNPs was carried out. For the heat treatment, the NiNPs were placed in a silica crucible and heated in an oven at 150 °C for 8 hours. The NiNPs was kept in an air tight container with ample dessicator beads to absorb any moisture present until further use. Nickel does not oxidise at 150 °C [26] therefore not much changes in the properties of NiNPs would be observed. Similar procedure to that in section 3.2.3 was used to test the catalytic activity of heat treated NiNPs. Detailed results and discussion on this experiment have been presented in chapter 6 section 6.5.

3.2.13 Mineralization of CO₂ using gypsum and sodium chloride

The final part of this study was to design a process for the mineralization of CO₂ to CaCO₃. As seen in chapter 2 section 2.2.3.1 various mineral processes for mineralization of CO₂ are reported. The literature review indicated no reports on the use of natural gypsum as a alkali metal source for CO₂ mineralization, although flue-gas desulfurization (FGD) gypsum (i.e. an industrial waste) has been reported (table 2.1). Therefore the mineralization of CO₂ was performed by the conversion of gypsum (calcium sulphate, CaSO₄·2H₂O) to calcium carbonate. One of the major parameters that affect the precipitation of CaCO₃ is the pH of the solution as discussed in chapter 2 section 2.2.3.4. At a low pH, the dissociation of the HCO₃⁻ to CO₃²⁻ is low and thus no precipitation of calcium carbonate can be observed [23, 27]. Therefore

in order to avoid the lowering of pH to acidic values while precipitating CaCO_3 from CO_2 , a novel reactor has been designed (figure 3.6).

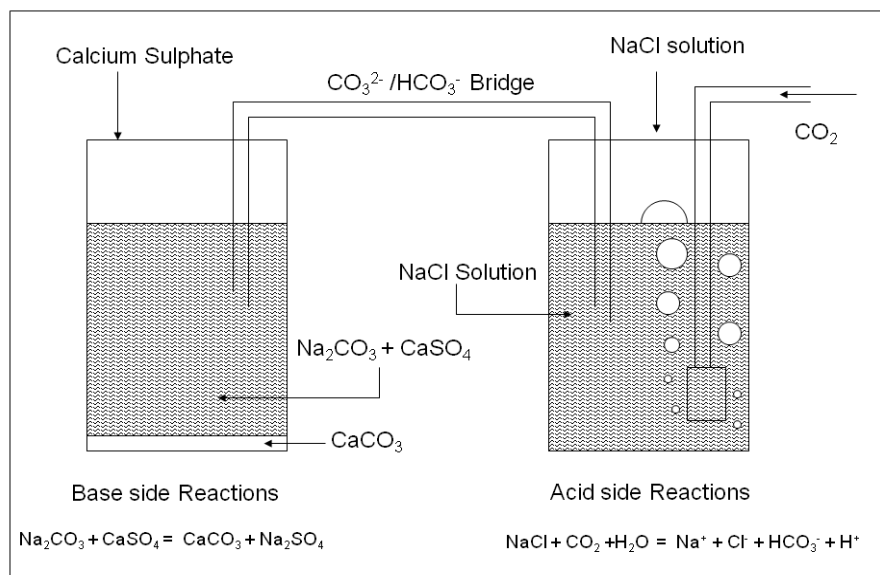


Figure 3.6: The experimental setup and chemical reactions involved for mineralization of CO_2 using gypsum and sodium chloride.

Figure 3.6 shows the schematic of the bridge reactor. The bridge reactor consists of two reservoirs, one acidic and the other basic. The names of the reservoirs are given with respect to the pH of the solution during the working of the reactor. On the side of the reactor where CO_2 enters the NaCl solution and the pH of the solution is lowered due to the generation of carbonic acid, is called the acid side. On the other side of the reactor, the pH of the solution is high due to the presence of sodium carbonate and is thus called the basic side. A salt bridge mechanism is used to transfer the ions ($\text{CO}_3^{2-} / \text{HCO}_3^-$ and Na^+) which move from the acid side to the basic side due to the concentration gradient.

The reactions associated with the process are follow:



The overall process utilizes the sodium ions from the sodium chloride act as the carriers of the bicarbonate ions from the acid side of the bridge to the base side of the bridge. The bridge consists of sodium carbonate solution. The role of the bridge is to facilitate the movement of ions from the acid side to the base side of the reactor. As reaction (6) proceeds, the concentration of the Na_2CO_3 decreases in the basic side of the bridge. At the same time carbonic acid is generated in the acid side of the reactor. The acid side of the reactor consists of NaCl solution. Thus the ions thus present in the acid side after carbonic acid is formed are H_3O^+ , Na^+ , Cl^- and HCO_3^- . It is expected that the ions would transfer from one side of the reactor to the other side due to the $\text{CO}_3^{2-}/\text{HCO}_3^-$ common ion effect. Thus as the concentration of the CO_3^{2-} ions tends to decrease the bridge would provide the CO_3^{2-} ions from the HCO_3^- for further precipitation of CaCO_3 .

The experimental setup consisted of two 250 ml glass jars connected with an inverted glass U tube. The glassware used was 250 ml glass jars (Weaton Industries) and a custom U tube was made by making a 90° bend on either ends of a $\text{Ø}4$ mm ID glass pipe of 25 mm distance between the bends. The total volume of the pipe is ~5 ml.

0.1 M sodium carbonate aqueous solution, 0.5 M sodium chloride aqueous solution and a 0.2 M calcium sulphate uniform aqueous suspension was prepared using deionised water. 100 ml of sodium carbonate solution and 100 ml of sodium chloride solution was taken in two 250 mL glass jars. 100 μL of phenolphthalein indicator was added in the sodium carbonate solution to check the pH of solution in the bridge. A bridge was put between the two solutions with use of a rubber bubble. Care was taken that the bridge contained only the sodium carbonate solution. Both the solutions (sodium chloride and

sodium carbonate) were placed on magnetic stirrers having the same elevation to maintain the hydrodynamic head within both the solutions. A control sample (for the reaction) of carbonate solution (100 mL) was kept on separated magnetic stirrer for comparison.

A gas sparger (Pyrex© Grade 1, porosity 100-150 μM ; Sigma Aldrich, UK) was added in the sodium chloride solution glass jar. The CO_2 gas was bubbled through the solution at a rate of 1.96 mol/min. To avoid the CO_2 bubbles entering the glass bridge, a PTFE partition was added between the gas sparger and the glass bridge inlet. The calcium sulphate suspension was stirred continuously to until no clustering of calcium sulphate were observed, thus providing a suspension with a uniform concentration.

1 ml of the calcium sulphate suspension was added to the control sample and the sodium carbonate base end of the bridge reactor every 5 min for 5 hours (i.e. total 60 ml of CaSO_4) and 1 ml of deionised water was added to the sodium chloride side of the bridge reactor using 2 ml plastic syringes. Care should be taken to inject/add the calcium sulphate and deionised water on the two sides of the bridge reactor at the same time to keep levels of liquid in the bridge the same at all times.

After the 5 hours the reaction was kept running with the CO_2 bubbling for another one hour. After that the bridge was lifted off and all its contents emptied into the carbonate reservoir. The control and the bridge reactor samples were then filtered using a vacuum filter and No 52 Wattman filter paper. During filtration the precipitate samples were carefully washed with deionised water to remove any sodium sulphate and/or calcium sulphate. The filtered samples were then dried for an hour at 60 $^\circ\text{C}$ and weighed. The weight

of the precipitate was used to calculate the yield. Detailed results and discussion on this experiment have been presented in chapter 7 section 7.2.

3.2.14 Validation of mass transport of ions in Bridge reactor:

Due to lack of experimental proof that mass transport of ions would occur in the bridge reactor (experimental methodology described in section 3.2.12) the current study was carried out to validate the hypothesis. In order to validate the mass transfer of material in the bridge reactor the following methodology was used. The similar experimental setup was used as mentioned in section 3.2.11. 0.1 M sodium carbonate solution was prepared and 100 ml of the solution was placed in both the glass jars. The bridge was set up with sodium carbonate solution in the bridge. 3 drops of phenolphthalein indicator was added on the right hand side glass jar and was stirred to give uniform pink colour. The movement of indicator dye would show how the mass transfer would proceed. A control sample was kept running simultaneously to compare the efficiency of the bridge reactor.

1 ml of 0.2 M calcium sulphate was added to the left hand glass jar and 1 ml of DI water was added into the right hand jar simultaneously after every 5 minutes for 5 hours. After every 1 hour photographic images of the experimental setup was taken (see chapter 10, section 10.3) in order to trace the movement of the indicator from right side of the bridge to the left side of the bridge. After 5 hours the bridge was removed and the solid sample (from the bridge and control reactors) was filtered using a vacuum filter and No 52 Wattman filter paper. The filtered sample was dried at 60 °C for 1 hour and then weighed. The weight of the precipitate was used to calculate the yield of CaCO_3 . Detailed results and discussion on this experiment have been presented in chapter 7 section 7.4.

As the experiment mentioned above proceeded the concentration in the right hand side of the bridge reactor decreased due to the dilution with added DI water. Therefore the experiment was again repeated and the stock solution of the right hand side of the bridge was changed to 0.3 M sodium carbonate solution to keep the concentration of carbonate on the right hand side higher than the left hand side. Another change made in this repeat was that during the carbonation reaction 1 ml of 0.3 M carbonate solution was added into the right hand side of the bridge reactor (instead of DI water in the previous case) in order to maintain a constant concentration on the right hand side of the bridge reactor throughout the reaction. Detailed results and discussion on this experiment have been resented in chapter 10 section 10.3.

3.3 Characterization Techniques

This section of the experimental methodology explains the various characterization techniques used during this study for chemical and physical characterization of the NiNPs, Fe₂O₃NPs, NiONPs and CaCO₃ precipitate samples. Transmission electron microscopy (TEM) scanning electron microscopy (SEM) and Dynamic light scattering (DLS) were used to morphological identification, whereas the chemical analysis was done using of X-ray diffraction spectroscopy (XRD), selected area electron diffraction spectroscopy (SAED), energy dispersive X-ray spectroscopy (EDX), X-ray photoelectron spectroscopy (XPS), Fourier transform infrared spectroscopy (FTIR), UV-Vis spectroscopy and zeta potential will be discussed in this chapter. Equipment details and related brief theory of the experimental method are described below.

3.3.1 High-Resolution and Transmission Electron Microscopy

Electron microscopes are high resolution electron device used to observe submicron details of the object using a high energy beam of electrons (100-200 keV for TEM and 300 keV for HRTEM) [29]. There are three major types of electron microscopes that are classified into transmission, scanning and emission.

Transmission electron microscopy (TEM) is a common technique used to observe structures (or materials) in the nanometer range. TEM can be used to observe particles that are as small as 1 nm [29] where as an HRTEM can give resolution up to 0.5 Å (i.e. 0.05 nm). It works on a similar principle as that of an optical microscope but utilizes a high energy electron beam with wavelengths of the order 0.001 nm (300 keV pass energy) to 0.01nm (100 keV pass energy) [30]. The image in the TEM is formed by the electron beam passing through the sample, thus in the resultant beam the electrons that did not interact with the sample travel with same velocity and direction, but the ones that interact with the sample there is a change in either one or both (i.e. velocity and direction). Therefore TEM can be used to get information about internal structures of thin films. The general thickness of sample required for TEM is 100 nm or lower [31]. In the case of HRTEM the atomic columns can be observed with sample of thickness between 5-20 nm [31]. As the electron are easily scattered than light by gases, thus high vacuum of 10^{-2} Pa is required.

The TEM or HRTEM is both a projection and a photomicroscope. As the image cannot be directly viewed by the eye being an electron image, it is projected on a fluorescent screen and then transferred to a photographic plate or paper, today it is recoded digitally using a computer using a charge-coupled device (CCD) camera. The beam of electrons are emitted by a pointed filament

in a vacuum chamber, which then passes through a series of condenser lenses then the sample followed by the objective lens and then is projected on the fluorescent screen enlarged by the projector lens [29]. Thus the principle of working of the TEM or HRTEM can be compared with an optical microscope. This can be seen in figure 3.7.

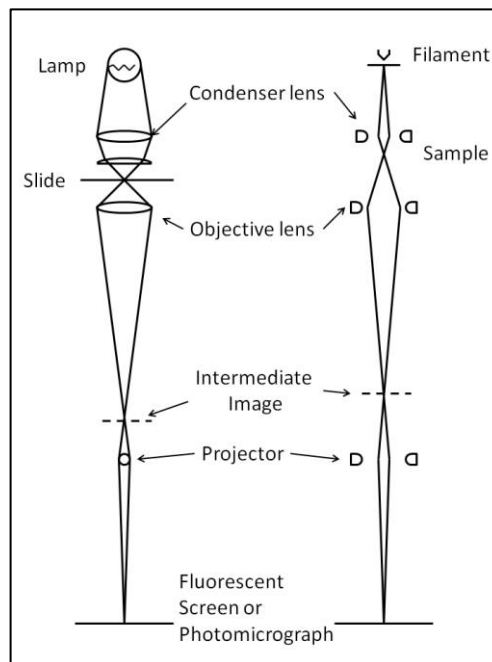


Figure 3.7: Light projecting microscope (left) and electron microscope (right) compared schematically [29]

The lenses used in the TEM or HRTEM are all electro-magnetic lenses and the objective lens, which is the main lens for TEM or HRTEM, has an aperture that is used to generate high resolution images [29]. The electron beam of the TEM or HRTEM can be used to determine the crystal lattice plains of the sample (using dark field mode) and also the chemical elemental composition of the sample (using Energy dispersive X-ray spectroscopy (EDX)). In a TEM the crystallographic details are studied by using electron diffraction pattern (see section 3.3.4) due to the low resolution of the technique. In HRTEM, the resolution of the image shows lattice planes of the atoms and the spacing for the atoms is measured from the bright field images directly and can be confirmed by the electron diffraction obtained for the same particle.

The HRTEM characterization for NiNPs is performed at Durham University, where as for Fe₂O₃NPs HR-TEM analysis is performed at University of Manchester and characterization of NiONPs carried out at Newcastle University using TEM. The particle size of the NiNPs was determined using a JEOL 2100F field emission gun transmission electron microscope (FEG TEM) instrument operating at 200 keV giving a 2.3 Å resolution, along with Gatan GIF tridium with 4 megapixel Ultrascan™ 1000 CCD camera used for energy filtered imaging. The HR-TEM samples of NiNPs were prepared by drop and dry method, on a 300 mesh Cu grid with lacey carbon film. In the drop and dry method one drop of a dilute NiNPs suspension is dropped on the Cu grid and then air dried. Results of the NiNPs analysis is and discussed in chapter 4 section 4.1, whereas for the Fe₂O₃NPs and NiONPs are discussed in chapter 5 section 5.4.1.

3.3.2 Scanning Electron Microscopy (SEM)

Scanning electron microscope is another electron microscopy technique that utilizes an electron gun for measuring the images of small dimensions (in the order of nanometers). In the SEM the image is formed on a LED screen that is synchronized with the electron probe as the electron beam scans the specimen surface [29, 32]. As compared to the TEM, the SEM provides the surface morphology of the specimen rather than the bulk of the specimen [29]. The similarity between the SEM and the TEM is that both utilize an electron for analysis and thus have the similar electron beam generation assembly, vacuum chamber, condenser and objective lens assembly [30]. The energy of the accelerated electrons in the SEM is about 2-40 keV as compared with that of the TEM (~80-200 keV).

When the electron beam is scattered from the surface of the specimen, various events will occur. Figure 3.8 shows the schematic of the event generated in the SEM. These events include secondary electron emission, backscattering of electrons, characteristic X-ray emission, Auger electron emission and emission of photons of various energies [29, 30, 32].

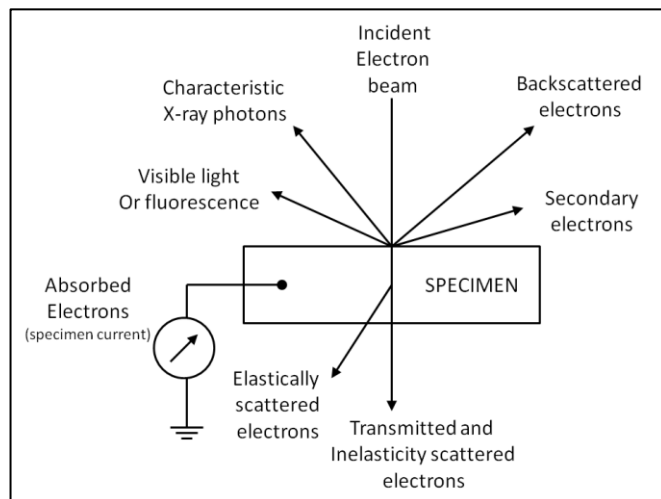


Figure 3.8: Signal type generated by electron-specimen interactions [29]

In a typical SEM instrument there is an electron gun to generate the electron beam that passes through multiple condenser lenses followed by the objective lens and then passing through the scan coil through an aperture of the final lens to the specimen [29]. Schematic diagram showing the main components of the SEM can be seen in figure 3.9 [29]. The secondary electrons emissions can be at various angles and are collectively used to generate the topographical image of the surface of the specimen [30]. The image of the specimen can be seen on the LED and the brightness of the spot can be modulated by amplifying the current of the detector [30]. The SEM images have many attributes contributing to visibility, resolution of a particularity, contrast, focus depth and morphology. Most striking feature of the SEM is that the secondary and backscattered electrons have a unique similarity and clarity with elevations and depressions as if the image has been produced by illuminating

the sample with an oblique stream of light [29]. At times, especially for biological samples where the electron beam may damage the sample it is coated with gold or carbon so that they are conductive and may emit electrons [33].

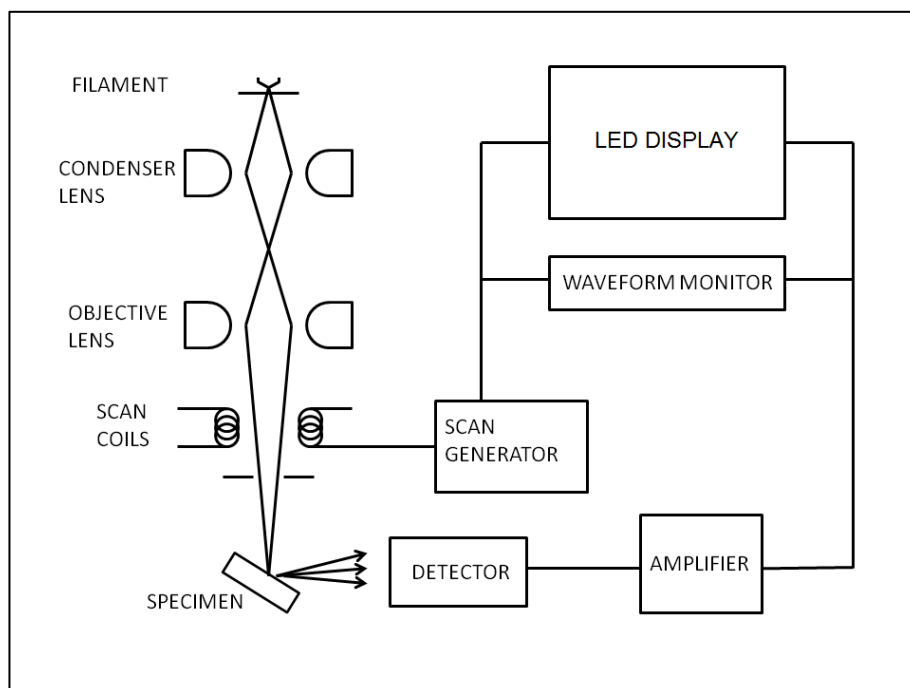


Figure 3.9: Schematic diagram showing the working of the SEM [30]

The SEM in this study is performed using an environmental scanning electron microscope (ESEM) at Newcastle University. The surface morphology of the calcium carbonate samples was carried out using Phillips XL30 ESEM-FEG (30 keV) having an operating pressure of 1.65×10^{-5} torr equipped with a wide angle detector (Everhart-Thornley detector) and EDX detector (FP6892/21). The calcium carbonate samples were dry power and were put on the aluminium stubs using carbon tape. Detailed results and discussion on this experiment are presented in chapter 6 section 6.1.

3.3.3 Energy Dispersive X-ray Spectroscopy

Energy dispersive X-ray spectroscopy (EDX) is an analytical technique that determines the elemental composition of a sample by exciting it with an electron beam and emission of characteristic X-rays [29, 30]. When the electron

beam strikes the solid surface it can penetrate the surface with both elastic and non-elastic scattering [34]. This electron beam can displace an electron from the core level creating an electron hole. An electron from the outer energy shell then fills this vacancy and the difference in energy of the shells is emitted as an X-ray. This X-ray is characteristic for relaxation between different shells of an element and is detected using an X-ray detector [32]. EDX can be carried out in both SEM and TEM using a Si(Li) solid-state X-ray detector [32]. These X-rays are then converted into an electrical signal with the help of a Si(Li) semiconductor (p-i-n type (i.e. p-type, intrinsic, n-type)) for interpretation. This electrical signal is then interpreted by peak determination and identification using a computer processor [32]. In the current study EDX was used during the HRTEM analysis of the NiNPs performed at Durham University. Results are discussed in chapter 4 section 4.1.

3.3.4 Selected Area Electron Diffraction

Selected area electron diffraction (SAED) is an analytical technique used to determine the crystal lattice planes of the sample [30]. SAED can be carried out in the TEM or HRTEM machine. The high energy electron beam is transmitted through the specimen (thin film) and the beam can either be projected on the fluorescent screen to show morphology (particle size) or can be diffracted by the specimen and projected in the form of a diffraction ring (for polycrystalline material) or spots (for single crystals). The SEAD pattern represents the data in reciprocal space.

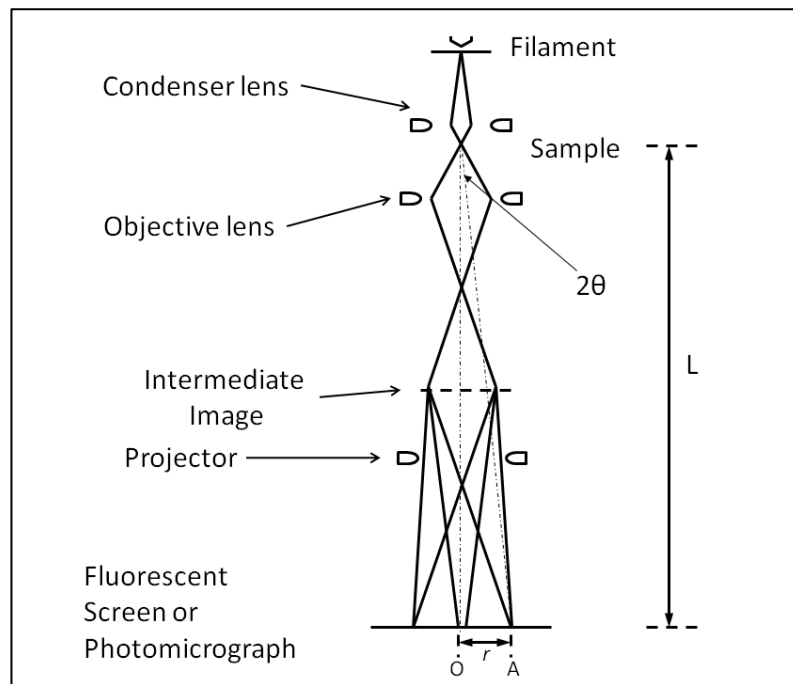


Figure 3.10: Schematic of the diffraction pattern obtained in SAED adapted from Rochow and Turner [29] and Goodhew and Humphreys[30].

The scattering of the electron beam from the specimen can be interpreted in a simplified form [30]. If the existence of the lenses is ignored then the ray diagram for the SAED can be simplified as shown in figure 3.10. Assuming that the sample is crystalline. Some of the electrons pass through the sample without interaction and are projected on the screen at point O. Some of the electrons are diffracted with an angle of θ by the crystal planes of the sample having an molecular spacing d . These electrons are projected on the screen at point A. The distance between point A and point O is r . Thus by simple geometric interpretation the angle of diffraction can be represented as

$$\frac{r}{L} = \tan 2\theta \approx 2\theta \quad \text{E 3.3}$$

In electron diffraction the wavelength of the electron beam is very small (1.97 pm for 300 keV) thus the angle θ is also small ($< 3^\circ$) [35]. Thus from Bragg's law, it can be deduced that [30]

$$\lambda = 2d\theta = 2d \sin\theta \quad \text{E 3.4}$$

Thus equating both these equations

$$\frac{r}{L} = \frac{\lambda}{d} \text{ or } rd = L\lambda \quad \text{E3.5}$$

L the length between the screen and the sample and λ the wavelength of the electron beam are constant and independent of the specimen. This $L\lambda$ is called as camera constant. Therefore the r is inversely proportional to the d atomic plane spacing of the specimen material and is a characteristic for a given material. Based on the d atomic plane spacing value the Miller indices of the material can be assigned using a database. It should be noted that L is not a physical distance it is a notional distance and can be adjusted by the microscopist [30].

In the current study the SAED diffraction of the NiNPs was carried out. The images were interpreted using the ImageJ programme for calculation of the d spacing. After the calculation of the d spacing, the Miller indices were assigned using the chemical database service (CDS) at Daresbury [36]. The SAED analysis was carried out for the NiNPs using HRTEM microscope at Durham University. Results and discussion on this experiment have been presented in chapter 4 section 4.1.

3.3.5 X-ray Diffraction

X-ray diffraction (XRD) is a technique used for the determination of the crystal lattice structure of a material. The principle working of this technique is based on Bragg's law which is summarized as

$$n\lambda = 2d \sin \theta$$

E 3.6

where λ is the wavelength of the monochromatic x-rays, d is the distance between n layers of atoms in a crystal ($n= 1, 2, 3\dots$) and θ is Bragg's angle. In x-ray diffraction spectroscopy a beam of x-rays, of known wavelength, is diffracted from a crystal surface and the Bragg's angle is measured. Based on this the d-spacing of the particular material can be calculated [37].

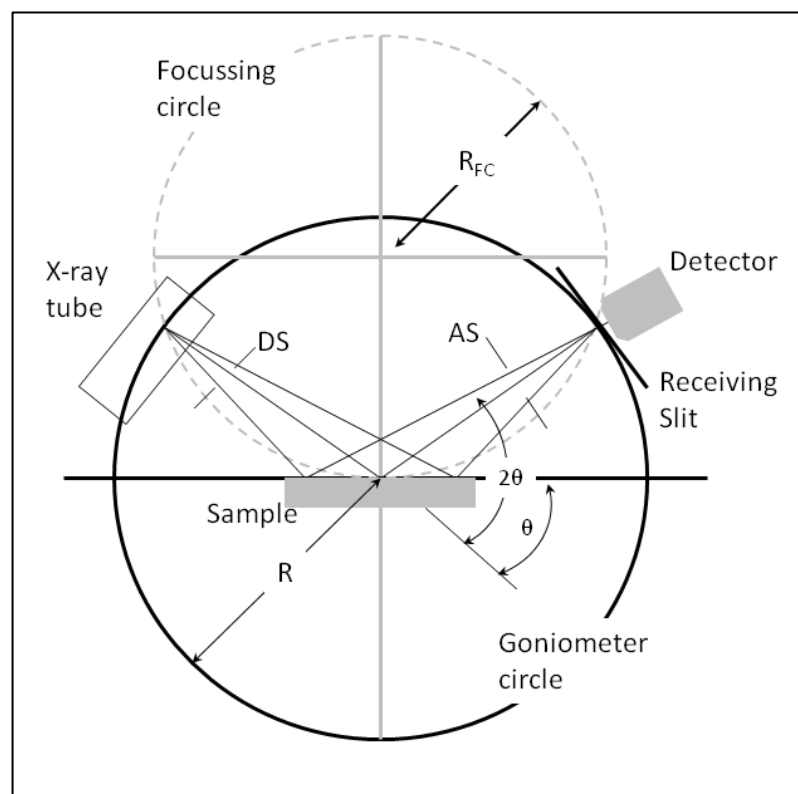


Figure 3.11 Schematic representation of $\theta/2\theta$ diffraction in Bragg-Brentano geometry [38]

When the monochromatic X-ray photons impinge on the crystal surface they are diffracted from the crystal and are detected in the detector. The crystal is placed at an angle of θ from the incident beam, and the detector is placed in

a particular angle of 2θ so that it can be rotated across the point of contact between the incident beam and the crystal (figure 3.11). The X-ray beam and the detector are arranged positioned along the circumference of a goniometric circle. The sample is placed at the centre of the goniometric circle. The XRD equipment used in Newcastle University (details below) works on the operation where the sample is fixed but the X-ray beam and the detector work in clockwise and anticlockwise manner along the goniometric circle (figure 3.11) with an angle θ with respect to the sample simultaneously. The rotation is done by a goniometer.

The X-ray beams cannot be easily be refracted due to the limitation of lack of focusing lenses as in the case with optics. Therefore apertures are used to condition the $\theta/2\theta$ X-ray beams using slits and aperture (like divergence slit (DS) and anti-scatter (AS) in figure 3.11), which may be termed as shadow casting optics. One of the other parameters that has to be considered in powder diffraction is the divergence of the X-ray beam emitted from the X-ray source. Therefore powder diffraction equipment work on the Bragg-Brentano or parafocusing mode. In this configuration the focusing circle is defined by placing the X-ray source and detector along a focusing circle that is tangent to the sample surface (figure 3.11). True focusing would only occur if the sample is bent at the radius of the focusing circle R_{FC} , that is not possible; as the R_{FC} is a variable dependent on the scattering angle 2θ . Therefore true focussing cannot be achieved in the $\theta/2\theta$ scan and the arrangement is thus termed as parafocusing geometry.

The diffracted rays may be in phase with the incident wave or out of phase. When the incident and the diffracted waves have a constructive

interference the interplanar distance can be calculated. This is due to the fact that the time required for the wave to travel to the detector and the path length travelled can be associated with the d spacing by the equation $\Delta = d_{hkl} \sin \theta$ where Δ is the path difference. In the case of constructive interference $2\Delta = n\lambda$ where n is an integer and λ is the wavelength of the incident wave. Simple mathematical association of this leads to Bragg's law $n\lambda = 2d_{hkl} \sin \theta$. The Miller indices of the lattice can be assigned to the respective d spacing by using a database [37-39].

The XRD of the NiNPs and calcium carbonate precipitate is carried out at Newcastle University (Advanced Chemical and Materials Analysis Unit). The instrument used for XRD is a PANalytical X'Pert Pro MPD, powered by a Philips PW3040/60 X-ray generator and fitted with an X'Celerator* detector. The X'Celerator is an ultra-fast X-ray detector that uses RTMS (Real Time Multiple Strip) technology. It operates as an array of a hundred channels which can simultaneously count X-rays diffracted from a sample over the range of 2θ angles specified during a scan. The X'Celerator is therefore able to give produce high quality diffraction data in a significantly shorter time period than an older style diffractometer would require. The diffraction data is acquired by exposing powder samples to Cu-K α X-ray radiation, which has a characteristic wavelength (λ) of 1.5418 Å. X-rays were generated from a Cu anode supplied with 40 kV and a current of 40 mA.

The data were collected over a range of 0-100 ° 2θ with a step size of 0.0167 (for NiNPs) and 0.0334 (for CaCO₃ samples) ° 2θ and nominal time per step of 200 sec, using the scanning X'Celerator detector (hence the counting time per step). Fixed anti-scatter and divergence slits of 0.38 mm were used

together with a beam mask of 10mm and all scans were carried out in 'continuous' mode.

Phase identification was carried out by means of the X'Pert accompanying software program PANalytical High Score Plus in conjunction with the ICDD Powder Diffraction File 2 Database (2001), ICDD Powder Diffraction File 4 - Minerals (2013), the American Mineralogist Crystal Structure Database (March 2011) and the Crystallography Open Database (February 2013; www.crystallography.net)

3.3.6 X-ray Photoelectron Spectroscopy

X-ray photoelectron spectroscopy (XPS) is a technique commonly used in surface science studies of solids and especially in heterogeneous catalysis [40, 41]. In heterogeneous catalysis it is used for identification of chemical species on the solid surface and prediction of reaction mechanism [41]. When high energy photons (i.e x-rays or UV) interact with the electrons of the atoms on the solid surface, electrons are emitted (photoemission). The binding energy of these ejected electron is related to the energy of the incident photon. The emitted electrons include core level, valance and secondary electrons [41]. Hofmann [42] suggest that the photoemission consists of a series of three steps (1) the X-rays interact with the electrons of the atoms and photoelectrons (and Auger electrons) are generated, (2) these electrons then travel through the bulk of the solid to the surface subjected to various scattering within the solid (inelastic scattering), (3) the electrons that reach the surface are then emitted to vacuum after surpassing the threshold work function.

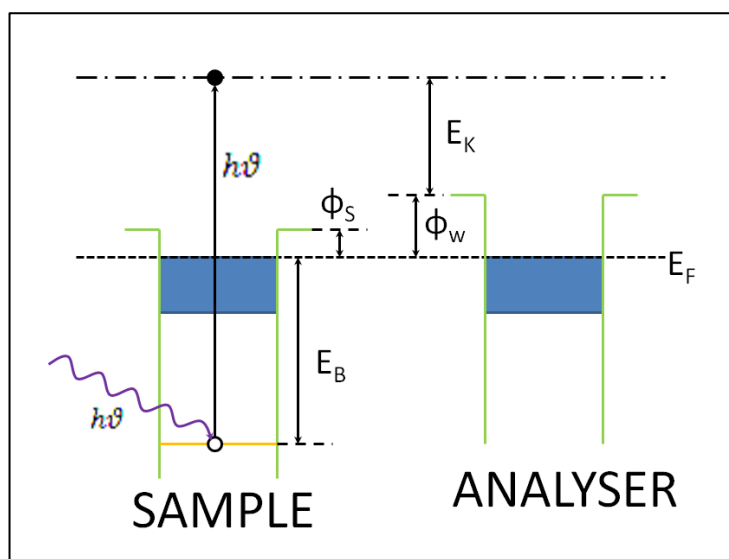


Figure 3.12 Schematic explaining relevant energy terms in XPS of solid surfaces. An X-ray (of energy $h\nu$) generates a vacancy in the core electron in solid sample having a binding energy of E_B . The emitted electron has to overcome the work function ϕ_s of the sample and the energy is measured by the analyser with reference to the Fermi energy E_F of the emitted electron diminished by the work function ϕ_s and ϕ_w [42].

Figure 3.12 shows a schematic derivation of the photoelectron kinetic energy from the energy levels. The kinetic energy of the emitted photoelectron can be determined using Einstein equation [41-43]

$$E_B = h\nu - E_K - \phi_w \quad \text{E 3.7}$$

where E_B is the binding energy of the atom, E_K is the kinetic energy of the emitted photoelectron, $h\nu$ is the photon energy and ϕ_w is the work function of the analyser. The characteristic X-ray transfers its energy $h\nu$ to the electrons in the atom with a binding energy E_B (with reference to the Fermi level E_F). This electron, upon gaining the energy, is emitted from the solid have a kinetic energy that is gives as

$$E_K = h\nu - E_B - \phi_s \quad \text{E 3.8}$$

where ϕ_s is the work function of the sample. As ϕ_w is the work function of the detector and therefore the kinetic energy measured by the detector is given as

$$E_K = h\nu - E_B - \phi_s - (\phi_w - \phi_s) \quad \text{E 3.9}$$

that can be rearranged to equation E 3.8. After calibration the work function becomes zero and can thus be ignored from the equation [42] considering the sample and analyser have same Fermi level.

The photoemission of the electrons is an inelastic process as the photoelectron suffers energy loss from atom in the sample and detection by the analyser. The secondary electron emission due to inelastic photoemission leads to a generation of the background at the higher binding energy of the spectrum [44]. The electrons having kinetic energies in the range of 15-1000eV have a very short mean free electron path in matter ($< 10\text{\AA}$) [45]. The binding energy of the electron is sensitive to the atomic identity of the element [45]. For example the binding energy of Ni $2p_{3/2}$ is different in different oxidation states: Ni^{3+} (856.1 eV) $>$ Ni^{2+} (854.6 eV) $>$ Ni^0 (852.6 eV) respectively [46]. The surface specific elemental information can thus be evaluated from kinetic energy of the electrons emitted from the solid after photo (or electron) irradiation.

The intensity of the measured electrons depends on the escape depth of the emitted photoelectron from within the solid surface. This intensity is given by the function [42]

$$I = K \int_0^{\infty} \phi(z, E_i, E_p, \alpha) \psi(z, E_p, \theta) dz \quad \text{E 3.10}$$

where ϕ is the excitation depth distribution function, dependent on the angle of incidence of photons (α), the overall depth of emission (z), ionization potential (E_i), their primary incident energy (E_p), and ψ is the emission depth distribution function dependent on the overall depth of emission (z), kinetic energy of the generated photoelectron (E_p), and the emission angle (θ). The excitation depth

distribution function (ϕ) is strongly dependent on the depth of the photoelectron emission. This makes XPS a surface sensitive method [42].

Upon interaction with the sample the X-ray photons ejects photoelectrons from core or valence levels of the sample that have to escape without any inelastic collisions within the matrix lattice of the sample. The flux of the escaping photoelectrons from the depth (z) of the sample matrix without inelastic collision decays as $\exp(z/\lambda \cos\theta)$ from the point of origin z , and where λ is the inelastic mean free path (IMFP) and θ is the angle of emission normal to the surface. IMFR is defined as "the mean distance an electron travels before engaging in an interaction in which it experiences an energy loss" [42]. The term $\lambda \cos\theta$ is referred to as escape depth. The values of λ range from 2-10 atom layers shown in the figure 3.13 [45, 47]. Although X-rays (or high energy electrons) can penetrate solid sample up to relatively large depths ($\sim 1-3 \mu\text{m}$), but the generated photoelectrons can only escape from the depth of a few nanometers ($\sim <5 \text{ nm}$) [34, 42]. This makes XPS a surface sensitive analysis technique.

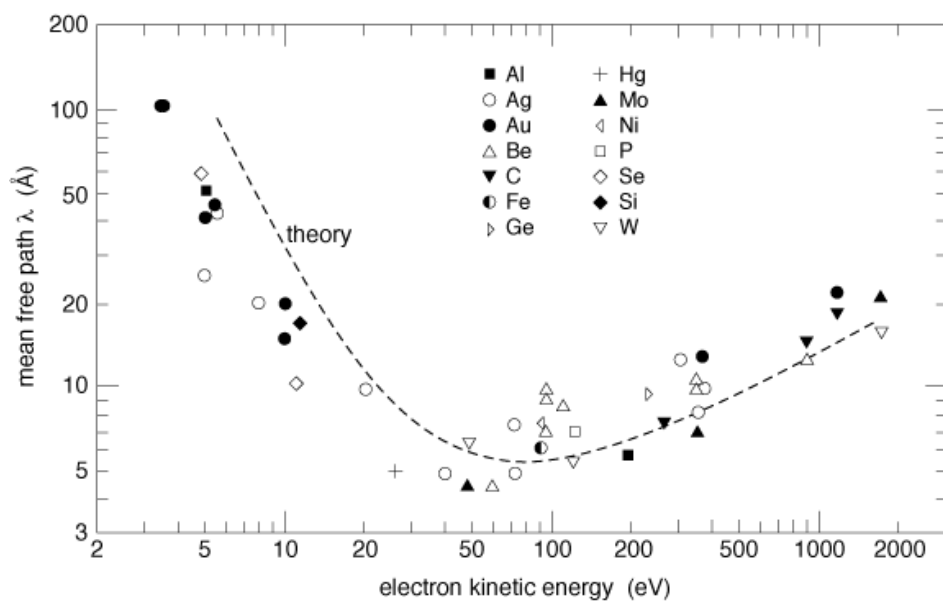


Figure 3.13 Universal curve of electron inelastic mean free path (λ) dependence on electron energy for different elements [47]

The XPS spectra are denoted as a plot of intensity (counts per second) as a function of binding energy. The peaks therefore observed in the XPS spectral plot consists of three different types of peaks that include peaks due to photoemission from the core and valence levels and peaks due to Auger emission excited by X-rays [44]. The binding energy values for some compounds are provided in handbooks and can be used for the determination of the particular compound [42]. There are chemical shifts observed in the spectra of the atoms due to different bonding environments, in particular, on the oxidation states of the atom [41]. XPS can also be used to observed solid state excitations (like interband transition, plasmons etc) [44]. These solid state excitations can be analysed analysing the shape of the spectral line. For example when the photoelectron is emitted from the solid sample there is an increase in the nuclear charge. This leads to the rearrangement of the valence electrons, which may involve excitation of one or more of the valence electrons to higher unfilled levels. The primary photoelectron is void of this transition and the two electron process leads to the formation of a discrete peak on the low KE of the photoelectron spectrum. This is known as a satellite peak and is very strong in some transition metals and rare earth metal [44].

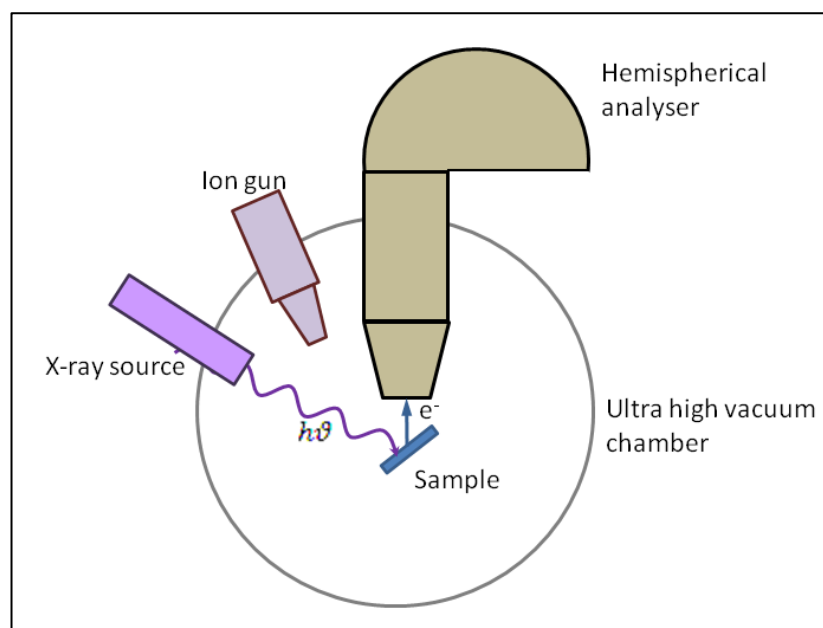


Figure 3.14: Schematic of a conventional XPS machine [42].

Figure 3.14 shows the schematic of the conventional XPS machine [42]. The XPS machine consists of four major parts an X-ray source, an Ar ion gun, ultra-high vacuum (UHV) chamber and a concentric hemispherical electron analyser (CHA). The monochromatic X-rays source is preferred for XPS analysis as it reduces satellite peaks and selects a natural emission [42]. UHV chamber a pressure upto 10^{-1} Pa ($\sim 10^{-3}$ Torr) is used so as to have negligible gas molecules in the chamber and its mean free path becomes equal to that of the chamber [42]. The CHA is used more commonly for detection of the kinetic energy of the electrons due to its superior energy resolution and areal transmission. The CHA consists of two concentric hemispheres where is a high potential applied between the two hemispheres. The emitted photoelectron from the sample travels along a semi-circular path before being detected by the detector. The potential between the two hemispheres helps determine the kinetic energy of the electron particles and the detector (Delay-line detector (DLD)) then sends the signal that can be taken as a graph on the computer [42, 43].

In the current study XPS was used to determine the surface groups present on the surface of the NiNPs before and after bubbling of CO₂. Also it was used to observe the changes on the surface after heat treatment on the NiNPs. The NiNPs for heat treatment were put on a carbon tape mounted on Si substrate. The other samples were prepared by dropping the NiNPs (from aqueous sedimentation) on Ta wafer and then air dried. Similar procedure was used for XPS analysis of Fe₂O₃NPs and NiONPs. The XPS analysis was carried out in an X-Ray Photoelectron Spectrophotometer (Kartos Axis Ultra 165) equipped with a monochromatic Al K α X-ray source at Newcastle University in the Nanoscale Science and Nanotechnology group. The pass energy used was 20 eV for specific regions (i.e. C1s, O1s etc) and 80 eV for survey spectrum.

The XPS data was analysed using WinSpec© software. The spectrum was fitted with Shirley Background [48] and Gaussian-Lorentzian (mixed) singlet [49] peak lines. All the spectra were calibrated by assigning the first peak of the C 1s peak line to 284.8 eV corresponding to amorphous carbon [50]. For the NiNPs samples the background was subtracted and the fitting was done using mixed singlets. The Fe2p peaks were fit using mixed doublet. XPS results of the catalysis of NiNPs are discussed in chapter 4 section 4.4 and the XPS results of the heat treated NiNPs are discussed in chapter 7 section 7.5. The XPS analysis of Fe₂O₃NPs and NiONPs are discussed in chapter 5 section 5.4.

3.3.7 Fourier Transform Infrared Spectroscopy

Fourier Transform Infrared spectroscopy (FTIR) is an experimental technique that measures the infrared absorption of a material. FTIR is based on the interaction of infrared light (IR) with material. FITR equipment operate on three energy ranges i.e. near IR ($\lambda=0.8-2.5 \mu\text{m}$), mid IR ($\lambda=2.5-25 \mu\text{m}$), far IR

($\lambda=25-1000 \mu\text{m}$) [51]. The IR light does not have enough energy to split a molecule. When a compound absorbs infrared light its chemical bonds vibrate close to an equilibrium position (symmetric and asymmetric stretching) due to the increase in its energy. This is because of the change in dipole moment of the molecule. This is a selection rule for IR spectroscopy [52].

In FTIR a beam of light containing many frequencies is passed through the sample at once. The amount this light absorbed by the sample is then measured. The beam of light is then modified to contain a different range of frequencies and the process is repeated. The computer is then used to record and work out the absorbance at different wavelengths. An interferometer is used to obtain a light beam of variable frequency. Fourier transform (mathematical process) is used to convert the raw data obtained from the interferometer to generate the FTIR spectrum.

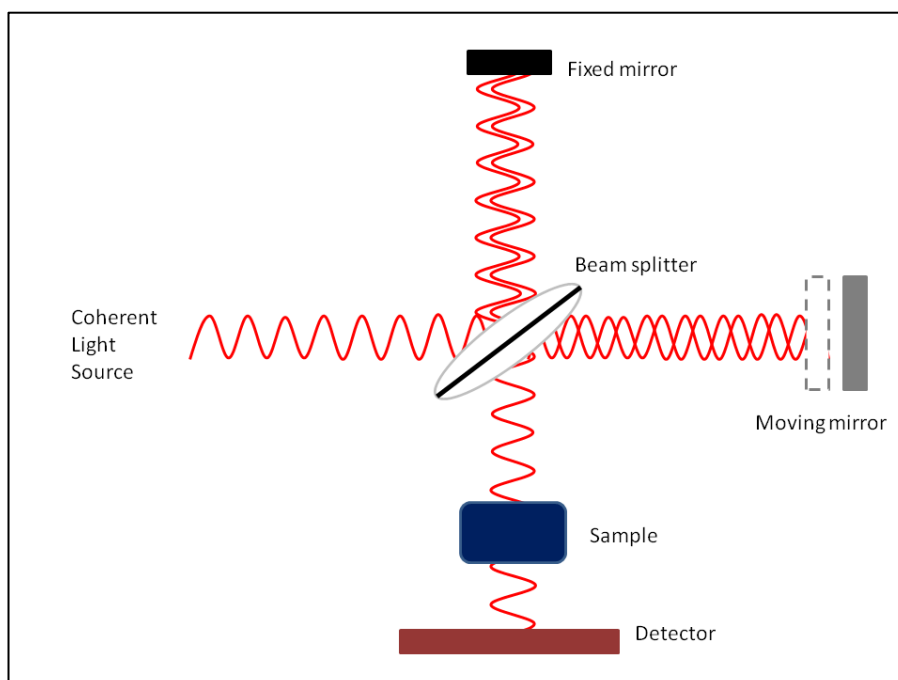


Figure 3.15: Schematic of the working of the FTIR [52].

Figure 3.9 shows the schematic of a typical FTIR interferometer [52]. The interferometer consists of an coherent IR light source ($\lambda=2.5-25 \mu\text{m}$), beam

splitter, a moving and fixed mirror assemble, sample holder and detector. The coherent beam of light is split into two beams by the beam splitter and the two rays of light are directed to the fixed mirror and moving mirror. Based on the position of the moving mirror there can be a constructive or destructive interference of the incident beam of light. This is then again recombined in the beam splitter and the recombined beam then passes through the sample to the detector (photoionic detector). The interferometer is used to record the spectra in length domain rather than in frequency domain.

The intensity of the incoming wave to the detector is given by the equation [51]

$$I(\delta) = \int_0^{\infty} B(\omega) \cos 2\pi\omega\delta \, d\omega \quad \text{E 3.11}$$

where δ is the wavelength of the incoming wave to the detector, $I(\delta)$ is intensity the length domain spectrum, ω is the wavenumber and $B(\omega)$ is the source intensity at that wavenumber. Fourier transform is used to convert the wavelength domain intensity (E3.11) recorded by the detector to the wavenumber domain (E3.12) [51].

$$B(\omega) = 2 \int_0^{\infty} I(\delta) \cos 2\pi\omega\delta \, d\delta \quad \text{E 3.12}$$

A wide number of wavenumbers is emitted by the IR source for adsorption in the IR absorption experiment. The dedicated computer is used to convert the signal to the data point display. The equipment used to convert the signal to the data is called as an interferogram. The final data is then converted to a FTIR spectrum. Figure 3.16 shows an example of conversion of interferogram data to FTIR spectrum.

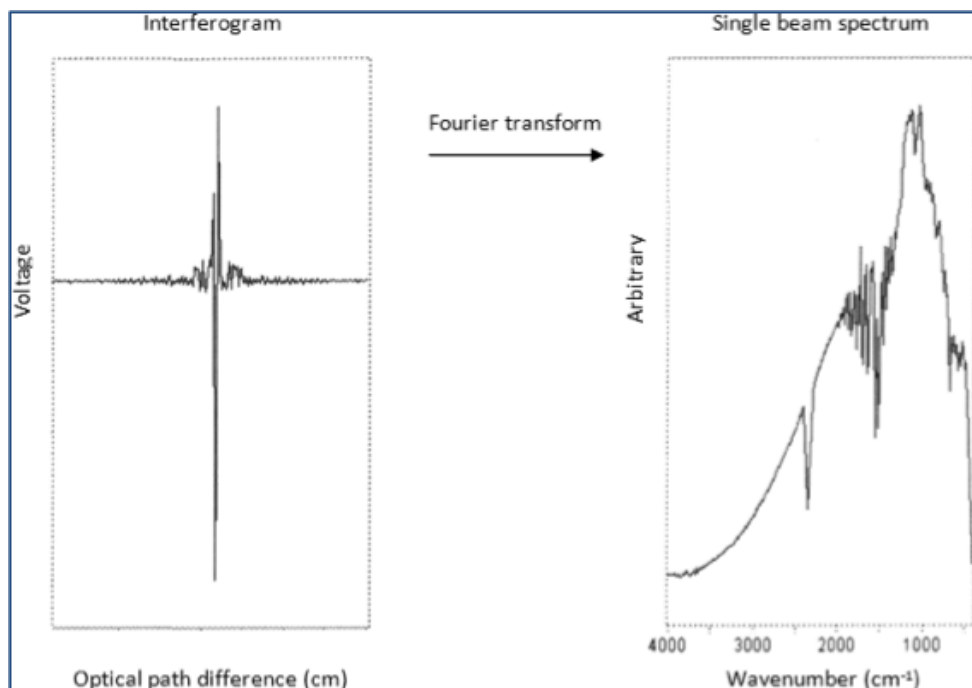


Figure 3.16 Example of Fourier transform used for conversion of interferogram data to FTIR spectrum [53].

The vibrations observed in molecules excited by IR radiation are stretching or bending vibrations collectively called as modes of vibrations (figure 3.17) [52]. The mode of vibration in which there is a change in the bond length is termed as stretching vibration and when there is a change in bond angle is termed as bending vibration. Based on the structure of the molecule in consideration the stretching vibration can be symmetric or asymmetric and depending on the angle of movement of the molecular rearrangement its bending vibration can be in-plane (scissoring and rocking) or out-of-plane (wagging and twisting) (seen in figure 3.17) [54].

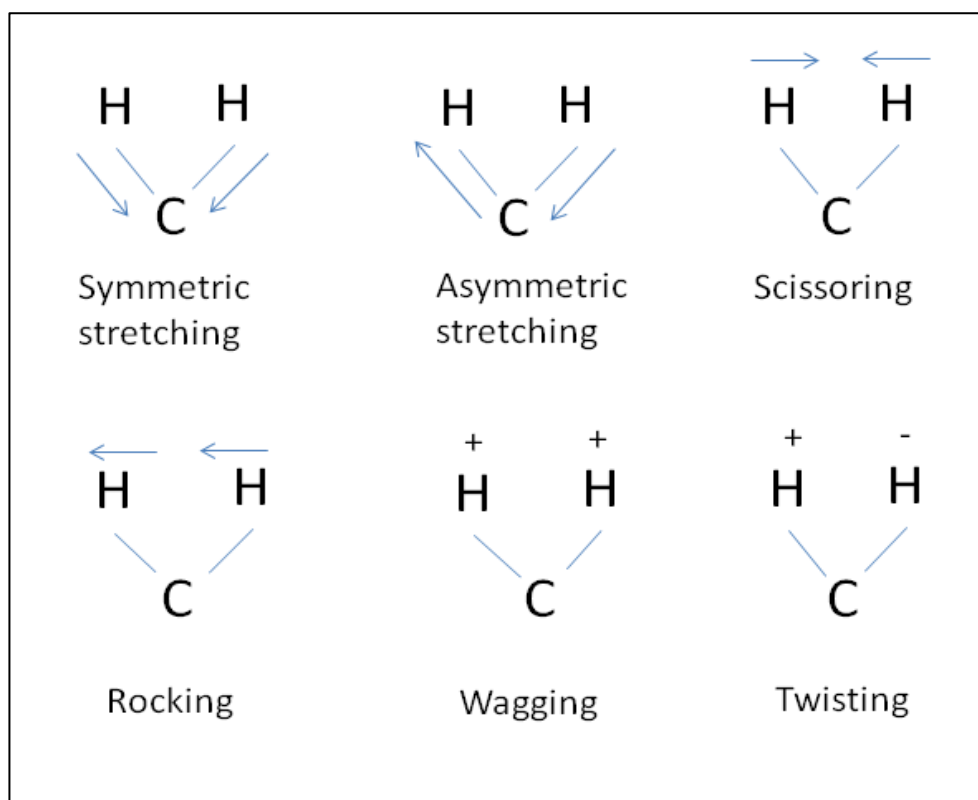


Figure 3.17 Various vibrations observed in a molecule on absorbance of IR light. The carbon atom is bonded to other atoms in the molecule (to have four bonds) not shown in figure. The figure also does not show the recoil of the C atom, which is necessary but is very small as compared to movement of the light H atoms [51, 52].

The CaCO₃ samples were characterised using a Varian 800 Scimitar Series FTIR over the range of 700–4000 cm⁻¹ at the School of Chemistry, Newcastle University. The CaCO₃ samples were prepared by washing the samples obtained in the mineralization experiments (section 3.2.11) and used as solid. The results are presented in chapter 7 section 7.3.

3.3.8 Dynamic Light Scattering

Dynamic light scattering is an analytic technique used to measure particle size of suspended solids in a solvent. It works on the principle of scattering of light from the surface of suspended particles [55]. The suspended material in solvent, its size and shape leads to fluctuations and changes in the frequency, angular distribution, polarization and intensity of the scattered light. This information can be used, in accordance with electrodynamic theory and

time dependent statistical mechanics to obtain structural and molecular information about the suspended solids.

The two major theories used for the development of DLS are Rayleigh's theory and Mie theory. Rayleigh's theory is formulated to model the scattering of light from particles, smaller than the wavelength of the incident electromagnetic wave. Rayleigh's theory considered non-absorbing dielectric characteristic of the material, Mie extends the theory to the absorbing and non-absorbing dielectric material and had no size limitation for the particles, converging to the geometry of the optics [55]. The criterion for Rayleigh's scattering is defined by considering a dimensionless parameter $\beta = 2\pi r/\lambda$ where r is the radius of the particle and λ is the wavelength of the incident electromagnetic wave. The electric field associated with the wave is given as

$$E = E_0 e^{i(\mathbf{k}\cdot\mathbf{r}-\omega t)} \quad \text{E 3.13}$$

where \mathbf{k} is the wave vector with the magnitude of $k = \omega/c = 2\pi/\lambda$ and ω is the frequency. The incident and scattered wave (i.e. \mathbf{k}_i and \mathbf{k}_s) for practical applications are characterized as elastic scattering of light to the horizontal plane so the magnitude of the vector is unaffected (i.e. $k_i = k_s = 2\pi/\lambda$). The polarization of the light is also considered in the analysis.

This consideration can be used to derive the *Rayleigh ratio* $R(\theta)$ under two conditions of β . The first one is for particles smaller than the wavelength of light where $\beta = 2\pi r/\lambda \ll 1$ and $n\beta \ll 1$. The second being where the particles are larger and $|n - 1| \ll 1$ and $2\beta|n - 1| \ll 1$, assuming that the incident light beam that generates the dipole is unaffected (either in phase or in magnitude) by the presence of the particles. Where the refractive index ratio $n (= n_p/n_m)$ is

defined as the refractive index of the particle material n_p to that of the suspending medium n_m [55].

In the first case the *Rayleigh ratio* $R(\theta)$ is defined by the equation

$$R(\theta) = CKMP(\theta) \quad \text{E 3.14} \quad \text{where} \quad K = \frac{4\pi^2 n_m^2}{\lambda^4 N_A} \left(\frac{dn_s}{dC} \right) \quad \text{E 3.15}$$

C is mass concentration $C = N_p M / N_A$ and n_s is the refractive index of the suspension of the particles (particles and medium combined), M is the molar mass of the particle, N_p is the number of suspended particles, $P(\theta)$ is a function dependent on the polarization of the incident and scattered light for scattering angle θ .

In the second case the *Rayleigh ratio* $R(\theta)$ is defined as $R(\theta) = CKMP(\theta)$ but for practical purpose is written as

$$\frac{CK}{R(\theta)} = [MP(\theta)]^{-1} = \frac{1}{M} \left[1 + \frac{16}{3} \frac{\pi^2 n_m^2}{\lambda_0^2} a_G^2 \sin^2(\theta/2) + Q^4 \right] \quad \text{E 3.16}$$

where a_G is radius of gyration of particle, Q is the scattering vector defined as $Q = 2 k \sin(\theta/2)$ and λ_0 is the wavelength of light in vacuum.

These equations used to describe the intensity I of the scattered light having frequency ω is given by [55]

$$I(\omega) = A_1 \frac{DQ^2}{(\omega - \omega_0)^2 + (DQ^2)^2} \quad \text{E 3.17}$$

where ω_0 is the frequency of the incident radiation, A_1 is a constant, D is diffusion coefficient and Q is the magnitude of the scattering vector given as [55]

$$Q = (4\pi n_m / \lambda_0) \sin(\theta/2) \quad \text{E 3.18}$$

The autocorrelation function used to characterize the time dependent intensity function of the scattered light at a particular angle θ [56]

$$c(Q, \tau) = \lim_{t_k \rightarrow \infty} \frac{1}{\int_{t_{k0}}^{t_k} I(Q, t) \cdot I(Q, t + \tau) dt} \quad \text{E3.19}$$

where $\tau = i \Delta t$ is the delay time, representing the time delay between two signals $I(Q, i\Delta t)$ and $I(Q, (i + j)\Delta t)$. The equation E3.19 shows how the autocorrelation function is calculated when the intensity of the scattered light is measured in discrete time intervals [56]. Figure 3.18 shows the autocorrelation decay graph, the scattering intensity of light with time and the particle size of dispersed particles.

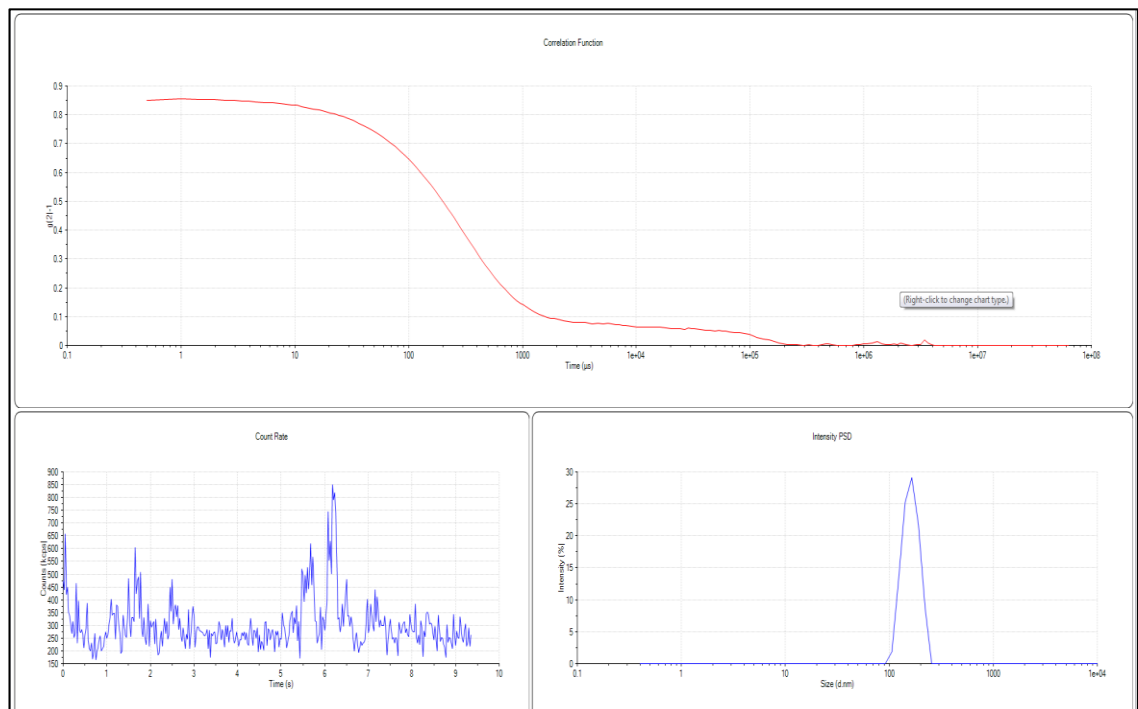


Figure 3.18 Autocorrelation function obtained from the varying intensity of light obtained in the dynamic light scattering experiment from Zetasizer Nano ZS (Malvern, UK). (autocorrelation function on top, time dependent intensity on bottom left and particle size distribution on bottom right.)

The particle size can be determined by using Stoke-Einstein equation [55]

$$r = kT/6\pi\eta D \quad \text{E 3.19}$$

where η is the viscosity of the suspending medium, T is the temperature and k is Boltzmann's constant.

The experiments for DLS measurements is performed at Newcastle University using Zetasizer Nano ZS (Malverin, UK). 1 ml of sample was used for analysis in plastic cuvettes. The suspension was prepared by suspending the nanoparticles in DI water (10 ml) with further dilution. The NiNPs were sonicated for 5 min just before the DLS measurements. The results of the DLS measurements are discussed in Chapter 4.

3.3.9 Zeta potential measurement

When particles are in solution due to the interaction with the solvent the surface of the particles may store charge. If the particles are charged it develops an electric bilayer on its surface. Nanometer sized particles in solution are in random motion called as Brownian motion [55]. When the particles in suspension is subjected to a spatially uniform electric field, due to the presence of the electrochemical bilayer on the surface of the particles the charged particle would travel towards the oppositely charged electrode. This phenomenon is called as electrophoresis (i.e. the motion of dispersed particles relative to a fluid under the influence of a spatially uniform electric field). If the solid remains stationary and the charge at the adjoining solid-liquid interface moves under the influence of an electric field, this phenomenon is called as electro-osmosis.

Using the electrophoresis approach it was shown that the velocity of particle v in the applied electric field E is given by the equation [55]

$$v = [\epsilon\zeta/\eta]E \quad \text{E 3.20}$$

where ϵ is the permittivity, η is the viscosity of the suspending medium and ζ is the zeta potential. The zeta potential is dependent on the thickness of the bilayer (κ_a) on the surface of the particles. When particles are suspended in a solvent they acquire a surface charge due to formation of bilayer, these charged particles are subjected to an external electric field then velocity of the particle is given by the equation [55]

$$v = \mu_e E \quad \text{E 3.21}$$

where μ_e is the electrophoretic mobility. The electrophoretic mobility is related to zeta potential as [55]

$$\mu_e = \epsilon\zeta/\eta \quad \text{E 3.22}$$

This condition is only applicable to the particle when particle dimension is much larger than the thickness of the surface bilayer. This process can be applied to the DLS measurements by superimposing to the Brownian motion of the particles. If an electric field is applied to the particles in the DLS experiment, the particle would drift under the influence of the electric field causing the Doppler shift and broadening.

The intensity spectrum shifts along the frequency axis in this case and the shift is given by the equation [55]

$$Q \cdot v_e = Q \cdot v_e \cos\left(\frac{\theta}{2}\right) = Q \cdot \mu_e E \cos\left(\frac{\theta}{2}\right) \quad \text{E 3.23}$$

where θ is the scattering angle and Q is the scattering vector ($Q = (4\pi n_m / \lambda_0) \sin(\theta/2)$). This shows that as the shift becomes smaller as the scattering angle becomes larger. Therefore the resolution of the method is defined as a ratio of Doppler shift ($Q \cdot v_e$) to the Doppler broadening (DQ^2) [55]

$$R = \frac{Q \cdot v_e}{DQ^2} = \frac{|v_e|}{DQ} = \frac{\mu_e \lambda_0 E}{2\pi n D \tan \theta} \quad \text{E 3.24}$$

when θ is small $\tan \theta \approx \theta$. Therefore small colloidal particles move in phase when an electric field is applied at frequency values in the kilohertz range.

The zeta potential measurements were carried out at Newcastle University using Zetasizer Nano S (Malvern, UK). 1 ml of sample was used for analysis in plastic cuvettes. The suspension was prepared by suspending 30 ppm NiNPs in DI water (10 ml) with and without CO₂. The NiNPs suspension was saturated using dry ice (BOC, UK). The results of the zeta potential measurements are discussed in Chapter 4.

3.4.10 UV-Visible spectroscopy

UV-Vis spectroscopy is an analytical technique used to study the absorption or transmission of light from a liquid sample. It works on the principle of Beer-Lambert's law given by the equation [57]

$$T = \frac{I}{I_0} = e^{-\epsilon lc} \quad \text{E 3.25}$$

where I and I_0 are intensity of transmitted and incident radiation respectively, ϵ is the attenuation constant, l is the path length of light or path travelled by light within the sample and c is the concentration of the component. The absorbance of the sample can be calculated by the equation

$$A = -\ln\left(\frac{I}{I_0}\right) = -\ln\left(\frac{1}{T}\right) = \epsilon lc \quad \text{E 3.26}$$

The absorbance of the UV-Vis light may be due to change in the electronic and vibrational states of molecules or the energy state of the electrons of solid particles. For the study in the thesis, the interaction of the free conduction electrons on the surface of metallic particles with electromagnetic radiation, known as surface plasmonic resonance (SPR), has been studied. Surface plasmonic resonance is characteristic of the particle size and the material of the particle. Noble metals like gold and silver have a strong SPR due to the interactive oscillation of the conduction electrons under the influence of the electromagnetic field of light (figure 3.19).

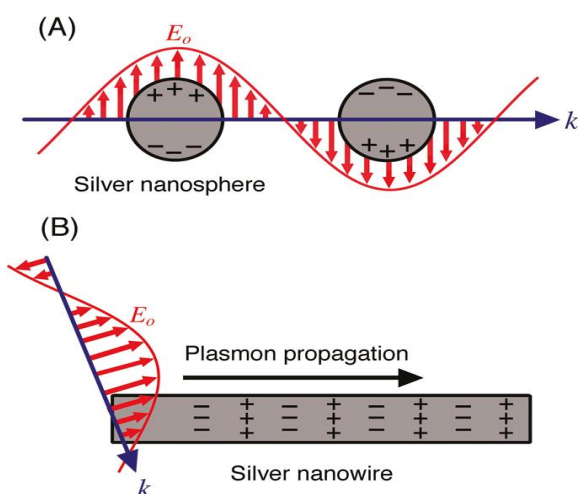


Figure 3.19: Surface plasmonic resonance observed in silver nanoparticles and nanorods influenced by the incident electromagnetic field [58]

The SPR can be described by Mie theory for the excitation on a spherical nanoparticle given by the equation [58, 59]

$$C_{ext} = \frac{24\pi^2 R^3 \epsilon_m^{3/2}}{\lambda} \left[\frac{\epsilon_i}{(\epsilon_r + 2\epsilon_m)^2 + \epsilon_i^2} \right] \quad \text{E 3.27}$$

where C_{ext} is the excitation cross section, R is the radius, ϵ_m is the dielectric constant of the dispersing media and ϵ_r and ϵ_i are the real and imaginary part of the dielectric constant of the metallic nanoparticle that may vary with the

excitation wavelength λ . The SPR strength can be described using the quality function Q

$$Q = \frac{w(d\varepsilon_r/dw)}{2(\varepsilon_i)^2} \quad \text{E 3.28}$$

The surface plasmonic strength is directly related to Q ; for the high Q values the SPR is high with high C_{ext} as in the case of silver and gold nanoparticles [58, 59] whereas Q is low in the case of NiNPs [60].

The UV-Vis spectroscopy was performed at Newcastle University using a Spectrostar Nano, BMG Labtech, UK. The analysis was carried out with 30 ppm NiNPs suspension, prepared by suspending 3 mg of NiNPs in 100 ml of DI water. The results of UV-Vis spectroscopy are discussed in Chapter 6.

3.4.11 Surface area determination of nanoparticles

The surface area of catalyst is an important factor in heterogeneous catalysis [61, 62]. It provides the active surface area where the surface reaction taking place. The most commonly used technique for surface area determination is Brunauer-Emmet-Teller (BET) method [63, 64]. This method allows comparison surface areas of various materials based on benchmarks of some standard materials like alumina or silica with a known surface area [65, 66].

The basic assumptions for the BET adsorption is that multi layers of the adsorbate can be adsorbed on the surface as compared to the rigid adsorption layer used in the Langmuir adsorption isotherm [67]. BET assumes that the net amount of surface that is empty or associated with the monolayer, bilayer and so on is constant at a particular equilibrium condition [67]. It is assumed that the rate of adsorption is proportional to the rate at which the gas molecule strikes

the adsorbent surface and the area of the adsorbent surface. The BET isotherm in its final form is given as [67]

$$\frac{V_s}{V_s^1} = B_2 \frac{P}{P_0} \frac{[1-(n+1)(P/P_0)^n + n(P/P_0)^{n+1}]}{(1-P/P_0)[1+(B_2-1)(P/P_0) - B_2(P/P_0)^{n+1}]} \quad \text{E3.29}$$

where V_s is the total volume of the adsorbent and V_s^1 is the specific volume of the adsorbent contained in a single monolayer. (P/P_0) is the relative pressure of the adsorbent gas and P_0 is the saturated vapour pressure of the gas and B_2 is a constant. Nitrogen is a gas commonly used for physical adsorption and surface area determination [67]. n is the number of atomic layers adsorbed on the surface. If $n = 1$ then equation E3.29 reduces down to Langmuir adsorption isotherm, but when $n = \infty$ then $(P/P_0)^n$ tends to approach zero and thus the equation E3.21 can be written in linear form as

$$\frac{P/P_0}{V_s(1-P/P_0)} = \frac{1}{V_s^1 B_2} + \frac{B_2-1}{V_s^1 B_2} \left(\frac{P}{P_0}\right) \quad \text{E3.30}$$

The plot of $\left(\frac{P}{P_0}\right)$ and $\frac{P/P_0}{V_s(1-P/P_0)}$ if is a linear plot then the adsorption is said to be determined by n^{th} order BET isotherm (or infinite form of BET). The plot of these two terms may lead to formation five different types of graphs seen in figure 3.20 [68].

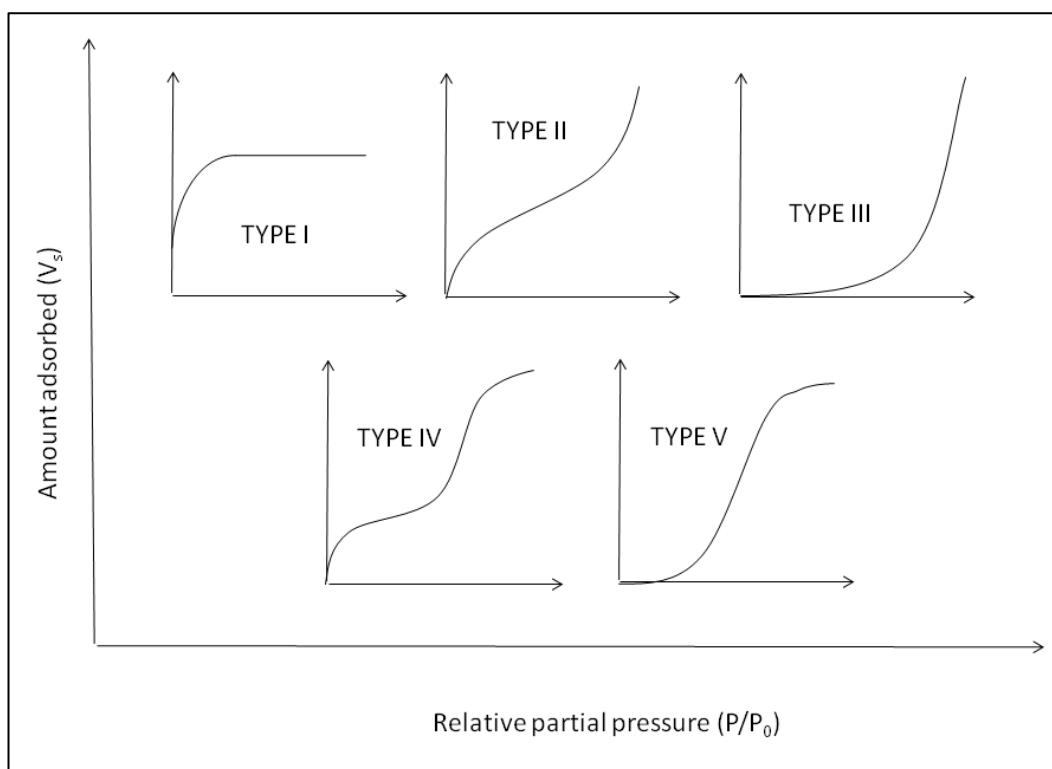


Figure 3.20: Different isotherms obtained from BET isotherm where there abscissa represents the relative partial pressure of the adsorbent (P/P_0) and the ordinate represents the amount of adsorbent adsorbed on the surface (reproduced similar to that reported by Brunauer *et al.* [68])

The possibility of prediction of the shape of the isotherm for a given material is not possible, although some shapes of the isotherms are observed to be often associated with a particular adsorbent or adsorbate properties [67]. Type I and Type II are the most commonly observed isotherm and the type II isotherm is used for determination of the surface area of minute particles. Most non-porous solids tend to show the type II isotherm, whereas materials having minute porosity like charcoal [67] (where is porosity is a few molecules in diameter) type I isotherm is observed. When the cohesive forces of the between the adsorbent molecules is greater than the adhesive forces of the adsorbent surface and adsorbate molecules then type III (non-porous material) and type V (porous materials) isotherms are observed [67]. Type IV isotherm is a special case that is distinctive for a given adsorption system e.g. water adsorption on

alumina surface [67]. In this isotherm curve a concave region is observed at low gas concentration due to monolayer adsorption of gas on the surface followed by a convex region where the multilayer formation is observed and then followed again by a concave region where condensation of the adsorbent takes place in the pores of the adsorbate [67]. By plotting the linear form of the BET in infinite form the V_s and the V_s^1 can be determined from the plot and resultant ratio of the two terms provides the surface area of the particles [67].

The BET analysis was carried out at Newcastle University using SURFER (Thermo Fisher Scientific). The results of the BET analysis are summarised in table 3.1

Nanoparticle material	Surface area (m ² /g)
Nickel	10.25
Iron(III) oxide	31.24
Nickel oxide	26.55
Nickel nanowires	4.66

References:

- [1] N. Favre, M.L. Christ, A.C. Pierre, Biocatalytic capture of CO₂ with carbonic anhydrase and its transformation to solid carbonate, *Journal of Molecular Catalysis B: Enzymatic*, 60 (2009) 163-170.
- [2] P.V. Danckwerts, *Gas Liquid Reactions*, McGraw Hill Publishers, New York, 1970.
- [3] D.M. Kern, The hydration of carbon dioxide, *Journal of Chemical Education*, 37 (1960) 14.
- [4] J.M. Smith, H.C.A. Van Ness, M.M., *Introduction to Chemical Engineering Thermodynamics*, McGraw Hill Publishers (International Edition), 2005.
- [5] G.A. Bhaduri, L. Šiller, Nickel nanoparticles catalyse reversible hydration of carbon dioxide for mineralization carbon capture and storage, *Catalysis Science & Technology*, 3 (2013) 1234-1239.
- [6] D.-H. Kim, M. Vinoba, W.-S. Shin, K.-S. Lim, S.-K. Jeong, S.-H. Kim, Biomimetic sequestration of carbon dioxide using an enzyme extracted from oyster shell, *Korean J. Chem. Eng.*, 28 (2011) 2081-2085.
- [7] R.M. Noyes, M.B. Rubin, P.G. Bowers, Transport of Carbon Dioxide between the Gas Phase and Water under Well-Stirred Conditions: Rate Constants and Mass Accommodation Coefficients, *The Journal of Physical Chemistry*, 100 (1996) 4167-4172.
- [8] V.L.J. Snoeyink, David, *Water Chemistry*, John Wiley & Sons, New York, 1980.
- [9] L.K. Doraiswami, M.M. Sharma, *Heterogeneous reactions: Analysis, Examples and Reactor Design*, Volume 2, John Wiley & Sons, New York, USA, 1984.
- [10] N. Hernández, R. Moreno, A.J. Sánchez-Herencia, J.L.G. Fierro, Surface Behavior of Nickel Powders in Aqueous Suspensions, *The Journal of Physical Chemistry B*, 109 (2005) 4470-4474.
- [11] N. Kitakatsu, V. Maurice, C. Hinnen, P. Marcus, Surface hydroxylation and local structure of NiO thin films formed on Ni(111), *Surface Science*, 407 (1998) 36-58.
- [12] L.L. Shreir, R.A. Jarman, G.T. Burstein, *Corrosion Volume 1 Metal/Environment Reactions*, in, Butterworth Heinemann, London, 1994, pp. 4:122-124:123.
- [13] B. Beverskog, I. Puigdomenech, Revised Pourbaix diagrams for nickel at 25–300 °C, *Corrosion Science*, 39 (1997) 969-980.

- [14] P. Drodten, Carbonic acid, in: M.R. Schutze, Raul B., R. Bender (Eds.) Corrosion resistance of nickel and nickel alloys against acids and lyes, Wiley-VCH, Weinheim, 2014, pp. 31.
- [15] S. Piticharoenphun, Investigation into the availability of man-made nanoparticles and their interaction with exposed sea urchin (*Paracentrotus lividus*), PhD Thesis, Newcastle University, Newcastle upon tyne, 2013, pp. 224.
- [16] X. Wang, W. Conway, R. Burns, N. McCann, M. Maeder, Comprehensive Study of the Hydration and Dehydration Reactions of Carbon Dioxide in Aqueous Solution, *The Journal of Physical Chemistry A*, 114 (2009) 1734-1740.
- [17] D.R. Reyes, D. Iossifidis, P.-A. Auroux, A. Manz, Micro Total Analysis Systems. 1. Introduction, Theory, and Technology, *Analytical Chemistry*, 74 (2002) 2623-2636.
- [18] B. Chance, Rapid and Sensitive Spectrophotometry. III. A Double Beam Apparatus, *Review of Scientific Instruments*, 22 (1951) 634-638.
- [19] B. Chance, Rapid and Sensitive Spectrophotometry. I. The Accelerated and Stopped-Flow Methods for the Measurement of the Reaction Kinetics and Spectra of Unstable Compounds in the Visible Region of the Spectrum, *Review of Scientific Instruments*, 22 (1951) 619-627.
- [20] B. Chance, V. Legallais, Rapid and Sensitive Spectrophotometry. II. A Stopped-Flow Attachment for a Stabilized Quartz Spectrophotometer, *Review of Scientific Instruments*, 22 (1951) 627-634.
- [21] A. Gomez-Hens, D. Perez-Bendito, The stopped-flow technique in analytical chemistry, *Analytica Chimica Acta*, 242 (1991) 147-177.
- [22] G.A. Bhaduri, R.A. Henderson, L. Šiller, Reply to the 'Comment on "Nickel nanoparticles catalyse reversible hydration of carbon dioxide for mineralization carbon capture and storage"' by D. Britt, *Catal. Sci. Technol.*, 2013, 3, DOI: 10.1039/C3CY00142C, *Catalysis Science & Technology*, 3 (2013) 2197-2198.
- [23] P. Mirjafari, K. Asghari, N. Mahinpey, Investigating the Application of Enzyme Carbonic Anhydrase for CO₂ Sequestration Purposes, *Industrial & Engineering Chemistry Research*, 46 (2007) 921-926.
- [24] A.K. Bentley, M. Farhoud, A.B. Ellis, A.-M.L. Nickel, G.C. Lisensky, W.C. Crone, Template Synthesis and Magnetic Manipulation of Nickel Nanowires, *Journal of Chemical Education*, 82 (2005) 765.
- [25] A.N. Alekhovich, N.V. Artem'eva, V.V. Bogomolov, Allowable gas temperature at outlet from furnace subject to slagging, *Power Technol Eng*, 41 (2007) 105-110.
- [26] R. Haugsrud, On the high-temperature oxidation of nickel, *Corrosion Science*, 45 (2003) 211-235.

- [27] J.N. Butler, Carbon dioxide equilibria and their applications, Lewis Publishers, Chelsea, 1991.
- [28] L. Šiller, G.A. Bhaduri, Carbon Storage, World Patent WO2013/171480 (A2), 2013.
- [29] T.G. Rochow, P.A. Tuncker, Introduction to Microscopy by means of Light, Electrons, X-rays or Acoustics, Plenum Press, New York, 1994.
- [30] P.J. Goodhew, F.J. Humphreys, Electron microscopy and analysis, Taylor & Francis Ltd, London, 1992.
- [31] J.G. Thomas, Thomas, Analytical Transmission Electron Microscopy: An Introduction for operators, Springer Netherlands, Netherlands, 2014.
- [32] J.I. Goldstein, D.E. Newbury, P. Echlin, D.C. Joy, A.D. Romig Jr, C.E. Lyman, C. Fiori, E. Lifshin, Scanning Electron Microscopy and X-Ray Microanalysis: A text for Biologists, Material Scientist and Geologists, Plenum Press, New York, 1992.
- [33] J.B. Pawley, J.T. Norton, A chamber attached to the SEM for fracturing and coating frozen biological samples, Journal of Microscopy, 112 (1978) 169-182.
- [34] M.P. Seah, Quantification of AES and XPS, in: D.S. Briggs, M. P. (Ed.) Practical Surface Analysis, Volume 1 Auger and X-ray Photoelectron Spectroscopy, Chichester, 1990, pp. 201-251.
- [35] K.W.D. Andrews, D. J. , S.R. Keown, Interpretation of Electron Diffraction Patterns, Plenum Press, New York, 1967.
- [36] CDS, Chemical Database Service, Daresbury, <https://cds.dl.ac.uk/>
- [37] B.D. Cullity, Elements of X-ray diffraction, Addison-Wesley Publishing Company, INC, Reading, 1978.
- [38] M. Birkholz, Thin film analysis by X-ray scattering, WILEY-VCH Verlag GmbH and Co. KGaA, Weinheim, 2006.
- [39] V.K. Pecharsky, P.Y. Zavalij, Fundamentals of powder diffraction and structural characterization of materials, Springer, New York, 2009.
- [40] T.L. Barr, Applications of Electron spectroscopy to Heterogeneous Catalysis, in: D. Briggs, M.P. Sean (Eds.) Practical Surface Analysis by Auger and X-ray Photoemission Spectroscopy, John Wiley & Sons, New York, 1983.
- [41] K.W. Kolasinski, Surface Science: Foundations of Catalysis and Nanoscience, John Wiley & Sons, Chichester, 2008.
- [42] S. Hofmann, Auger and X-Ray Photoelectron Spectroscopy in Material Science A user-oriented Guide, Springer, London, 2013.

- [43] J.C. Riviere, Instrumentation, in: D. Briggs, M.P. Sean (Eds.) Practical Surface Analysis by Auger and X-ray Photoelectron Spectroscopy, John Wiley & Sons, Chichester, 1983.
- [44] D. Briggs, J.C. Riviere, Spectral Interpretation, in: D. Briggs, M.P. Sean (Eds.) Auger and X-ray Photoemission Spectroscopy, John Wiley and Sons, 1983, pp. 87-139.
- [45] A. Zangwill, Physics at surface, Cambridge University Press, Cambridge, 1988.
- [46] A.P. Grosvenor, M.C. Biesinger, R.S.C. Smart, N.S. McIntyre, New interpretations of XPS spectra of nickel metal and oxides, Surface Science, 600 (2006) 1771-1779.
- [47] <http://www.globalsino.com/micro/TEM/TEM9923.html>(accessed,1/01/2014)
- [48] D.A. Shirley, High-Resolution X-Ray Photoemission Spectrum of the Valence Bands of Gold, Physical Review B, 5 (1972) 4709-4714.
- [49] J. Yu, Q. Xiang, M. Zhou, Preparation, characterization and visible-light-driven photocatalytic activity of Fe-doped titania nanorods and first-principles study for electronic structures, Applied Catalysis B: Environmental, 90 (2009) 595-602.
- [50] B.P. Payne, M.C. Biesinger, N.S. McIntyre, The study of polycrystalline nickel metal oxidation by water vapour, Journal of Electron Spectroscopy and Related Phenomena, 175 (2009) 55-65.
- [51] J.M. Hollas, Modern Spectroscopy, John Wiley & Sons, Chichester, 1996.
- [52] B.C. Smith, Fundamentals of Fourier Transform Infrared Spectroscopy, CRC Press, London, 1996.
- [53] http://chemwiki.ucdavis.edu/Physical_Chemistry/Spectroscopy/Fundamentals/The_Power_of_the_Fourier_Transform_for_Spectroscopists.(accessed 12/03/2015)
- [54] J.W. Robinson, E.M.S. Frame, G.M. Frame II, Undergraduate instrumental analysis, Marcel Dekker, New York, 2005.
- [55] R.J. Hunter, Foundations of Colloid Science, Oxford University Press, Oxford, 2001.
- [56] J. Lim, S. Yeap, H. Che, S. Low, Characterization of magnetic nanoparticle by dynamic light scattering, Nanoscale Research Letters, 8 (2013) 381.
- [57] D.A. Skoog, D.M.H. West, F James, Fundamentals of Analytical Chemistry, Harcourt College Publishers, Orlando, USA, 1997.

- [58] M. Rycenga, C.M. Cobley, J. Zeng, W. Li, C.H. Moran, Q. Zhang, D. Qin, Y. Xia, Controlling the Synthesis and Assembly of Silver Nanostructures for Plasmonic Applications, *Chemical Reviews*, 111 (2011) 3669-3712.
- [59] U.K. Ghosh, S.E. Kentish, G.W. Stevens, Absorption of carbon dioxide into aqueous potassium carbonate promoted by boric acid, *Energy Procedia*, 1 (2009) 1075-1081.
- [60] X. Xiang, X.T. Zu, S. Zhu, L.M. Wang, Optical properties of metallic nanoparticles in Ni-ion-implanted α -Al₂O₃ single crystals, *Applied Physics Letters*, 84 (2004) 52-54.
- [61] L.M. Dormant, A.W. Adamson, Application of the BET equation to heterogeneous surfaces, *Journal of Colloid and Interface Science*, 38 (1972) 285-289.
- [62] C.N. Satterfield, *Heterogeneous Catalysis*, McGraw-Hill Book Company, New York, 1980.
- [63] S. Brunauer, P.H. Emmett, E. Teller, Adsorption of Gases in Multimolecular Layers, *Journal of the American Chemical Society*, 60 (1938) 309-319.
- [64] P.H. Emmett, T. De Witt, Determination of Surface areas pigments, carbon blacks. cements and miscellaneous finely divided or porous materials, *Industrial & Engineering Chemistry Analytical Edition*, 13 (1941) 28-33.
- [65] K.S.W. Sing, D.H. Everett, R.A.W. Haul, L. Moscou, R.A. Pierotti, J. Rouquerol, T. Siemieniewska, Reporting physisorption data for gas/solid systems with special reference to determination of surface area and porosity, *Pure and Applied Chemistry*, 54 (1985) 603-619.
- [66] K.S. Walton, R.Q. Snurr, Applicability of the BET Method for Determining Surface Areas of Microporous Metal–Organic Frameworks, *Journal of the American Chemical Society*, 129 (2007) 8552-8556.
- [67] J.F. Richardson, J.H. Harker, J.R. Backhurst, *Coulson and Richardson's Chemical Engineering Series, Volume 2 Particle Technology and Separation Processes*, Butterworth Heinemann, London, 2002.
- [68] S. Brunauer, L.S.D. Demming, W. Edwards, E. Teller, On a theory of the van der Waals Adsorption of Gases, *Journal of the American Chemical Society*, 62 (1940) 1723-1732.

Catalytic activity of NiNPs for hydration of CO₂ (Part I)

Chapter 4 reports the catalysis of the reversible hydration of CO₂ using nickel nanoparticles (NiNPs) at room temperature and atmospheric pressure. The catalytic activity of the NiNPs is pH independent and as they are water insoluble and magnetic they can be magnetically separated for reuse. The reaction steps were characterized using X-ray photoemission spectroscopy and a possible reaction mechanism is described.

4.1 HRTEM and XRD of the NiNPs

Commercially purchased NiNPs were characterized using high resolution transmission electron microscopy to determine their size distribution (figure 4.1). The particle size distribution measured from the HRTEM images is shown in

figure 4.1. The data was fitted using a Gaussian curve and the average particle size was about ~43 nm. The majority of the particles have characteristic lengths below 100 nm. The presence of nickel was confirmed using energy dispersive X-ray spectroscopy (EDX) (figure 4.2). The crystal planes of the nanoparticles can be seen in the Selected Area Electron Diffraction [SEAD] pattern [Fig. 4.3] and correspond to the [220], [222], [311], [400], [422] and [531] lattice planes respectively [1] The planes have been assigned by measuring the diameter of the rings obtained in reciprocal space and then assigned to a database entry [2].

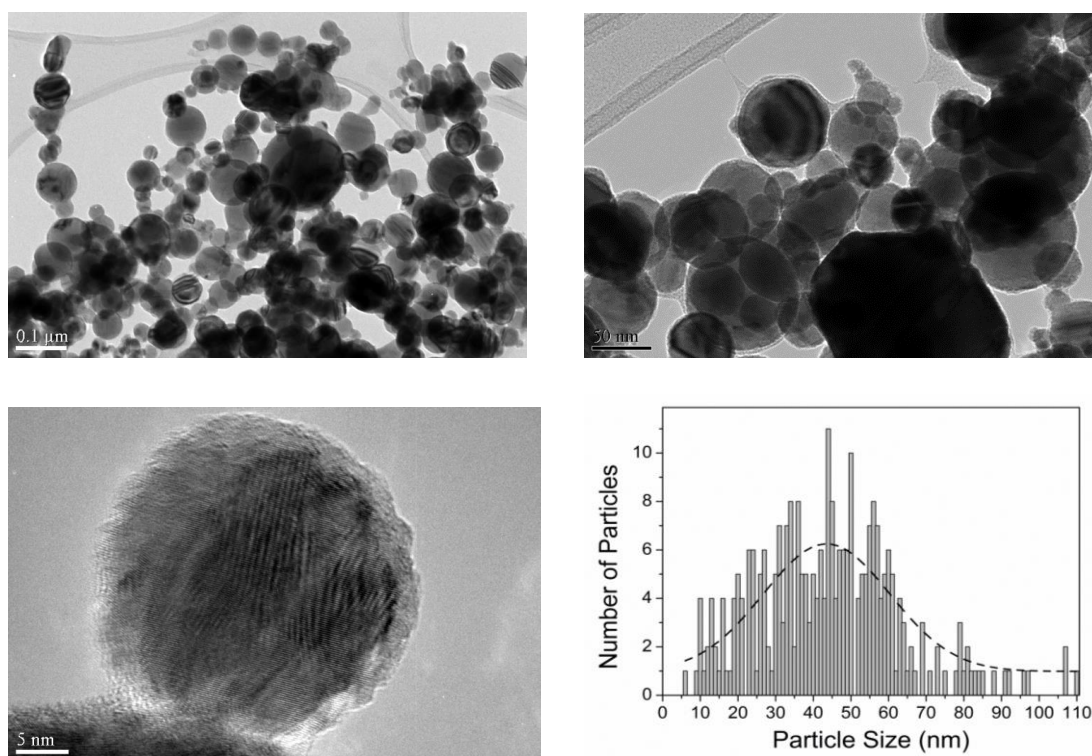


Figure 4.1: High Resolution Transmission Electron Microscopy images of NiNPs as purchased and particle size distribution [3]

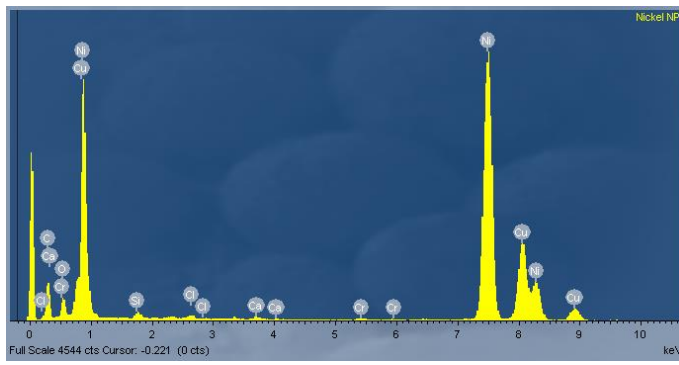


Figure 4.2: Energy dispersive x-ray spectroscopy of NiNPs [3].

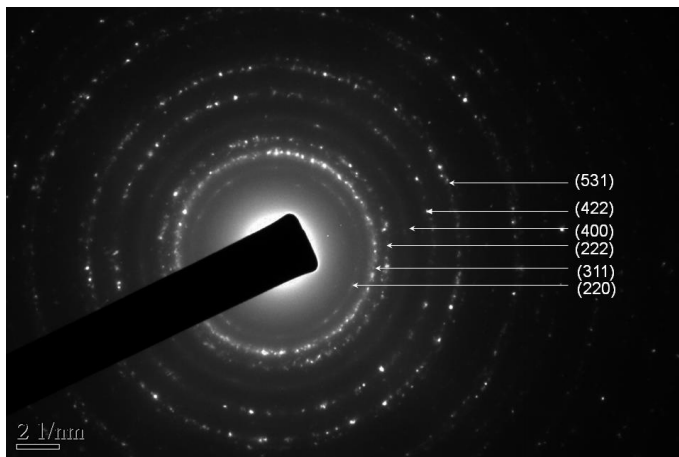


Figure 4.3: Selected area electron diffraction of the NiNPs [3].

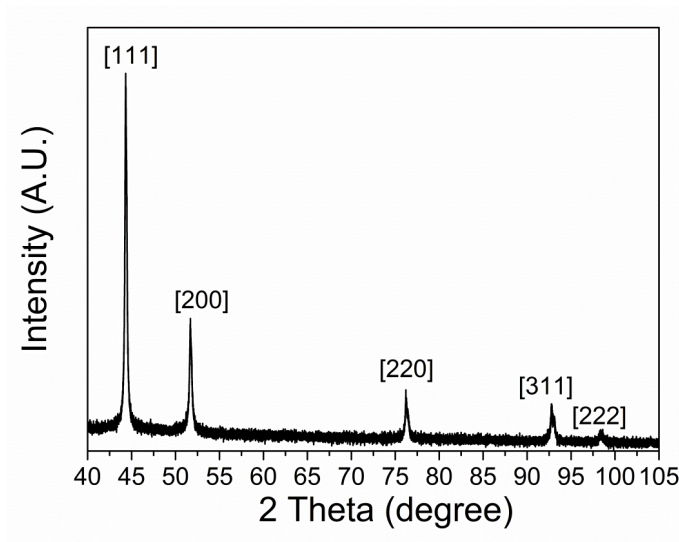


Figure 4.4 X-ray diffraction pattern of Nickel nanoparticles.

Figure 4.4 shows the X-ray diffraction (XRD) pattern for NiNPs. The diffraction pattern of the NiNPs is cubic. The diffraction pattern corresponds to the crystal

plane [111], [200], [220], [311] and [222] respectively [4, 5]. Both the XRD and the SAED pattern show similar planes for NiNPs.

4.2 CO₂ saturation experiments

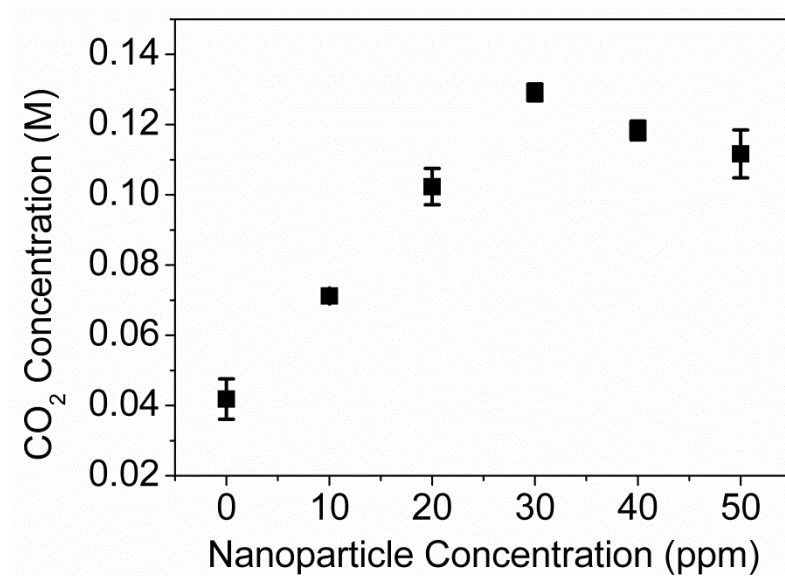


Figure 4.5: Average values of increase in the amount of CO₂ absorbed in aqueous suspension of NiNPs as a function of particle concentration at room temperature and atmospheric pressure when CO₂ is bubbled for 30 mins. [3, 6]

The results of the CO₂ saturation experiments can be seen in figure 4.5 procedure of which was described in chapter 3 section 3.3.2. Figure 4.5 shows the enhancement of CO₂ solution concentration (all species of CO₂, i.e. CO_{2(aq)}, H₂CO₃ and H₃O⁺ and HCO₃⁻, present in water) as a function of the NiNP concentration. The concentration of dissolved CO₂ was determined by titrating the CO₂ solution with 0.1 M NaOH solution. The amount of CO₂ dissolved in water (without the NiNPs) was similar to that reported in the literature (lit. [7] ~39 mM). A maximum is observed at 30 ppm [three times the capacity of de-ionized water], as compared with that of water without NiNPs. By further increasing the particle concentration a decrease in the CO₂ dissolution was

observed. Based on this result all further analysis were performed with a NiNP concentration of 30 ppm.

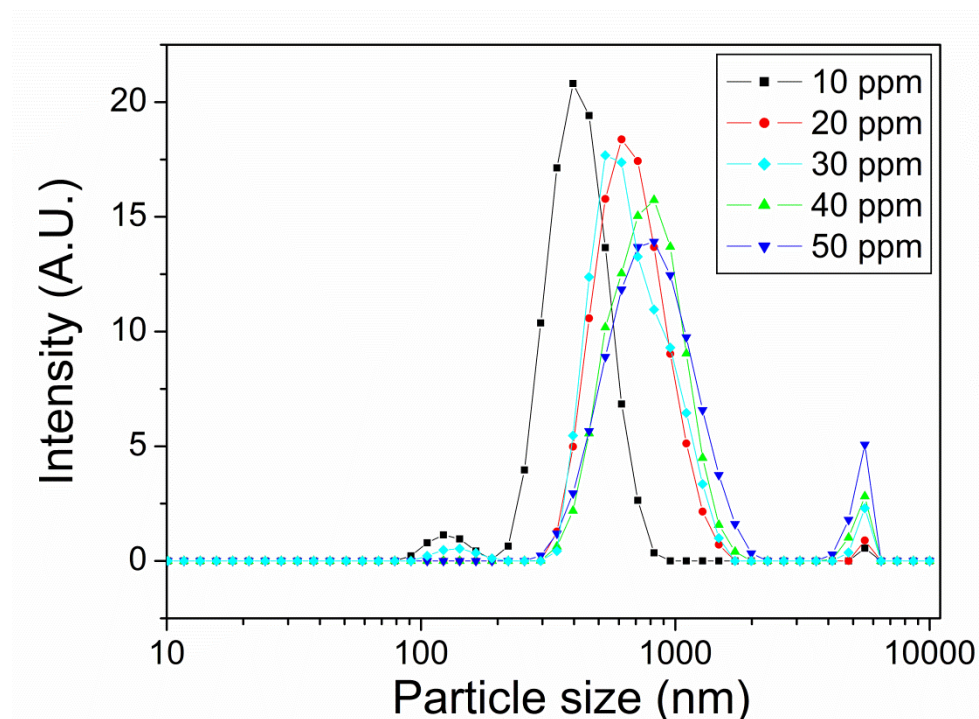


Figure 4.6: Dynamic light scattering results of NiNPs at different concentrations suspended in DI water.

However, another factor that may lead to reduction of CO_2 absorption in the NiNPs suspension at high concentration is agglomeration of the NiNPs. This was not considered by Bhaduri and Šiller [3] previously. As the amount of NiNPs increase in suspension, the probability of agglomeration also increases. Figure 4.6 shows the DLS measurements of the NiNPs at different concentrations when suspended in DI water. It is observed that the intensity of the main peak ($\sim <1000$ nm) decreases and there is a shift of the peak towards the larger size with the increasing concentration of NiNPs. Thus indeed the particle size increases with increasing concentration of NiNPs in suspension. It should also be noted that DLS measurements show higher particles sizes than

that of HRTEM due to presence of a passive hydrodynamic layer on the surface of the particles that causes also agglomeration of the particles [8, 9]. Lim *et al.* [8] showed with increasing the particle concentration of magnetic particles (nickel nanoparticles) like in this case, the DLS estimation and error will increase drastically. In the present study the nanoparticles have no surfactant coating to protect them from agglomeration, leading to their rapid agglomeration.

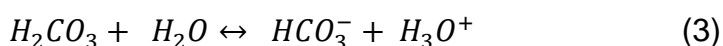
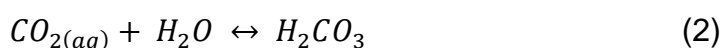
Along with particle size the zeta potential of 30 ppm NiNPs was measured in DI water and in CO₂ saturated solution (chapter 3, section 3.3.9). The zeta potential of NiNPs in DI water was -11 ± 1 mV. The zeta potential is negative due to presence of the OH groups present on the NiNPs surface [10]. In the saturated CO₂ solution the zeta potential increased to -5 ± 1 mV. The increase in the zeta potential is due to the presence of the acid. It known that the zeta potential is higher in acid solutions as compared with basic solutions [11]. This is due to the formation of positive bilayer on the nanoparticle surface due to the excess of H₃O⁺ in acid solutions and negative bilayer formation on the nanoparticle surface due to the excess of OH⁻ in basic solutions [11]. The reduction in the zeta potential of the NiNPs suspensions suggest rapid rate of agglomeration after CO₂ bubbling as compared to before CO₂ bubbling.

4.3 CO₂ hydration kinetics (gas-liquid reaction)

Since the pH drop of the solution is a function of the formation of carbonic acid, the rate of pH change can be related to the rate of the overall reaction $[r_A]$ [12] i.e. reactions (1–3, pg 151). Similar approaches have been reported for the study of the catalytic activity of CA [12]. The rate of change of pH and conductivity are shown in figure 4.7. Two sets of experiments were

performed at different initial pH values to test the catalytic activity of Ni nanoparticles at pH values above and below 6. CA is not stable at low pH values (below pH of 5) [12, 13] and thus study of the catalytic activity of NiNPs becomes important at low pH values. It can be seen from Fig. 4.7 a and c that the change in pH in the presence of the catalyst [filled circles] is significantly more rapid than that without the catalyst [filled squares] for the two different initial pH values [at pH 6.2 and 5.5]. It should be noted that Bhaduri and Šiller [3] are the first to report the use of heterogeneous catalyst for hydration of CO₂

The reactions associated with this process are [14, 15]



As there are no additional ions generated in the reaction the change in conductivity of the solution is a measure of the formation of bicarbonate ions from CO₂. CO_{2(aq)} being neutral in charge would not be responsible for the increase in conductivity of the solution. Thus the increase in the conductivity of the solution is due to the generation of carbonic acid, providing proof of the catalytic activity. It can be observed from figure 4.7 b and d that the initial rate of increase in the conductivity of the solution is higher in the presence of the NiNPs than in their absence. Thus the NiNPs act as a catalyst until the solution is saturated with bicarbonate ions and the surface of the NiNPs adsorbs some of those bicarbonates [see XPS analysis, section 4.4] and/or CO₂ gas.

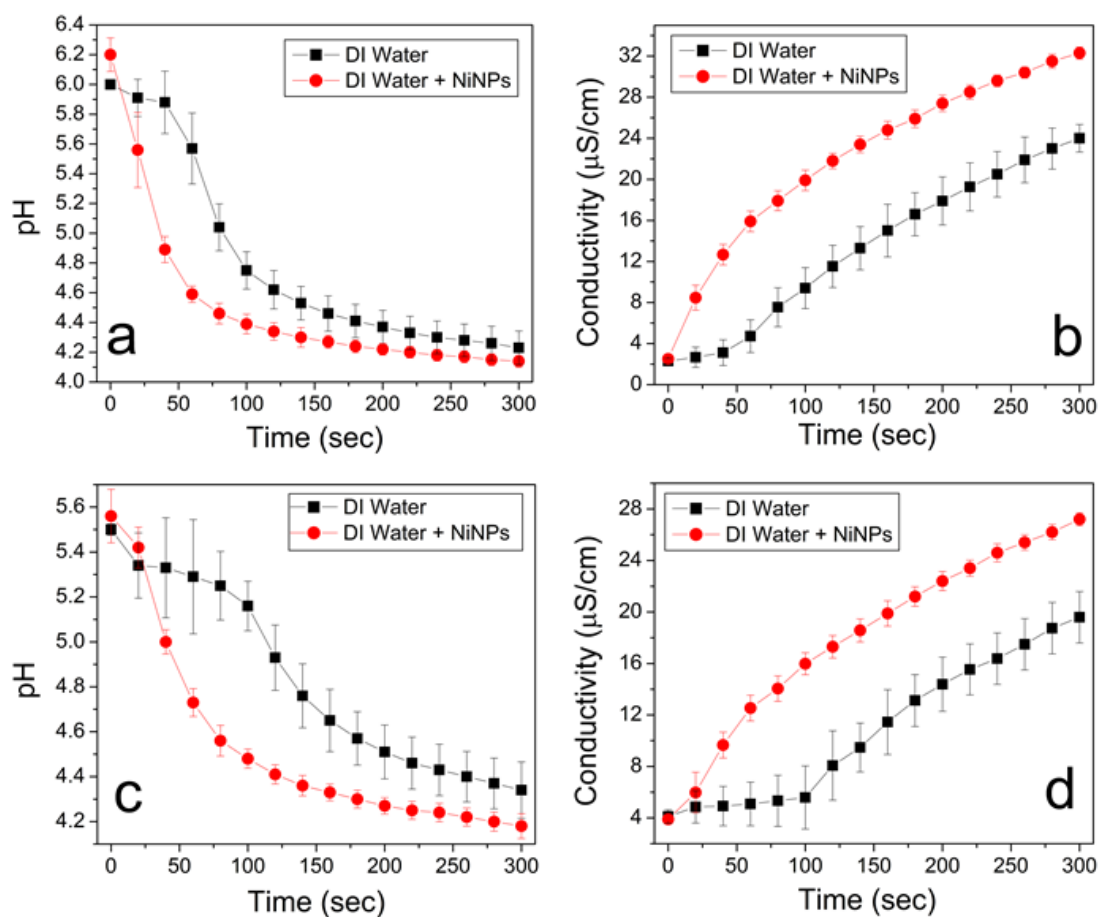


Figure 4.7: Average values of pH and ionic conductivity changes during bubbling of CO₂ through DI water and aqueous NiNPs suspension. (a) pH change starting from pH above 6, (b) ionic conductivity change corresponding to pH change from above 6, (c) pH changes starting at pH value below 6 and (d) ionic conductivity change corresponding to pH change from below 6. [3, 6]

It can be observed from figure 4.7 a and c that there is a sudden increase in the pH change in DI water when CO₂ is bubbled in DI water. This is due to catalytic activity of the H⁺ ions [16] and thus the reaction of CO₂ with DI water is autocatalytic. The theoretical calculation with known rate of reaction for reaction (1) and reaction (2) are shown in Appendix-II. Appendix-II also shows calculations for the apparent rate of CO₂ hydration reaction (uncatalysed and catalysed) calculated from the data represented in figure 4.7 a. (Data for up to 40 sec was used as beyond 40 sec, the autocatalytic activity is observed.) The

theoretical rate of reaction (1) is 2.442×10^{-6} mol/s and reaction (2) is 8.547×10^{-9} mol/s respectively whereas the experimental rate of reaction in the absence of NiNPs is 7.95×10^{-9} mol/s and in presence of NiNPs is 3.80×10^{-7} mol/s respectively. It can be observed from the calculations that the rate of uncatalysed reaction is close to one another where as that of the NiNP catalysed reaction rate is closer to the phase transfer rate (reaction 1). This suggest that the NiNPs catalysed reaction is mass transfer dependent.

In order to confirm that the increase in ion conductivity is not purely due to the ions leached into the water from the NiNPs themselves, changes in conductivity of solutions which only contains NiNPs were analysed (Fig. 4.8 a and b). It could be seen that this contribution to the ionic conductivity is negligible. Therefore, we can conclude that the increase in conductivity of the solution is purely due to an increase in the amount of bicarbonate ions alone. It was also observed that there was an initial immediate increase in the pH of DI water by 0.4–0.5 (Fig. 4.7a and b, observe the pH drop at 0 min) due to the addition of NiNPs and we suggest on the basis of our X-ray photoemission spectroscopy (XPS) analysis (section 4.4) that this is likely due to the dissociation of water and formation of OH groups on the NiNP surface. This assertion is supported by the observation of OH species on the [111] [17] and [110] [18] surfaces of single crystal Ni when exposed to H₂O at 300 K [17, 18]. Thermal analysis of nickel hydroxides show that physical desorption of the water from the surface of nickel hydroxide starts at ~ 100-150 °C [19, 20] and the decomposition of nickel (II) hydroxide to nickel (II) oxide starts at approximately 260 °C [19, 20]. The operating temperature in this study is 20 °C and therefore water desorption and nickel (II) hydroxide decomposition is unlikely.

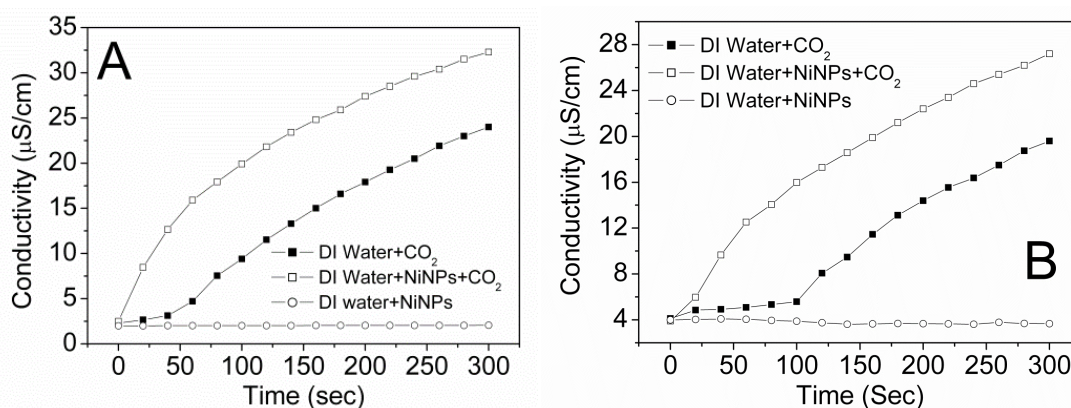


Figure 4.8: Average values of conductivity change of the Ni nanoparticle suspension compared with that of the blank and Ni suspension when bubbled with CO₂ for (a) pH above 6 and (b) pH below 6. [3, 6]

pH is a function of H⁺ ion concentration due to the acid formation (figure 4.7a and 4.7c). In addition the conductivity of the solution is also measured and the leaching of Ni²⁺ ions is minimal as seen from figure 4.8, therefore the changes in conductivity must be related to the formation of carbonic acid alone. In the literature it has been reported that the H⁺ ions catalyse the formation of carbonic acid [21, 22] at low pH values, pH range ~ 4.9-4.6 (the alkalinity of the CO₂-H₂O solution is zero and only the acid is present) [23]. There is also consensus in literature that the hydration reaction of CO₂ is faster in the presence of hydroxyl groups in solution on pH values above 8 [24]. In Figure 4.7b, at ~ 80 sec in both DI water with and without NiNPs the conductivity slope is changed, and from Figure 4.7a we can read out that the pH at that time is ~4.9 and ~ 4.5, respectively, which is close to the suggested range from ref [25] when H⁺ ion catalysis would exist. This is also observed in Fig 4.7 d at 120 sec with the similar pH values. The XPS (see below) results show the surface of the nickel have -OH groups, so from the initial value until the pH of 4.5 the gas – liquid hydration reaction is catalysed by OH groups present on the Ni surface.

Hernandez *et al.* [10] studied the influence of pH on the surface species and dissolution of Ni and NiO microparticles. It is known that Ni²⁺ ions do not leach in DI water but forms a passive Ni(OH)_x layer on the surface of solid Ni [10, 26]. The formation of Ni(OH)_x species leads to the change in pH of water [10] which is observed in figure 4.7a and 4.7c. Dissolution of Ni under acidic conditions depends on the nature of the acid and its concentration, for example dilute HNO₃ dissolves Ni whereas concentrated HNO₃ forms a passive layer on the Ni surface [10]. The low dissolution of solid nickel in solutions because nickel has an electrochemical potential of -0.227V with reference to Standard Hydrogen Electrode (SHE) (see figure 3.3), suggesting that the Ni leaching rate is slow in acidic solutions in absence of an oxidizing agent stronger than H⁺ [27]. Hernandez *et al.* [10] reported that in presence of a mineral acid (like HCl) Ni leaching is high (>100 ppm) for pH <4 but is low (< 50 ppm) between pH 4-12 for studied for 1000 ppm Ni microparticle suspension.

Therefore additional dialysis measurements are used to study the leaching of NiNPs in carbonic acid solution. Two reading of Ni²⁺ leaching from NiNPs in carbonic acid are presented one after 30 min and another after 60 min. These time values are far greater than the reaction time. Table 4.1 summarizes the results of the dialysis experiment. The results show that there was no detectable leaching of Ni²⁺ ions observed during the time of the reaction during rapid pH changes.

Table 4.1 Dialysis results of Ni²⁺ ion leaching from NiNPs in carbonic acid solution

Time (min)	Ni ²⁺ ion concentration (ppm or mg/lit)
0	<0.005
30	<0.005
60	<0.005

Following the dialysis results a 0.005 mg/lit (i.e. 0.005 ppm) NiSO₄ solution was prepared to test the effect of Ni²⁺ ions on CO₂ hydration rate using same methodology as used above to test the catalytic activity of NiNPs. Figure 4.9 shows the pH changes in presence and absence of Ni²⁺ ions in DI water. The pH change profile in present and absence of Ni²⁺ ions are similar as compared the NiNPs have a faster rate of pH change. This clearly suggests that NiNPs are catalyst and not Ni²⁺ ions for hydration of CO₂.

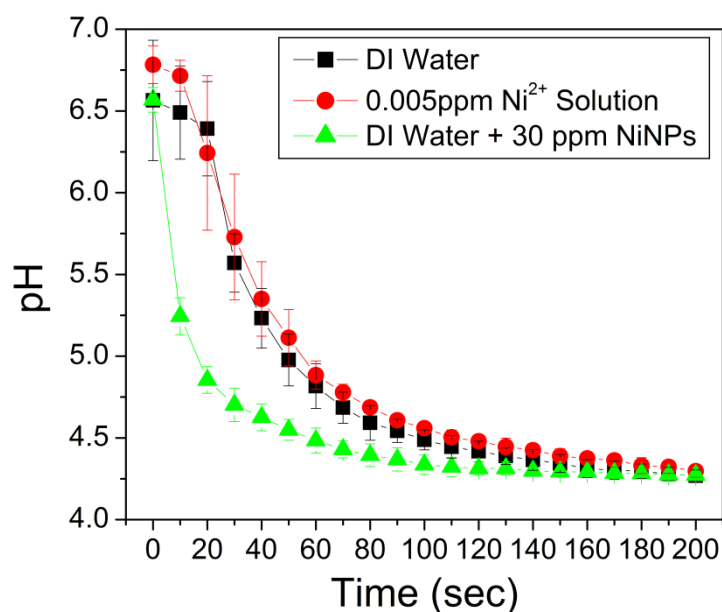


Figure 4.9: Average values of pH changes during bubbling of CO₂ through DI water, 0.005 ppm Ni²⁺ solution and 30 ppm NiNPs suspension.

4.4 Chemical characterization of the NiNPs surface before and after CO₂ bubbling

In order to have an insight into the reaction mechanism and the species present on the nanoparticle surface, X-ray photoelectron spectroscopy [XPS] was performed on the Ni nanoparticles before [Fig. 4.10] and after carbon dioxide bubbling [Fig. 4.11]. All in energy positions reported are within ± 0.1 eV.

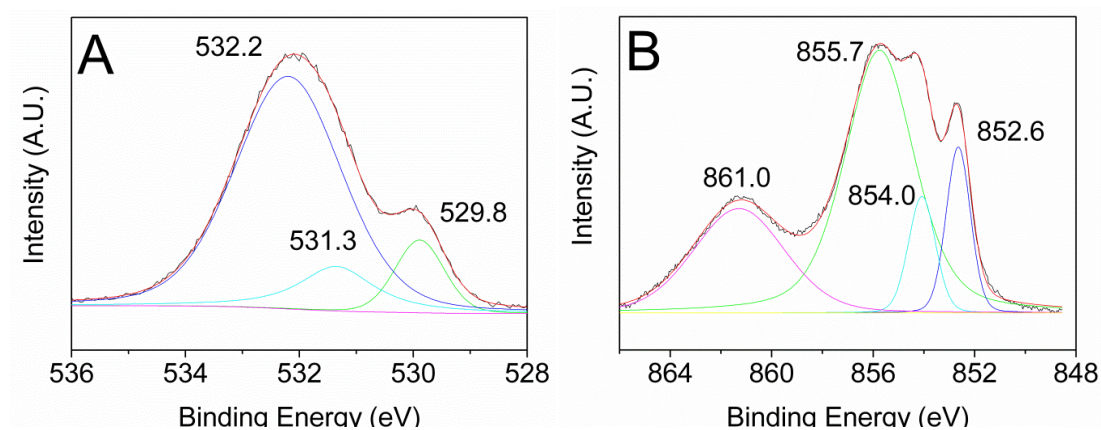


Figure 4.10: XPS spectra of NiNPs before bubbling of CO₂; (A) O 1s and (B) Ni 2p_{3/2}. [3, 6]

An insight into the chemical state of the NiNPs after dissolution in DI water without carbon dioxide exposure can be obtained by examination of the Ni 2p_{3/2} and O 1s core lines (Fig. 4.10). The Ni 2p_{3/2} line can be decomposed into peaks located at binding energies of 852.6 eV, 854.0 eV, 855.7 eV and a plasmon peak at 861.0 eV [28, 29]. The O 1s line was fitted by three peaks located at 529.8 eV, 531.3 eV and 532.2 eV. The Ni 2p_{3/2} peak at 852.6 eV binding energy is associated with Ni⁰ [30] while that at 855.7 eV corresponds to nickel in the Ni²⁺ oxidation state and has a binding energy corresponding to that of Ni(OH)₂ [28, 31]. Moreover, the O 1s peak at 531.3 eV corresponds to oxygen in the hydroxyl (-OH) group associated with Ni(OH)₂ [28]. The binding energy of the O 1s in multilayers of H₂O (532.4 eV) [17] is at a higher binding energy than that of the -OH group (530.9 eV) [17] thus the peak observed at 532.2 eV can be assigned to water adsorbed at the surface of the NiNPs [17, 18]. The Ni 2p_{3/2} peak at 854.0 eV corresponds to NiO which is confirmed by the presence of the O 1s peak at 529.8 eV [28, 29].

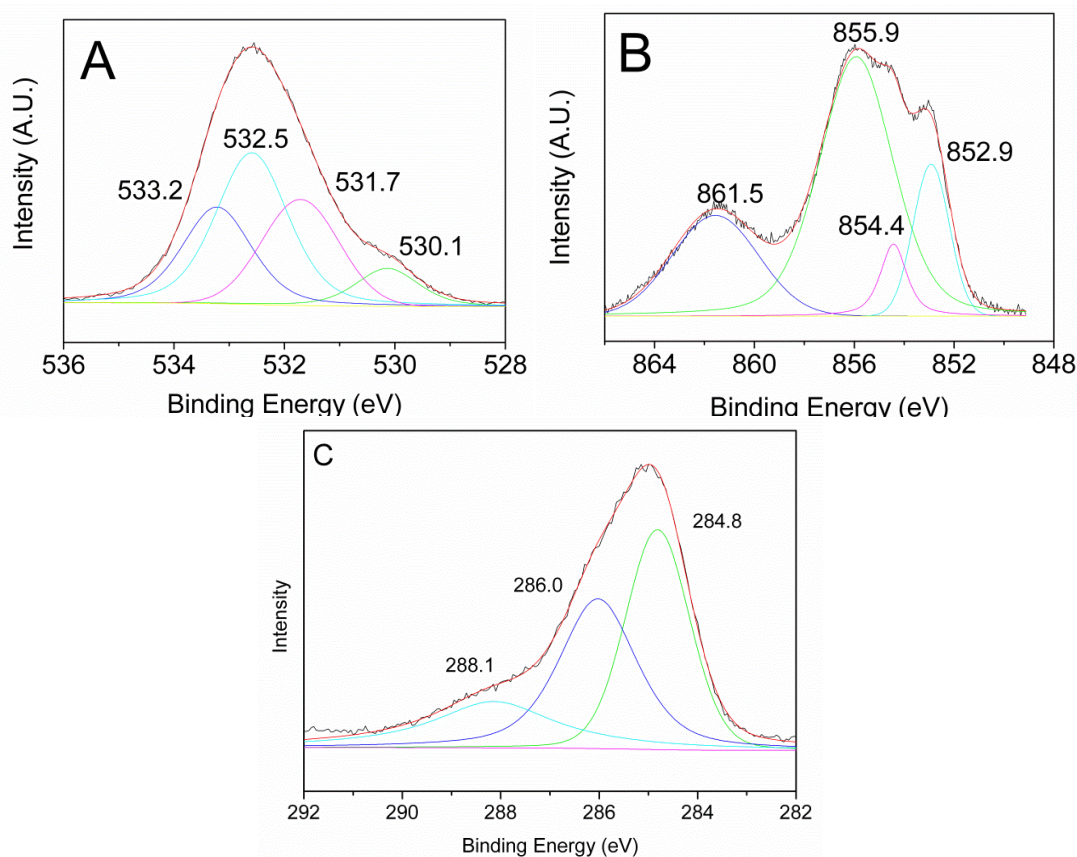


Figure 4.11. XPS spectra of NiNPs after bubbling with carbon dioxide; (A) O 1s, (B) Ni $2p_{3/2}$ and (C) C 1s. [3, 6]

XPS of the NiNPs after carbon dioxide bubbling is shown in Fig. 4.11. The Ni $2p_{3/2}$ is again fitted using three peaks, which are located at binding energies of 852.9 eV, 854.4 eV, and 855.9 eV, respectively, and a plasmon peak at 861.5 eV [28, 29]. The Ni peak at 852.9 eV corresponds to Ni^0 [29] whereas the peaks at 854.4 eV and 855.9 eV correspond to the Ni^{2+} oxidation state [29]. The carbon C 1s line is also fitted with three peaks located at 284.8 eV, 286.0 eV, and 288.1 eV. The C 1s component at 284.8 eV binding energy is assigned to adventitious carbon [28]. The C 1s peak at 286.0 eV corresponds to carbon in alcohol groups and that at 288.1 eV to carbon in ester groups [28]. The O 1s line is fitted with four peaks located at 530.1 eV, 531.7 eV, 532.5 eV and 533.2 eV. The peak for O 1s at 530.1 eV and the Ni $2p_{3/2}$ peak at 854.4 eV are assigned to NiO on NiNPs [29]. The O 1s peaks at 531.7 eV and 533.2 eV

correspond to the two different oxygen sites in the ester ($-\text{COO}-$) group (the first corresponding to the oxygen double bonded to carbon and the second to the oxygen single bonded to carbon) and the O 1s peak at 532.5 eV corresponds to the alcohol group ($-\text{C}-\text{OH}$) [28, 32]. Bicarbonate molecules contain both an ester and an alcoholic carbon, therefore we interpret the presence as a signature of bicarbonate species present on the nickel surface. We suggest that the Ni $2p_{3/2}$ peak at 855.9 eV corresponds to $\text{Ni}(\text{HCO}_3)_x$ adsorbed at the Ni surface.

4.5 Mechanism of hydration reaction by NiNPs.

Based on the interpretation of the XPS results we can derive a possible reaction mechanism which is presented in figure 4.12. In the aqueous environment there is the generation of hydroxyl groups on the surface of the Ni nanoparticles. These hydroxyl groups are then attacked by the carbon dioxide molecule to form bicarbonate ions on the Ni surface which are then displaced by water molecules, which then lose hydrogen ions and regenerate the hydroxyl ions on the Ni surface. The absence of the $-\text{OH}$ group on the surface of NiNPs (figure 4.12) in the XPS results suggests a possible conversion of $-\text{OH}$ groups to $-\text{HCO}_3$ groups when CO_2 is bubbled in the NiNPs aqueous suspension. There were no hydroxyl groups observed in the XPS results of the Ni nanoparticles after CO_2 bubbling, indicating the conversion of the hydroxyl groups to bicarbonate groups in the reaction.

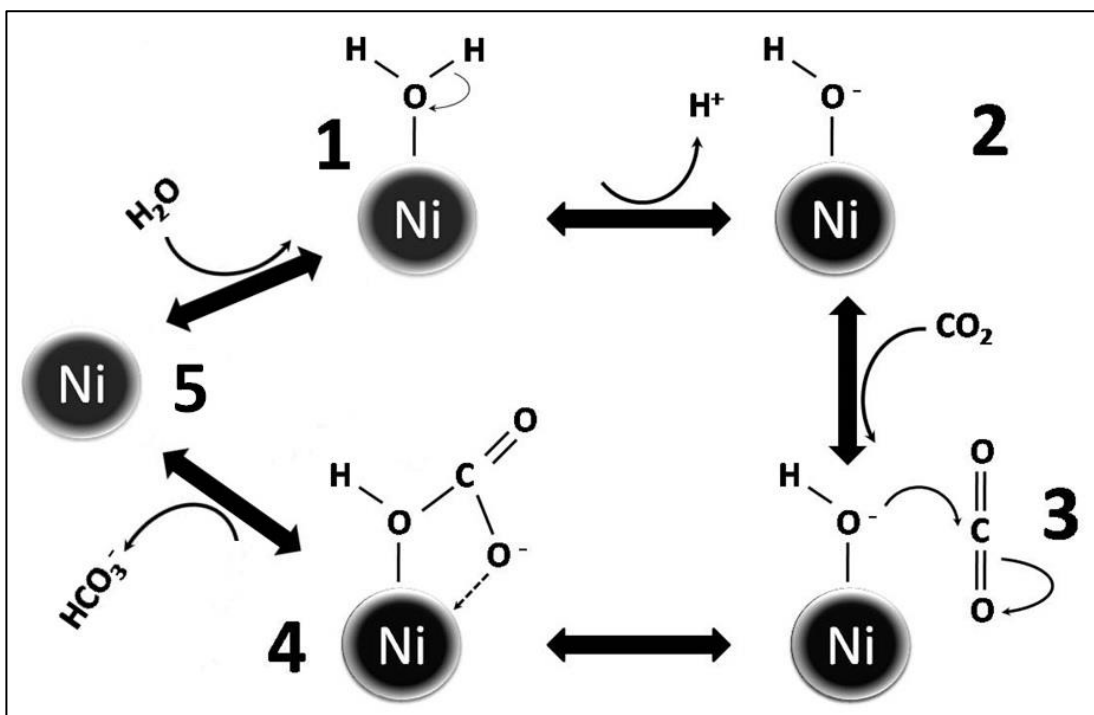


Figure 4.12: Schematic of the reaction mechanism of hydration of CO_2 by NiNPs. [3, 6]

4.6 Conclusion

The current chapter presents proof that NiNPs catalyse the hydration of CO_2 . Catalysis is observed by the comparison of the pH and conductivity changes when CO_2 is bubbled in DI water and NiNPs suspensions. A threefold enhancement in the dissolution of CO_2 in water was observed in the presence of NiNPs (30 ppm). There was also an initial increase in the pH of water by addition of NiNPs, which was due to the formation of $\text{Ni}(\text{OH})_x$ on the NiNP surface as seen from the XPS analysis. NiNPs do not leach detectable amounts Ni^{2+} ions in DI water and in carbonic acid solution. Ni^{2+} ions do not catalyse the hydration of CO_2 . The XPS analysis provided the reaction steps on the basis of which the reaction mechanism is suggested.

References

- [1] G. Grimvall, J. Häglund, A. Fernández Guillermet, Spin fluctuations in paramagnetic chromium determined from entropy considerations, *Physical Review B*, 47 (1993) 15338-15341.
- [2] CDS, Chemical Database Service, <https://cds.dl.ac.uk/>
- [3] G.A. Bhaduri, L. Šiller, Nickel nanoparticles catalyse reversible hydration of carbon dioxide for mineralization carbon capture and storage, *Catalysis Science & Technology*, 3 (2013) 1234-1239.
- [4] H.T. Takeshita, T. Oishi, N. Kuriyama, Disproportionation of CaNi_3 hydride: formation of new hydride, CaNiH_3 , *Journal of Alloys and Compounds*, 333 (2002) 266-273.
- [5] S. Dellis, A. Christoulaki, N. Spiliopoulos, D.L. Anastassopoulos, A.A. Vradis, Electrochemical synthesis of large diameter monocrystalline nickel nanowires in porous alumina membranes, *Journal of Applied Physics*, 114 (2013) 164308.
- [6] L. Šiller, G.A. Bhaduri, Carbon capture, in, World Patent WO2013/171480 (A2), 2013.
- [7] N. Favre, M.L. Christ, A.C. Pierre, Biocatalytic capture of CO_2 with carbonic anhydrase and its transformation to solid carbonate, *Journal of Molecular Catalysis B: Enzymatic*, 60 (2009) 163-170.
- [8] J. Lim, S. Yeap, H. Che, S. Low, Characterization of magnetic nanoparticle by dynamic light scattering, *Nanoscale Research Letters*, 8 (2013) 381.
- [9] B.N. Khlebtsov, N.G. Khlebtsov, On the measurement of gold nanoparticle sizes by the dynamic light scattering method, *Colloid Journal*, 73 (2011) 118-127.
- [10] N. Hernández, R. Moreno, A.J. Sánchez-Herencia, J.L.G. Fierro, Surface Behavior of Nickel Powders in Aqueous Suspensions, *The Journal of Physical Chemistry B*, 109 (2005) 4470-4474.
- [11] R.J. Hunter, *Foundations of Colloid Science*, Oxford University Press, Oxford, 2001.
- [12] G.M. Bond, J. Stringer, D.K. Brandvold, F.A. Simsek, M.-G. Medina, G. Egeland, Development of Integrated System for Biomimetic CO_2 Sequestration Using the Enzyme Carbonic Anhydrase, *Energy & Fuels*, 15 (2001) 309-316.
- [13] J.C. Kernohan, The pH-activity curve of bovine carbonic anhydrase and its relationship to the inhibition of the enzyme by anions, *Biochimica et Biophysica Acta (BBA) - Nucleic Acids and Protein Synthesis*, 96 (1965) 304-317.
- [14] M. Vinoba, D.H. Kim, K.S. Lim, S.K. Jeong, S.W. Lee, M. Alagar, Biomimetic Sequestration of CO_2 and Reformation to CaCO_3 Using Bovine

Carbonic Anhydrase Immobilized on SBA-15, *Energy & Fuels*, 25 (2010) 438-445.

[15] D.-H. Kim, M. Vinoba, W.-S. Shin, K.-S. Lim, S.-K. Jeong, S.-H. Kim, Biomimetic sequestration of carbon dioxide using an enzyme extracted from oyster shell, *Korean Journal of Chemical Engineering*, 28 (2011) 2081-2085.

[16] G.A. Bhaduri, R.A. Henderson, L. Šiller, Reply to the 'Comment on "Nickel nanoparticles catalyse reversible hydration of carbon dioxide for mineralization carbon capture and storage"' by D. Britt, *Catal. Sci. Technol.*, 2013, 3, DOI: 10.1039/C3CY00142C, *Catalysis Science & Technology*, 3 (2013) 2197-2198.

[17] M. Schulze, R. Reißner, K. Bolwin, W. Kuch, Interaction of water with clean and oxygen precovered nickel surfaces, *Fresenius Journal of Analytical Chemistry*, 353 (1995) 661-665.

[18] H. Guo, F. Zaera, Reactivity of Hydroxyl Species from Coadsorption of Oxygen and Water on Ni(110) Single-Crystal Surfaces, *Catalysis Letters*, 88 (2003) 95-104.

[19] A.M. Gaddala, T.W. Livingstone, Thermal behaviour of oxides and hydroxides of iron and nickel, *Thermochimica Acta*, 145 (1989) 1-9

[20] V. Logvinenko, V. Bakovets and L. Trusnikova, Decomposition process of nickel hydroxide, *Journal of Thermal Analysis and Calorimetry*, 107 (2012) 983-987.

[21] R. Brinkman, R. Margaria, F.J.W. Roughton, The Kinetics of the Carbon Dioxide-Carbonic Acid Reaction, *Philosophical Transactions of the Royal Society of London. Series A, Containing Papers of a Mathematical or Physical Character*, 232 (1934) 65-97.

[22] F.J.J. Buytendyk, R. Brinkman, H.W. Mook, A Study of the System Carbonic Acid, Carbon Dioxide and Water, *Biochemical Journal*, 21 (1927) 576-584.

[23] J.N. Butler, *Carbon dioxide equilibria and their applications*, Lewis Publishers, Chelsea, 1991.

[24] F.J.W. Roughton, V.H. Booth, The catalytic effect of buffers on the reaction $\text{CO}_2 + \text{H}_2\text{O} = \text{H}_2\text{CO}_3$, *Biochemical Journal*, 32 (1938) 2049-2069.

[25] D.M. Kern, The hydration of carbon dioxide, *Journal of Chemical Education*, 37 (1960) 14.

[26] N. Kitakatsu, V. Maurice, C. Hinnen, P. Marcus, Surface hydroxylation and local structure of NiO thin films formed on Ni(111), *Surface Science*, 407 (1998) 36-58.

- [27] L.L. Shreir, R.A. Jarman, G.T. Burstein, Corrosion Volume 1 Metal/Environment Reactions, Butterworth Heinemann, London, 1994, pp. 4:122-124:123.
- [28] B.P. Payne, M.C. Biesinger, N.S. McIntyre, The study of polycrystalline nickel metal oxidation by water vapour, Journal of Electron Spectroscopy and Related Phenomena, 175 (2009) 55-65.
- [29] M.C. Biesinger, B.P. Payne, L.W.M. Lau, A. Gerson, R.S.C. Smart, X-ray photoelectron spectroscopic chemical state quantification of mixed nickel metal, oxide and hydroxide systems, Surface and Interface Analysis, 41 (2009) 324-332.
- [30] R.J. Behm, C.R. Brundle, On the formation and bonding of a surface carbonate on Ni(100), Surface Science, 255 (1991) 327-343.
- [31] S. Chou, F. Cheng, J. Chen, Electrochemical Deposition of Ni(OH)₂ and Fe-Doped Ni(OH)₂ Tubes, European Journal of Inorganic Chemistry, 2005 (2005) 4035-4039.
- [32] A.B. Christie, I. Sutherland, J.M. Walls, An XPS study of ion-induced dissociation on metal carbonate surfaces, Vacuum, 31 (1981) 513-517.

Catalytic activity of NiNPs for hydration of CO₂ (Part II)

In this chapter results of stopped flow spectrophotometry method used for analysis of kinetics of CO₂ hydration are presented. To test the influence of mass transfer enhancement and increased saturation of CO₂ due to presence of nanoparticles on observed pH change, inorganic nanoparticles (NiO and Fe₂O₃) have been used. pH changes of saturated CO₂ solution added to buffer (with and without NiNPs) have been noted to qualitatively validate the catalysis of hydration of CO₂ by NiNPs (method similar Mirjafari *et al.* [1]). The chapter also presents the effect of CO₂ partial pressure on CO₂ hydration in the presence and absence of NiNPs. Nickel nanowires (NiNWs) have been synthesised and have been tested for enhancement in CO₂ saturation concentration and catalytic activity for CO₂ hydration reaction. The results conclusively show that the NiNPs act as catalyst for the hydration of CO₂.

5.1. Comment by David Britt [2].

David Britt [2] commented on the paper published by Bhaduri and Šiller [3] that the experimentally observed increase in the rate of pH drop (figure 4.8a and 4.8c, chapter 4) is due to observed increase in the CO₂ saturation concentration (figure 4.6, chapter 4) and is not due to catalytic activity of NiNPs as discussed in the paper. Britt [2] has recommended another commonly used methodology, where the pH change is observed when a saturated CO₂ solution is mixed with a buffer solution (e.g. reported by Mirjafari *et al.* [1], chapter 3 section 3.3.5 for detailed experimental procedure) be used with a modification of replacing the buffer solution with DI water.

5.2 Stopped flow spectrophotometric analysis for reaction kinetics

Stopped flow spectrophotometry is a method of analysis for the measurement of kinetics of fast chemical reaction (i.e. for reactions that reach completion within 1-5 min) and is based on the principle that the light absorbance of a tracer dye or chemical compound changes as the reaction proceeds [4] (chapter 3, section 3.3.4). It has been commonly used for the measurement of kinetics of hydration of CO₂ [5-9]. Recently Wang *et al.* [9] reported the hydration and dehydration of CO₂ using the stopped flow spectrophotometer for accurate determination of the rate of hydration of CO₂. In their methodology a saturated CO₂ aqueous solution is brought into contact with Na₂CO₃ solution of a known concentration and the progress of the neutralization reaction is observed by a change in absorbance of the tracer dye [9].

The results (figure 5.1) of the stopped-flow spectrophotometry to determine the use of NiNPs on the rate of hydration of CO₂ was carried out following a similar methodology as Wang *et al.* [9]. The kinetic constant of the

reaction was calculated by fitting the data with an exponential function using Origin 6.1 software (an example of the curve fitting is provided in figure 5.1b). In the stopped flow experiments the concentration of CO₂ solution was kept constant and the concentration of carbonate solution was changed. The resultant kinetic constants at different Na₂CO₃ concentrations are plotted in figure 5.1a. The change in the kinetic constants is due to the change in the final pH of the resultant solution of saturated CO₂ solution and Na₂CO₃ solution. The CO₂ hydration kinetics is higher at lower pH but is slower at near neutral pH [6] and the results are similar to those observed by Wang *et al* [9] It is observed from the figure that there is no appreciable change in the rate constant of the reaction in the presence of NiNPs. This indicates that the NiNPs did not affect the equilibrium coefficient of the hydration reaction.

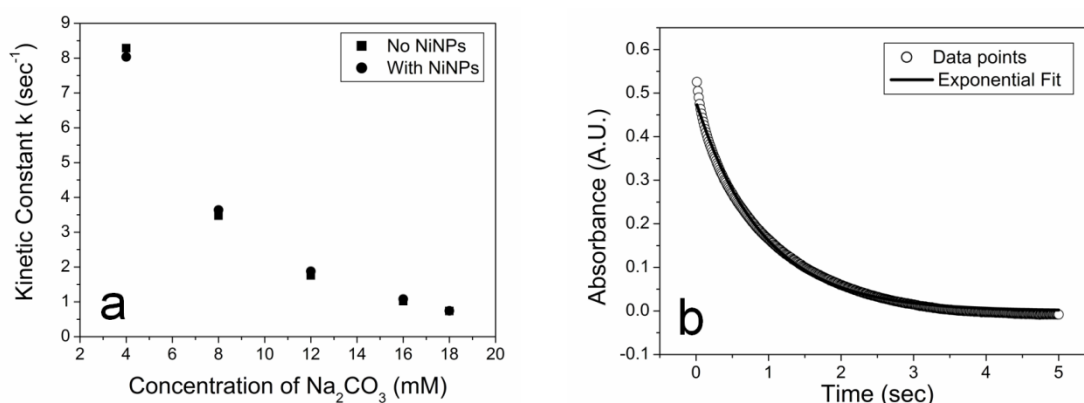


Figure 5.1: Kinetic constants as a function of Na₂CO₃ concentration and an example of the exponential fit for the data obtained from the spectropotometer. [10]

The lack of difference in kinetic constants in stopped-flow results is due to two possibilities [10]: firstly, that the pH range during the reaction is below 4.9 and therefore the catalytic activity is dominated by H₃O⁺ ions [6, 11, 12] and that the NiNPs are poisoned by the phenolphthalein indicator because oxygen

(active site of phenolphthalein) has a higher binding energy than hydroxyl groups chemisorbed at the Ni surface [13] so they are hard to remove.

5.3 CO₂ hydration kinetics using pH change method using saturated CO₂ solution.

A qualitative method was used to test the pH dependence of the NiNPs' activity for CO₂ hydration. This method is commonly used to observe the catalytic activity of carbonic anhydrase (ref in Table 2.4, chapter 2). In this methodology a saturated solution of CO₂ (pH 4) is mixed with a buffer solution at a known pH and the rate of change in pH is observed. The change in pH is due to the formation of carbonic acid from CO_{2(aq)} of the saturated CO₂ solution. This methodology was adapted from kinetic study of CA hydration as described by Mirjafari et al [1], described in section 3.2.5 chapter 3.

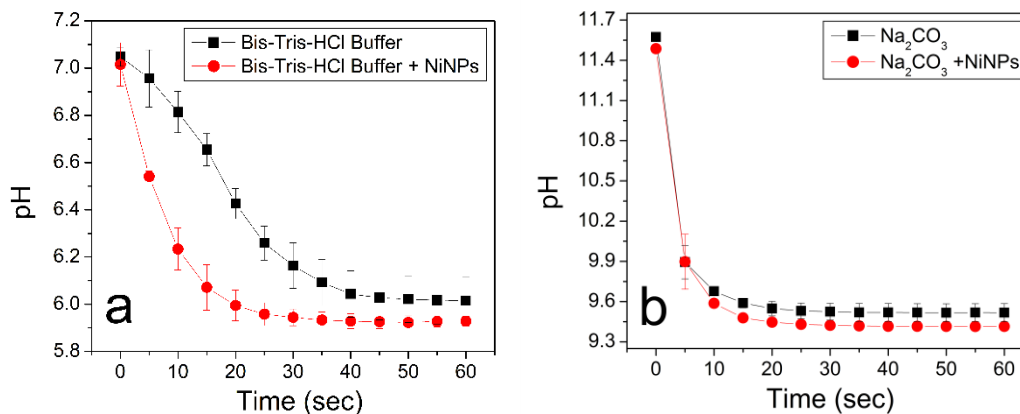


Figure 5.2: Average values of pH dependent hydration of CO₂ in presence of NiNPs at different pH A) at pH 7 using Bis-Tris-HCl buffer and B) at pH 11.5 using sodium carbonate solution.

Figure 5.2 shows the pH changes in Bis-Tris-HCl buffer (figure 5.2A) and sodium carbonate solutions (figure 5.2B) when a CO₂ saturated solution is added in presence and absence of NiNPs. Figure 5.2A shows a faster pH drop in Bis-Tris-HCl buffer solution in the presence of NiNPs than its absence. This indicates the catalytic activity due to the presence of NiNPs at pH values below

8, with CO₂ hydration following the H₂O reaction mechanism ($CO_{2(aq)} + H_2O \leftrightarrow H_2CO_3$). Figure 5.2B shows the pH changes at alkaline pH values (i.e. pH >10) in Na₂CO₃ solution. The NiNPs catalysis is minimal at alkaline pH (i.e. pH >10).

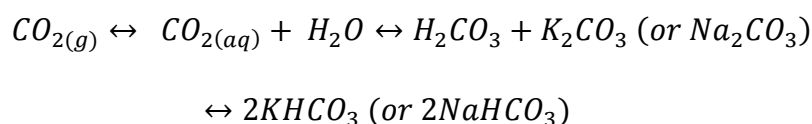
Above pH 10, CO₂ hydration can be described by the OH reaction mechanism ($CO_{2(aq)} + OH^- \leftrightarrow HCO_3^-$) whilst it operates via a mixed mechanism (OH and H₂O reaction mechanism) at pH values between 10 and 8 [6]. Therefore the results from figure 5.2 indicate that NiNPs helps in catalysis when the alkaline pH value is below 10 and does not help in catalysis when the pH value is above 10.

5.4 NiNPs enhancement of CO₂ absorption kinetics in carbonate solutions

Both the above methodologies (section 5.2 and 5.3) study kinetics of the hydration of CO₂ based on saturated CO₂ solution. Kim *et al.* [14] used a different approach for analysis of hydration of CO₂. In their process CO₂ is bubbled in a quiescent liquid (buffer solution) and the pH change response is observed in presence and absence of different bio-catalyst (see chapter 3 section 3.33 for details). Their assumption is that, the physical mass transfer (the rate of CO₂ transfer across the gas-liquid interface) is not affected by the presence of the catalyst and therefore rate of pH change is a direct measure of the kinetic rate enhancement of CO₂ hydration. Bhaduri and Šiller [3] used the same reaction methodology and the same assumption for analysis of catalytic activity of NiNPs (section 4.3). They observed an enhanced rate of pH change in the presence of NiNPs than in its absence (figure 4.7) similar to the results observed by Kim *et al.* [14] (figure 3.2).

In order to test whether these assumptions are correct a new set of experiments were designed for analysis. In these experiments CO₂ gas was

bubbled in a 0.1 M Na_2CO_3 and 0.1 M K_2CO_3 solutions and the pH changes were measured with and without the NiNPs (chapter 3, section 3.2.5). The CO_2 from the gas phase dissolves in the carbonate solution and reacts with water to form carbonic acid which then reacts with the carbonate ion to form bicarbonate ions. The reactions can be represented in series as



The conversion of carbonate to bicarbonate results in a drop in pH when CO_2 is bubbled in carbonate solution. The pH changes shows the overall rate of the reaction of $\text{CO}_{2(aq)}$ to bicarbonate formation. As all the chemical species in the above reaction are ionic species the reaction of carbonic acid with carbonate is a protonation step $\text{H}_2\text{CO}_3 + \text{CO}_3^{2-} \leftrightarrow 2\text{HCO}_3^-$. The protonation step is an instantaneous process [15]. Therefore the rate of change of pH is dependent on the hydration reaction of CO_2 .

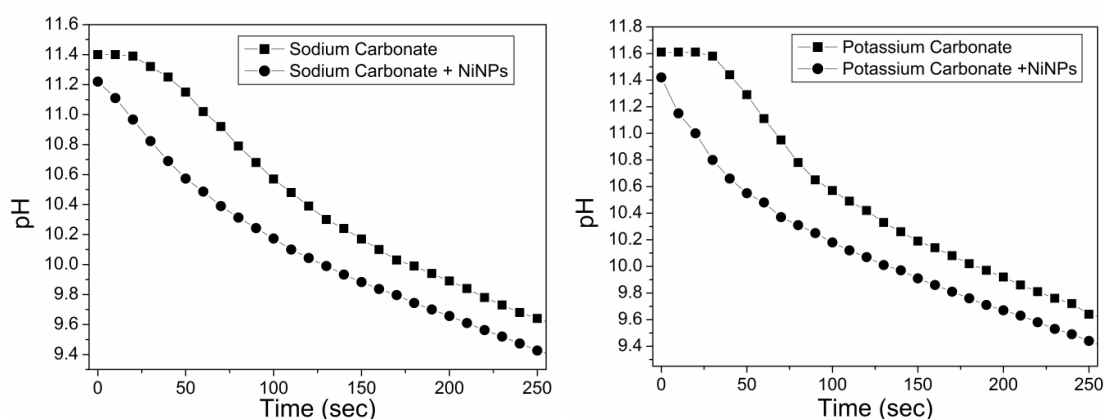


Figure 5.3: pH profiles during bubbling of CO_2 in sodium and potassium carbonate solutions with and without NiNPs.[10]

Figure 5.3 shows the results of the CO_2 bubbling in Na_2CO_3 and K_2CO_3 solutions. It can be seen from the figure 5.3 that in the presence of the NiNPs the rate of CO_2 absorption is faster than without the NiNPs. These results are

similar to the results observed in section 4.3 (figure 4.8). Therefore it can be concluded that there is an enhancement in the hydration of CO_2 in the gas-liquid form in the presence of the NiNPs. It is also known that K_2CO_3 has higher reaction kinetics than Na_2CO_3 with $\text{CO}_{2(\text{aq})}$ [16]. This is the reason that the pH change is faster, in the presence of NiNPs, in K_2CO_3 solution than in Na_2CO_3 solution when CO_2 is bubbled through the solutions, respectively.

A direct comparison with the stopped flow or pH change method with the CO_2 bubbling method is not possible. In the experiments in section 5.1 and 5.2, an initial equilibrium is reached between the $\text{CO}_{2(\text{aq})}$ and HCO_3^- (when we have a CO_2 saturated solution). This equilibrium is then disturbed by adding a buffer or carbonate solution into it and depending on the pH of the solution, a new equilibrium is achieved between $\text{CO}_{2(\text{aq})}$ and HCO_3^- . This change in equilibrium from initial to final is reflected in the pH change of the solution. By studying how fast this equilibrium is achieved, the kinetics of the forward reaction $\text{CO}_{2(\text{aq})} + \text{H}_2\text{O}$ (or OH^-) $\leftrightarrow \text{H}_2\text{CO}_3$ (pH dependent) can be studied. In the case of CO_2 bubbling i.e. when CO_2 is bubbled in carbonate solution, $\text{CO}_{2(\text{aq})}$ reacts rapidly with OH^- in the carbonate solution leading to an equilibrium between $\text{CO}_{2(\text{aq})}$ and HCO_3^- , this is influenced by presence of NiNPs which is observed in the pH change profiles in figure 5.3. This also indicates that NiNPs could just act as enhancers in transfer of CO_2 from gas phase to liquid phase (mass transfer) and not act as a catalyst. In order to distinguish between these two effects (i.e. CO_2 mass transfer enhancement and CO_2 hydration catalysis) the experiment in section 3.2.2 and 3.2.3., chapter 3, was repeated in presence of other inorganic nanoparticles and are discussed below in section 5.5.

5.5 Comparison of catalytic activity of different inorganic nanoparticles for CO₂ hydration.

A major concern raised by Britt [2] for the catalytic activity of NiNPs for hydration of CO₂ is that the increased CO₂ saturation concentration may affect the results of CO₂ hydration kinetics. The theoretical background of the experimental methodology used by Bhaduri and Šiller [3] is presented in section 3.2.3, chapter 3.

Baltrusaitis *et al.* [17-21] reported that Fe₂O₃ and Al₂O₃ nanoparticles (Fe₂O₃NPs of 30 nm) can adsorb CO₂ on their surface in the presence of moisture as carbonates. If an additional thin layer of water is present on the nanoparticle surface the amount of CO₂ adsorbed can be increased up to 5 times (as bicarbonates) to that in the absence of the thin water layer [19]. Therefore another set of experiments were carried out in DI water with Fe₂O₃ nanoparticles, as it was reported that Fe₂O₃ nanoparticles have similar surface chemistry as NiNPs in H₂O environment (see section 4.4, chapter 4 for NiNPs data) [17-21]. Experimental procedure similar to sections 4.2 and 4.3 was repeated with Fe₂O₃ nanoparticles. Since the activity of NiNPs might be also affected by the presence of NiO species on the NiNPs surface (NiO has been detected by XPS, figure 4.10 & figure 4.11[3]), pure NiO nanoparticles were also tested for their catalytic activity for hydration of CO₂.

5.5.1 HRTEM and XRD of the Fe₂O₃ and NiO Nanoparticles

Figure 5.4 and 5.5 shows the TEM images of the Fe₂O₃ and NiO nanoparticles, respectively. The size distribution confirms all the particle size is below the size specified by the manufacturer (i.e. <50 nm) and the majority of the particles have size 8±5 nm and 12±7 nm, for Fe₂O₃ and NiO nanoparticles

respectively. The Fe_2O_3 NPs show presence of a few rod like structures (figure 5.4(a)) and the NiONPs also show some elongated structures (figure 5.5(b & c)). This elongation could be because both particles are magnetic and in presence of electron beam and its electric field they align during the imaging process. For example, similar alignment is observed in HRTEM images of the NiNPs (figure 4.1 top left).

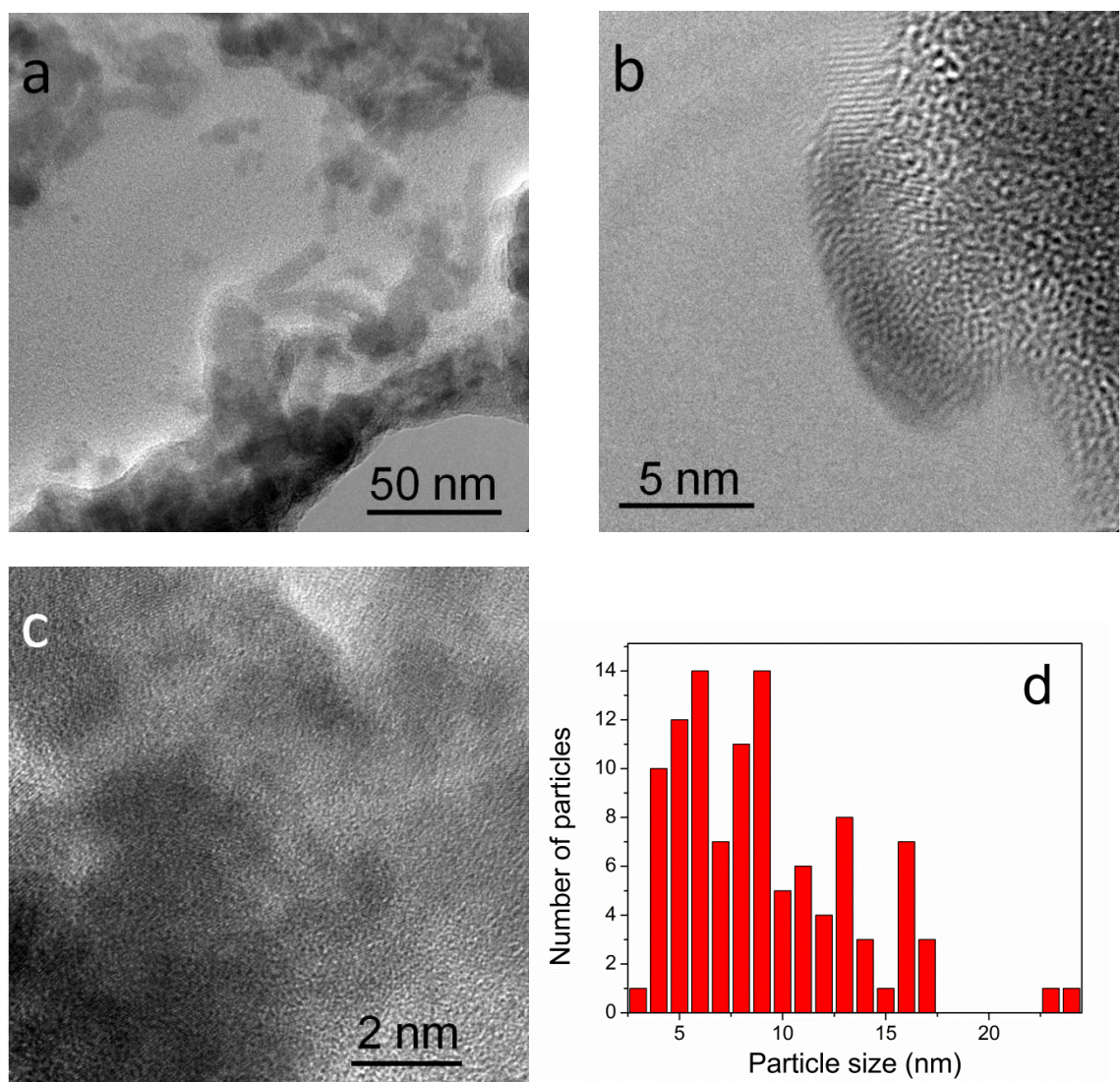


Figure 5.4: Shows the TEM images of the Fe_2O_3 nanoparticles (a, b, and c) and particle size distribution (d).

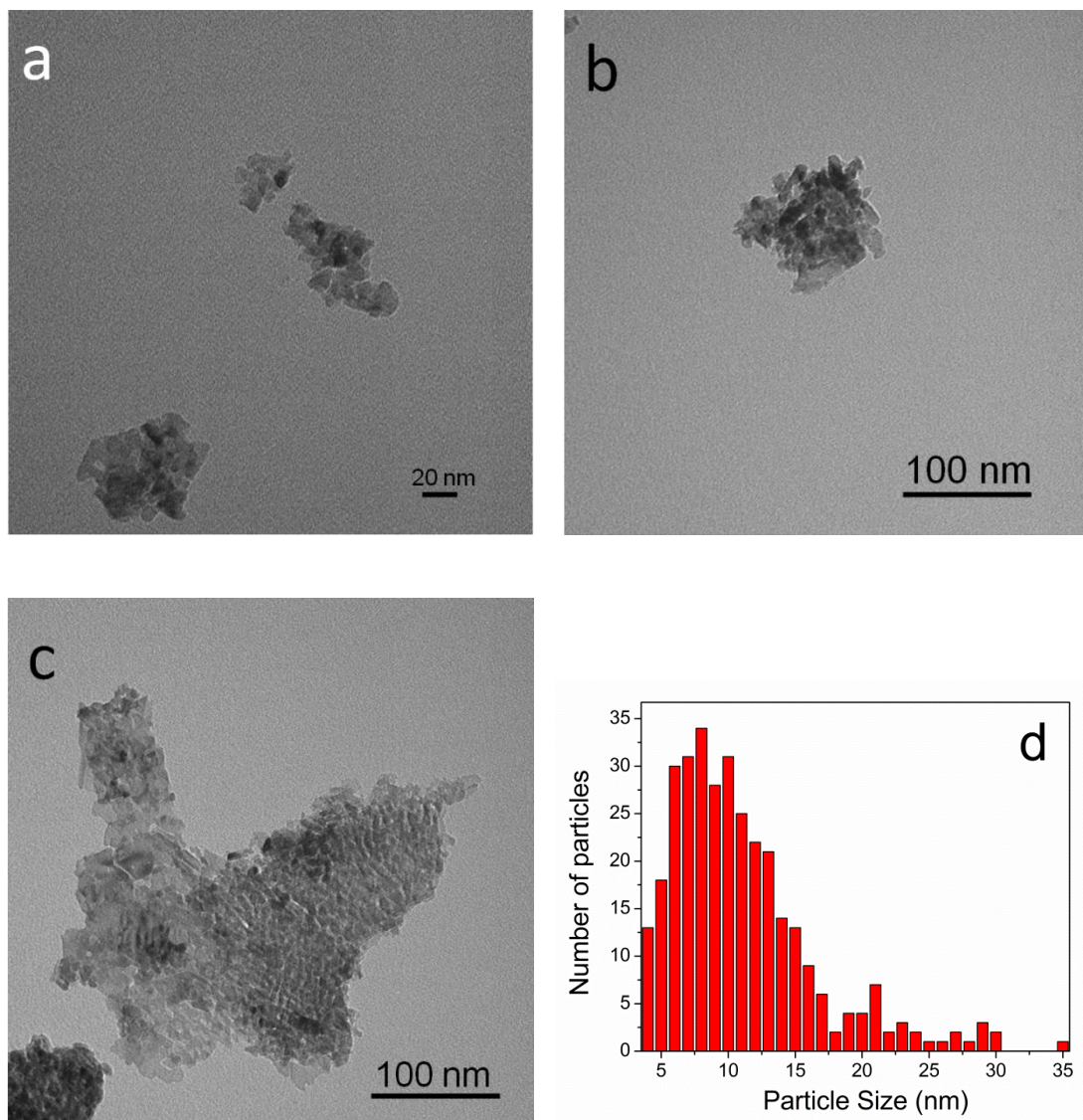


Figure 5.5: Shows the TEM images of the NiO nanoparticles (a, b, and c) and particle size distribution (d).

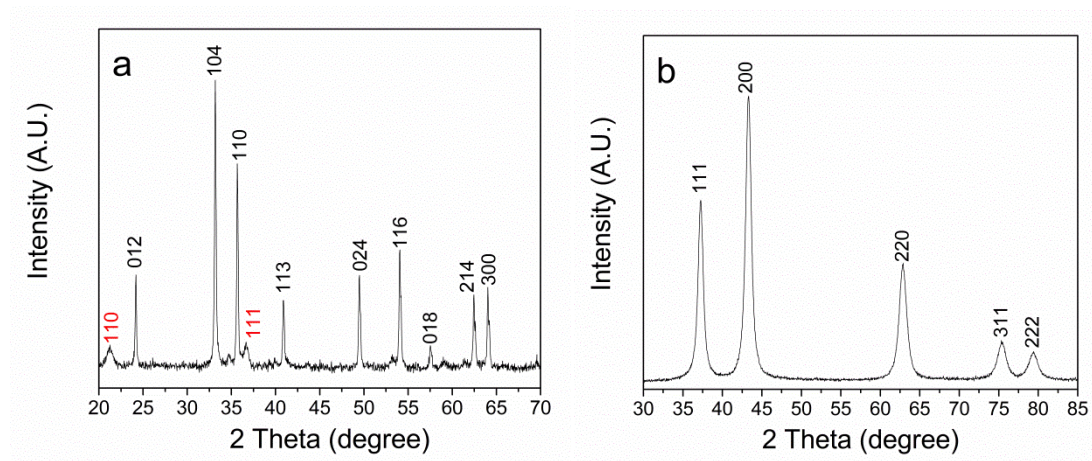


Figure 5.6 X-ray diffraction pattern of a) Fe₂O₃NPs (Fe₂O₃ planes in black and α -FeOOH planes in red) and b) NiONPs respectively.

Figure 5.6a and 5.6b shows the XRD pattern of the Fe₂O₃NPs and NiONPs respectively. The XRD of Fe₂O₃NPs (figure 5.6a) shows presence of the peaks for the following crystal planes (012), (104), (110), (113), (024), (116), (018), (214) and (300), respectively [22]. The Fe₂O₃NPs are very small in size (figure 5.4) and there is some hydration of the nanoparticles which can be seen from the presence of the peaks (110) and (111) peak of FeO(OH) (figure 5.6a indicated in red) [23]. The hydration could be due to the adsorption of moisture from the atmosphere. Figure 5.6b shows the presence of (111), (200), (220), (311) and (222) lattice planes respectively of NiONPs [24].

5.5.2 CO₂ saturation and CO₂ hydration kinetics.

Figure 5.7 shows results of the saturation experiments (chapter 3, section 3.3.3) when CO₂ is bubbled in Fe₂O₃NPs or NiONPs suspension (calculation of the titration in appendix I). In presence of all types of nanoparticles in suspension there is an increase in the amount of CO₂ saturation. The Fe₂O₃NPs and NiONPs suspensions show an increase in CO₂ uptake but there is no dependency on the particle concentration. There is a

three times increase in the CO₂ uptake in presence of Fe₂O₃NPs and NiONPs but NiNPs has a different trend as can be observed in figure 5.7. At 30 ppm nanoparticle concentration, the CO₂ saturation concentration is almost identical for all nanoparticles, therefore 30 ppm concentration was chosen for the bubbling of CO₂ in nanoparticle suspension.

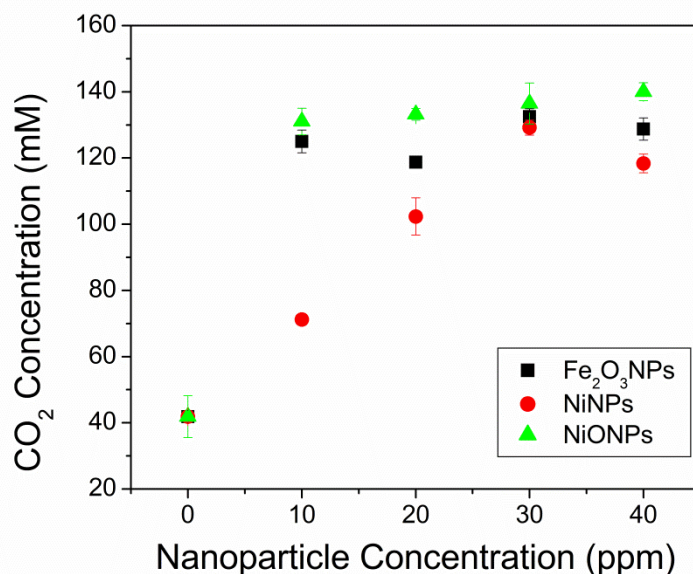


Figure 5.7: Average values of increase in the saturation concentration of CO₂ absorbed in aqueous suspension of Fe₂O₃NPs, NiONPs and NiNPs as a function of particle concentration at room temperature and atmospheric pressure.

As discussed previously in chapter 4 section 4.2 that agglomeration of the nanoparticles is one of the factors that affects the CO₂ saturation concentration in nanoparticle suspension. Figure 5.8 shows the dynamic light scattering data for aggregate size determination of Fe₂O₃NPs, NiONPs and NiNPs suspensions respectively. The agglomerate sizes obtained in the DLS measurements as a function of nanoparticle concentration are summarized in table 5.1. DLS shows particle size larger than those observed in the TEM images due to the formation of passive hydrodynamic layer on the surface of the particles [25, 26].

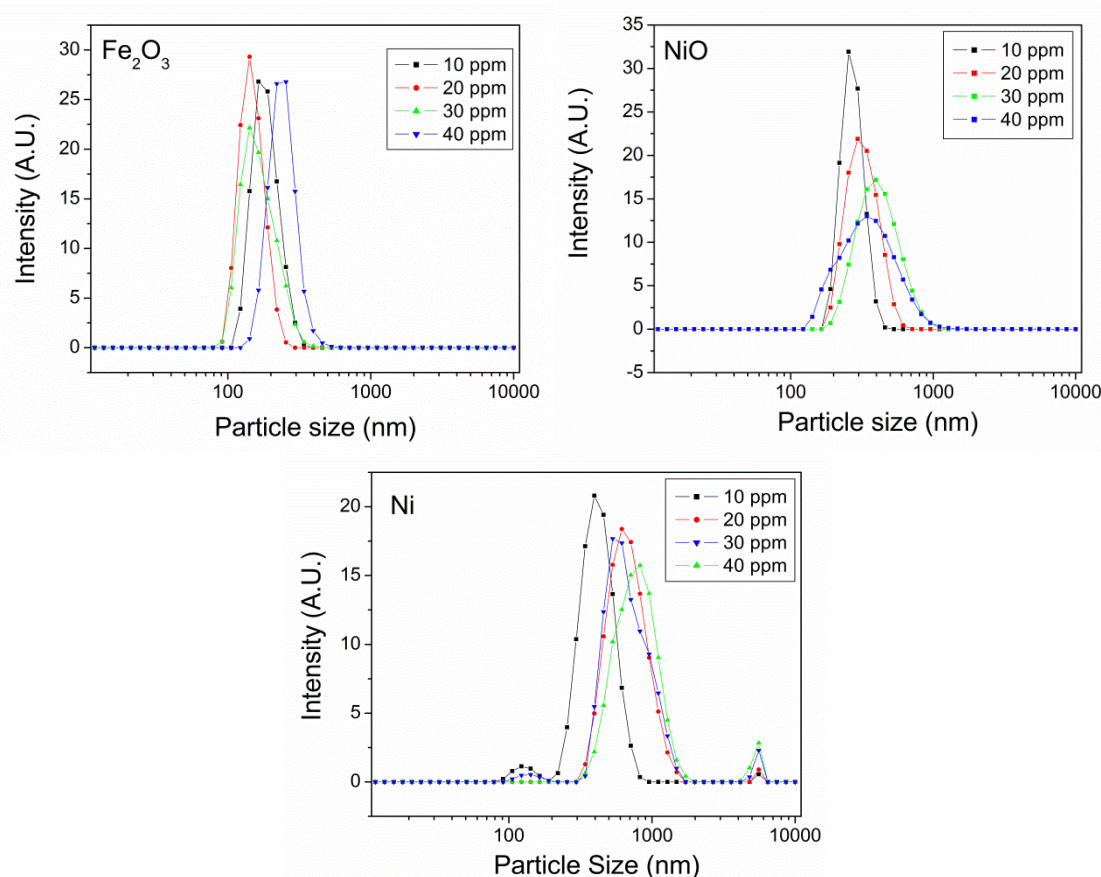


Figure 5.8 Dynamic light scattering data obtained for different nanoparticles suspended in DI water at concentration of 10 ppm, 20 ppm, 30 ppm and 40 ppm respectively.

In DLS the wide peaks indicate high particle size distribution whereas narrow peaks indicate monodispersed particles [26]. Zang *et al.* [27] reported that commercial oxide nanoparticle suspensions in DI water show higher particle size in DLS as compared to TEM because sonication cannot completely de-agglomerate commercial oxide nanoparticles when suspended in DI water. They observed that for commercial Fe₂O₃NPs (5-25 nm particle size) and NiONPs (10-20 nm particle size) the DLS measurements show particle size of 200 ± 10 nm and 750 ± 30 nm respectively at a concentration of 10 ppm dispersed in DI water (18 M Ω /cm conductivity). They also observed that for lab synthesized Fe₂O₃ nanoparticles there was not much difference in particle size obtained by TEM (80-90 nm) and DLS (85 ± 3 nm). Therefore they concluded that sonication cannot completely de-agglomerate nanoparticles to their principle size in suspension [27].

Table 5.1 The nanoparticle aggregate size obtained (in nm) from DLS of different nanoparticle suspensions with increase in nanoparticle concentration.

Particle concentration (ppm)	Aggregate size of Fe ₂ O ₃ (nm)	Aggregate size of Ni (nm)	Aggregate size of NiO (nm)
10	142	389	254
20	163	606	292
30	140	528	384
40	254	821	339

It is observed from Table 5.1 that for particle concentration of 40 ppm Fe₂O₃NPs show large increase in the particle size indicative of particle agglomeration of nanoparticles while for particle concentration of 10, 20 and 30 ppm some variation in particle size is observed. The width of the peaks observed in the DLS results of Fe₂O₃NPs (figure 5.8) show narrow size distribution of the agglomerated nanoparticles as compared to NiONPs and NiNPs at all measured concentrations (10-40 ppm). It was also observed that Fe₂O₃NPs suspension retained a red colour even after 2 years from the preparation of the dispersion. The Fe₂O₃NPs at 10 ppm concentration show similar results as reported by Zhang *et al.* [27].

The NiONPs suspension show a steady increase in the particle size with increase in particle concentration from 10 ppm to 30 ppm respectively (figure 5.8 and table 5.1). It can also be observed that the width of the peak increased with increasing the NiONPs concentration. This indicates that there is a larger size distribution of aggregates formed with increasing NiONPs concentration. At the concentration of 40 ppm NiONPs shows smaller aggregate sized (table 5.1), but the aggregate distribution is larger than those observed at lower

concentrations (see figure 5.8). The DLS results of NiONPs aggregate at 10 ppm concentration show smaller hydrodynamic diameter than that observed by Zhang *et al.* [27].

The DLS results of NiNPs show highest value of particle size of all the studied nanoparticles. There is a small peak observed at an aggregate size of 120 nm at 10 ppm concentration and disappears with increasing particle concentration. The peak observed at 5.58 μm increases with increasing particle concentration. There is an increase in the aggregate size of NiNPs in suspension with increasing NiNPs concentration as observed in table 5.1. Figure 5.8 shows that the width of DLS peaks for NiNPs increases with increasing particle concentration. In this study there is no surfactant used to protect the nanoparticles from agglomeration, leading to rapid agglomeration. As sonication time was the same for all the nanoparticles for DLS analysis it is observed that NiNPs aggregate quicker than the oxide nanoparticles.

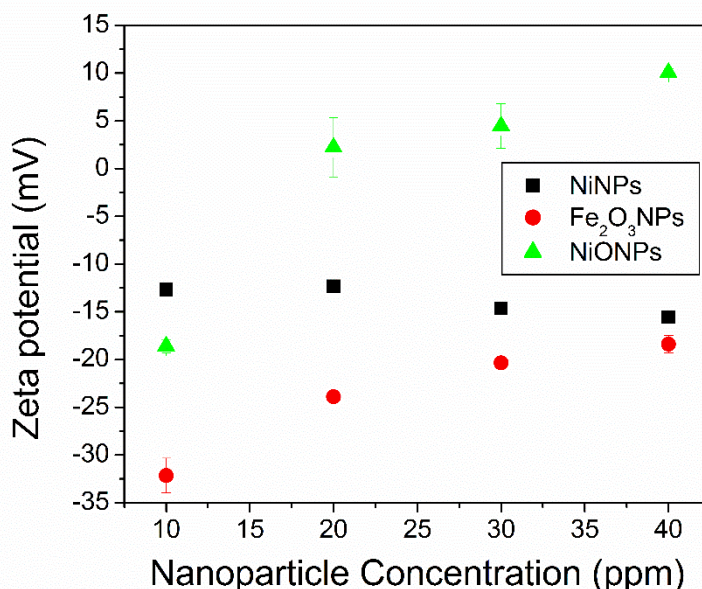


Figure 5.9: Zeta potential values for different nanoparticles (Fe₂O₃NPs- circles, NiNPs- squares, NiONPs-triangles) suspended in DI water at different concentration, measured at room temperature and atmospheric pressure.

Zeta potential is the measure of the surface charge of a particles in suspension. The greater the surface charge of the particles, higher is the repulsive forces between the particles, therefore lower is the rate of agglomeration. Suspensions having high surface charge (positive or negative) have higher suspension stability [26]. At the iso-electric point (when zeta potential value is 0 mV) the particles readily come out of suspension [26]. Figure 5.9 shows the zeta potential values of different nanoparticles suspended in DI water at different nanoparticle concentration. The experimental procedure for zeta potential measurements is given in section 3.3.9, chapter 3. All readings were repeated thrice and average data is presented here. It can be observed that, for oxide nanoparticles (NiONPs and Fe₂O₃NPs) the zeta potential increases with increasing nanoparticle concentration. However, for NiNPs the there is a slight decrease in zeta potential with increasing particle concentration. The Zeta potential for Fe₂O₃NPs is below -20 eV which suggests better stability of the Fe₂O₃NPs suspension [26] as compared to NiNPs and NiONPs suspensions. Both the NiONPs and NiNPs suspension zeta potentials is close to the iso-electric point of 0 eV, suggesting that the suspension stability is poor. The results of zeta potential show similar trend of suspension stability as the DLS results.

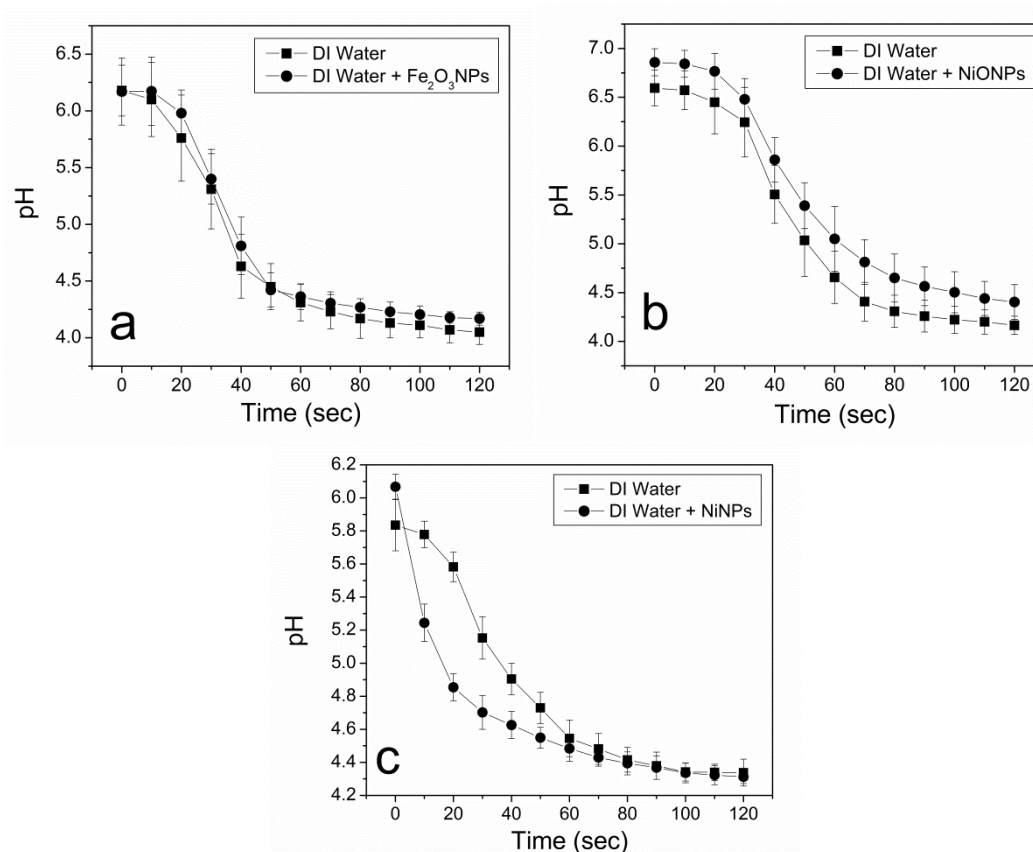


Figure 5.10: Average values of pH change when CO₂ is bubbled through DI water and 30 ppm concentration of a) Fe₂O₃ suspension, b) NiONPs suspension and c) NiNPs suspension.

Figure 5.10 shows the pH changes in 30 ppm suspension of different nanoparticle suspensions when CO₂ is bubbled through a pool of liquid. The experimental methodology is as described in chapter 3, section 3.2.3. (Each experiment was repeated 5 times and average values are presented in figure 5.8.) It is seen from the figure 5.9 in presence of Fe₂O₃NPs and NiONPs the rate of pH change profile is almost identical to that of DI water, but in the presence of NiNPs and NiONPs there is an initial increase in the pH of the solutions. All the nanoparticles at 30 ppm concentration showed almost identical increase in the saturation concentration of CO₂ (figure 5.7). In the pH change experiment only NiNPs show a different pH change profile as compared to DI water, proving that the final CO₂ saturation concentration is not related to the catalytic activity of

CO₂ hydration. Baltrusaitis *et al.* [17-21] proposed the formation for carbonic acid on Fe₂O₃NPs surface based on their gas phase FTIR studies using 40% relative humidity and pure CO₂. The above results indicate that even though the Fe₂O₃NPs show similar surface chemistry as NiNPs in the presence of water followed by exposure to CO₂ (see XPS results, section 5.4.3), they just absorb the CO₂ on the surface and do not catalyse the hydration reaction of CO₂ in solution.

It is also known that nanoparticles can increase the rate of mass transfer in gas-liquid absorption process [28, 29]. There are three plausible mechanisms available for mass transfer enhancement. They are as follows [29]

- a) The presence of nanoparticles increases the transport of gas species from the hydrodynamic boundary layer of the gas-liquid interface to the bulk of the solid. This is done by the adsorption of gas on the nanoparticle surface in the diffusion driven hydrodynamic boundary layer and desorption in the bulk liquid. This is called as shuttle effect or grazing effect.
- b) Another mechanism suggests that the presence of the nanoparticles facilitates the formation of eddy currents in the hydrodynamic boundary layer (due to Brownian motion), leading to reduction in the thickness of the hydrodynamic boundary layer. This reduces the diffusion barrier along the gas-liquid interface and enhances mass transfer coefficient.
- c) The nanoparticles may also affect the gas-liquid interface area by adsorption on the surface of the gas-liquid interface. This increases the diffusion coefficient of the gas in the liquid. For bubble column reactors

the bubble size are affected with the presence of the nanoparticles due to this effect. Thus enhancing the surface area for mass transfer.

All the above mentioned mechanisms have earlier been studied independent of the particle surface chemistry and are generalized observations [28, 29]. Therefore in the presence of Fe₂O₃NPs, NiONPs and NiNPs the enhancement in mass transfer rates are plausible. As stated previously the change in pH of the nanoparticle suspension is due to the formation of carbonic acid alone. Therefore from figure 5.10 it is observed that only in the case of NiNPs there is an increase in the rate of change of pH as compared to DI water and no difference is observed in the case of Fe₂O₃NPs and NiONPs. This suggests that the increase in rate of pH change is due to a chemical reaction and is not just due to increase in rate of mass transfer of CO₂ gas into the nanoparticle suspension.

5.4.3 Chemical characterization of the oxide nanoparticle surfaces before and after CO₂ bubbling.

XPS analysis was carried out only for NiONPs and Fe₂O₃NPs to determine the chemical species on the surface of the nanoparticles in order to suggest and understand the steps in the reaction mechanism. The XPS results of Fe₂O₃NPs before and after CO₂ bubbling can be seen in figure 5.11 and figure 5.12, respectively. The experimental methodology for the XPS analysis is presented in Chapter 3 section 3.3.6. The fitting of the Fe2p peaks were carried out using mixed doublets.

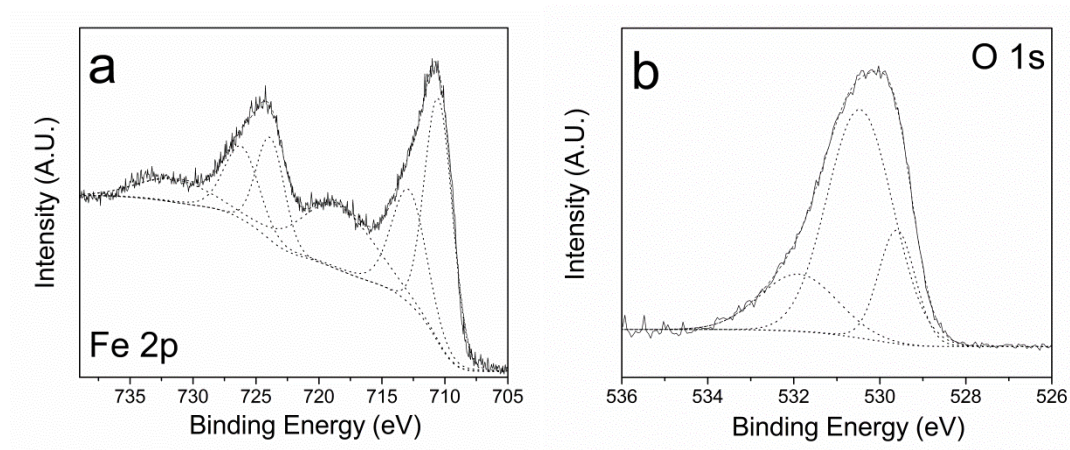


Figure 5.11: XPS spectrum of Fe₂O₃NPs before (a. Fe2p, b. O1s) and after CO₂ bubbling (c. Fe2p and d. O1s).

The chemical species present on the surface of the Fe₂O₃NPs suspended in water can be analysed by observing the Fe2p and O1s spectra seen in figures 5.11a and 5.11b, respectively. The Fe 2p_{3/2} spectrum is fitted with two oxidation states i.e. Fe²⁺ is assigned to the peak at 710.5 eV [30] and Fe³⁺ assigned to peak at 712.8 eV [30]. The O 1s peaks show the presence of three components at 529.6 eV, 530.4 eV and 531.8 eV. The peaks at binding energy of 529.6 eV (O) and 531.8 eV (OH) correspond to the presence of FeOOH species [31, 32] and peak at 529.6 eV also suggests presence of unreacted Fe₂O₃ species [32]. The peak at 530.4 eV indicated presence of Fe₃O₄ species on the surface of the Fe₂O₃NPs [32]. Therefore the XPS results confirm the presence of OH species on the Fe₂O₃NPs, similar results were reported by Baltrusaitis *et al.* [17-21] in their gas adsorption studies using FTIR.

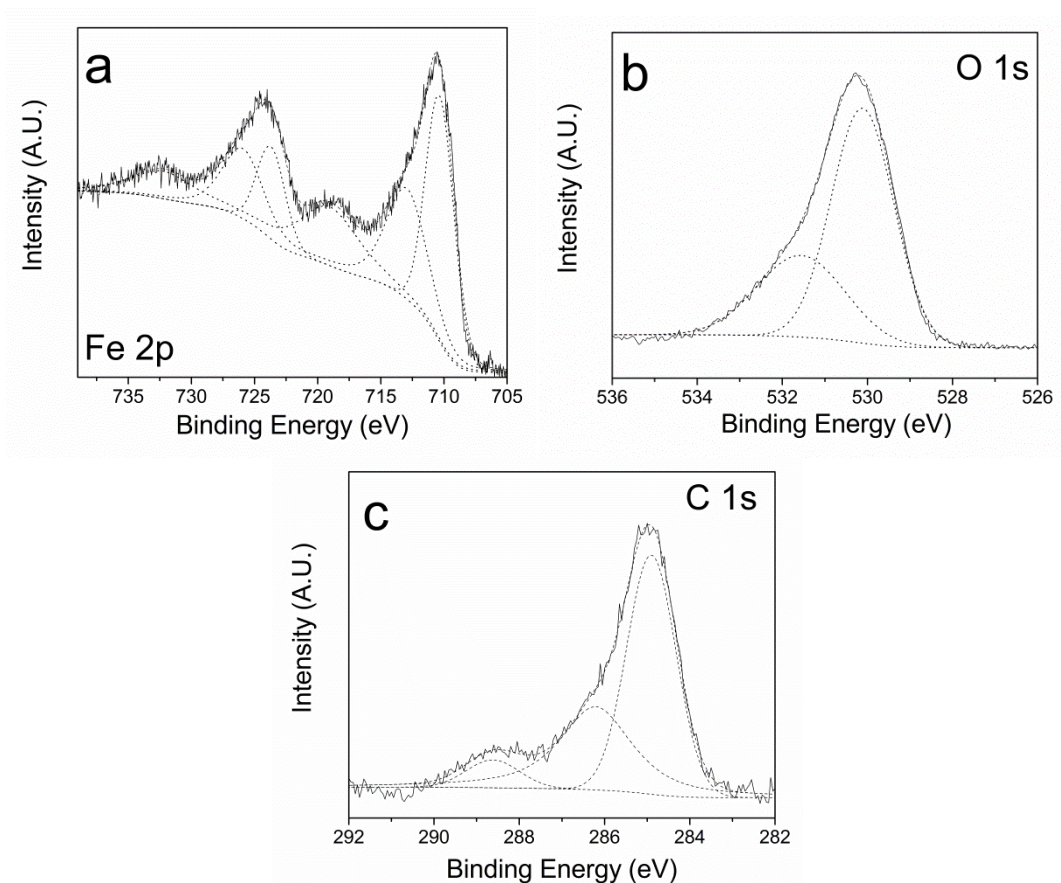


Figure 5.12: XPS spectrum of Fe₂O₃NPs after CO₂ bubbling a) Fe2p, b) O1s and c) C1s.

The surface species present on the Fe₂O₃NPs after CO₂ bubbling can be analysed fitting the by Fe 2p_{3/2}, O 1s and C 1s XPS spectra in figure 5.12a and 5.12b and 5.12c, respectively. The Fe 2p_{3/2} peaks show presence of iron in two oxidation states i.e. 710.3 eV and 712.9 eV assigned to Fe²⁺ and Fe³⁺ respectively [30]. The O1s peak shows presence of two oxygen species on the Fe₂O₃NPs surface at 530.1 eV and 531.7 eV respectively. The first O 1s peak at 530.1 eV can be assigned to chemisorbed CO₂ on the Fe₂O₃NPs surface [33]. The peak at 531.7 eV can be assigned to the presence of CO₃²⁺ species present on the Fe₂O₃NPs surface [34]. The carbon peak at 284.8 is assigned to adventitious carbon, the peak at 286.2 eV is assigned to chemisorbed CO₂ [33] and the peak at 288.9 eV is assigned to CO₃²⁺ [34] on the Fe₂O₃NPs surface. Baltrusaitis *et al.* [17-21] did gas phase studies of adsorption of CO₂ adsorption

on Fe₂O₃NPs in presence of water vapour using attenuated total reflectance Fourier transform Infrared spectroscopy (ATR-FTIR). They also observed presence of OH groups on Fe₂O₃NPs surface after exposure to water vapour and transformation of the OH to CO₃ groups when exposed to CO₂ [19]. Based on their results Baltrusaitis *et al.* [17, 19, 21] suggested that Fe₂O₃NPs would catalyse the hydration of CO₂. Similar chemical species are observed on the surface of Fe₂O₃NPs in this study when the Fe₂O₃NPs are suspended in water and after CO₂ bubbling, but no catalytic activity was observed (section 5.4.2).

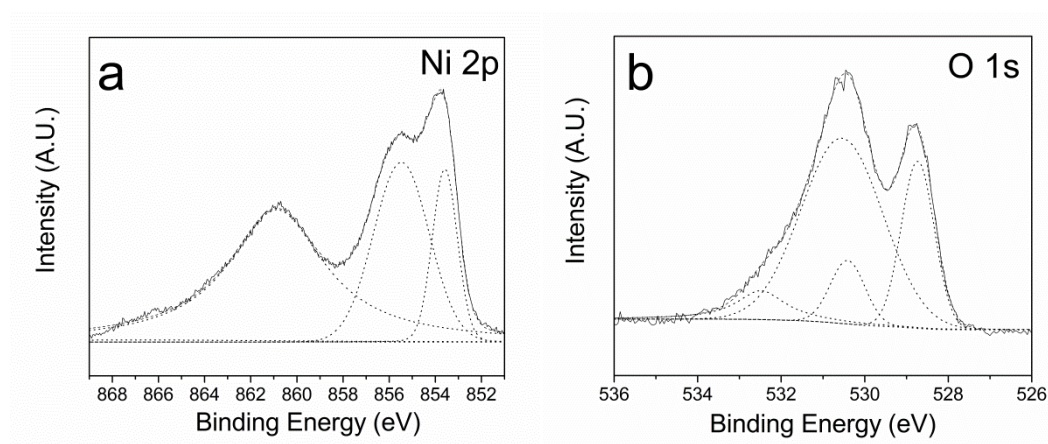


Figure 5.13: XPS spectrum of NiONPs before CO₂ bubbling (a. Ni2p, b. O1s) (c. Ni2p and d. O1s).

The surface chemistry of the NiONPs after suspending in DI water before the introduction of CO₂ was analysed by examination of the Ni 2p_{3/2} and the O 1s core lines (figure 5.13a and 5.13b). The peaks of Ni 2p_{3/2} can be assigned to two components at binding energy of 853.5 eV and 855.4 eV. The peak at 853.5 eV is associated to Ni species present in Ni²⁺ oxidation state [35] and the peak at 855.4 eV is due to presence of Ni³⁺ oxidation state [35]. The O 1s peak shows presence of four different species at binding energies of 528.8 eV, 530.4 eV, 530.5 eV and 532.4 eV respectively. The peak observed at binding energy of 528.8 eV is assigned to presence of NiO and Ni₂O₃ species [36, 37]. The

presence of Ni_2O_3 species also would have a presence of NiOH species at 530.4 eV [36] and associated water at 532.4 eV [38]. The presence of peak at 530.5 eV indicates the presence of NiO-OH species present on the NiONPs surface [38].

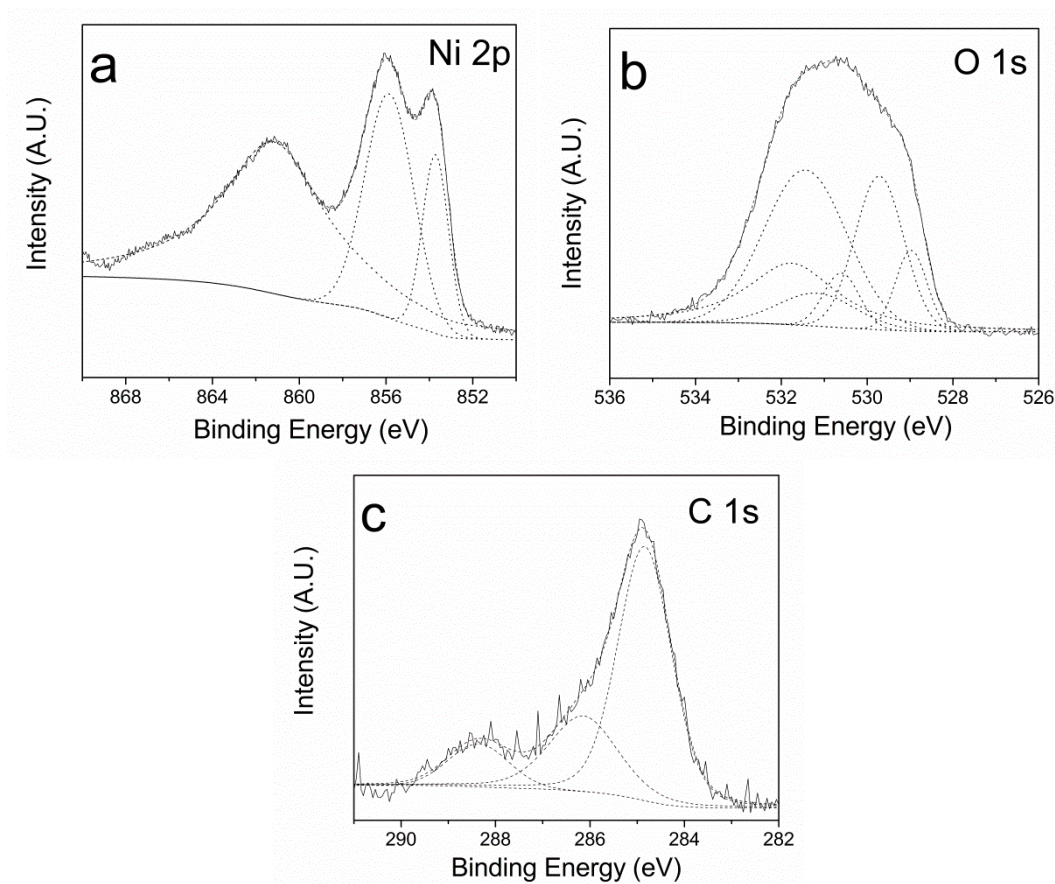


Figure 5.14: XPS spectrum of NiONPs after CO_2 bubbling a) $\text{Ni}2p$, b) $\text{O}1s$ and c) $\text{C}1s$.

The change in surface species after CO_2 bubbling can be analysed by interpretation of the $\text{Ni}2p_{3/2}$, $\text{O}1s$ and $\text{C}1s$ core lines in figure 5.14a, 5.14b and 5.14c, respectively. The $\text{C}1s$ core line shows presence of three peaks at 284.4 eV, 286.2 eV and 288.5 eV, respectively. The peak at 284.8 eV is assigned to adventitious carbon [38]. The peaks in the $\text{Ni}2p_{3/2}$ spectrum shows presence of two oxidation species of Ni i.e. Ni^{2+} at 583.6 eV [35] and Ni^{3+} at 855.6 eV [35] respectively. The $\text{O}1s$ spectra show presence of six different species of oxygen at 528.9 eV, 529.7 eV, 530.5 eV, 531.1 eV, 531.4 eV and 531.7 eV respectively.

The peak at 528.9 eV is assigned to Ni_2O_3 species present on the surface along with the peak 530.6 eV for NiOH and 531.7 eV as associated water with Ni_2O_3 [36]. The O 1s peak at 530.6 eV and the C 1s peak at 286.2 eV is assigned to chemisorbed CO_2 on the surface of the NiONPs [39]. The peak at 529.7 eV can be assigned to NiO [38] and the peak at 531.1 eV can be assigned to NiOOH species [38]. The peak at 531.4 eV can show the presence of CO_3^{2-} species [40, 41] on the surface of the NiONPs. The C 1s peak at 288.5 eV is assigned to the carbonate species of NiCO_3 [42].

The XPS analysis shows the presence of the carbonate species on the NiONPs surface when CO_2 is bubbled in NiONPs suspension in DI water. The presence of the OH groups on the NiONPs surface, when NiONPs are dispersed in DI water and their transformation to CO_3^{2-} species on the NiONPs surface indicates similar reaction steps to that of NiNPs [3] (section 4.4, Chapter 4) and Fe_2O_3 NPs.

5.5 Effect of partial pressure of CO_2 on NiNPs catalysis.

In order to investigate further if the NiNPs are catalyst for hydration of CO_2 , the activity observed in the CO_2 bubbling experiments (section 4.3, section 5.4.2) was studied under different partial pressure of CO_2 . In all the studies discussed above 100% CO_2 gas was used for the analysis of the hydration reaction. In this section the partial pressure of CO_2 is changed to 12% in air and the kinetics has been studied. As described in section 3.2.3, chapter 3, the rate of CO_2 hydration reaction is dependent on the partial pressure of the CO_2 in the gas phase. It can be seen from the calculations in Appendix II, that the rate of CO_2 hydration is dependent on the concentration of $\text{CO}_{2(\text{aq})}$. $\text{CO}_{2(\text{aq})}$ concentration depends on the partial pressure of CO_2 in the gas phase. As the partial pressure decreases in the gas phase, the concentration of CO_2

molecules decreases at the interface and thus the reaction kinetics should decrease [43]. The experimental description can be found in chapter 3, section 3.2.3. Every experiment is repeated five times and average data is presented.

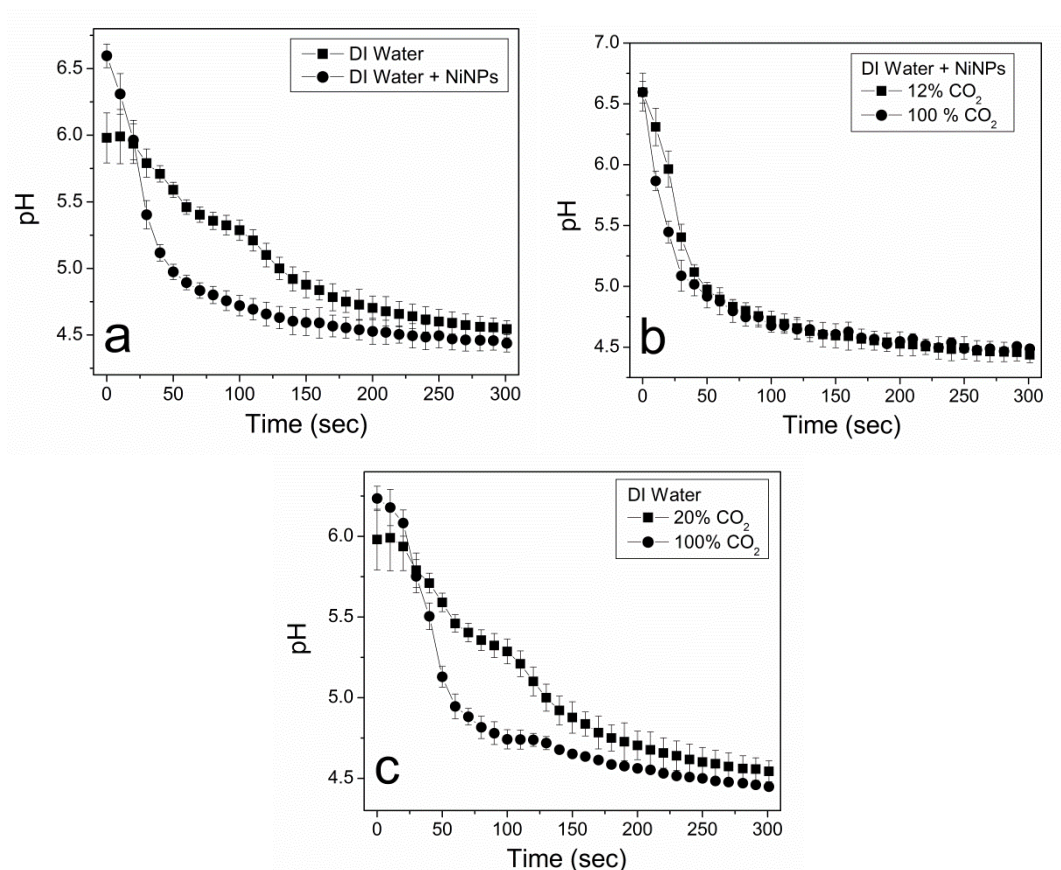


Figure 5.15: a) Average values of pH changes when 12% CO₂-Air mixture is bubbled in DI water and 30ppm NiNPs suspension, b) Average values of pH change pH change when 12% and 100% CO₂ is bubbled in 30 ppm NiNPs suspension and c) Average values of pH change when 12% and 100% CO₂ is bubbled in DI water.

Figure 5.15a shows the change in pH is still more rapid in the presence of NiNPs in suspension as compared to DI water when 12% CO₂-Air gas mixture is bubbled through them. This result is similar to the results observed previously (section 4.3 and section 5.4.2). The results in figure 5.15b show that the catalytic hydration rate of CO₂ (in presence of NiNPs) slightly decreases when the partial pressure of the CO₂ in the gas phase is decreased. However, it

is observed from figure 5.15c that the autocatalytic activity of CO₂ hydration in DI water is highly reduced when the partial pressure of CO₂ is reduced. This proves the assumption made previously about partial pressure of CO₂ affecting the rate of CO₂ hydration.

All the above data suggest that in the presence of the NiNPs the rate limiting step is the transfer of CO_{2g} to CO_{2(aq)} rather than the hydration of reaction of CO₂. The reduction in rate of CO₂ hydration (observed as the rate of pH change in figure 5.15b) is due to the slow gas-liquid mass transfer due to the low partial pressure of CO₂. As described in chapter 3 section 3.2.3 and appendix II, the CO₂ phase transfer rate from gas to DI water is dependent on the partial pressure of CO₂.

5.7 Catalytic activity of synthesised nickel nanowires for hydration of CO₂.

5.7.1 HRTEM, SEM and XRD of nickel nanowires

Figure 5.16 shows the SEM, EDX and TEM images of the synthesised NiNWs following the procedure described in chapter 3, section 3.2.7. The SEM images show similar morphology of the NiNWs as reported by Bentley *et al.* [44]. It is seen from the TEM micrographs (figure 5.16c) that NiNWs are uniform in diameter of 400 ± 100 nm. The insitu EDX of the SEM images of the nanowires confirm the presence of Ni in the observed nanostructures and no presence of any impurities (Al signal is from the aluminium stub). Figure 5.17 shows the XRD pattern for the synthesised nanowires. The peaks observed in the pattern correspond to the lattice planes of (111), (200) and (220) respectively [45].

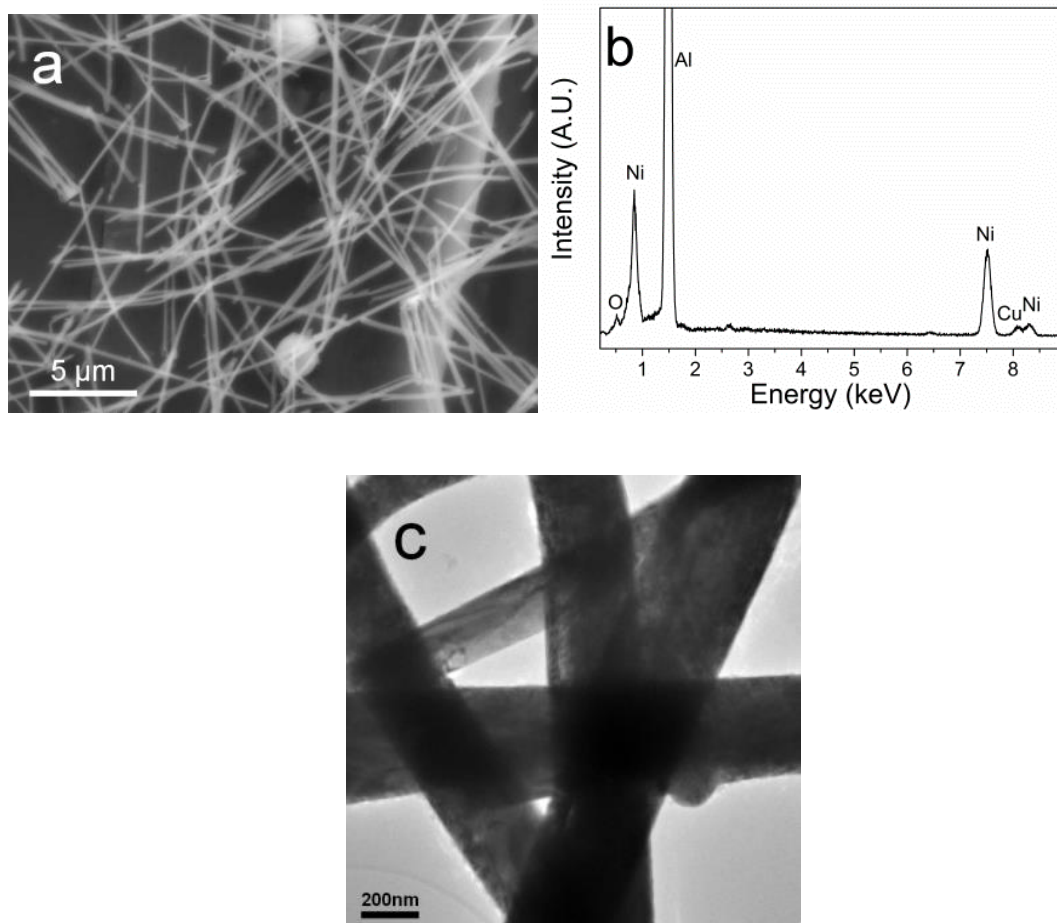


Figure 5.16 a) SEM image and b) EDX of the synthesised NiNWs and C) TEM image of the synthesised NiNWs

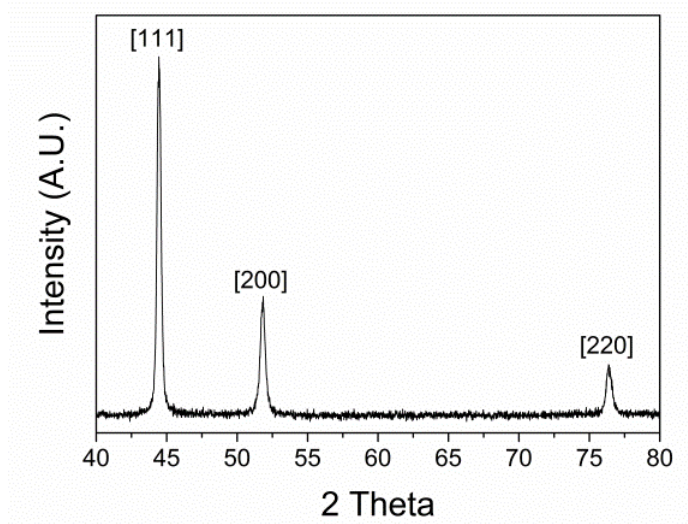


Figure 5.17: XRD pattern of the synthesised NiNWs.

5.7.2 CO₂ saturation and catalytic activity of NiNWs for hydration of CO₂

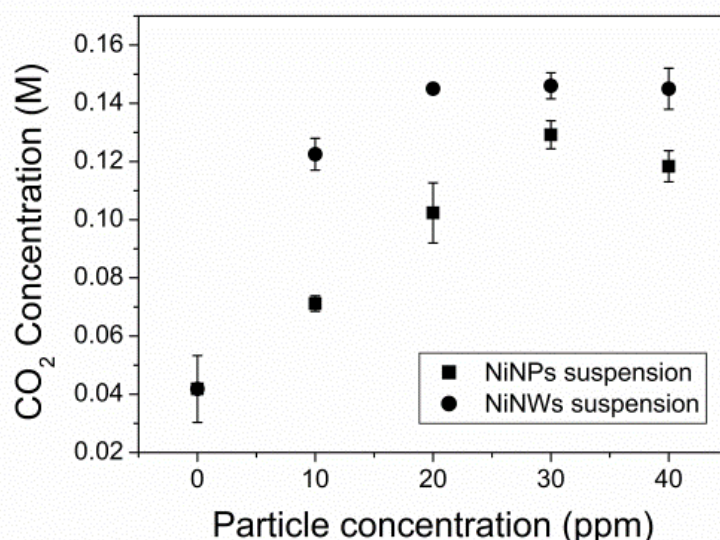


Figure 5.18 Average values of increase in the saturation concentration of CO₂ absorbed with NiNPs and NiNWs suspension as a function of particle concentration at room temperature and atmospheric pressure.

Figure 5.18 shows the saturation concentration of CO₂ in NiNPs and NiNWs suspension with respect to the increase in concentration of the Ni nanostructure. It is observed that the NiNWs are more effective than the NiNPs in the uptake of CO₂ in DI water. The maximum uptake of NiNWs is 3.6 times more than that of DI water at a concentration of 20 ppm as compared to 3 times with NiNPs at 30 ppm concentration. It is observed that the increase in the CO₂ uptake with the NiNPs is linear with the increasing NiNPs concentration till 30 ppm and then there is a decrease in the uptake of CO₂ with further NiNP increase. In the case of the NiNWs there is an exponential increase in the uptake of CO₂ with increase of NiNWs concentration. The maxima is obtained at 20 ppm and with further increase in the NiNWs concentration there is no considerable increase or decrease in the CO₂ uptake.

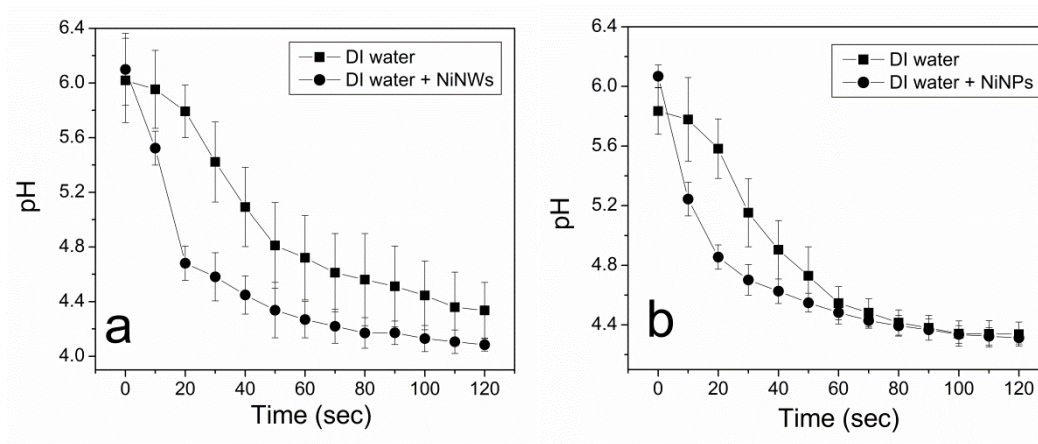


Figure 5.19 Average values of change in pH when CO₂ is bubbled through the liquid at atmospheric pressure and maintained at room temperature, a) in DI water and 30 ppm NiNWs suspension and b) in DI water and 30 ppm NiNPs suspension.

The figure 5.19a shows the pH change in DI water, NiNPs suspension and NiNWs suspension when CO₂ is bubbled through them. The experimental procedure is presented in chapter 3, section 3.2.3. (Each experiment was repeated five times and average data is presented). It can be observed that the presence of the NiNWs show faster pH drop as compared to that of DI water. The change in pH in NiNPs suspension is also faster as compared to pH change in DI water. Both NiNPs and NiNWs show similar catalytic activity for hydration of CO₂.

5.7.3 Chemical characterization of NiNWs surfaces before and after CO₂ bubbling.

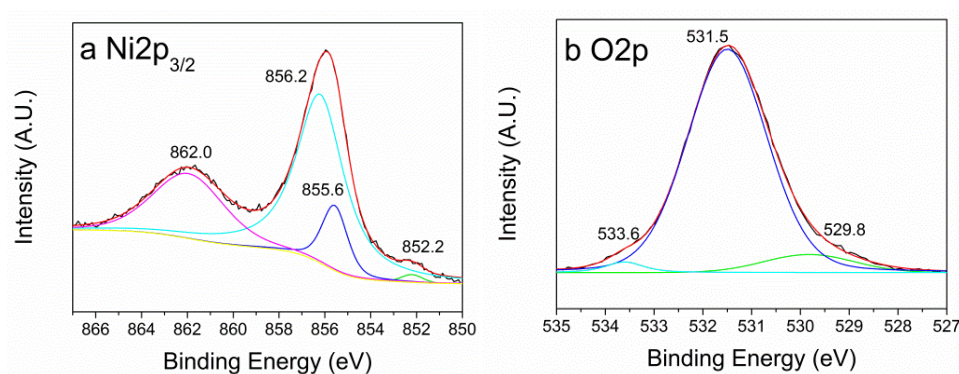


Figure 5.20: X-ray photoemission spectroscopy of NiNWs surface before (a Ni 2p_{3/2} & b O 1s) CO₂ bubbling.

The comparison of different surface species present on the NiNWs is done by examination of the XPS peaks shown in figure 5.20a and 5.20b obtained for Ni 2p_{3/2} and O 2s core lines respectively of the NiNWs before CO₂ bubbling. Figure 5.19a indicates presence of three Ni oxidation peaks at 852.2 eV, 855.6 eV and 856.2 eV respectively. The collective plasmon peak of Ni can be observed at 862.0 eV. The O 2s core line spectrum shows presence of three different oxygen species at binding energies of 529.8 eV, 531.5 eV and 533.6 eV respectively. The Ni 2p_{3/2} peak at 852.2 eV corresponds to metallic Ni⁰ [38, 46] whereas the peaks at 855.6 eV and 856.2 eV correspond to the Ni²⁺ oxidation [38, 46, 47]. The O 1s peak at 529.8 eV corresponds to NiO [47] whereas the peak at 531.5 eV corresponds to that of Ni(OH)_x [47], respectively. It is known that the difference between the hydroxyl oxygen and NiO is about 1.7 eV [48]. The O 1s peak at 533.6 eV is associated to multilayer of adsorbed water on the NiNWs surface [47, 49]. The relative intensity of O 2s peaks of NiO and Ni(OH)_x is higher in the NiNWs as compared to NiNPs (see figure 4.10a, section 4.4, chapter 4) [3]. This may be one of the reasons for the increased CO₂ saturation value observed in figure 5.17.

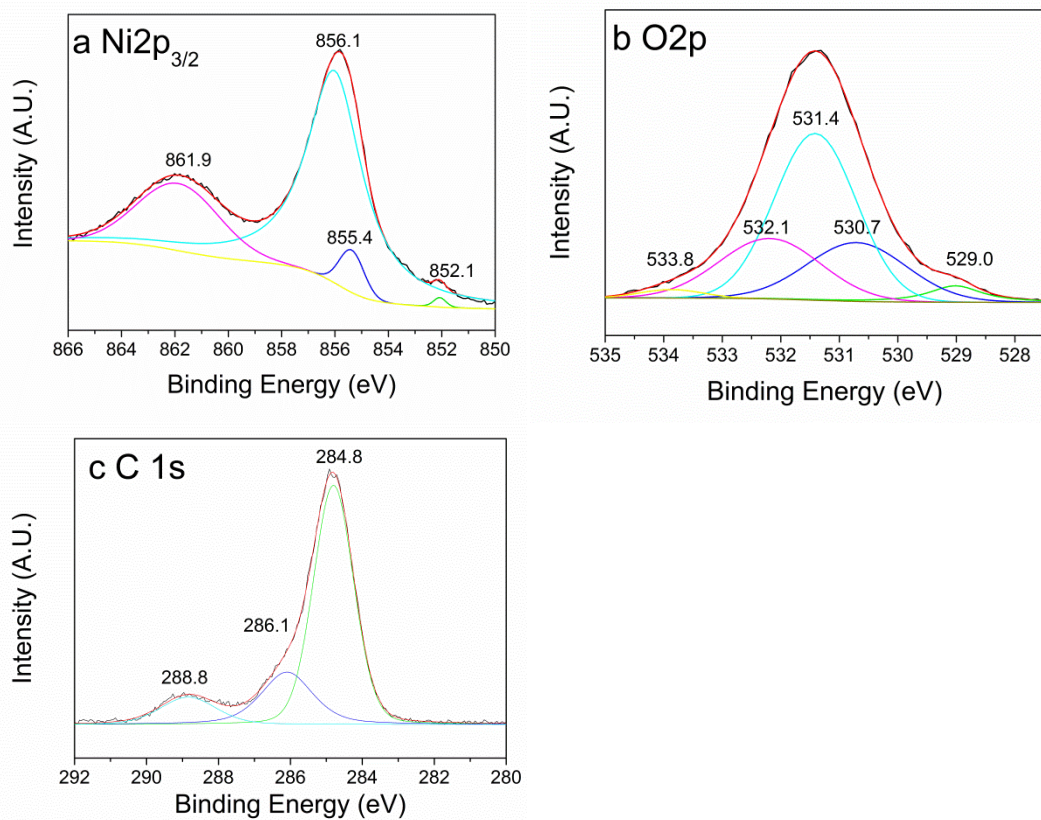


Figure 5.21: XPS spectra of NiNWs after bubbling with carbon dioxide; (a) Ni 2p_{3/2}, (b) O 1s and (C) C 1s.

Figures 5.21a, 5.21b and 5.21c show the XPS core lines of Ni2p_{3/2}, O1s and C1s after CO₂ bubbling. After the CO₂ introduction to the NiNWs suspension it is observed that there is a considerable change in the O 1s core line spectrum of the NiNWs. It can be observed that Ni 2p_{3/2} spectral line can be fitted with three Ni oxidation states at 852.1 eV, 855.4 eV and 856.1 eV, respectively and the O 1s spectral line can be fitted with five components at 529.0 eV, 530.7 eV, 531.4 eV, 532.1 eV, and 533.8 eV respectively. The Ni 2p_{3/2} peak at 852.1 eV corresponds to metallic Ni⁰ [38, 46], whereas the peaks at 855.4 eV and 856.1 eV correspond to Ni²⁺ oxidation state of Ni [38, 46, 47]. The O 1s peak at 529.0 eV corresponds to the NiO [35] and the peak at 533.8 eV corresponds to the multilayer of water on the NiNWs surface [47]. The O1s peak at 532.1 eV is assigned to adsorbed O₂ on the NiNWs surface [46]. The O 1s peaks at 530.7 eV indicates the presence of CO₂ adsorbed on the NiNWs

surface [39]. The peak at 531.4 eV is assigned to the carbonate on the NiNWs [50]. The C 1s peak at 286.1 eV corresponds to chemisorbed CO₂ [39] and that at 288.1 eV to carbonate species [51]. From the XPS results therefore the presence of Ni(CO₃)_x species can be confirmed.

5.8 Conclusion

The NiNPs catalysis for CO₂ hydration was proven by the method used by Mirjafari *et al.* [1] and was found to be pH dependent. Fe₂O₃NPs and NiONPs were used for comparison in order to show that the NiNP catalysed CO₂ hydration is independent of final saturation concentration of dissolved CO₂. Although it has been suggested by Baltrusaitis *et al.* [17-21] based on their gas phase analysis that oxide nanoparticles (Fe₂O₃NPs) can enhance the CO₂ hydration. In this study it was observed that it is not valid for bulk aqueous systems. Furthermore NiONPs have similar surface chemistry as NiNPs, they do not show any catalytic activity in the CO₂ bubbling experiment. It was also found that the partial pressure of CO₂ affects the hydration of CO₂. Even at low CO₂ partial pressure NiNPs showed catalytic activity for hydration of CO₂. The reduction of the partial pressure of CO₂ reduces the catalysed reaction rate of CO₂ hydration in presence of NiNPs because the rate limiting step is the transfer of CO_{2g} to CO_{2(aq)} rather than the hydration reaction of CO₂. Nickel nanowires were synthesised using the method described by Bentley *et al.* [44]. The NiNWs show higher saturation amount of CO₂ than NiNPs. The XPS analysis of the NiNWs show similar surface species as NiNPs when exposed to DI water and CO₂ (bubbled in NiNWs suspension). The relative intensity of Ni(OH)_x and H₂O_{ads} on the NiNWs is higher than NiNPs which could be one of the reasons for the higher CO₂ absorption in solution.

References

- [1] P. Mirjafari, K. Asghari, N. Mahinpey, Investigating the Application of Enzyme Carbonic Anhydrase for CO₂ Sequestration Purposes, *Industrial & Engineering Chemistry Research*, 46 (2007) 921-926.
- [2] D. Britt, Comment on "Nickel nanoparticles catalyse reversible hydration of carbon dioxide for mineralization carbon capture and storage" by G. Bhaduri and L. Šiller, *Catal. Sci. Technol.*, 2013, 3, 1234, *Catalysis Science & Technology*, 3 (2013) 2195-2196.
- [3] G.A. Bhaduri, L. Šiller, Nickel nanoparticles catalyse reversible hydration of carbon dioxide for mineralization carbon capture and storage, *Catalysis Science & Technology*, 3 (2013) 1234-1239.
- [4] A. Gomez-Hens, D. Perez-Bendito, The stopped-flow technique in analytical chemistry, *Analytica Chimica Acta*, 242 (1991) 147-177.
- [5] D.A. Palmer, R. Van Eldik, The chemistry of metal carbonato and carbon dioxide complexes, *Chemical Reviews*, 83 (1983) 651-731.
- [6] D.M. Kern, The hydration of carbon dioxide, *Journal of Chemical Education*, 37 (1960) 14.
- [7] R.G. Khalifah, The Carbon Dioxide Hydration Activity of Carbonic Anhydrase: I. stop-flow kinetic study of native human isoenzymen B and C, *Journal of Biological Chemistry*, 246 (1971) 2561-2573.
- [8] Y. Pocker, D.W. Bjorkquist, Stopped-flow studies of carbon dioxide hydration and bicarbonate dehydration in water and water-d₂. Acid-base and metal ion catalysis, *Journal of the American Chemical Society*, 99 (1977) 6537-6543.
- [9] X. Wang, W. Conway, R. Burns, N. McCann, M. Maeder, Comprehensive Study of the Hydration and Dehydration Reactions of Carbon Dioxide in Aqueous Solution, *The Journal of Physical Chemistry A*, 114 (2009) 1734-1740.
- [10] G.A. Bhaduri, R.A. Henderson, L. Šiller, Reply to the 'Comment on "Nickel nanoparticles catalyse reversible hydration of carbon dioxide for mineralization carbon capture and storage"' by D. Britt, *Catal. Sci. Technol.*, 2013, 3, DOI: 10.1039/C3CY00142C, *Catalysis Science & Technology*, 3 (2013) 2197-2198.
- [11] R. Brinkman, R. Margaria, F.J.W. Roughton, The Kinetics of the Carbon Dioxide-Carbonic Acid Reaction, *Philosophical Transactions of the Royal Society of London. Series A, Containing Papers of a Mathematical or Physical Character*, 232 (1934) 65-97.
- [12] F.J.J. Buytendyk, R. Brinkman, H.W. Mook, A Study of the System Carbonic Acid, Carbon Dioxide and Water, *Biochemical Journal*, 21 (1927) 576-584.

- [13] N.K. Das, T. Shoji, A density functional study of atomic oxygen and water molecule adsorption on Ni(001) and chromium-substituted Ni(001) surfaces, *Applied Surface Science*, 258 (2011) 442-447.
- [14] D.-H. Kim, M. Vinoba, W.-S. Shin, K.-S. Lim, S.-K. Jeong, S.-H. Kim, Biomimetic sequestration of carbon dioxide using an enzyme extracted from oyster shell, *Korean J. Chem. Eng.*, 28 (2011) 2081-2085.
- [15] R.E. Loewenthal, G.V.R. Marais, *Carbonate Chemistry of Aquatic Systems: Theory and Applications*, Ann Arbor Science, Ann Arbor, 1976.
- [16] I.R.A.T.O. Nysing, I.H. Kramers, Absorption of CO₂ in carbonate bicarbonate buffer solutions in a wetted wall column, *Chemical Engineering Science*, 8 (1958) 81-89.
- [17] J. Baltrusaitis, J.D. Schuttlefield, E. Zeitler, J.H. Jensen, V.H. Grassian, Surface reactions of carbon dioxide at the adsorbed water-oxide interface, *Journal of Physical Chemistry C*, 111 (2007) 14870-14880.
- [18] J. Baltrusaitis, J. Schuttlefield, E. Zeitler, V.H. Grassian, Carbon dioxide adsorption on oxide nanoparticle surfaces, *Chemical Engineering Journal*, 170 (2011) 471-481.
- [19] J. Baltrusaitis, V.H. Grassian, Surface reactions of carbon dioxide at the adsorbed water-iron oxide interface, *Journal of Physical Chemistry B*, 109 (2005) 12227-12230.
- [20] J. Baltrusaitis, V.H. Grassian, Carbonic Acid Formation from Reaction of Carbon Dioxide and Water Coordinated to Al(OH)₃: A Quantum Chemical Study, *The Journal of Physical Chemistry A*, 114 (2010) 2350-2356.
- [21] J. Baltrusaitis, J.H. Jensen, V.H. Grassian, FTIR Spectroscopy Combined with Isotope Labeling and Quantum Chemical Calculations to Investigate Adsorbed Bicarbonate Formation Following Reaction of Carbon Dioxide with Surface Hydroxyl Groups on Fe₂O₃ and Al₂O₃, *The Journal of Physical Chemistry B*, 110 (2006) 12005-12016.
- [22] M.R. Joya, J. Baron-Jaimez, J. Barba-Ortega, Preparation and characterization of Fe₂O₃ nanoparticles, *Journal of Physics: Conference Series*, 466, (2013), 012004.
- [23] G.H. Lee, S.H. Kim, B.J. Choi, S.H. Huh, Y. Chang, B. Kim, J. Park, S.J. Oh, Magnetic properties of needle like α -FeOOH and γ -FeOOH nanoparticles, *Journal of the Korean Physical Society*, 45 (2004) 1019-1024.
- [24] H. Qiao, Z. Wei, H. Yang, L. Zhu, X. Yan, Preparation and characterization of NiO nanoparticles by anodic arc plasma method, *Journal of Nanomaterials*, (2009) 795928 (795921-795925).
- [25] J. Lim, S. Yeap, H. Che, S. Low, Characterization of magnetic nanoparticle by dynamic light scattering, *Nanoscale Research Letters*, 8 (2013) 381.

- [26] R.J. Hunter, Foundations of Colloid Science, Oxford University Press, Oxford, 2001.
- [27] Y. Zhang, Y. Chen, P. Westerhoff, K. Hristovski, J.C. Crittenden, Stability of commercial metal oxide nanoparticles in water, *Water Research*, 42 (2008) 2204-2212.
- [28] S.-S. Ashrafmansouri, M. Nasr Esfahany, Mass transfer in nanofluids: A review, *International Journal of Thermal Sciences*, 82 (2014) 84-99.
- [29] C. Pang, J.W. Lee, Y.T. Kang, Review on combined heat and mass transfer characteristics in nanofluids, *International Journal of Thermal Sciences*, 87 (2015) 49-67.
- [30] D. Brion, Etude par spectroscopie de photoelectrons de la degradation superficielle de FeS₂, CuFeS₂, ZnS et PbS a l'air et dans l'eau, *Applications of Surface Science*, 5 (1980) 133-152.
- [31] A.P. Grosvenor, B.A. Kobe, M.C. Biesinger, N.S. McIntyre, Investigation of multiplet splitting of Fe 2p XPS spectra and bonding in iron compounds, *Surface and Interface Analysis*, 36 (2004) 1564-1574.
- [32] A.P. Grosvenor, B.A. Kobe, N.S. McIntyre, Studies of the oxidation of iron by water vapour using X-ray photoelectron spectroscopy and QUASES™, *Surface Science*, 572 (2004) 217-227.
- [33] H.M. Ismail, D.A. Cadenhead, M.I. Zaki, Surface Reactivity of Iron Oxide Pigmentary Powders toward Atmospheric Components: XPS, FESEM, and Gravimetry of CO and CO₂ Adsorption, *Journal of Colloid and Interface Science*, 194 (1997) 482-488.
- [34] J.K. Heuer, J.F. Stubbins, An XPS characterization of FeCO₃ films from CO₂ corrosion, *Corrosion Science*, 41 (1999) 1231-1243.
- [35] K. Lian, S.J. Thorpe, D.W. Kirk, Electrochemical and surface characterization of electrocatalytically active amorphous Ni-Co alloys, *Electrochimica Acta*, 37 (1992) 2029-2041.
- [36] A.N. Mansour, C.A. Melendres, Characterization of Ni₂O₃·6H₂O by XPS, *Surface Science Spectra*, 3 (1994) 263-270.
- [37] A.N. Mansour, Characterization of NiO by XPS, *Surface Science Spectra*, 3 (1994) 231-238.
- [38] B.P. Payne, M.C. Biesinger, N.S. McIntyre, The study of polycrystalline nickel metal oxidation by water vapour, *Journal of Electron Spectroscopy and Related Phenomena*, 175 (2009) 55-65.
- [39] E. Vesselli, L.D. Rogatis, X. Ding, A. Baraldi, L. Savio, L. Vattuone, M. Rocca, P. Fornasiero, M. Peressi, A. Baldereschi, R. Rosei, G. Comelli, Carbon Dioxide Hydrogenation on Ni (110), *Journal of the American Chemical Society*, 130 (2008) 11417-11422.

- [40] R.J. Behm, C.R. Brundle, On the formation and bonding of a surface carbonate on Ni (100), *Surface Science*, 255 (1991) 327-343.
- [41] D.E.A. Gordon, R.M. Lambert, CO₂ adsorption on oxygen-modified Ni(111), *Surface Science*, 287–288, Part 1 (1993) 114-118.
- [42] Y. Jia, T. Luo, X.-Y. Yu, J.-H. Liu, X.-J. Huang, Surfactant-free preparation of nickel carbonate hydroxide in aqueous solution and its toxic ion-exchange properties, *New Journal of Chemistry*, 37 (2013) 534-539.
- [43] L.K. Doraiswami, M.M. Sharma, *Heterogeneous reactions: Analysis, Examples and Reactor Design*, Volume 2, John Wiley & Sons, New York, USA, 1984.
- [44] A.K. Bentley, M. Farhoud, A.B. Ellis, A.-M.L. Nickel, G.C. Lisensky, W.C. Crone, Template Synthesis and Magnetic Manipulation of Nickel Nanowires, *Journal of Chemical Education*, 82 (2005) 765.
- [45] S. Dellis, A. Christoulaki, N. Spiliopoulos, D.L. Anastassopoulos, A.A. Vradis, Electrochemical synthesis of large diameter monocrystalline nickel nanowires in porous alumina membranes, *Journal of Applied Physics*, 114 (2013) 164308.
- [46] M.C. Biesinger, B.P. Payne, L.W.M. Lau, A. Gerson, R.S.C. Smart, X-ray photoelectron spectroscopic chemical state quantification of mixed nickel metal, oxide and hydroxide systems, *Surface and Interface Analysis*, 41 (2009) 324-332.
- [47] N. Kitakatsu, V. Maurice, C. Hinnen, P. Marcus, Surface hydroxylation and local structure of NiO thin films formed on Ni(111), *Surface Science*, 407 (1998) 36-58.
- [48] J. Ciston, A. Subramanian, D.M. Kienzle, L.D. Marks, Why the case for clean surfaces does not hold water: Structure and morphology of hydroxylated nickel oxide (001), *Surface Science*, 604 (2010) 155-164.
- [49] A.F. Carley, S. Rassias, M.W. Roberts, The specificity of surface oxygen in the activation of adsorbed water at metal surfaces, *Surface Science*, 135 (1983) 35-51.
- [50] S.L. Stipp, M.F. Hochella Jr, Structure and bonding environments at the calcite surface as observed with X-ray photoelectron spectroscopy (XPS) and low energy electron diffraction (LEED), *Geochimica et Cosmochimica Acta*, 55 (1991) 1723-1736.
- [51] M. Cerruti, C.L. Bianchi, F. Bonino, A. Damin, A. Perardi, C. Morterra, Surface Modifications of Bioglass Immersed in TRIS-Buffered Solution. A Multitechnical Spectroscopic Study, *The Journal of Physical Chemistry B*, 109 (2005) 14496-14505.

Catalytic activity of NiNPs for hydration of CO₂ (Part III): Photo-catalysis and temperature dependence

Chapter 6 presents data on the photo-catalytic activity of NiNPs and the temperature dependence of the NiNPs catalysis for hydration of CO₂. The NiNPs show higher catalytic activity in presence of sunlight than in its absence. It is observed that sunlight has an influence on the clathrate structure of liquid water which reduces its reaction rate with CO₂. NiNPs surface are unaffected with the change in clathrate structure of DI water. This is one of the reasons for the observed enhancement in the catalytic activity of NiNPs. The NiNPs also have a surface plasmon resonance (SPR) in the visible range that could lead to increased rate of H₂O dissociation on the NiNPs surface. Dissociation of H₂O on the NiNPs surface is the first step of hydration of CO₂. Therefore the increase in H₂O dissociation due to SPR is considered as another reason for the photo-

catalytic enhancement of CO₂ hydration by NiNPs. CO₂ saturation in NiNPs suspension and catalytic activity of NiNPs is tested at temperatures between 10-60 °C. There is a threefold increase in CO₂ saturation concentration in presence of NiNPs and is independent of temperature. The NiNPs catalysis show temperature dependence in the temperature range of 10-60 °C. The optimum catalytic activity was observed between 20-30 °C.

6.1 Photo- catalysed hydration of CO₂ by NiNPs

Nickel is an active photo-catalyst for various oxidation and reduction reactions like hydrogenation, desulfurization, reduction of organic compounds etc [1-3]. Therefore the the photo-catalytic activity of NiNPs for the hydration of CO₂ is studied. The experimental procedure for the photochemical study is presented in chapter 3 section 3.3.7. All the experiments were repeated five times and the average data is presented below.

6.1.1 CO₂ hydration kinetics in absence and presence of light (with and without IR filter)

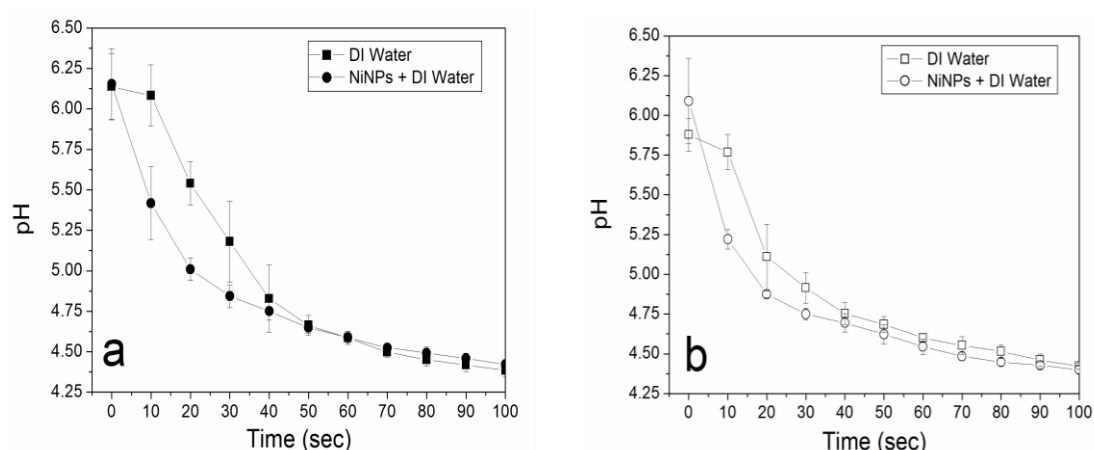


Figure 6.1: The average values of change in pH of DI water (squares) and NiNPs suspension (circle) when CO₂ is bubbled (a) in the presence of solar simulator with wavelength range of 200-2400 nm and (b) in the dark.

Figure 6.1a and 6.1b show the pH changes when CO₂ is bubbled in DI water or NiNPs suspension in the presence and absence of light, respectively. The solar simulator used as a light source had an emission of light in the wavelength range of 200-2400 nm. The pH profiles show a rapid change in the pH in the presence of the NiNPs than in its absence. The results observed in this study are similar to the ones observed previously [4-6] (chapter 4 section 4.3 and chapter 5 section 5.7.2). The activity of the NiNP catalysis can be evaluated by determining the proximity of the catalysed and uncatalysed pH profiles. This is done by comparing the area under the uncatalysed and catalysed pH change curves.

Comparison of the area between the pH profiles in figure 6.1a and 6.1b can be used to demonstrate an effect of light on the catalytic rate of CO₂ hydration in the presence of NiNPs. The integration of the curves provides a numerical value for comparison of catalytic activity. The difference in the integral value (between catalysed and uncatalysed curves) gives a numerical comparison of the proximity of the catalysed and uncatalysed pH profile curves. Comparing the area thus obtained under different irradiation conditions provides information on the enhancement in the activity of the catalyst. Numerical integration of the pH profiles in figure 6.1a and 6.1b was carried out in order to determine the area between the pH profiles in both the graphs. It was observed that area obtained under the curve shown in fig 6.1a is 24.1 % higher than that obtained under the curve shown in fig 6.1b. This qualitatively proves that there is an enhancement in the comparative activity of NiNPs in the presence of light than in dark.

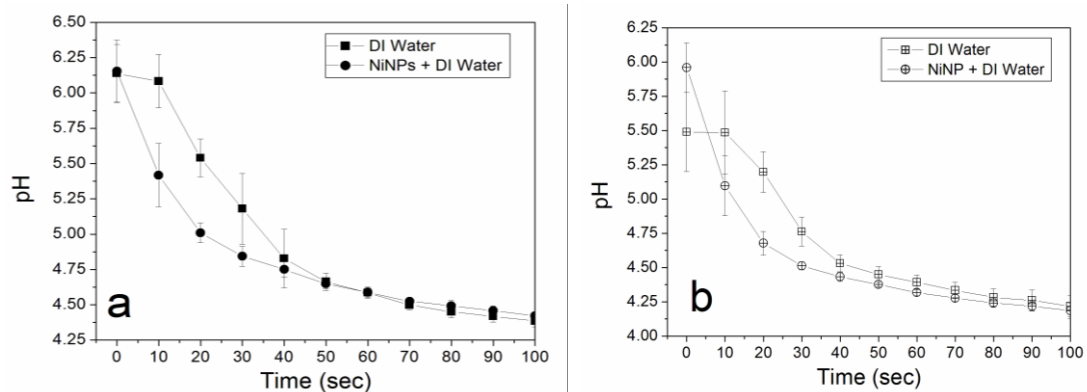


Figure 6.2: Average values of pH change profile when CO₂ is bubbled in DI water (square) or NiNPs suspension (circle) with light but in the (a) absence and (b) presence of IR filter with solar simulator emission wavelength range of 200-1200 nm.

To investigate the effect of IR radiation from solar light simulator on the CO₂ hydration reaction another set of experiments were carried out using an IR filter. The IR filter limited the emission of the wavelength of the solar simulator to 200-1100 nm (see emission spectra in Appendix III). The power of the radiation received at the sample position did not show any considerable decrease due to the presence of the IR filter. The power of the solar simulator was measured at the sample position as mentioned in chapter 3 section 3.3.8. Figure 6.2a and 6.2b shows the pH profiles in the absence and presence of the IR filter, respectively, when CO₂ was bubbled in DI water or NiNPs suspension. It is observed from the figures 6.2a and 6.2b that the pH change in the presence of NiNPs is faster than in its absence. The NiNPs show similar pH profile (figure 6.2a and 6.2b) in presence and absence of the IR filter when compared to the uncatalysed reaction. For the uncatalysed CO₂ hydration reaction pH change profile is slower in presence of IR filter as compared to its absence. It can thus be concluded that the uncatalysed reaction is also affected by the presence of IR filtered light.

In order to evaluate the effect of NiNPs in the presence and absence of the IR irradiations, numerical integration was also carried out to determine the

area between the catalysed and uncatalysed pH profiles. It was observed that there was an increase in area by 12.0% in absence of the IR filter than in its presence. Therefore IR irradiation plays an important role in the hydration of CO₂.

Comparing the area under the curves in figure 6.1b and figure 6.2b it was found that there was an increase in the area by 10.8% under solar irradiation using IR filter as compared to the dark. The increase in area between the curves provides a qualitative proof that light does have an effect on the comparative activity of NiNP catalysed and uncatalysed CO₂ hydration.

6.1.2. Chemical characterization of the NiNPs before and after CO₂ bubbling

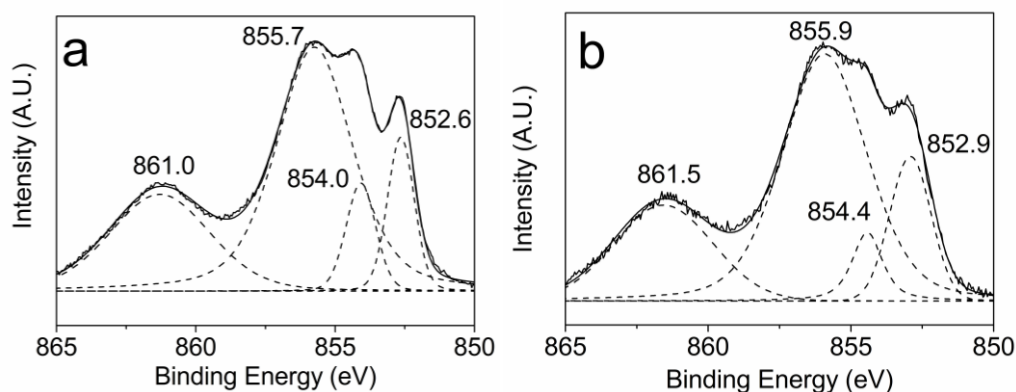


Figure 6.3: XPS spectrum of NiNPs a) before bubbling and b) after bubbling of CO₂ under solar irradiation without filter

In figure 6.3a and 6.3b the X-ray photoemission spectra of NiNPs before and after CO₂ bubbling (in presence of light without filter) show that the NiNPs have presence of NiO component (at 854.0 eV and 854.4 eV in figure 6.3a and 6.3b, respectively [4, 7, 8]) and larger metallic Ni (at 852.6 eV and 852.9 eV in figures 6.3a and 6.3b, respectively [4, 7, 8]) on its surface. The peaks at 855.7 eV and 855.9 eV are assigned to Ni(OH)_x and Ni(HCO₃)_x species [4] whereas the peak at 861.0 eV and 861.5 eV correspond to the collective plasmon peak of Ni [4, 7, 8]

6.1.3 Discussion on photochemical effect on hydration of CO₂ (catalytic and non-catalytic)

It has been reported that metallic Ni and NiO both collectively work as a photo-catalyst for water splitting reaction in the presence of semiconductor (TiO₂) materials [9-11]. In this process the semiconductor generates an electron-hole pair by absorption of light. The electron is then used by metallic nickel to produce H₂ gas and the hole is used by NiO to produce O₂ gas [9-11]. It is also known that water can dissociate on both the Ni and NiO surface [12]. Therefore it is reasonable to assume here that the water dissociation is enhanced on the NiNPs surfaces in the presence of light, enhancing the observed hydration of CO₂.

It is known that water absorbs light in the UV-Vis and IR range for excitation of various OH stretching and bending vibrations [13-15]. Liquid water exists in form of clathrate like structure and on absorbance of sunlight there are changes in this structure [16-18]. Liquid water consists of two different types of clathrate structures, structure 1 (SI) and structure 2 (SII) [16-18] each consisting of the 5¹² (pentagonal dodecahedra) because there are 12 faces of pentagonally bonded water molecules encapsulating a cavity [19]. It is known that upon sunlight irradiation the water molecule itself acts as a guest molecule in this cavity of its clathrate structure [16-18]. Other gas molecules can stay within this cavity of the clathrate structure of water, having less transitional motion, but more rotational and vibrational motion [19]. The CO₂ molecule is a guest molecule in this clathrate structure of liquid water [18, 20] (generally termed as CO_{2(aq)}) when CO₂ is bubbled in water before undergoing hydration reaction. Liquid water clathrate structures can accommodate guest molecules

between diameters 0.4-0.7 nm [19]. The CO₂ molecule has a diameter of 0.33 nm [21]. Therefore it is expected that the change in the clathrate structure of liquid water may provide additional stability to the guest CO₂ molecule from the hydration reaction before undergoing the hydration reaction itself. This could explain the slow lowering of the pH change in the uncatalysed hydration of CO₂.

It has been demonstrated that defects in the Ni lattice (i.e. steps in the lattice) are one of the active sites for the dissociation of water to H_(ads) and OH_(ads) [22-25]. The dissociation energy of water on Ni surface can be calculated by density functional theory (DFT) simulation. The dissociation energy was calculated to be 90.69 kJ/mol for Ni [111] surface and 36.66 kJ/mol for Ni [211] surface [24]. The uncatalysed dissociation energy of water is 493.04 kJ/mol [26, 27]. This reduction in dissociation energy of water on the NiNPs surface is the first step in the catalytic hydration of CO₂. The change in the clathrate structure of water does not affect the water dissociation on the NiNPs surface. Therefore, whether there is light or dark, an enhancement in the rate of hydration of CO₂ is observed in the presence of NiNPs.

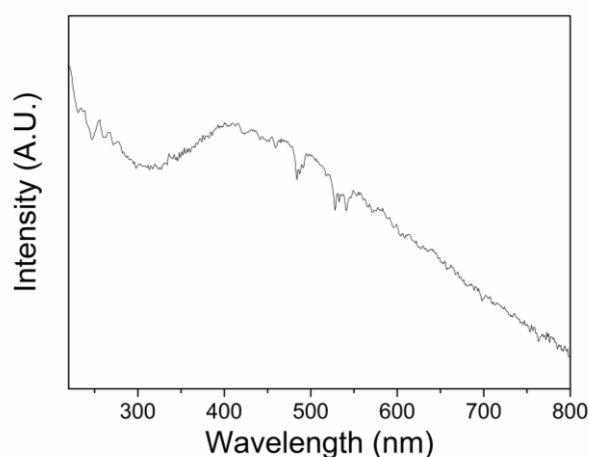


Figure 6.4: UV-Vis absorption spectrum of 30 ppm NiNPs suspension.

It is also known that NiNPs have a surface plasmon resonance (SPR) in the UV-Vis range. SPR have been extensively used for surface enhanced

Raman scattering (SERS) [28, 29], and recently used for catalytic applications as well [30-33]. Figure 6.4 shows the UV-Vis absorption spectrum of 30 ppm suspended NiNPs. It can be observed from figure 6.4 that NiNPs have a SPR peak at 400 nm. The SPR peak for NiNPs that have been reported lie between 355-422 nm [34, 35]. The presence of the peak shows that NiNPs absorb light in the UV-Vis range and this SPR may also contribute in further enhancing the catalytic activity of NiNPs for hydration of CO₂ in presence of light.

Christopher *et al.* [32, 33] recently showed that silver nanoparticles (AgNPs) can enhance the rate of oxidation of ammonia and carbon mono oxide under sunlight irradiation. The excited AgNPs plasmons help populate the O₂ molecules on their surface to form negative ion state enhancing the O₂ dissociation reaction [33]. Similarly Xu *et al.* [30] demonstrated that AgNPs can work as surface plasmon assisted catalyst (SPAC) for the reversible reactions of 4-aminothiophenol (4ATP) to 4,4'-dimercaptoazobenzene (DMAB). They found that the reversible nature of 4ATP-DMAB conversions by surface plasmon excitation is a function of their respective oxidative or reductive environments [30]. It is postulated here that in this study the surface plasmon resonance of NiNPs may enhance the H₂O dissociation on the Ni surface leading to higher reaction rates of CO₂ hydration.

6.2 Temperature dependent study of kinetics of CO₂ hydration

6.2.1 Effect of temperature on the saturation of CO₂ in presence of NiNPs.

Chapter 3 section 3.2.1 describes the procedure used for studying the CO₂ saturation concentration in NiNPs suspension and DI water at different temperatures. Each experiment was repeated five times and average data is presented. It is known that solubility of gases decrease with increase in

temperature [36]. The same trend of decrease of the amount of CO₂ saturation concentration (with and without NiNPs) at temperatures between 10-60 °C is observed here as seen from figure 6.5. There is a linear decrease in the concentration of CO₂ with increase in temperature in the absence of NiNPs. The values of the titration at 20 °C were same as those reported in section 4.2, chapter 4 [4] and section 5.3.2, chapter 5. The increase in the saturation concentration of CO₂ in presence of NiNPs is approximately constant at all given temperatures at about 85.3 ±7 mM. The data suggest that the enhancement in CO₂ saturation concentration is not affected with temperature. (see further discussion in chapter 8)

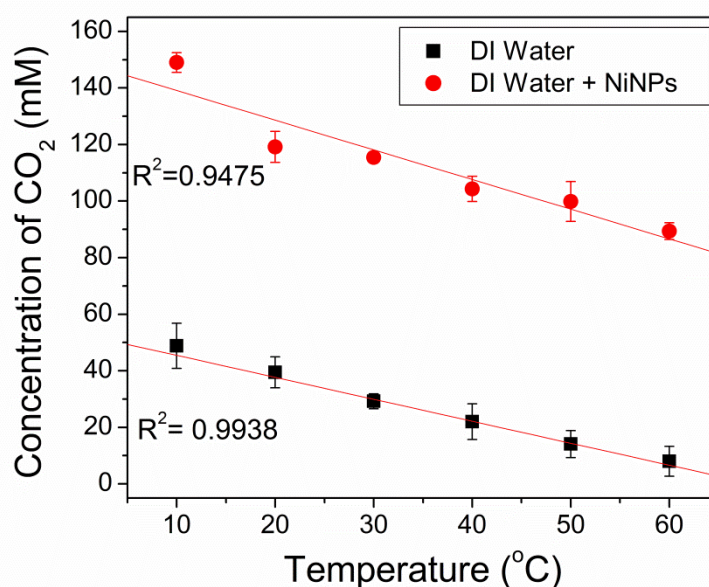


Figure 6.5 Average values of saturated CO₂ concentration in DI water and NiNPs suspension as a function of increase in temperature.

6.2.2 Kinetic study of CO₂ hydration at different temperatures

The pH of solutions depends on the temperature [37, 38]. The pH change profiles of CO₂ bubbling experiments were also carried out at different temperatures to validate the observation of catalytic activity of the NiNPs catalyst following the procedure described in chapter 3 section 3.3.8.

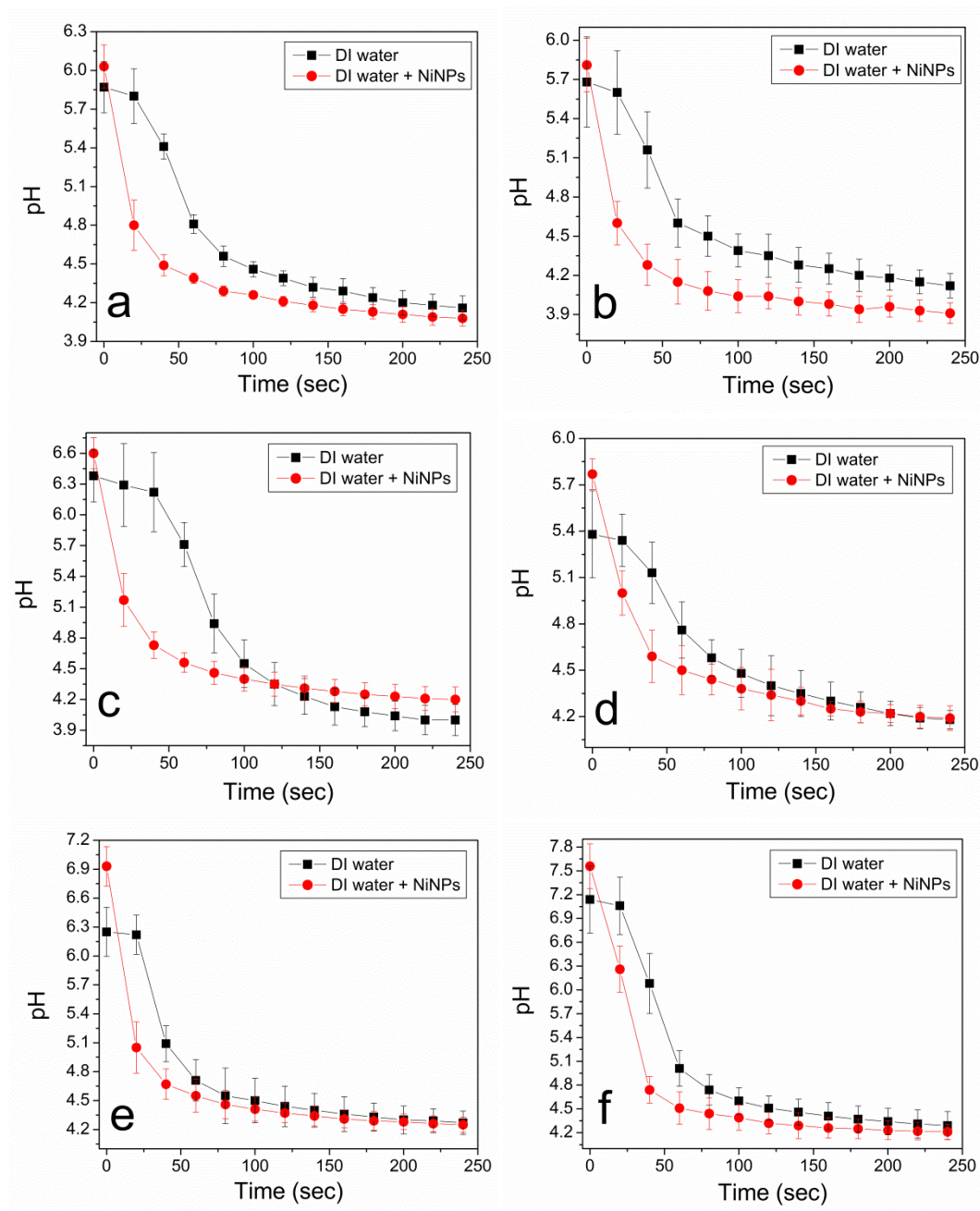


Figure 6.6: Average values of change in pH of DI water (square) or NiNPs suspension (circle) when CO₂ is bubbled through liquid maintained at temperatures (a) 10 °C, (b) 20 °C, (c) 30 °C, (d) 40 °C, (e) 50 °C and (f) 60 °C.

Figure 6.6 shows the pH change profile of DI water and NiNPs suspension at different temperatures. pH is a function of temperature therefore there is a change observed in the initial pH of the suspension or DI water at different temperatures. Catalytic activity of NiNPs was observed in the temperature range 10-60 °C. It is observed from the figure 6.6 that as the temperature changes difference in the area under the catalysed and

uncatalysed pH profile curves also change. A larger catalytic activity was observed for the NiNPs to catalyse the hydration of CO₂ at ambient temperatures (20-30 °C) than that at lower (10-20 °C) or higher (40-60 °C). It is observed that with the change in temperature there is a change in the reaction kinetics of the non-catalysed hydration of CO₂. For all the profiles for the pH change for non-catalytic reaction (the filled squares in figure 6.6 (a-f)) of CO₂ hydration a reverse S-shaped curve observed consistent with the previously observed results ((chapter 4 section 4.3, chapter 5 section 5.5.2) and chapter 6 section 6.1)). It is evident from figure 6.6 (c) that the reaction rate is slowest at 30 °C. It is known that solubility of CO₂ decreases with increase in temperature [39, 40] that would also affect the rate of hydration reaction of CO₂. The NiNPs suspension show similar exponential pH change profile at in the temperature range of 10-60 °C.

6.3 Conclusion

The catalytic activity of the NiNPs was considered in the presence of the artificial solar simulator, with and without IR and dark as control. It is observed that the rate of hydration of CO₂ is photo catalytically enhanced in presence of NiNPs with both IR and visible spectrum. It was also found that the rate of uncatalysed hydration of CO₂ depends on the structure of liquid water and is affected by sunlight. The change in the clathrate structure of liquid water does not affect the NiNPs surface that being the one of the reason for the observed catalytic activity of NiNPs. The NiNPs absorb light in the UV-Vis range and this might be another reason for the observed enhancement in the catalytic hydration of CO₂ by NiNPs in presence of light. It was also observed that the amount of CO₂ saturation in DI water in the presence of the NiNPs is

independent of temperature. The NiNPs showed catalytic activity at all tested temperatures with best activity at ambient temperatures (20-30 °C).

References

- [1] Y. Yamada, T. Miyahigashi, H. Kotani, K. Ohkubo, S. Fukuzumi, Photocatalytic hydrogen evolution with Ni nanoparticles by using 2-phenyl-4-(1-naphthyl)quinolinium ion as a photocatalyst, *Energy & Environmental Science*, 5 (2012) 6111-6118.
- [2] D. Hong, Y. Yamada, T. Nagatomi, Y. Takai, S. Fukuzumi, Catalysis of Nickel Ferrite for Photocatalytic Water Oxidation Using $[\text{Ru}(\text{bpy})_3]^{2+}$ and $\text{S}_2\text{O}_8^{2-}$, *Journal of the American Chemical Society*, 134 (2012) 19572-19575.
- [3] X. Cai, Y. Cai, Y. Liu, H. Li, F. Zhang, Y. Wang, Structural and photocatalytic properties of nickel-doped zinc oxide powders with variable dopant contents, *Journal of Physics and Chemistry of Solids*, 74 (2013) 1196-1203.
- [4] G.A. Bhaduri, L. Šiller, Nickel nanoparticles catalyse reversible hydration of carbon dioxide for mineralization carbon capture and storage, *Catalysis Science & Technology*, 3 (2013) 1234-1239.
- [5] G.A. Bhaduri, R.A. Henderson, L. Šiller, Reply to the 'Comment on "Nickel nanoparticles catalyse reversible hydration of carbon dioxide for mineralization carbon capture and storage"' by D. Britt, *Catal. Sci. Technol.*, 2013, 3, DOI: 10.1039/C3CY00142C, *Catalysis Science & Technology*, 3 (2013) 2197-2198.
- [6] D.-H. Kim, M. Vinoba, W.-S. Shin, K.-S. Lim, S.-K. Jeong, S.-H. Kim, Biomimetic sequestration of carbon dioxide using an enzyme extracted from oyster shell, *Korean Journal of Chemical Engineering*, 28 (2011) 2081-2085.
- [7] M.C. Biesinger, B.P. Payne, L.W.M. Lau, A. Gerson, R.S.C. Smart, X-ray photoelectron spectroscopic chemical state quantification of mixed nickel metal, oxide and hydroxide systems, *Surface and Interface Analysis*, 41 (2009) 324-332.
- [8] B.P. Payne, M.C. Biesinger, N.S. McIntyre, The study of polycrystalline nickel metal oxidation by water vapour, *Journal of Electron Spectroscopy and Related Phenomena*, 175 (2009) 55-65.
- [9] T.K. Townsend, N.D. Browning, F.E. Osterloh, Overall photocatalytic water splitting with $\text{NiO}_x\text{-SrTiO}_3$ - a revised mechanism, *Energy & Environmental Science*, 5 (2012) 9543-9550.
- [10] M.E.G. Lyons, M.P. Brandon, The oxygen evolution reaction on passive oxide covered transition metal electrodes in aqueous alkaline solution. Part 1- Nickel, *International Journal of Electrochemical Science*, 3 (2008) 1386-1424.
- [11] S. Fukuzumi, D. Hong, Y. Yamada, Bioinspired photocatalytic water reduction and oxidation with earth-abundant metal catalysts, *Journal of Physical Chemistry Letters*, 4 (2013) 3458-3467.
- [12] M. Schulze, R. Reißner, K. Bolwin, W. Kuch, Interaction of water with clean and oxygen precovered nickel surfaces, *Fresenius Journal of Analytical Chemistry*, 353 (1995) 661-665.

- [13] B. Wozniak, J. Dera, *Light Absorption in Sea Water*, Springer, 2007.
- [14] W.S. Pegau, D. Gray, J.R.V. Zaneveld, Absorption and attenuation of visible and near-infrared light in water: dependence on temperature and salinity, *Applied Optics*, 36 (1997) 6035-6046.
- [15] V. Engel, V. Staemmler, R.L. Vander Wal, F.F. Crim, R.J. Sension, B. Hudson, P. Andresen, S. Hennig, K. Weide, R. Schinke, Photodissociation of water in the first absorption band: a prototype for dissociation on a repulsive potential energy surface, *The Journal of Physical Chemistry*, 96 (1992) 3201-3213.
- [16] S. Shigezo, Y. Tetsuro, Y. Makio, Y. Toshio, A. Tsunehisa, Effect of Sunlight on Liquid Structure of Water, *Japanese Journal of Applied Physics*, 46 (2007) 333.
- [17] Y. Tetsuro, S. Shigezo, M. Tadahiko, Y. Makio, Y. Toshio, Clathrate-like Ordering in Liquid Water Induced by Infrared Irradiation, *Japanese Journal of Applied Physics*, 43 (2004) L1436.
- [18] T. Yokono, S. Shimokawa, M. Yokono, H. Hattori, Infra-red spectroscopic study of structural change of liquid water induced by sunlight irradiation, *Water*, 1 (2009) 29-34.
- [19] D. Dloan, Thermodynamics of natural gas clathrate hydrates, in: T. Letcher (Ed.) *Chemical Thermodynamics for Industry*, The Royal Society of Chemistry, 2004, pp. 57-75.
- [20] K. Tumba, P. Reddy, P. Naidoo, D. Ramjugernath, A. Eslamimanesh, A.H. Mohammadi, D. Richon, Phase Equilibria of Methane and Carbon Dioxide Clathrate Hydrates in the Presence of Aqueous Solutions of Tributylmethylphosphonium Methylsulfate Ionic Liquid, *Journal of Chemical & Engineering Data*, 56 (2011) 3620-3629.
- [21] J.-R. Li, Y. Ma, M.C. McCarthy, J. Sculley, J. Yu, H.-K. Jeong, P.B. Balbuena, H.-C. Zhou, Carbon dioxide capture-related gas adsorption and separation in metal-organic frameworks, *Coordination Chemistry Reviews*, 255 (2011) 1791-1823.
- [22] C. Benndorf, C. Mundt, H₂O adsorption on Ni(s) (111) surfaces: Evidence for a step induced influence on the adsorption geometry, *Journal of Vacuum Science & Technology A*, 10 (1992) 3026-3031.
- [23] G. Pirug, O. Knauff, H.P. Bonzel, Structural and chemical aspects of H₂O adsorption on Ni (110), *Surface Science*, 321 (1994) 58-70.
- [24] H.S. Benggaard, J.K. Nørskov, J. Sehested, B.S. Clausen, L.P. Nielsen, A.M. Molenbroek, J.R. Rostrup-Nielsen, Steam Reforming and Graphite Formation on Ni Catalysts, *Journal of Catalysis*, 209 (2002) 365-384.

- [25] R.V. Kasza, K. Griffiths, J.G. Shapter, P.R. Norton, D.A. Harrington, Interaction of water with stepped Ni (760): associative versus dissociative adsorption and autocatalytic decomposition, *Surface Science*, 356 (1996) 195-208.
- [26] P. Maksyutenko, J.S. Muentner, N.F. Zobov, S.V. Shirin, O.L. Polyansky, T.R. Rizzo, O.V. Boyarkin, Approaching the full set of energy levels of water, *The Journal of Chemical Physics*, 126 (2007) 241101.
- [27] P. Maksyutenko, T.R. Rizzo, O.V. Boyarkin, A direct measurement of the dissociation energy of water, *The Journal of Chemical Physics*, 125 (2006) 181101.
- [28] A. Champion, P. Kambhampati, Surface-enhanced Raman scattering, *Chemical Society Reviews*, 27 (1998) 241-250.
- [29] P.L. Stiles, J.A. Dieringer, N.C. Shah, R.P. Van Duyne, Surface-Enhanced Raman Spectroscopy, *Annual review of Analytical Chemistry*, 1 (2008) 601-626.
- [30] P. Xu, L. Kang, N.H. Mack, K.S. Schanze, X. Han, H.-L. Wang, Mechanistic understanding of surface plasmon assisted catalysis on a single particle: cyclic redox of 4-aminothiophenol, *Scientific Reports*, 3 (2013).
- [31] W. Hou, S.B. Cronin, A Review of Surface Plasmon Resonance-Enhanced Photocatalysis, *Advanced Functional Materials*, 23 (2013) 1612-1619.
- [32] P. Christopher, H. Xin, A. Marimuthu, S. Linic, Singular characteristics and unique chemical bond activation mechanisms of photocatalytic reactions on plasmonic nanostructures, *Nature Materials*, 11 (2012) 1044-1050.
- [33] P. Christopher, H. Xin, S. Linic, Visible-light-enhanced catalytic oxidation reactions on plasmonic silver nanostructures, *Nature Chemistry*, 3 (2011) 467-472.
- [34] K. Nouneh, M. Oyama, R. Diaz, M. Abd-Lefdil, I.V. Kityk, M. Bousmina, Nanoscale synthesis and optical features of metallic nickel nanoparticles by wet chemical approaches, *Journal of Alloys and Compounds*, 509 (2011) 5882-5886.
- [35] J. Zhang, C.Q. Lan, Nickel and cobalt nanoparticles produced by laser ablation of solids in organic solution, *Materials Letters*, 62 (2008) 1521-1524.
- [36] B.E. Poling, J.M. Prausnitz, J.P. O'Connell, *The properties of gases and liquids*, McGraw Hill, London, 2000.
- [37] P. Atkins, J. de Paula, *Atkins' Physical Chemistry*, Oxford University Press Oxford, 2010.
- [38] C.C. Westcott, *pH measurements*, Academic Press, London, 1978.

[39] R. Wiebe, V.L. Gaddy, The Solubility of Carbon Dioxide in Water at Various Temperatures from 12 to 40° and at Pressures to 500 Atmospheres. *Critical Phenomena, Journal of the American Chemical Society*, 62 (1940) 815-817.

[40] X. Li, D. Yang, Determination of Mutual Solubility between CO₂ and Water by Using the Peng–Robinson Equation of State with Modified Alpha Function and Binary Interaction Parameter, *Industrial & Engineering Chemistry Research*, 52 (2013) 13829-13838.

Catalytic activity of NiNPs for hydration of CO₂ (Part IV): Possible applications

Chapter 7 considers the possible applications for the NiNPs catalysis for hydration of CO₂. These studies include CaCO₃ precipitation in a non-saturated CO₂ solution and the CO₂ absorption in carbonate solutions. The influence of heating on the catalytic activity of NiNPs was investigated. The oxidation of the NiNPs surface due to the heating was analysed using XPS and XRD.

7.1 CaCO₃ precipitation yields and analysis

The results obtained in chapter 4 and 6 show that there is an increase in the saturation (equilibrium) concentration of CO₂ in NiNP suspension as compared to DI water. The aim of this study is to observe the amount of CO₂ absorption in a non-equilibrium condition, by monitoring the concentration of CO₂ in a pre-saturation condition, by CaCO₃ precipitation. The experimental details are described in chapter 3, section 3.2.10 where CO₂ is bubbled in DI water or NiNPs suspension and the CaCO₃ is precipitated using 0.1M NaOH and 0.1M CaCl₂ solution. Similar experiments were carried out by Favre *et al.*

[1] to determine the catalytic activity Carbonic Anhydrase for CO_2 hydration by CaCO_3 precipitation.

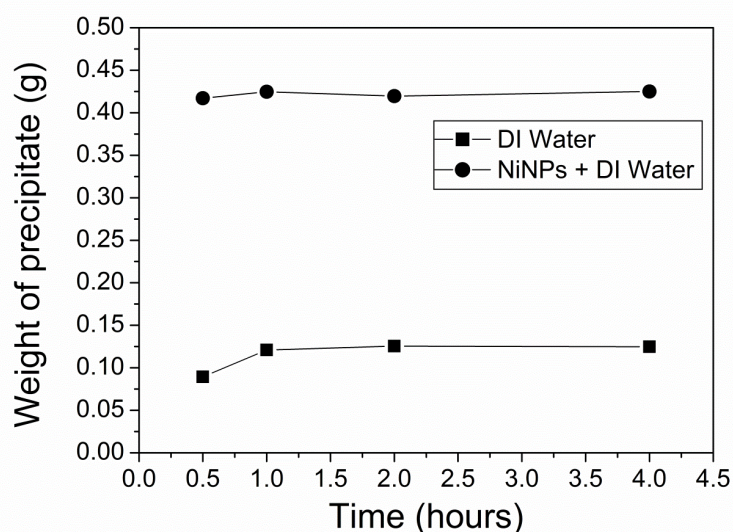


Figure 7.1: Average values of CaCO_3 precipitate obtained by addition of CaCl_2 and NaOH in DI water and NiNPs suspension after CO_2 bubbling at different time intervals.

Figure 7.1 shows the amount of CaCO_3 precipitated in presence and absence of NiNPs in DI water as a function of CO_2 gas bubbling of time. The calcite phase of CaCO_3 was confirmed using XRD (see below figure 7.4). The CaCO_3 precipitate yield in the presence of the NiNPs was three times higher than that of DI water, similar to the results observed by Bhaduri and Šiller [2] and chapter 4 (section 4.2) and chapter 6 (section 6.2.1). The experiments were performed at constant temperature of $20\text{ }^\circ\text{C}$. Figure 7.2a and 7.2b, are optical images of the precipitates obtained in absence and presence of NiNPs, respectively.

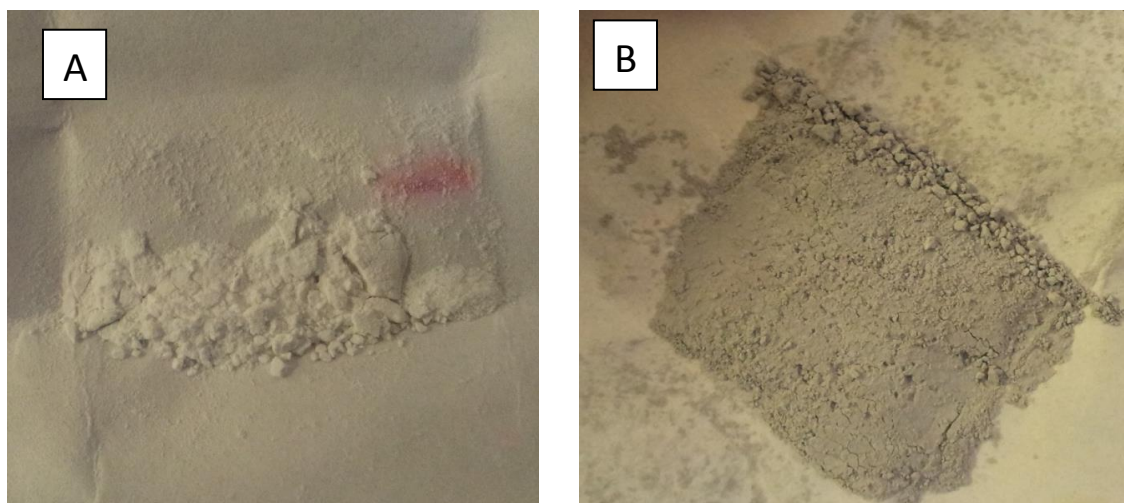


Figure 7.2: Precipitate of CaCO_3 by NaOH and CaCl_2 solution; a) Control and b) with NiNPs.

SEM Figure 7.3 shows the SEM images of the CaCO_3 precipitate in presence of NiNPs. Micron sized (2-10 μm) spherical precipitates are observed. XRD of the precipitate is shown in figure 7.4, which confirms the presence of the calcite phase of CaCO_3 [3]. The diffraction plane of Ni [111] is also present [4] which indicates also the presence of NiNPs in the precipitates. Therefore the NiNPs could act as nucleation sites for the crystals to grow, since the NiNPs are spherical in shape (see figure 4.1 in chapter 4), the carbonate precipitate are also spherical (instead of normal cubic shape [5, 6]).

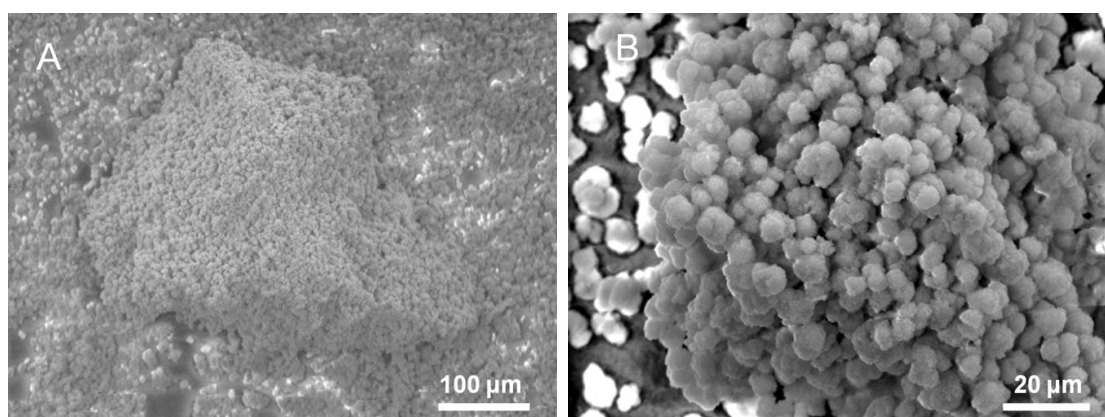


Figure 7.3: SEM images of the precipitate of CaCO_3 obtained in presence of NiNPs catalysed hydration of CO_2 using NaOH and CaCl_2 .

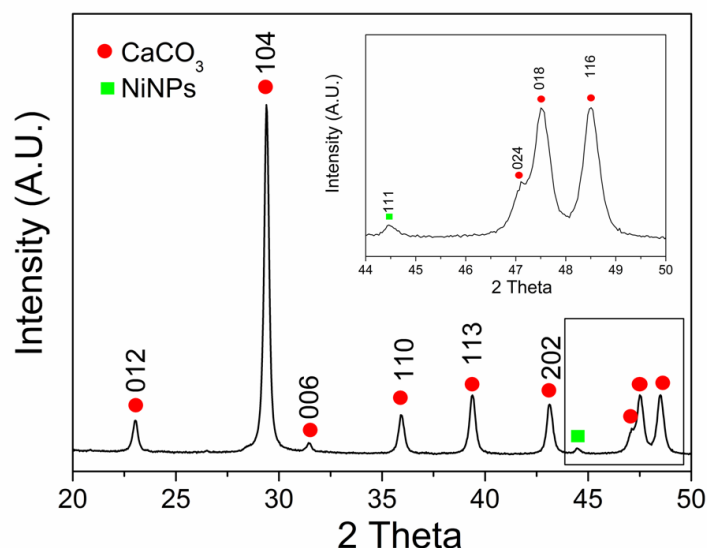


Figure 7.4: XRD of the precipitate of CaCO_3 obtained in presence of NiNPs catalysed hydration of CO_2 using NaOH and CaCl_2 [3]. Insert is the magnification of the later end of the XRD pattern to show the Ni [111] peak [4].

7.2 Enhancement of CO_2 absorption rate in 50 wt% potassium carbonate solution

In the previous section the precipitation of CaCO_3 confirmed that the NiNPs enhance the CO_2 saturation capacity of DI water. Enhanced rate of hydration reaction can also affect the performance of many gas absorbers [7], specially amines [8] and carbonate [7] absorption systems that are commonly used for separation of CO_2 . In order to study the effect of NiNPs on absorption solutions for enhanced separation of CO_2 , 30 ppm of NiNPs were dispersed in 50% (weight %) of potassium carbonate (this concentration is used industrial application [9]) and CO_2 gas was passed through the solution (for details of the experiment see chapter 3 section 3.2.11). Potassium carbonate solutions are commonly used in industry for separation of CO_2 due to its higher CO_2 loading capacity as compared to sodium carbonate solutions [7, 9, 10]. The carbonate absorption process for CO_2 separation is limited with low reaction kinetic rates [9]. Therefore the current study focuses on the effect of NiNPs on the rate of CO_2 absorption in 50 wt% K_2CO_3 solution by measuring the increase in weight

of the carbonate solution for a prolonged exposure to CO₂ gas bubbled through the solution (for experimental details see chapter 3, section 3.2.9). The increase in weight is proportional to the amount of CO₂ captured by the 50 wt% K₂CO₃ solution.

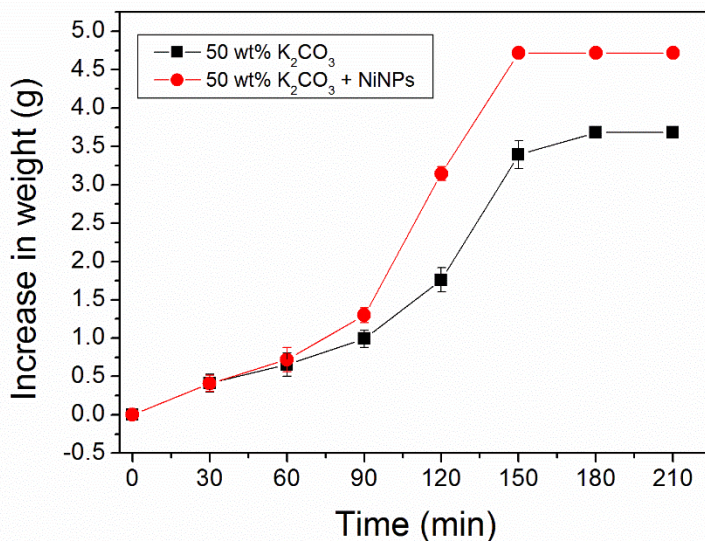


Figure 7.5 Average values of gravimetric uptake of CO₂ in potassium carbonate solution (with and without NiNPs circles and squares, respectively) with a fine bubbler (Pyrex 1, porosity 100-150 μm).

Figure 7.5 shows the results of gravimetric uptake of CO₂ in 50 wt% K₂CO₃ solution in the absence and presence of NiNPs. The experiment was carried out until no additional change in the weight of the reaction vessel was observed. The reactions of the absorption process are given by the following reaction equations 3a-3e.



Carbonate solutions (K_2CO_3 and Na_2CO_3) have a high pH (i.e. >11) and as CO_2 is bubbled into the carbonate solution its pH drops [11]. The reaction 3a takes place when the K_2CO_3 is instantaneously dissolved in DI water and CO_2 hydration reaction takes place via reaction 3b till the pH reaches 10 [12]. Reaction mechanisms 3b and 3c simultaneously occur between pH 10 and 8 with reaction 3c being the slowest step [12]. The reactions 3d and 3e like 3a are instantaneous [13]. Thus CO_2 hydration is the most important step in the CO_2 capture when using potassium carbonate solutions. Therefore, in summary as the CO_2 and carbonic acid starts reacting with the carbonate solution, the pH of the solution changes and the reaction mechanisms of CO_2 hydration changes [11] from 3b to 3c depending on the pH of the solution [12]. From figure 7.5 it can be observed that initial rate of CO_2 absorption is similar for both 50 wt% K_2CO_3 solution with and without NiNPs catalyst but after 60 minutes the rate of reaction is faster in presence of the NiNPs. This kind of enhancement in CO_2 absorption is a result of the carbonate-bicarbonate buffering ability of carbonate solutions. Pinsent and Roughton [14] report that the rate of CO_2 hydration increases as the bicarbonate/carbonate ($[HCO_3^-]/[CO_3^{2-}]$) ratio increases. Therefore as CO_2 reacts with the carbonate solution the bicarbonate ions are formed (following reaction 3b) (the value of the numerator increases while that of the denominator decreases), leading to the observed autocatalytic enhancement absorption of CO_2 .

Figure 7.5 shows that in the presence of NiNPs there is the increase in weight of the carbonate solution (after saturation) due to enhanced kinetic rate of CO_2 hydration (but lower than the full capacity of the carbonate solution, which is 15.92 g, if there is 100% conversion of K_2CO_3 to $KHCO_3$). There is an increase in CO_2 loading (mol of CO_2 per mol of K_2CO_3) by $\sim 27\%$.

Table 7.1: Rate of CO₂ absorption in K₂CO₃ solutions in with and without of NiNPs.

System	Rate (moles/min)	Regression (R ²)
Potassium carbonate	0.0048	0.963
Potassium carbonate + NiNPs	0.00852	0.971

In figure 7.5 the rapid increase in CO₂ absorption after 60 min until saturation is used to estimate the in enhancement in absorption rate of CO₂ in carbonate solutions in presence of NiNPs. The data points between 60 min and saturation are linearly fitted (see appendix III) and the data is shown in table 7.1. It can be observed that the data showed a good linear fit (R²>0.96) and the slope can be used to compare the enhancement in rate. There is ~77% increase in the absorption rate of CO₂ in carbonate solution in the presence of NiNPs under the same operating conditions.

7.3 Temperature treatment of NiNPs

7.3.1 Chemical characterization of NiNPs after temperature treatment

When carbonates are used for the separation of CO₂ from flue gases, the solvent is regenerated by heating the CO₂-saturated carbonate solution to release the trapped in CO₂ [7]. Therefore in order to use NiNPs as enhancers in carbonate separation technology as set of experiments were performed to test the effect of heating on the catalytic activity of NiNPs was studied by XPS.

Figure 7.6 shows the surface species present on the NiNPs surface before and after heat treatment (experimental detail in chapter 3 section 3.2.10). Three different species were observed in Ni 2p_{3/2} spectra for NiNPs before and after heat treatment respectively. In figure 7.6a the peaks at 852.5 eV, 854.1 eV and 855.7 eV can be assigned to Ni⁰, NiO and Ni(OH)_x respectively [15] and figure

7.6b the peaks at 852.4 eV, 854.0 eV and 855.7 eV can be assigned to Ni⁰, NiO and Ni(OH)_x respectively [15]. The peak at 861.0 eV in figure 7.6a (or 860.9 eV in figure 7.6b) is assigned the value for a collective plasmon peak of Ni [2, 16, 17]. The presence of the two peaks in the O 2s spectra shows the presence of oxygen in two oxidation states. In figure 7.6c the peak at 529.3 eV corresponds to NiO [15] whereas the peak at 531.0 eV corresponds to NiOH_x [18]. The existence of the NiOH_x is due to the dissociative adsorption of water from the atmosphere. It is known that the OH bond on the surface has a binding energy difference of 1.8 eV higher than that of NiO [18]. Thus the peak at 531.0 eV is assigned to NiOH_x. The peaks in O 1s at 529.5 eV and 531.2 eV after heat treatment observed in figure 7.6d also correspond to NiO [15] and NiOH_x [18, 19]. The C 1s peak in figure 7.6e and 7.6f at 284.4 eV can be attributed to adventitious carbon [2, 16, 17]. The survey spectrum shows presence of Ni 3p, Ni 2p, C 1s and O 1s peaks for NiNPs before (figure 7.6g) and after (figure 7.6b) heat treatment.

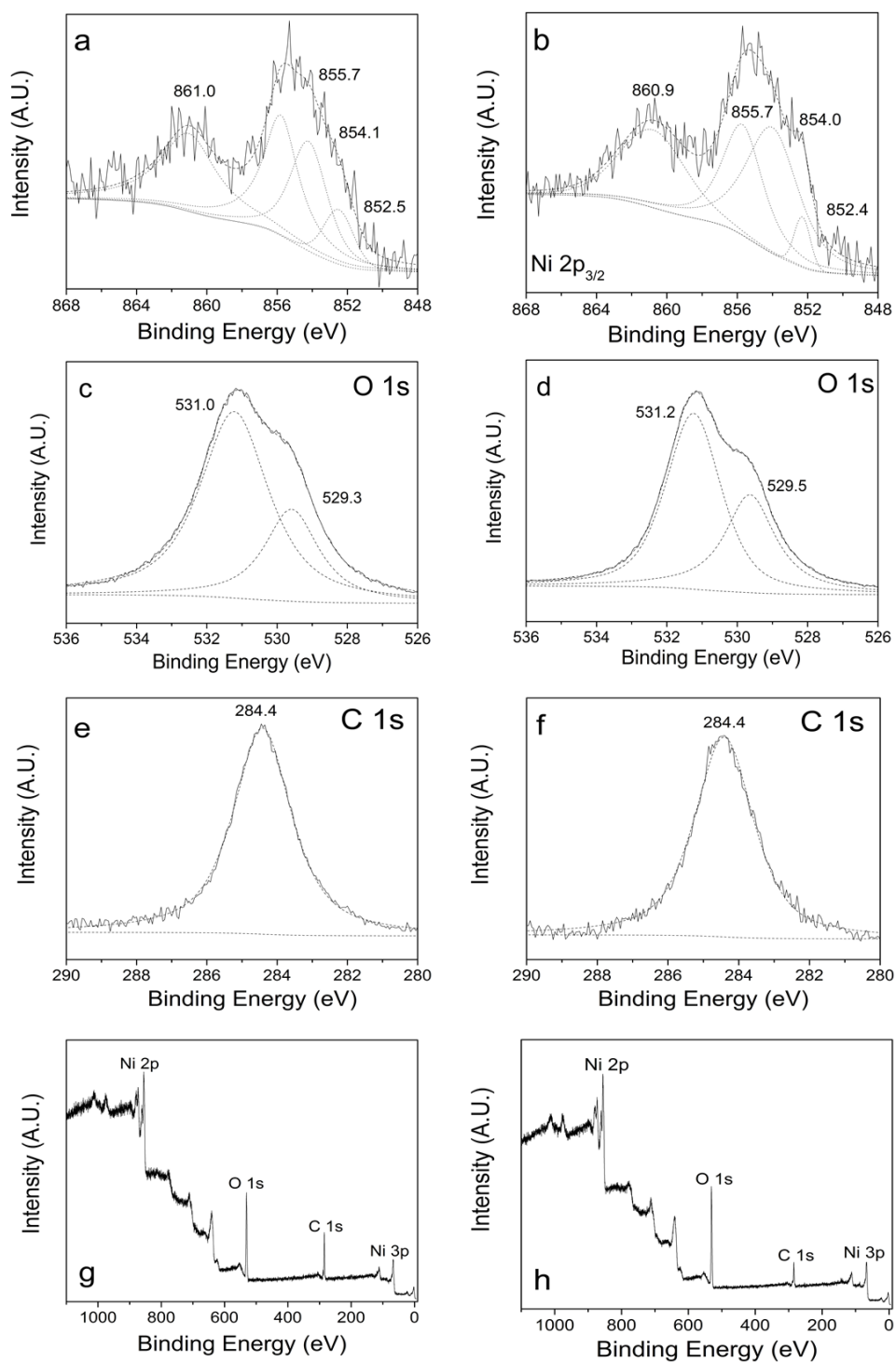


Figure 7.6: XPS results of the NiNPs before (a. Ni 2p_{3/2}, c. O 1s, e. C 1s and g. Survey) heat treatment and after (b. Ni 2p_{3/2}, d. O1s, f. C1s and h. Survey) heat treatment at 150 °C for 8 hours in air.

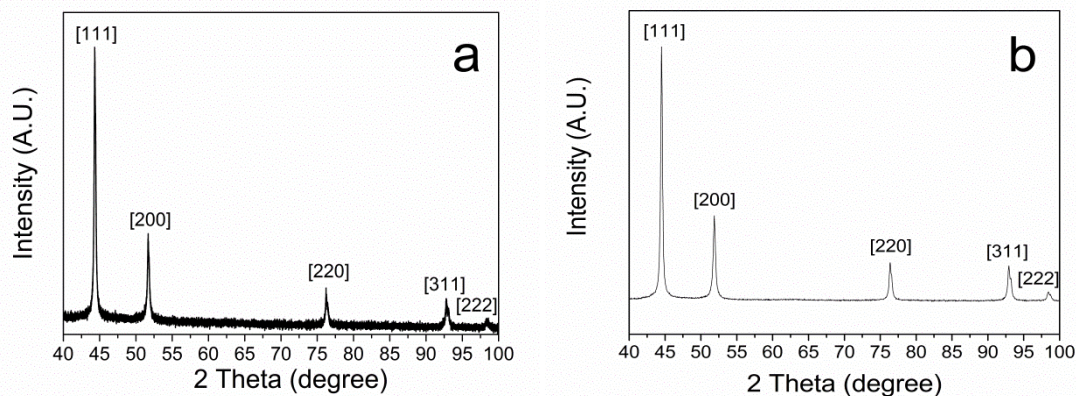


Figure 7.7: X-ray diffraction pattern of the NiNPs (a) before and (b) after heat treatment at 150 °C for 8 hours.

The figure 7.7 shows the X-ray diffraction pattern of the NiNPs before and after heat treatment at 150 °C for 8 hours. The XRD pattern detects the bulk changes taking place in the NiNPs due to heat treatment. The crystal planes observed as peaks can be associated to the [111], [200], [220], [311], and [222] planes associated with $2\theta = 44.43^\circ$, 51.78° , 76.26° , 92.77° and 98.27° respectively of cubic nickel lattice with space group of Fm-m3 [20, 21]. The absence of NiO peaks ($2\theta = 43.20^\circ$ (most intensive), 62.87° , 75.20° and 79.38°) from the XRD diffraction patterns shows that no any significant bulk oxidation of the NiNPs occurred during the heat treatment.

7.3.2 Catalytic activity of temperature treated NiNPs for CO₂ hydration

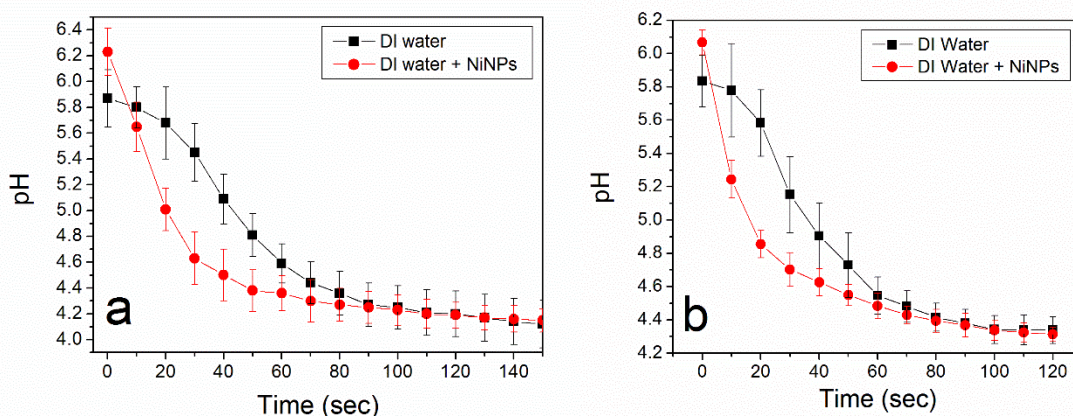


Figure 7.8: average values of pH changes during bubbling of CO₂ through DI water (a) heat treated NiNPs (at 150 °C for 8 hours in air) suspension and (b) without heat treatment.

The catalytic activity of the heat treated NiNPs was also studied. The experiment was repeated 3 times and average data is presented. The figure 7.8 shows the pH change profile when CO₂ is bubbled in heat treated NiNPs suspension and NiNPs suspension without heat treatment. The catalytic activity of NiNPs was observed even after heat treatment (150 °C for 8 hours in air) thus making the NiNPs suitable for use as enhancers in carbonate absorber systems.

7.4 Conclusion

It was observed that the presence of NiNPs increased the precipitation of CaCO₃ three times in DI water compared to the precipitation without NiNPs. The XRD and SEM results show that the precipitate are calcite with small spherical structures. The results show that the NiNPs work as active enhancers for carbonate absorption tests. The gravimetric results show that the NiNPs enhance the absorption of CO₂ in K₂CO₃ solutions. The NiNPs with and without heat treatment show the presence of Ni and NiO species on the surface. The XRD of the NiNPs (with and without heat treatment) do not show any significant bulk oxidation of the NiNPs. The heat treated NiNPs showed catalytic activity for the hydration of CO₂.

References:

- [1] N. Favre, M.L. Christ, A.C. Pierre, Biocatalytic capture of CO₂ with carbonic anhydrase and its transformation to solid carbonate, *Journal of Molecular Catalysis B: Enzymatic*, 60 (2009) 163-170.
- [2] G.A. Bhaduri, L. Šiller, Nickel nanoparticles catalyse reversible hydration of carbon dioxide for mineralization carbon capture and storage, *Catalysis Science & Technology*, 3 (2013) 1234-1239.
- [3] H.E. Swanson, R.K. Fuyat, Standard X-ray diffraction powder patterns, National Bureau of Standards (U.S.) Circular, II (1953) 51.
- [4] D.E. Zhang, X.M. Ni, H.G. Zheng, Y. Li, X.J. Zhang, Z.P. Yang, Synthesis of needle-like nickel nanoparticles in water-in-oil microemulsion, *Materials Letters*, 59 (2005) 2011-2014.
- [5] R. Yadav, M. Joshi, S. Wanjari, C. Prabhu, S. Kotwal, T. Satyanarayanan, S. Rayalu, Immobilization of Carbonic Anhydrase on Chitosan Stabilized Iron Nanoparticles for the Carbonation Reaction, *Water Air and Soil Pollution*, 223 (2012) 5345-5356.
- [6] S. Wanjari, C. Prabhu, R. Yadav, T. Satyanarayana, N. Labhsetwar, S. Rayalu, Immobilization of carbonic anhydrase on chitosan beads for enhanced carbonation reaction, *Process Biochemistry*, 46 (2011) 1010-1018.
- [7] P.V. Danckwerts, *Gas Liquid Reactions*, McGraw Hill Publishers, New York, 1970.
- [8] F. Williamson, G.A. Bhaduri, L. Šiller, Enhancing carbon capture of alkanolamine using nickel nanoparticles, in preparation.
- [9] P.V. Danckwerts, Promotion of CO₂ mass-transfer in carbonate solutions, *Chemical Engineering Science*, 36 (1981) 1741-1742.
- [10] A. Tavares da Silva, P.V. Danckwerts, The effect of halogens on the rate of absorption of carbon dioxide, *Chemical Engineering Science*, 28 (1973) 847-854.
- [11] G.A. Bhaduri, R.A. Henderson, L. Šiller, Reply to the 'Comment on "Nickel nanoparticles catalyse reversible hydration of carbon dioxide for mineralization carbon capture and storage"' by D. Britt, *Catal. Sci. Technol.*, 2013, 3, DOI: 10.1039/C3CY00142C, *Catalysis Science & Technology*, 3 (2013) 2197-2198.
- [12] D.M. Kern, The hydration of carbon dioxide, *Journal of Chemical Education*, 37 (1960) 14.
- [13] V.L.J. Snoeyink, David, *Water Chemistry*, John Wiley & Sons, New York, 1980.

- [14] B.R.W. Pinsent, F.J.W. Roughton, The kinetics of combination of carbon dioxide with water and hydroxide ions, *Transactions of the Faraday Society*, 47 (1951) 263-269.
- [15] K.S. Kim, N. Winograd, X-ray photoelectron spectroscopic studies of nickel-oxygen surfaces using oxygen and argon ion-bombardment, *Surface Science*, 43 (1974) 625-643.
- [16] B.P. Payne, M.C. Biesinger, N.S. McIntyre, The study of polycrystalline nickel metal oxidation by water vapour, *Journal of Electron Spectroscopy and Related Phenomena*, 175 (2009) 55-65.
- [17] M.C. Biesinger, B.P. Payne, L.W.M. Lau, A. Gerson, R.S.C. Smart, X-ray photoelectron spectroscopic chemical state quantification of mixed nickel metal, oxide and hydroxide systems, *Surface and Interface Analysis*, 41 (2009) 324-332.
- [18] J. Ciston, A. Subramanian, D.M. Kienzle, L.D. Marks, Why the case for clean surfaces does not hold water: Structure and morphology of hydroxylated nickel oxide (001), *Surface Science*, 604 (2010) 155-164.
- [19] L. Salvati, L.E. Makovsky, J.M. Stencel, F.R. Brown, D.M. Hercules, Surface spectroscopic study of tungsten-alumina catalysts using x-ray photoelectron, ion scattering, and Raman spectroscopies, *The Journal of Physical Chemistry*, 85 (1981) 3700-3707.
- [20] S. Dellis, A. Christoulaki, N. Spiliopoulos, D.L. Anastassopoulos, A.A. Vradis, Electrochemical synthesis of large diameter monocrystalline nickel nanowires in porous alumina membranes, *Journal of Applied Physics*, 114 (2013) 164308.
- [21] H.T. Takeshita, T. Oishi, N. Kuriyama, Disproportionation of CaNi_3 hydride: formation of new hydride, CaNiH_3 , *Journal of Alloys and Compounds*, 333 (2002) 266-273.

Vapour-Liquid Equilibrium of CO₂-H₂O system in presence of nanoparticles

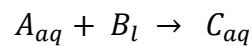
The present chapter draws a preliminary understanding of the vapour-liquid equilibrium (VLE) of the CO₂-H₂O system in presence of nanoparticles. Some results in chapter 4-7 have been used to develop this understanding of influence of nanoparticles (solid particles) on the VLE of CO₂-H₂O system. Surface tension of the liquid is one of the parameters that affect VLE. It is observed that there is change in surface tension of the nanoparticle suspension as compared to DI water. This could be reason for the new CO₂-H₂O VLE leading to the increase in saturation concentration of CO₂.

8.1 Vapour-liquid equilibrium of CO₂-H₂O

Vapour-liquid equilibrium (VLE) defines the distribution of the composition of the species i in the gas and liquid phase when gas absorption is involved. The distribution of the species i in the gas and liquid phase is given by Henry's law for ideal solution and Rault's law for dilute solutions. These laws

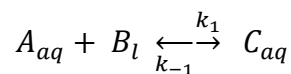
provide information of the final state of the absorption process that is governed by thermodynamic laws. Even though thermodynamics can predict the final absorption limit of a gaseous species i in a liquid it is unable to determine the rate of absorption.

When gas-absorption with chemical reaction is considered it is found that it is in violation of Henry's law [1]. Henry's law may provide information of the unreacted absorbed species but it does not account for the reacted species. Considering a non-reversible reaction of gas reactant A_g with the liquid reactant B_l (i.e. water) occurring in the liquid phase leading to a product C_{aq} in the aqueous phase. The reaction can be written as



Therefore the total amount of species A in the liquid is given as $A_{aq} + C_{aq}$ where the A_{aq} is the amount of unreacted A in the liquid and C_{aq} accounts for the amount of A converted to C, depending on the stoichiometric coefficient of the reaction [2].

In the case of a reversible reaction



the reaction itself has an equilibrium coefficient K that is given by the equation [2, 3]

$$K = \frac{k_1}{k_{-1}} = \frac{[C_{aq}]}{[A_{aq}][B_l]}$$

where k_1 is the kinetic constant for forward reaction, k_{-1} is the kinetic constant for the reverse reaction and $[A_{aq}]$, $[B_l]$, $[C_{aq}]$ are the concentration of the

reactants and products given by the above reaction. The equilibrium constant thus gives the relationship between the unreacted reactants and the products. In aqueous systems the concentration of water is not considered as it is the continuous phase. Thus CO₂-H₂O equilibrium is given as [3, 4]

$$K = \frac{k_1}{k_{-1}} = \frac{[HCO_3^-][H_3O^+]}{[CO_{2(aq)}]} = 10^{-2.8} = 1.6 \times 10^{-3}$$

Due to this relationship the amount of acid produced in the reaction is very low as compared to the CO_{2(aq)} value. The value of this acid is considerable when studying the reaction of CO₂ in DI water which can reduce the pH of water to 4 (at 1 atm partial pressure of CO₂). Due to the small amount of H₂CO₃ in relation of CO_{2(aq)}, leads to the vapour liquid equilibrium of CO₂-H₂O system to follow Henry's law.

8.2 CO₂-H₂O equilibrium in nanoparticle suspensions

The review of literature suggests that the reports on the effect of solid particles on the vapour-liquid equilibrium are scanty. However, the dynamic mass transfer process has been studied in detail [5, 6]. It may be noted that Bhaduri and Šiller [7] were the first to report that the solid particles of sub-micron size affect the vapour-liquid equilibrium. As their study was mainly related to catalysis, experimental observation were not analysed in detail. Recently Liu *et al.* [8] reported that the absorption capacity of solutions can be increased by addition of solid particles. They considered glycol with ZIF-8 (zeolitic imidazolate framework-8) as their system of analysis. CO₂ does not react with glycol and therefore the ZIF-8 and glycol system is a non-interactive system. Liu *et al.* [8] have not considered vapour-liquid equilibrium their study.

In the studies described in chapter 4-7 it is observed that the vapour liquid equilibrium is affected due to the presence of the nanoparticles. The study showed that the CO_2 is observed as absorbed specie on the nanoparticle surface and is also reacting with the solvent (i.e. water) to form carbonic acid in solution. A detailed analysis of vapour-liquid equilibrium was not carried out as it is beyond the scope of the thesis and area of study. However, some general comments have been made on the basis of the results presented in chapters 3-7.

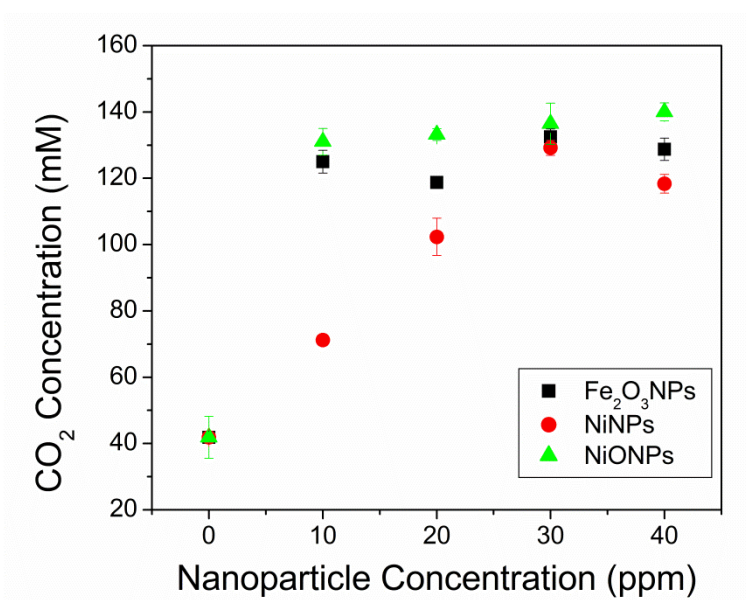


Figure 8.1: Average values of CO_2 equilibrium concentration in different nanoparticle suspension at different nanoparticle concentration.

It can be observed from figure 8.1 that the material of the nanoparticle and surface chemistry affect the of equilibrium concentration of CO_2 in the presence of nanoparticles in suspension. The concentration values observed in figure 8.1 reflect the total CO_2 concentration i.e. $\text{CO}_{2(\text{aq})}$ and H_2CO_3 together. It is observed that for different oxide nanoparticles the equilibrium concentration of CO_2 is independent of particle concentration. In the case of NiNPs the CO_2 equilibrium concentration increases initially with particle concentration, reaches

a maxima and then reduces with further increase in NiNPs concentration. These results show that the material of the nanoparticles, in particular their interaction with the solution (i.e. metallic, oxide etc) would be a factor affecting the CO₂ equilibrium concentration. Baltrusaitis and Grassian [9] observed that presence of a thin aqueous layer on oxide nanoparticle (Al₂O₃ and Fe₂O₃) surface can increase the CO₂ adsorption capacity (gas-solid equilibrium) up to 5 times compared to the absence of the aqueous layer. They suggest that this increase in adsorption capacity is due to the formation of hydroxyl (OH) groups on the nanoparticle surface.

8.3 Distinguishing between adsorbed and free CO_{2(aq)} in NiNPs suspension

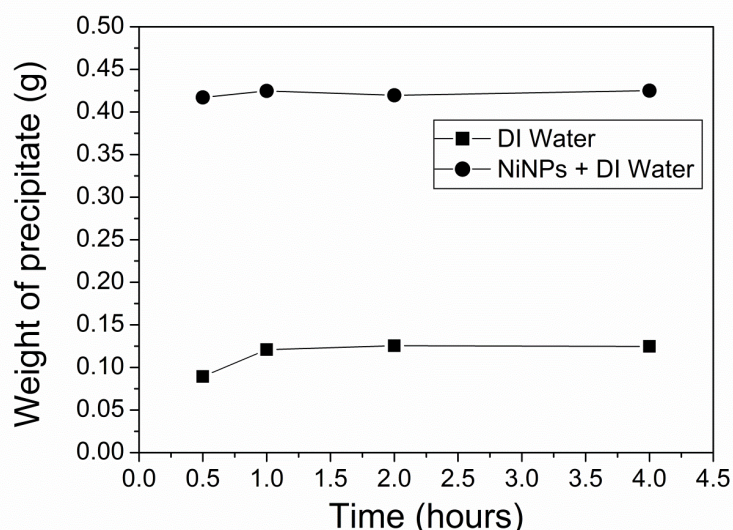


Figure 8.2: Average amount of CaCO₃ precipitated when CO₂ is bubbled in DI water or 30 ppm NiNPs suspension under the same different bubbling time.

As water reacts with CO₂ to form carbonic acid and there is bicarbonate ions on the surface of the NiNPs, there might exist a relationship between the free bicarbonate ions in solution and the bicarbonate ions on the surface of the NiNPs. The precipitation study (figure 8.2) indicates that the absorbed CO₂ can be precipitated as CaCO₃ out of solution. The amount of NiNPs added in the solution is ~3 mg whereas the amount of CaCO₃ precipitated from the NiNPs

solution is nearly 400 mg, compared to ≈ 120 mg of CaCO_3 obtained in the control sample. Therefore 3 mg compared with 400 mg is very low to contribute to ≈ 280 mg of excess carbonate obtained. This suggests that there is an interaction between the carbonate species in solution and the carbonate species on the NiNPs surface. A more detailed analysis of the absorption system would lead to a new understanding of VLE and Henry's law when applied to suspension or slurry systems, similar to the one suggested by Dankwerts for gas-liquid reaction system [1] (section 8.1).

8.4 Effect of temperature on CO_2 equilibrium concentration in NiNPs suspension

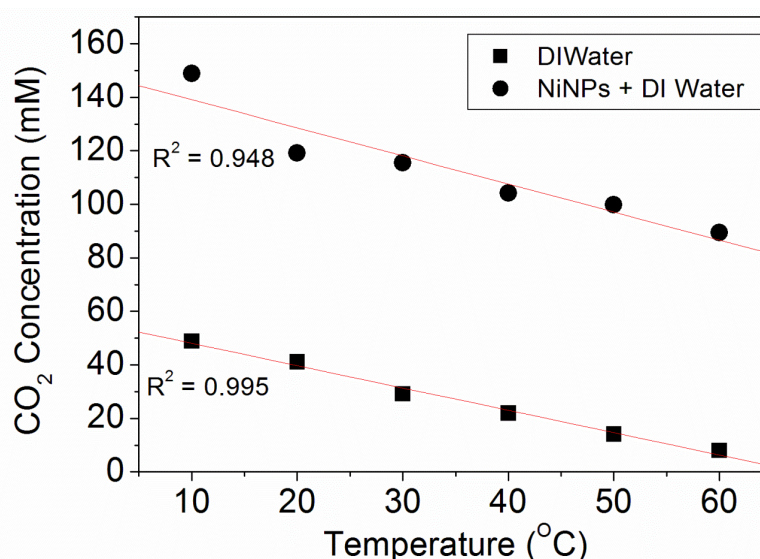


Figure 8.3: Average values of CO_2 equilibrium concentration at different temperatures in DI water and 30 ppm NiNPs suspension.

From figure 8.3 it is observed that the difference of amount of CO_2 absorbed by the NiNPs suspension as compared to that of DI water is independent of temperature. This might be due to the strong interaction between the adsorbed species of CO_2 (as bicarbonate ions) on the surface of the NiNPs which could be independent of temperature. The temperature range studied are low, higher temperatures ranges might have different effect on the

VLE of CO₂-H₂O-NiNPs system. Adsorption-desorption studies of bicarbonate ions on the NiNPs surface would provide an insight for why the excess CO₂ absorbed in the NiNPs suspension does not change with temperature.

8.5 Discussion on VLE of CO₂-H₂O system in presence of nanoparticles

All the above results suggest that there is a change in the vapour liquid equilibrium of CO₂-H₂O system in presence of nanoparticles. The previous assumptions made in chapter 4 section 4.2 and chapter 5 section 5.5.2 on adsorption of CO₂ on the surface of the NiNPs do not justify the results obtained in the above CaCO₃ precipitation studies (section 8.3). Therefore it is suspected that there would be another phenomena that would have affected the vapour-liquid equilibrium of CO₂-H₂O system in presence of the nanoparticles..

Surface tension of the liquid is one of the parameters that affect the dynamic equilibrium of distribution of molecules in gas and liquid phase of a species [10]. The presence of surfactants or nanoparticles can increase or decrease the free forces action at line of tension between the gas and liquid thus affecting the vapour-liquid equilibrium [10]. It is known that the presence of nanoparticles increases or decreases the tension of the liquid-gas interface [11]. In the case of oil recovery from oil wells (carbonate reservoir), SiO₂ nanoparticles have shown an enhancement in oil recovery [12]. The presence of the particles alters the wettability of the reservoir from oil-wet to water-wet thus enhancing the recovery of oil from oil fields [12]. Similarly Murshed *et al.* [13] show that the presence of nanoparticles at oil-water interface decreases the surface tension between the liquids and increases thermal diffusion across the interface. Therefore it is reasonable to assume here that, the influence of

nanoparticles on surface tension could lead to the new vapour liquid equilibrium in CO₂-H₂O system.

Esmailzadeh *et al.* [14] studied the effect of ZnO₂ nanoparticles including surfactants on liquid-liquid, liquid-air and liquid-solid interface properties. Their results show that at a given concentration of surfactants the surface tension of liquid-air system decreases with increasing particle concentration. Wi *et al.* [15] also reported similar decrease in surface tension of the nanoparticle suspension with increasing nanoparticle concentration. Vafaei *et al.* [16] studied the influence of Bi₂Te₃ nanoparticles on surface tension of air-nanoparticle suspension. They found that by increasing the nanoparticle concentration there was a decrease in the surface tension of the suspension.

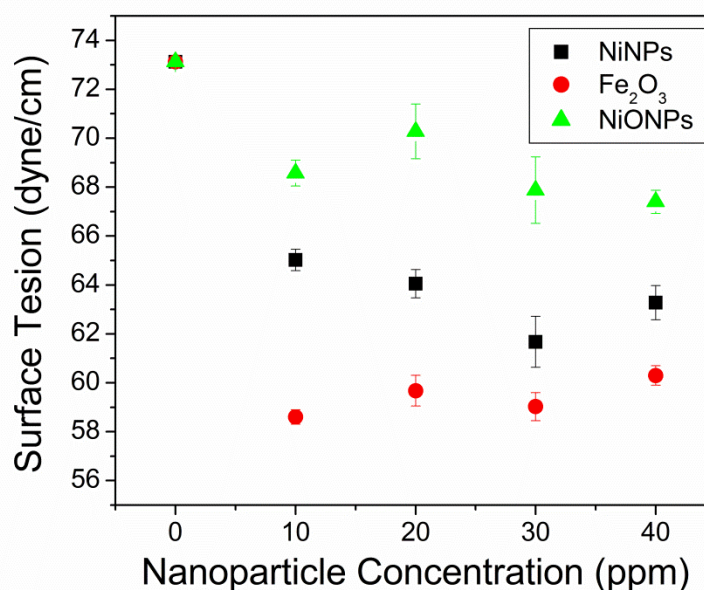


Figure 8.4 Average values of surface tension of different nanoparticle suspensions at different nanoparticle concentration at room temperature. (Square- NiNPs, Circle- Fe₂O₃NPs and Triangle- NiONPs)

Figure 8.4 shows the surface tension of different nanoparticle suspensions having different nanoparticle concentration measured at room temperature. The precision of the surface tension meter was checked by measuring the surface tension of water for ten repeats. The surface tension of

water was measured as 73.1 ± 0.1 dyne/cm which is close to the literature value of 72.7 dyne/cm [17, 18]. It can be observed from figure 8.4 that by increasing the concentration of nanoparticles in suspension there is a reduction in the surface tension of the suspension. For NiNPs (black square in figure 8.4) it can be seen that as the concentration of the NiNPs there is a decrease in the surface tension till a minima is reached at 30 ppm. After 30 ppm there is an increase observed in the surface tension of NiNPs suspension. The decrease in surface tension follows a similar trend of increase in saturated concentration of CO₂ observed in figure 8.1. The reason for this could be, at higher concentration the agglomeration of the particles in the bulk and low particle concentration at the surface of the suspension (section 5.2.2, chapter 5) [11]. Similar trend in decrease in surface tension with increasing nanoparticle concentration, reaching a minima and then increase in surface tension with increase in nanoparticle concentration was observed by Jeong *et al.* [19] (for Al₂O₃ nanoparticles in water) and Pantzali *et al.* [20] (for CuO nanoparticles in water).

Fe₂O₃NPs suspension (red circles in figure 8.4) show minimal increase in the surface tension with increase in concentration of the Fe₂O₃NPs. NiONPs suspension show a linear decrease in surface tension with increasing NiONPs concentration (green triangles in figure 8.1). Similar decrease in trend of surface tension with increase in nanoparticle concentration was observed by Chen *et al.* [21] (for laponite particles in DI water) and Okubo *et al.* [22] (for polystyrene and silica nanoparticles in water). The trend of change in surface tension of Fe₂O₃NPs and NiONPs are similar to the trends observed in the CO₂ saturation results in figure 8.1.

It can be observed from figure 8.4 that different nanoparticles have different values for reduction of the surface tension of DI water. This difference in the reduction of surface tension might be due to the different bulk densities of different nanoparticles. The change in density affects the interaction between the nanoparticles and water molecules affecting the van der Waals forces of the liquid surface. This causes the surface tension of the suspension to change [10, 23]. Bhuiyan *et al.* [23] also recently reported that smaller particles have greater effect on surface tension than larger particles.

8.6 Conclusion

It can be concluded from the results that the VLE of CO₂-H₂O does get affected in the presence of different nanoparticles. The presence of nanoparticles increases the amount of CO₂ absorbed in water as compared DI water alone. CO₂ exists on the surface of the nanoparticles in the form of M(HCO₃)_x species that may be in equilibrium with CO_{2(aq)} species in solution. This equilibrium between the adsorbed M(HCO₃)_x species and CO_{2(aq)} species is observed to be independent of temperature. Surface tension was also analysed as a parameter affecting the CO₂-H₂O VLE. The presence of nanoparticles in suspension reduced the surface tension of the suspension as compared to DI water. This reduction in surface tension could be the reason for the attainment of new CO₂-H₂O VLE in nanoparticle suspension.

References

- [1] P.V. Danckwerts, Gas Liquid Reactions, McGraw Hill Publishers, New York, 1970.
- [2] J.M. Smith, H.C.A. Van Ness, M.M., Introduction to Chemical Engineering Thermodynamics, McGraw Hill Publishers (International Edition), 2005.
- [3] V.L.J. Snoeyink, David, Water Chemistry, John Wiley & Sons, New York, 1980.
- [4] R.E. Loewenthal, G.V.R. Marais, Carbonate Chemistry of Aquatic Systems: Theory and Applications, Ann Arbor Science, Ann Arbor, 1976.
- [5] S.-S. Ashrafmansouri, M. Nasr Esfahany, Mass transfer in nanofluids: A review, International Journal of Thermal Sciences, 82 (2014) 84-99.
- [6] C. Pang, J.W. Lee, Y.T. Kang, Review on combined heat and mass transfer characteristics in nanofluids, International Journal of Thermal Sciences, 87 (2015) 49-67.
- [7] G.A. Bhaduri, L. Šiller, Nickel nanoparticles catalyse reversible hydration of carbon dioxide for mineralization carbon capture and storage, Catalysis Science & Technology, 3 (2013) 1234-1239.
- [8] H. Liu, B. Liu, L.-C. Lin, G. Chen, Y. Wu, J. Wang, X. Gao, Y. Lv, Y. Pan, X. Zhang, X. Zhang, L. Yang, C. Sun, B. Smit, W. Wang, A hybrid absorption-adsorption method to efficiently capture carbon, Nature Communications, 5 (2014).
- [9] J. Baltrusaitis, V.H. Grassian, Surface reactions of carbon dioxide at the adsorbed water-iron oxide interface, Journal of Physical Chemistry B, 109 (2005) 12227-12230.
- [10] F. Bresme, M. Oettel, Nanoparticle at fluid interfaces, Journal of Physics: Condensed Matter, 19 (2007) 413101(413101-413133).
- [11] S.S. Khaleduzzaman, M.I.S. Mahbulul, M.I., R. Saidur, Effect of particle concentration, temperature and surfactant on surface tension of nanofluids, International Communications in Heat and Mass Transfer, 49 (2013) 110-114.
- [12] A.B. Roustaei, Hadi, Experimental investigation of SiO₂ nanoparticles on enhanced oil recovery of carbonate reservoirs, Journal of Petroleum Exploration and Production Technology, 5 (2015) 27-33.
- [13] S.M.S. Murshed, S.-H. Tan, N.-T. Nguyen, Temperature dependence of interfacial properties and viscosity of nanofluids for droplet-based microfluidics, Journal of Physics D: Applied Physics 41 (2008) 085502 (085501-085505).
- [14] P. Esmailzadeh, Z. Fakhroueian, A. Bahramian, S. Arya, Influence of ZrO₂ nanoparticles including SDS and CTAB surfactants assembly on the interface

properties of liquid-liquid, liquid-air and liquid-solid surface layers, *Journal of Nano Research*, 21 (2013) 15-21.

[15] H.S. Wi, S.K. Cingarapu, Ken J., B.M. Law, Nanoparticle adsorption at liquid-vapour surfaces: Influence of nanoparticle thermodynamics, wettability and line tension, *Langmuir*, 27 (2011) 9979-9984.

[16] S. Vafaei, A. Purkayastha, A. Jain, G.B.-T. Ramanath, Theodorian, The effect of nanoparticle on the liquid-gas surface tension of Bi_2Te_3 nanofluids, *Nanotechnology*, 20 (2009) 185702 (185701-185706).

[17] D.R. Lide, *CRC Handbook of Physics and Chemistry*, in, CRC Press, Boca Raton, 2005.

[18] D. Green, R. Perry, *Perry's Chemical Engineers' Handbook*, Eighth Edition, McGraw-Hill Education, 2007.

[19] Y.H. Jeong, W.J. Chang, S.H. Chang, Wettability of heated surfaces under pool boiling using surfactant and nano-fluids, *International Journal of Heat and Mass Transfer*, 51 (2008) 3025-3031.

[20] M.N. Pantzali, A.G. Kanaris, K.D. Antoniadis, A.A. Mouza, S.V. Paras, Effect of nanofluids on the performance of a miniature plate heat exchanger with modulated surface, *International Journal of Heat and Fluid Flow*, 30 (2009) 691-699.

[21] R.-H.P. Chen, Tran X., D. Martello, Surface tension of evaporating nanofluid droplet, *International Journal of Heat and Mass Transfer*, 54 (2011) 2459-2466.

[22] T. Okubo, Surface tension of structured colloidal suspension of polystyrene and silica spheres at the air-water interface, *Journal of Colloid and Interface Science*, 171 (1995) 55-62.

[23] M.H.U. Bhuiyan, R.M. Saidur, R.M., I.M. Mahabubul, M.A. Amalina, Experimental investigation on surface tension of metal oxide-water nanofluids, *International Communications in Heat and Mass Transfer*, 65 (2015) 82-88.

Mineralization of CO₂ using gypsum and sodium chloride in novel bridge reactor

Chapter 9 describes a novel process developed for the mineralization of CO₂ using gypsum and sodium chloride. The reaction is carried out in a new reactor design termed as "bridge reactor". At first the theoretical background of the bridge reactor has been explained. Then the use of the bridge reactor for the mineralization of CO₂ using gypsum and sodium chloride is discussed. The calcium carbonate obtained was chemically analysed for impurities to validate the yield results. The mass transfer studies were performed to test the correlation between the concentration gradient and transfer of ions along the bridge of the bridge reactor.

9.1 Mineralization of CO₂ using "Bridge Reactor"

The working and design of the bridge reactor has been described in chapter 3, section 3.2.13. In the reaction Na₂CO₃ was taken as the limiting reagent to compare the effectiveness of the bridge to transfer CO₂ from acid side to the

base side of the reactor. CO_2 would react with Na_2CO_3 to form NaHCO_3 , therefore the amount of precipitate would be reduced by this and the yield of CaCO_3 in the base side of the reactor. Another possibility is that CO_2 would react to form carbonic acid and dissociate as bicarbonate ion, upon crossing the bridge that could then increase in yield of CaCO_3 which would be a proof of transfer and mineralization of CO_2 in the base side of the reactor. Salt bridges have been extensively used to link two halves of a galvanic cell and the transfer of ions in the bridge takes place when electrons flow from an external circuit [1]. The external circuit is an important part of the galvanic cell, lacking which there is no reaction possible. In the current application we use the salt bridge for the first time to transfer ions for a series reaction to mineralize CO_2 . The mass transfer is driven by concentration gradient alone (see section 3.2.12, chapter 3).

9.2 Chemical Characterization of precipitate obtained in bridge reactor

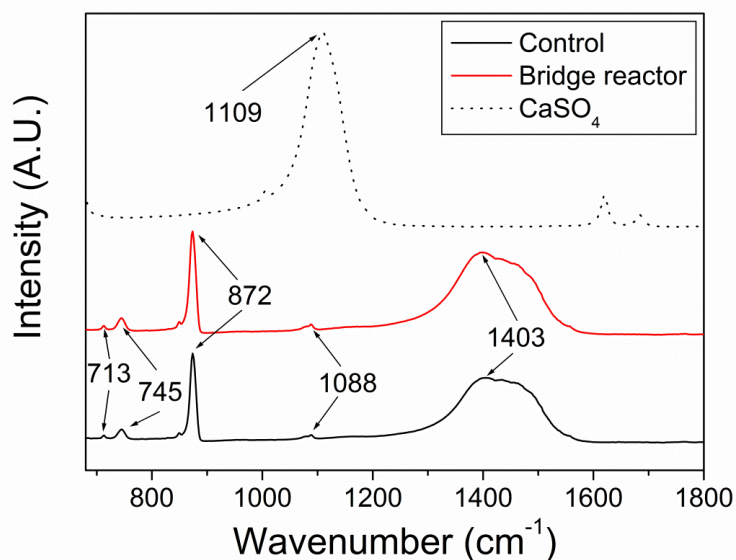


Figure 9.1: FTIR spectra of the CaCO_3 samples obtained from control and bridge reactors and $\text{CaSO}_4 \cdot 2\text{H}_2\text{O}$ (gypsum).

The precipitate obtained from the control and the bridge reactor was characterised using XRD and FTIR and was found to be pure calcium

carbonate. Figure 9.1 shows the FTIR spectra for controlled and bridge reactor sample. The peaks at 745 cm^{-1} , 874 cm^{-1} , 1088 cm^{-1} and 1403 cm^{-1} all correspond to the vaterite form of CaCO_3 [2, 3] whereas the peaks at 713 cm^{-1} , 874 cm^{-1} and 1043 cm^{-1} correspond to the calcite form of CaCO_3 [4, 5]. The peaks at 714 cm^{-1} (and 745 cm^{-1}) and 874 cm^{-1} are associated with the in-plane and out of plane vibration of O-C-O vibration and the peak at 1403 cm^{-1} is associated with the asymmetric stretching vibration [2, 3]. The gypsum characteristic peak of the SO_4 vibration at 1109 cm^{-1} [6] is very small which confirms the successful removal of gypsum from the precipitate.

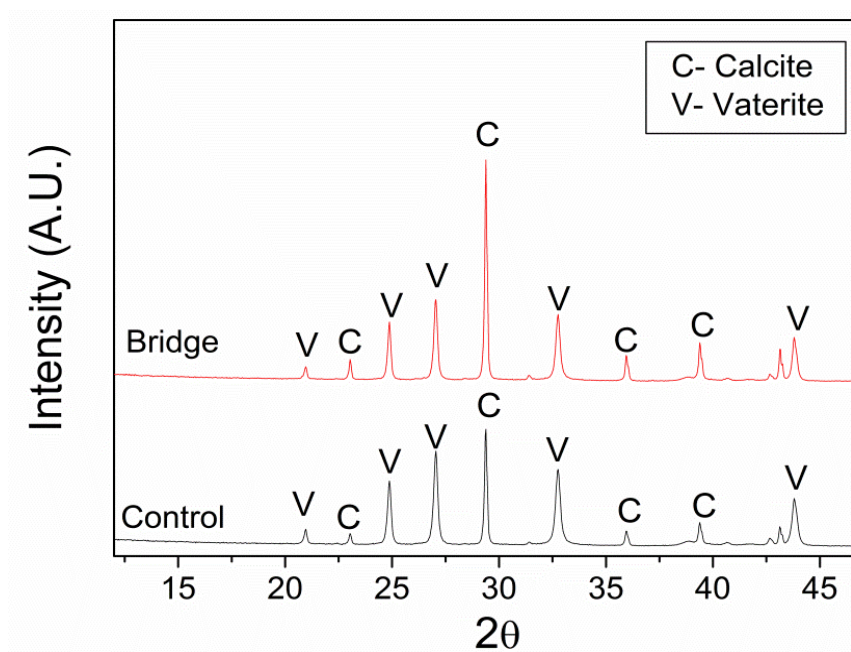


Figure 9.2: XRD spectra of the precipitated CaCO_3 in control and bridge reactor showing two crystal polymorphs of calcium carbonate (calcite and vaterite)

Figure 9.2 shows the XRD spectrum of the CaCO_3 precipitate obtained from the bridge reactor and the control [7]. In both of the samples calcite and vaterite polymorphs are observed [7], which are the same as the FTIR results. XRD data suggest that the calcite is the dominant phase of CaCO_3 in the bridge reactor rather than vaterite.

It is known that vaterite would transform to calcite in presence of water [8, 9]. Therefore during vaterite synthesis, care is taken for rapid separation of vaterite crystals with short reaction times (reaction time up to 30 min) [10-15]. As compared to these reports [10-15] the reaction time in bridge reactor is long (about 360 min) that could lead to transformation of vaterite to calcite.

9.3. Precipitation yields of CaCO_2 in bridge reactor and control

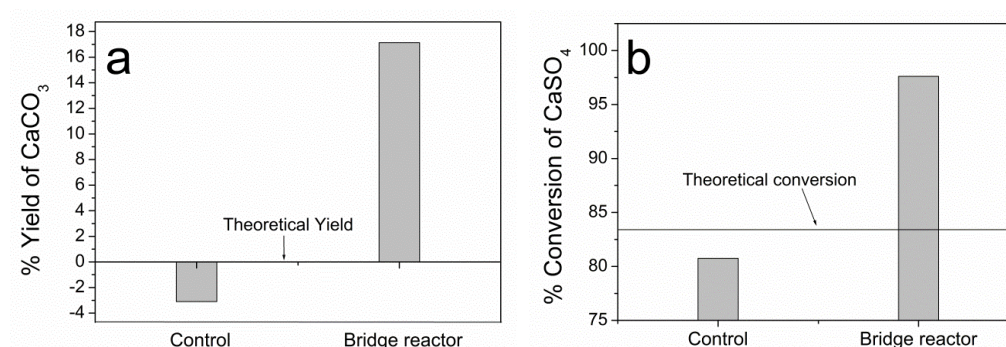


Figure 9.3: a) Percentage yield of CaCO_3 in bridge reactor and control, b) percentage conversion of CaSO_4 in bridge reactor and control.

Figure 9.3a shows the yields of CaCO_3 in the control and the bridge reactor obtained by the procedure described in chapter 3 section 3.2.12. All the experiments were repeated in triplets. The theoretical yield is considered as the base line for comparison between the yield in the bridge reactor and the control. Theoretical CaCO_3 yield was calculated taking the initial Na_2CO_3 as the limiting reagent in the reaction stoichiometry. The yield of the control and bridge reactor were calculated using the weight of the washed and dried precipitate. In the control there was $96 \pm 1\%$ yield as compared to theoretical yield, whereas in the bridge reactor there was $117 \pm 1\%$ yield as compared to the theoretical yield. Thus there is a $\sim 21\%$ increase in the amount of CaCO_3 obtained in the batch reactor compared to the control

Based on the assumptions made previously (chapter 3 section 3.2.12; that there is transfer of ions from the acid side of the bridge reactor to the base side of the bridge reactor), the increase in CaCO_3 precipitation is due to the transfer of CO_2 from the acid side to the base side of the reactor. Therefore the $20 \pm 1\%$ increase in yield obtained in the bridge reactor is due to CO_2 being trapped as carbonates without use of any additional basic material.

Figure 9.3b shows the conversion of CaSO_4 in the control and the bridge reactor. Na_2CO_3 is taken as the limiting reagent in the control reaction and CaSO_4 becomes the second limiting reagent in the series reaction in the bridge reactor. The amount of CaSO_4 added in control and bridge reactor was the same. In the control sample only ~81% conversion of CaSO_4 was observed. The theoretical conversion of CaSO_4 based on Na_2CO_3 limiting reagent is ~83%. The conversion of CaSO_4 observed in the bridge reactor is 97.6% that implies ~ 14% excess conversion of CaSO_4 compared to the theoretical limit of the control sample. This is due to the conversion of CaSO_4 to CaCO_3 due to the transfer of CO_2 from the acid side of the bridge reactor to the basic side of the bridge reactor. The same experiment was repeated successfully three times.

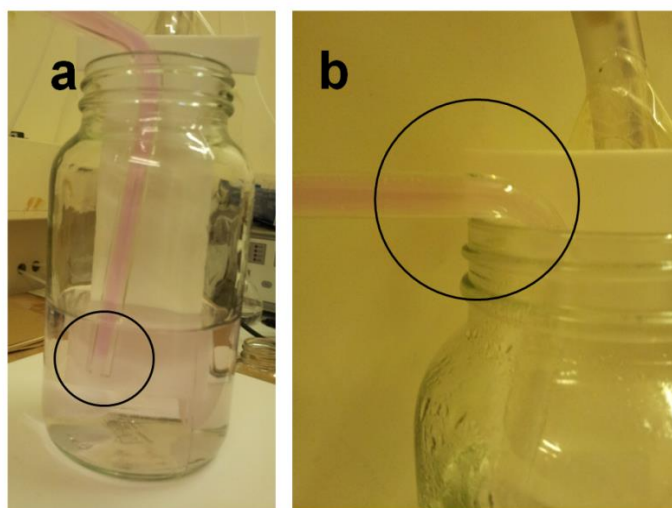


Figure 9.4 a) the pink colourless interface (between carbonate solution and NaCl solution-acid side of the reactor) before the start of the reaction and b) the pink colourless interface (between carbonate solution and NaCl solution) at the end of 300 min observed in the bridge in the acid side of the reactor.

Phenolphthalein was added as an indicator to keep a check on the bridge and observe the acidity and basicity of the bridge. Phenolphthalein being a basic indicator indicates the carbonate region of the bridge and colourless part indicates the non-carbonate region of the bridge. As phenolphthalein changes its colour below pH of 8.2 the colourless region indicates the existence of acid [16]. It was observed that at the beginning of the reaction (i.e. before the addition of calcium carbonate) the glass bridge was pink in colour till the bottom as seen in figure 9.4a. As the reaction proceeded for five hours this pink-colourless interface moved upward and was observed to be at the U-bend of the acid side of the bridge figure 9.4b. This interface represents the bicarbonate-acid interface and the movement of this interface in the bridge indicates the movement of the HCO_3^- ions within the bridge.

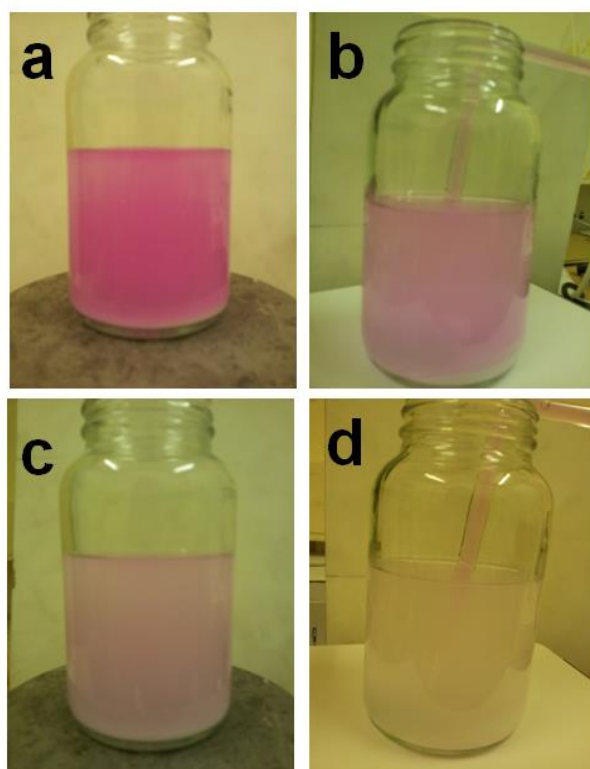


Figure 9.5: Pictures showing the changes in colour of phenolphthalein during reaction of sodium carbonate and gypsum for a) control sample after 230 min of reaction, b) base side of bridge reactor after 230 min of reaction, c) control sample after 250 min of reaction and d) base side of bridge after 250 min of reaction.

As the phenolphthalein indicator was added to the carbonate solution the change in the intensity of the pink colour gives an approximation about the kinetics of the reaction. It was observed that as the reaction completed the colour of the basic side of the bridge reactor and the control became lighter when compared to the control sample. Figures 9.5a and 9.5b shows the colour of the control and bridge reactor, respectively, after 230 min (i.e. 46 ml of CaSO_4 was added) and figures 9.5c and 9.5d show the control and bridge, respectively, after 250 min (i.e. 50 ml of CaSO_4 was added). It can be seen that figure 9.5a is darker pink in colour than figures 9.5b. Also figure 9.5c is more

faint pink in colour than figure 9.5d. This change in colour indicates that the reaction in the bridge reactor is faster than the reaction in the control sample. However this could also be because the bridge reactor has smaller volume of Na_2CO_3 solution than the control because part of the solution was used to prepare the bridge.

9.4 Mass transfer studies in the "bridge reactor"

In order to validate and understand the mass transfer process of ions within the bridge reactor (Section 3.2.14 chapter 3) used for the mineralization of CO_2 experiments above (section 9.1-9.3), a set of experiments were carried out with two different concentrations of Na_2CO_3 to see the effect of concentration gradient on the mass transfer process. It should be noted that this is the first report on the use of bridge reactor, thus there is no theoretical or experimental literature on the use of a salt bridge for mass transfer under a concentration gradient. Thus this section is important to prove that mass transfer of ions would occur across the salt bridge under a concentration gradient to validate the results obtained in the mineralization of CO_2 experiment in section 9.1-9.3. In this experiment two liquid samples were used and no gas was involved as described in section 3.2.13, chapter 3. Modifications were made to test the movement of a common ionic component through the bridge by following the movement of an indicator dye and checking the yield of the product at the end of the process. In these experiments the yield results were compared to that of a control. Chapter 3 section 3.2.12 provides the experimental details of the mass transfer experiments in the bridge reactor. All experiments were repeated twice.

In the first set of experiments 0.1 M Na_2CO_3 was taken in two sides of the bridge reactor and phenolphthalein indicator was added in to the right hand side of the reactor to test the movement of the material from the right hand cell to the left hand cell. The concept of the reaction was the same as in section 9.2, but CO_2 gas/ carbonic acid was replaced by Na_2CO_3 solution. The initial setup of the reaction cell can be seen in figure 9.6A at time zero. Then the movement of the dye was observed by taking snapshots after every 1 hour. Figure 9.6 gives the photographic images of the movement of the phenolphthalein indicator in the bridge showing the diffusion mass transfer in the bridge reactor as the reaction proceeds (In order to track the movement of the dye the main interface has been encircled in figure 9.6). In this experiment 1 ml of 0.2 M CaSO_4 solution was added to the left hand side of the reactor and 1 ml of water was added in to the right hand side of the reactor (to keep the bridge balanced and avoid movement of material from one side to another). It can be seen from figure 9.6(b-f) that there was a movement of the dye through the bridge as the reaction proceeded. This could confirm the movement of phenolphthalein from the right hand cell to the left hand cell of the reactor.

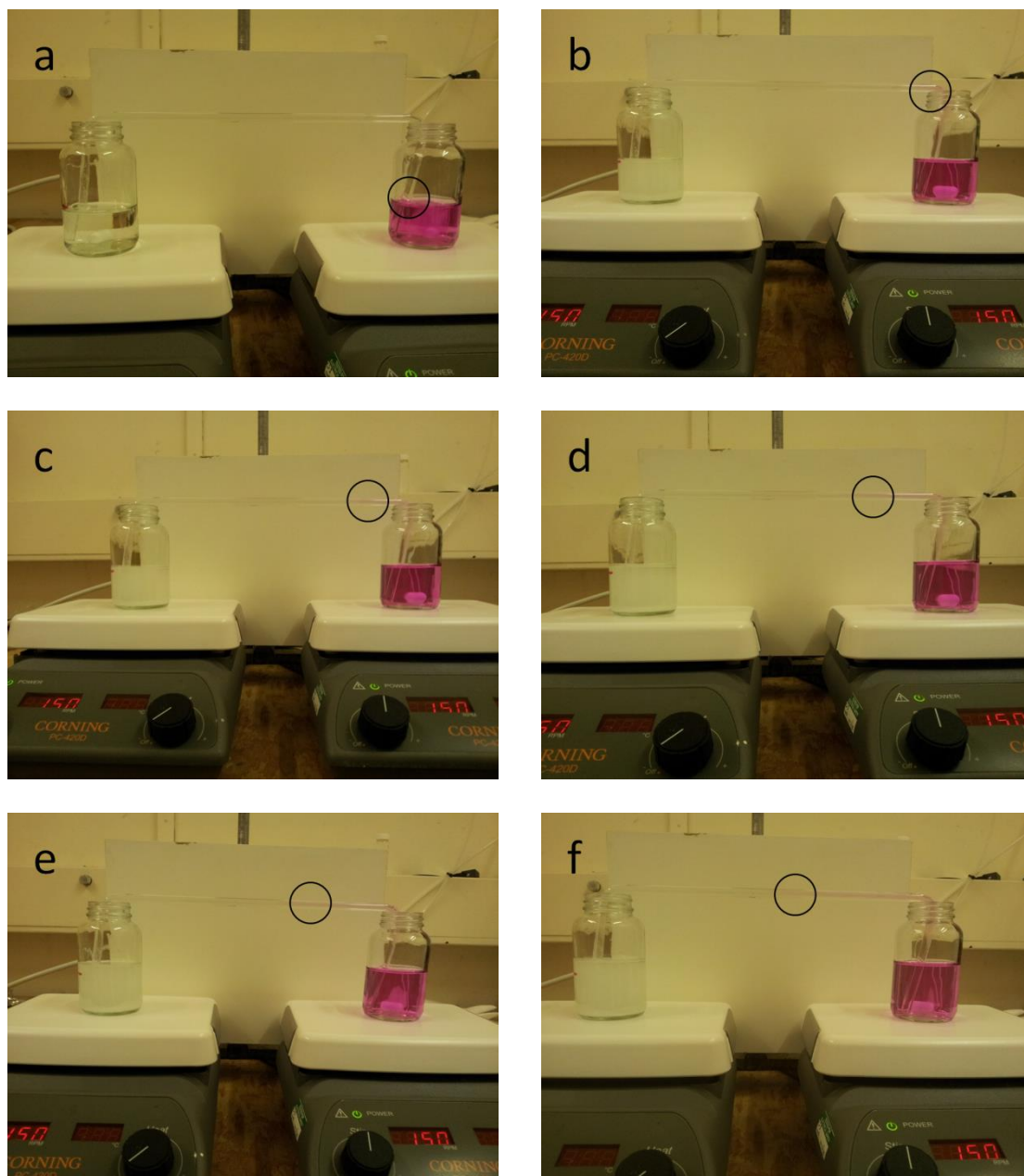


Figure 9.6: Dye diffusion test for bridge reactor with concentration of 0.1 M Na_2CO_3 (right hand side cell) and DI water dilution. (a) 0 min, (b) 60 min, (c) 120 min, (d) 180 min, (e) 240 min, and (f) 300 min.

After the end of the reaction the precipitated CaCO_3 was washed, dried and weighed and compared to that of the control sample. It was found that the precipitate obtained in the bridge reactor was less than that of the control by ~4%. One of the possible reasons for the reduction of the precipitate is that the concentration of the right hand side of the cell was very small to that of the left

hand of the cell. Thus the resultant concentration at the end of the reaction in the right hand cell was ~ 0.05 M of Na_2CO_3 which was less than the starting concentration of Na_2CO_3 (i.e. 0.1 M).

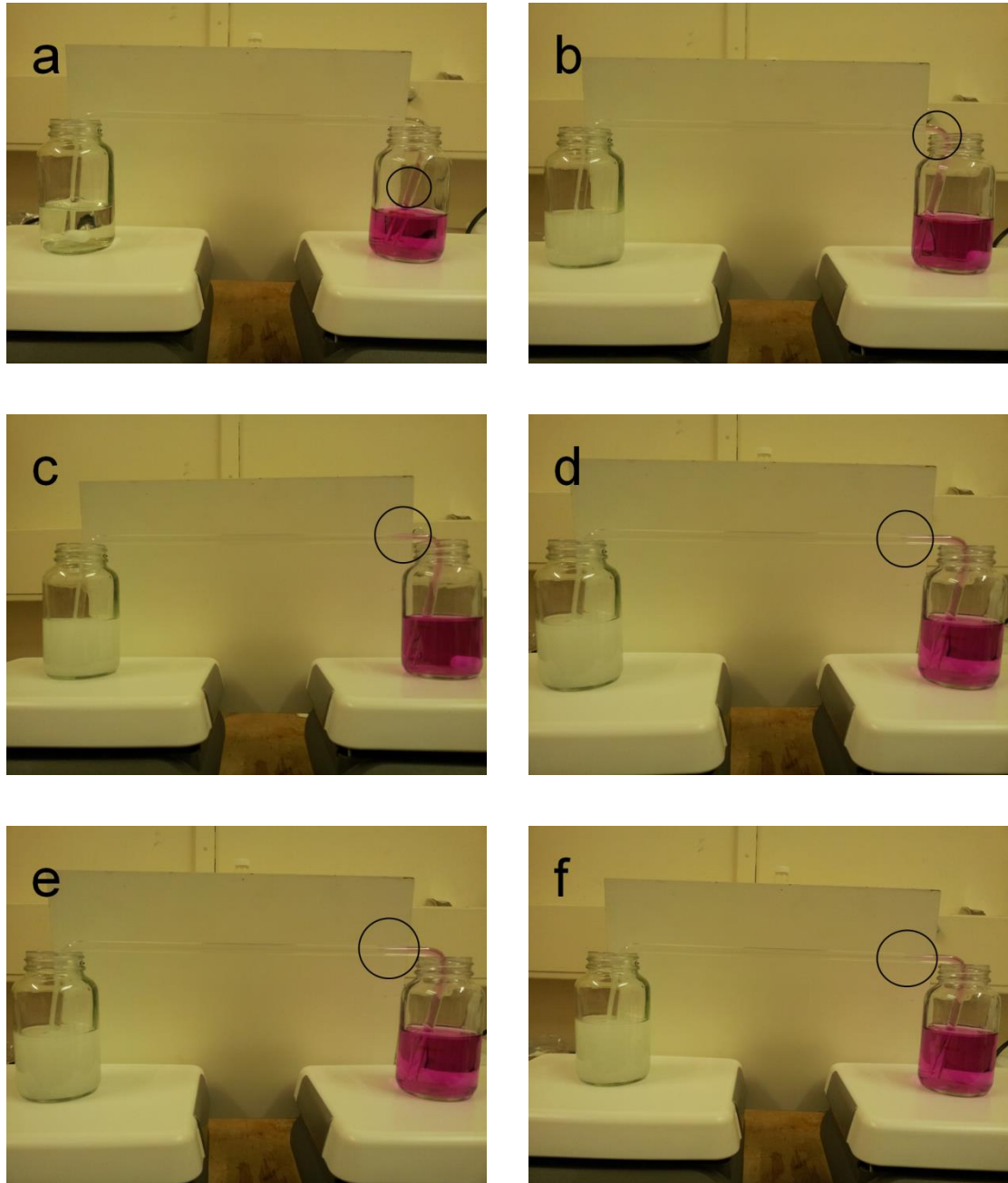


Figure 9.7: Dye diffusion test for bridge reactor with concentration of 0.3 M Na_2CO_3 (right hand side cell) without dilution. (a) 0 min, (b) 60 min, (c) 120 min, (d) 180 min, (e) 240 min, and (f) 300 min.

Therefore the above experiment was repeated with a concentration of 0.3 M Na_2CO_3 in the right hand cell of the bridge reactor and the left hand side

reactant concentration was same as in the above experiment (0.1 M Na₂CO₃). Additionally the concentration of the right hand side cell was kept constant by adding in 1 ml of 0.3 M Na₂CO₃ solution. The results of the experiments can be seen in figure 9.7. As compared to the low concentration experiments the diffusion of phenolphthalein was observed in the first 3 hours of the reaction but then remained approximately constant till the end of the reaction. After the end of the reaction the CaCO₃ precipitate was washed, dried and weighed. It was observed that there was ~14% enhancement in the CaCO₃ yield as compared to the control. This provides proof that if provided a proper concentration gradient the salt bridge can work as a selective mass transport operator for particular reaction sequence without use of electric current.

9.5 Conclusion

The chapter introduces the use of a novel reactor along with a novel process for the mineralization of CO₂. It was observed that the bridge reactor had higher yields than the control sample proving the capture of CO₂. The bridge reactor yielded 21% more carbonates as compared to the control and 17% more carbonates as compared to the theoretical yield. A mechanism for the working of the bridge reactor has also been presented. The mass transfer results show that there can be transfer of carbonate ions across the bridge based on a concentration gradient present at all times. Gypsum was chosen as a mineral source for Ca because gypsum is comparatively more soluble (i.e. 2 g/l) than most of the other Ca/Mg mineral sources as presented in chapter 2.

References

- [1] P. Atkins, J. de Paula, Atkins' Physical Chemistry, Oxford University Press Oxford, 2010.
- [2] M. Tatzber, M. Stemmer, H. Spiegel, C. Katzlberger, G. Haberhauer, M.H. Gerzabek, An alternative method to measure carbonate in soils by FT-IR spectroscopy, *Environmental Chemistry Letters*, 5 (2007) 9-12.
- [3] Z. Zhang, Y. Xie, X. Xu, H. Pan, R. Tang, Transformation of amorphous calcium carbonate into aragonite, *Journal of Crystal Growth*, 343 (2012) 62-67.
- [4] Ö. Cizer, C. Rodriguez-Navarro, E. Ruiz-Agudo, J. Elsen, D. Gemert, K. Balen, Phase and morphology evolution of calcium carbonate precipitated by carbonation of hydrated lime, *Journal of Material Science*, 47 (2012) 6151-6165.
- [5] K.N. Islam, M.Z.B.A. Bakar, M.E. Ali, M.Z.B. Hussein, M.M. Noordin, M.Y. Loqman, G. Miah, H. Wahid, U. Hashim, A novel method for the synthesis of calcium carbonate (aragonite) nanoparticles from cockle shells, *Powder Technology*, 235 (2013) 70-75.
- [6] M.F. La Russa, S.A. Ruffolo, G. Barone, G.M. Crisci, P. Mazzoleni, A. Pezzino, The use of FTIR and Micro-FTIR Spectroscopy: An example of application to cultural heritage, *International Journal of Spectroscopy*, 2009 (2009) 893528.
- [7] H.E. Swanson, R.K. Fuyat, Standard X-ray diffraction powder patterns, National Bureau of Standards (U.S.) Circular, II (1953) 51.
- [8] A.V. Radha, T.Z. Forbes, C.E. Killian, P.U.P.A. Gilbert, A. Navrotsky, Transformation and crystallization energetics of synthetic and biogenic amorphous calcium carbonate, *Proceedings of the National Academy of Sciences*, 107 (2010) 16438-16443.
- [9] D. Kralj, L. Brečević, J. Kontrec, Vaterite growth and dissolution in aqueous solution III. Kinetics of transformation, *Journal of Crystal Growth*, 177 (1997) 248-257.
- [10] M.A. Hood, K. Landfester, R. Muñoz-Espí, The Role of Residue Acidity on the Stabilization of Vaterite by Amino Acids and Oligopeptides, *Crystal Growth & Design*, 14 (2014) 1077-1085.
- [11] L. Chen, W.-H. Xu, Y.-G. Zhao, Y. Kang, S.-H. Liu, Z.-Y. Zhang, Synthesis of vaterite and aragonite crystals using biomolecules of tomato and capsicum, *Russian Journal of Physical Chemistry*, 86 (2012) 2071-2075.
- [12] C. Shivkumara, P. Singh, A. Gupta, M.S. Hegde, Synthesis of vaterite CaCO_3 by direct precipitation using glycine and L-alanine as directing agents, *Materials Research Bulletin*, 41 (2006) 1455-1460.

- [13] D. Rautaray, A. Sanyal, A. Bharde, A. Ahmad, M. Sastry, Biological synthesis of stable vaterite crystals by the reaction of calcium ions with germinating chickpea seeds, *Crystal Growth & Design*, 5 (2005) 399-402.
- [14] I. Sondi, E. Matijević, Homogeneous Precipitation of Calcium Carbonates by Enzyme Catalyzed Reaction, *Journal of Colloid and Interface Science*, 238 (2001) 208-214.
- [15] Y. Mori, T. Enomae, A. Isogai, Preparation of pure vaterite by simple mechanical mixing of two aqueous salt solutions, *Materials Science and Engineering: C*, 29 (2009) 1409-1414.
- [16] J.N. Butler, *Carbon dioxide equilibria and their applications*, Lewis Publishers, INC., Chelsea, 1991.

Conclusion and Roadmap to the Future

The current chapter provides conclusions for the study of NiNPs catalysis for hydration of CO₂ and its applications. All the major findings are presented and the further research areas have been suggested.

10.1 Overall conclusion of the thesis

Chapter 4 presents that NiNPs acted as catalyst for the hydration of CO₂. The catalytic activity of the NiNPs was shown by pH change method when CO₂ is bubbled in DI water. The steps of the catalytic process of hydration of CO₂ were based on the XPS results. NiNPs showed no leaching in acidic environments and there was no effect of Ni²⁺ ions on the catalytic activity of NiNPs.

Chapter 5 presented further validation of the catalytic activity of NiNPs. Different nanoparticles (Fe₂O₃ and NiO) were tested to for catalytic activity.

Although all the nanoparticles (Fe_2O_3 and NiO) showed an enhancement in the CO_2 uptake, no catalytic activity was observed in the pH change experiments. This asserted that the increase in CO_2 saturation was not a reason for the reported pH change. pH change experiments using 12% CO_2 -Air mixture also showed catalytic activity of NiNPs for hydration of CO_2 . This is important because the flue gas from power plants has a maximum concentration of 12% CO_2 .

In chapter 6 was presented the photochemical and temperature dependence of rate of catalytic hydration of CO_2 in presence of NiNPs. A qualitative analysis was performed and it was observed that NiNPs show the best activity in presence of light including IR range energy range, rather than in absence of IR or in dark. The mechanistic overview of the process has been discussed. The activity of NiNPs for hydration of CO_2 was also found to be dependent on temperature. The catalytic activity was highest at temperatures between 20-30 °C and reduced at higher and lower temperatures. This is the reason why Ni was observed in sea urchin larvae for bone growth.

Chapter 7 presented data on application of catalysis of NiNPs to enhance CO_2 precipitation as CaCO_3 and CO_2 absorption in potassium carbonate solution. The NiNPs showed threefold increase in the amount of precipitation of CaCO_3 as compared to DI water without NiNPs. The precipitated CaCO_3 (calcite) has spherical morphology due to the nucleation of CaCO_3 crystals on NiNPs surface. The NiNPs showed a two times enhancement in the rate of CO_2 absorption in 50% (by weight) potassium carbonate solution. This can help intensify the CO_2 absorption process using carbonate solutions and reduce equipment size.

Chapter 8 presents a brief understanding of the effect of nanoparticle on the vapour-liquid equilibrium of CO₂-H₂O system. The enhancement of CO₂ saturation is dependent on the elemental composition of the nanoparticles in suspension. The CO₂ saturation concentration is dependent on particle concentration for NiNPs but was observed to be independent for oxide nanoparticles. The surface tension of the nanoparticle suspension was lower than that of DI water without nanoparticles. This change in surface tension is the reason for increase in saturation concentration of CO₂ in nanoparticle suspensions. The increase in CO₂ saturation as compared to DI water is independent of temperature. This can be used to develop novel aqueous based CO₂ separation systems.

A new method for the mineralization of CO₂ to CaCO₃ is presented in chapter 9. A novel “bridge reactor” along with a novel process for the mineralization of CO₂ is demonstrated. Gypsum was chosen as a mineral source for Ca²⁺ ions because gypsum has a larger solubility (i.e. 2 g/l) than most of the other Ca/Mg mineral sources as overviewed in chapter 2 (table 2.1). It is observed that the bridge reactor has higher yields of CaCO₃ than the control sample proving the capture of CO₂ in mineral form. The bridge reactor yielded 21% more carbonates as compared to the control and 17% more carbonates as compared to the theoretical yield. A mechanism for the working of the bridge reactor has been discussed. The mass transfer results show that there can be transfer of carbonate ions across the bridge based on a concentration gradient present at all times. In order for mass to transfer from the acidic side of the reactor to the basic side of the reactor, the concentration of the reactant on the acidic side has to be higher than the concentration of the reactant on the basic side.

10.2 Suggestions for future work

The reduction of global greenhouse gases is important for maintaining further climate changes. Mineralization of CO₂ into carbonate minerals is one of the safest methods for long term storage of CO₂ in the lithosphere. The mineralization of CO₂ at the moment is limited by various factors and in the current study one of the factors i.e. the hydration of CO₂ was addressed

10.2.1 Application to mineralization of CO₂

Bodor *et al.* [1] used the NiNPs to show that the enhanced hydration rate of CO₂ could be used to enhance the precipitation of CaCO₃ from CaO solution. They also concluded that in concentrated CaO solutions, the dissolution of CaO becomes the rate limiting step. The results in their study show that the NiNPs are active in enhancing Ca carbonation in diluted solutions. Therefore it is likely that use of NiNPs would be aptly suited for diluted brine carbonation as there is a lot of dissolved Ca and Mg ions in industrial brine solutions. This is worth for future studies.

10.2.2 Immobilization of NiNPs

As the NiNPs are very small in size there are chances of loss of the catalyst during large scale operations. Therefore it would be interesting to study the immobilization of the NiNPs on a catalyst support like alumina or silica. This would enable the reuse of these catalysts.

10.2.3 Optimization of transport process in the bridge reactor

A novel reactor has been demonstrated in this study. There isn't any relevant literature on the use of such type of reactor. Thus it provides an opportunity to study the transport processes in this novel setup. This would

provide more insight into the various reactions that can be achieved using this novel reactor. The momentum transport (fluid mechanics) studies would provide insight of the actual fluid motion within the reactor and energy transport could open new possible applications into new reaction systems i.e. temperature dependent slow mass transferred reactions. These studies would not only propose the use of this reactor for other possible reactions but also provide insight to the current reaction mechanism of tri-phasic reaction of mineralization of CO₂ using gypsum.

10.2.4 Study of influence of nanoparticles on vapour-liquid equilibrium

Chapter 8 provides the stepping stone for the influence of nanoparticles on the vapour-liquid equilibrium of gas-slurry system. It was found that the nanoparticles in suspension reduce the surface tension of the suspending media. This change in surface tension affects the CO₂-H₂O vapour liquid equilibrium. The same should be tested for other vapour-liquid systems (like ammonia-water) as well. A thermodynamic and mathematical model to relate the change in surface tension to change in vapour liquid equilibrium needs to be developed and tested. Influence of particle size on both surface tension and vapour liquid equilibrium can also be studied. Using microchannel systems one could study the effect of nanoparticle on interface mass transfer for gas-liquid systems.

References

- [1] M. Bodor, R.M. Santos, Y.W. Chiang, M. Vlad, T.V. Gerven, Impact of Nickel Nanoparticel of Mineral Carbonation, The Scientific World Journal, 2014 (2014) 921974.

APPENDIX -I

Calculations for Concentration of CO₂ using titration

$$M_{\text{NaOH}} = 0.1012$$

Concentration of NiNPs (ppm)	Reading 1 (ml)	Reading 2 (ml)	Reading 3 (ml)	Reading 4 (ml)	Average (ml)	Conc. of CO ₂ (M)	Std. Dev.
0	4	4	3.4	4.7	4.03	0.0403	0.005315
10	7.2	7.2	7	7	7.10	0.0710	0.001155
20	10	10	10.4	11	10.35	0.1035	0.004726
30	13	12.5	13	13.2	12.93	0.1293	0.002986
40	12	11.4	11.6	12	11.75	0.1175	0.003
50	12	12	11	10.5	11.38	0.1138	0.0075

10 ml of the DI water (or nanoparticle suspension) saturated with CO₂.

Sample calculation

$$M_{\text{CO}_2} \times V_{\text{CO}_2} = M_{\text{NaOH}} \times V_{\text{NaOH}}$$

$$M_{\text{CO}_2} = \frac{M_{\text{NaOH}} \times V_{\text{NaOH}}}{V_{\text{CO}_2}} = \frac{0.1 \times 4.18}{10} = 0.0418 \text{ M}$$

$$M_{\text{NaOH}} = 0.1011$$

Concentration of Al ₂ O ₃ NPs (ppm)	Reading 1 (ml)	Reading 2 (ml)	Reading 3 (ml)	Reading 4 (ml)	Average (ml)	Conc. of CO ₂ (M)	Std. Dev.
0	4	4	3.4	4.7	4.18	0.0418	0.005315
10	13	13	13.5	13	13.13	0.1313	0.0025
20	12	13	13.5	13.5	13	0.13	0.007071
30	13	13	13.5	13.5	13.25	0.1325	0.002887
40	13	12.5	13	14	13.13	0.1313	0.006292

$$M_{\text{NaOH}} = 0.0998$$

Concentration of Fe ₂ O ₃ NPs (ppm)	Reading 1 (ml)	Reading 2 (ml)	Reading 3 (ml)	Reading 4 (ml)	Average (ml)	Conc. of CO ₂ (M)	Std. Dev.
0	4	4	3.4	4.7	4.18	0.0418	0.005315
10	12.5	13	12	12.5	12.5	0.1247	0.004082
20	12	10.5	12	13	11.88	0.1186	0.010308
30	13.5	13.5	13	13	13.25	0.1322	0.002887
40	13	13	12.5	13	12.87	0.1284	0.0025

$$M_{\text{NaOH}} = 0.0987$$

Concentration of NiONPs (ppm)	Reading 1 (ml)	Reading 2 (ml)	Reading 3 (ml)	Reading 4 (ml)	Average (ml)	Conc. of CO ₂ (M)	Std. Dev.
0	4	4	3.4	4.7	4.18	0.0418	0.005315
10	13	13.5	12.7	13.7	13.1	0.1310	0.003989
20	13.5	13.5	13.2	13.5	13.3	0.1332	0.001767
30	14	12.8	14	14.5	13.6	0.1365	0.006181
40	14.5	14.5	14	14	14	0.1400	0.002700

APPENDIX -II

Calculations and comparison of theoretical and experimental rate of hydration of CO₂ (uncatalysed and catalysed)

Observations:

Residence time: 0.1 s

Diameter of bubbles: 1 mm = 1×10^{-3} m

Gas flow rate: 1.69 moles/min = 0.633 ml/min

Diameter of the glass jar (ID): 59 mm = 5.9×10^{-2} m

kinetic constant for CO₂ interface transfer (k) [1] = 5.5×10^{-6} m/s

kinetic constant for hydration of CO₂ (k₂) = 0.0035 s^{-1} [2]

Theoretical Calculations:

Due to the small height of the bubble column reactor (75 mm) the bubble size did not increase and was assumed to be constant for the calculations.

1. Volume of the bubble: $\frac{4}{3} \pi r^3$
 $= (4 \times 3.14 \times (1 \times 10^{-3})^3) / 3 = 4.18 \times 10^{-9} \text{ m}^3 = 4.18 \times 10^{-3} \text{ cm}^3 = 4.18 \times 10^{-3} \text{ ml}$

2. Flow rate of bubble = $\frac{\text{gas flow rate}}{\text{volume of single bubble}} = \frac{0.633}{4.18 \times 10^{-3}} = 151.43 \text{ bubbles/sec} \sim 152 \text{ bubbles/sec}$

3. Number of bubbles = Flow rate of bubbles x residence time
 $= 152 \times 0.1 = 15.2 \text{ bubbles}$

4. Interface area (bubbles) = No of bubbles x Area of bubble
 $= 15.2 \times 4 \times \pi \times (1 \times 10^{-3})^2 = 2.009 \times 10^{-4} \text{ m}^2$

5. Cross section area of glass jar = $\pi r^2 = 3.14 \times (5.9 \times 10^{-2})^2 = 1.093 \times 10^{-2} \text{ m}^2$

6. Total interface area (A) = Cross section area + Interface area (bubbles)
 $= 1.093 \times 10^{-2} + 2.009 \times 10^{-4} = 1.11 \times 10^{-2} \text{ m}^2$

The concentration of the gas at the interface is given by the ideal gas equation and is
 $C = 40 \text{ moles/m}^3 = 4 \times 10^{-2} \text{ M.}$

7. Rate of CO₂ interface transfer = $A \times k \times C = 1.11 \times 10^{-2} \times 5.5 \times 10^{-6} \times 40 = \underline{2.442 \times 10^{-6} \text{ mol/s}}$

The rate constant for hydration of CO₂ is taken as pseudo-first order kinetics

8. Rate of CO₂ hydration = $k_2 \times \text{CO}_2 \text{ in solution} = 0.0035 \times 2.442 \times 10^{-6} = \underline{8.547 \times 10^{-9} \text{ mol/s}}$

Calculations for the experimental results:

The rates obtained from the figure 4.7a. The data considered till autocatalysis is observed in the figure (i.e. 40 sec).

$$\begin{aligned}\text{Rate of uncatalysed CO}_2 \text{ hydration} &= \frac{\text{Change in conc. of H}^+ \text{ ions}}{\text{Time}} \\ &= \frac{10^{-6} - 10^{-5.88}}{40} = \underline{7.95 \times 10^{-9} \text{ mol/s}}\end{aligned}$$

$$\begin{aligned}\text{Rate of catalysed CO}_2 \text{ hydration} &= \frac{\text{Change in conc. of H}^+ \text{ ions}}{\text{Time}} \\ &= \frac{10^{-6.2} - 10^{-4.8}}{40} = \underline{3.80 \times 10^{-7} \text{ mol/s}}\end{aligned}$$

It can be observed from the calculations that, the uncatalysed rate of CO₂ hydration in the experiment is close to the calculated theoretical value (i.e. 8.547 x 10⁻⁹ mol/s), whereas the catalysed rate value is higher than the theoretical value but lower than the mass transfer rate (i.e. 2.442 x 10⁻⁶ mol/s)

References

- [1] R.M. Noyes, M.B. Rubin, P.G. Bowers, Transport of Carbon Dioxide between the Gas Phase and Water under Well-Stirred Conditions: Rate Constants and Mass Accommodation Coefficients, The Journal of Physical Chemistry, 100 (1996) 4167-4172.
- [2] D.M. Kern, The hydration of carbon dioxide, Journal of Chemical Education, 37 (1960) 14.

APPENDIX -III

The emission spectra of the solar simulator with and without filter has been presented as obtained from the manufacturer.

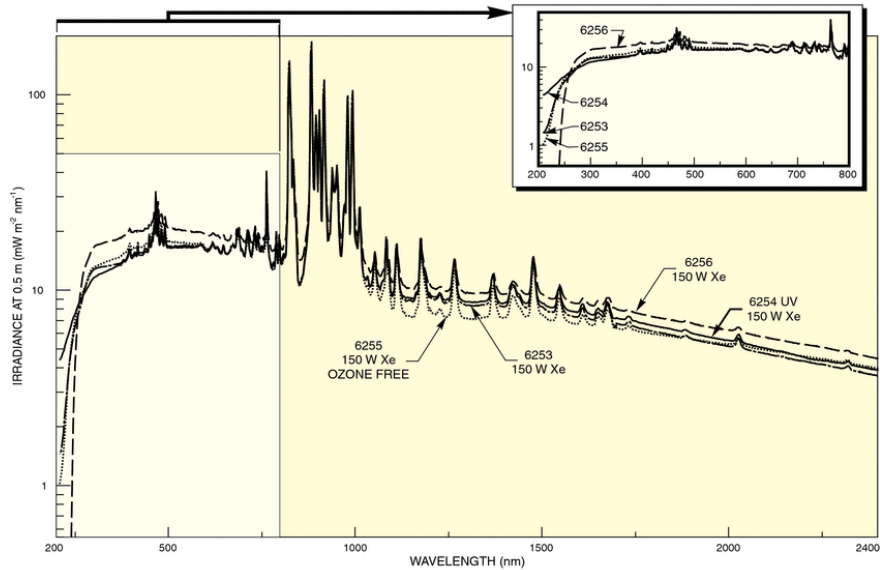


Figure A3.1: Emission spectrum of the solar simulator (6255, 150 W Xe Ozone free) for the entire wavelength range.

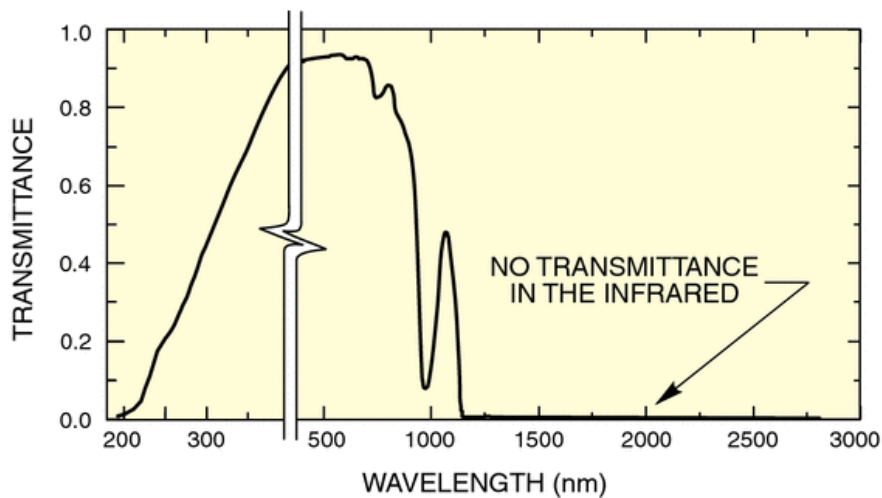


Figure A3.2: Emission spectrum obtained after using the IR filter.

APPENDIX -IV

Curve fitting of CO₂ absorption in 50% potassium carbonate solution in presence and absence of NiNPs.

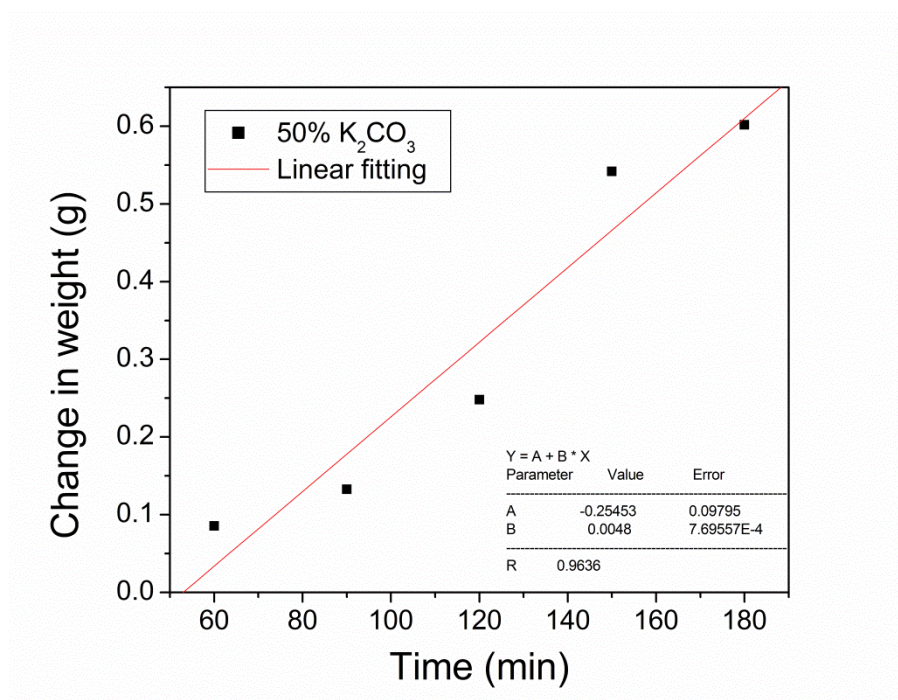


Figure A4.1: CO₂ absorption in 50% potassium carbonate solution using liner fit.

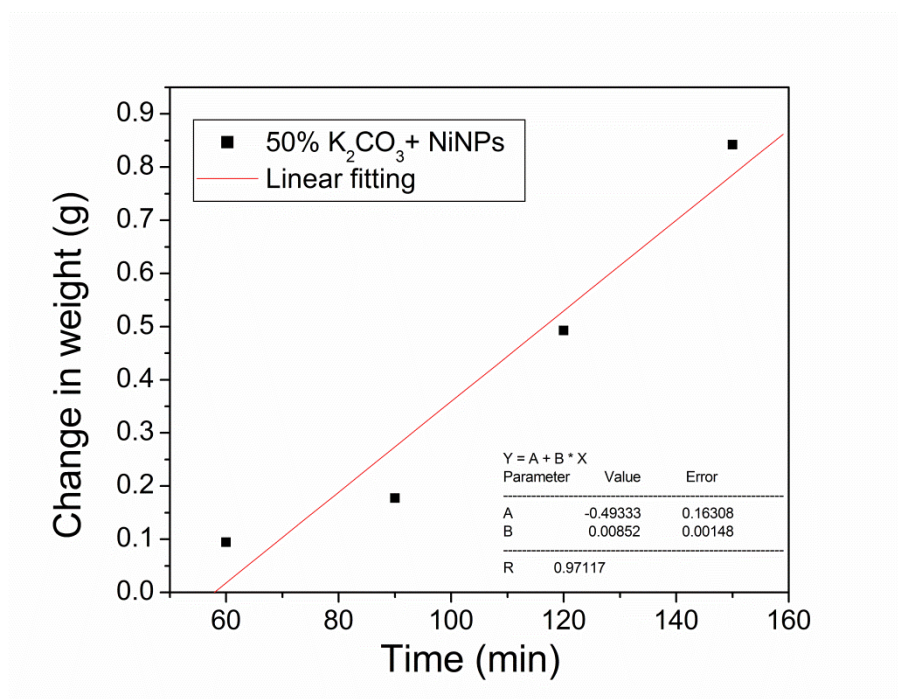


Figure A4.2: CO₂ absorption in 50% potassium carbonate solution in presence of NiNPs using liner fit.